Advanced Heat/Mass Exchanger Technology for Geothermal and Solar Renewable Energy Systems

Final Report

December 16, 2014

Reporting Period: September 20, 2010 – September 17, 2014

Project Monitor:
William Vandermeer, Project Officer
Geothermal Technologies Program
U.S. DOE Golden Field Office
1617 Cole Boulevard, B-22, Suite 350
Golden, CO 80401
Phone 303 275-4952
Facsimile 720 356-1350
william.vandermeer@go.doe.gov

Name of Contractor:
Board of Regent s, NSHE, OBO University of Nevada, Reno
Office of Sponsored Projects/MS 325
1664 N. Virginia Street
Reno, Nevada 89557

Contract Number: DE-EE0003231

Principal investigator:
Miles Greiner, Ph.D.
Mechanical Engineering Department (MS 312)
University of Nevada, Reno
Reno, NV 89556
Phone 775 784-4873
Facsimile 775 784-6714
greiner@unr.edu

Co-Principal Investigators:
Amy Childress, Ph.D.
Sage Hiibel, Ph.D.
Kwang Kim, Ph.D.
Chanwoo Park, Ph.D.
Richard Wirtz, Ph.D.

Background and Objectives

Northern Nevada has abundant geothermal and solar energy resources, and these renewable energy sources provide an ample opportunity to produce economically viable power. Heat/mass exchangers are essential components to any energy conversion system. Improvements in the heat/mass exchange process will lead to smaller, less costly (more efficient) systems.

There is an emerging heat transfer technology, based on micro/nano/molecular-scale surface science that can be applied to heat/mass exchanger design. The objective is to develop and characterize unique coating materials, surface configurations and membranes capable of accommodating a 10-fold increase in heat/mass exchanger performance via phase change processes (boiling, condensation, etc.) and single phase convective heat/mass transfer. The overall project includes five sub-projects:

Project 1: Efficient Boiling Surfaces for Geothermal Power Cycles (R. Wirtz)

Compressed laminations of fine filament metallic screen overlaying a heat transfer surface in subcooled flow boiling of water at 0.2atm have been shown to be able to accommodate in excess of 4.5MW/m2 with very small wall superheats of approximately 5.0K. The objective is to translate this scalable technology to the low-temperature geothermal energy environment where hydrocarbons such as pentane are the working fluids of the power cycle. A reduction in power cycle re-boiler (evaporator) tube wall superheat will lead to an improvement in power plant thermal efficiency.

Project 2: Heat and Mass Transfer in Membrane Contactor Processes (A. Childress, S. Hiibel)

For the fundamental study of membrane contactor processes focused on membrane distillation driven by renewable energy or low grade heat and pretreated using forward osmosis, the overall objectives are: 1) to improve understanding of mass and heat transfer in the membrane distillation process, 2) to improve understanding of mass transfer in the forward osmosis process, 3) to optimize process properties for the combined FO-MD system, and 4) to develop mass and energy balances for a membrane/renewable energy system.

Project 3: Enhanced Single Phase Heat Transfer in Intermittently-Grooved Channels (M. Greiner)

Cutting continuous transverse grooves into the walls of rectangular cross-section passages has been shown to enhance heat transfer by 55% compared to typical flat passages with the same pumping power. The current experimental and computational work will develop intermittently-grooved channels, which trigger developing and decaying Tollmien-Schlichting waves at Reynolds numbers of Re ~ 103. This configuration augments heat transfer with even lower pumping power requirements than continuously-grooved channels, and is suitable for direct dry-cooled power plant condenser units.

Project 4: Reinforced Super-hydrophobic Surfaces for High-Performance Condensers (K. Kim)

With proper promotion dropwise condensation produces much higher heat transfer rates than filmwise condensation. However, the enhancement significantly drops with the time due mainly to the degradation of organic promoters. The objective is to develop a material engineered and long term performance-effective technique for enhancing heat transfer rate in steam condensation, which would dramatically reduce the footprint and manufacturing cost of condensers. The main expected outcome of the proposed work is to craft a unique technique for promoting dropwise condensation.

Project 5: Nano-Coating, Structured Porous Surfaces for Evaporation/Boiling Heat Transfer Enhancement (C. Park)

The objectives are to develop advanced micro-scale, structured porous-layer surfaces (called a wick) and nano-coating materials/techniques for high performance two-phase heat transfer (e.g., boiling and evaporation) application. The structured wick provides an effective way of increasing surface area for vapor venting and liquid distribution which leads to a two-phase heat transfer enhancement. The nano-coating for a surface wetting control (hydrophilic or hydrophobic) can further improve the two-phase heat transfer. The enhancement of the two-phase heat transfer using the nano-coating, structured porous surfaces will be measured using a boiling/evaporation experimental setup. The physical properties (permeability, porosity and specific surface area and contact angle) of the wick materials will be measured to assist the characterization experiment of the two-phase transfer in the wick materials.

Advanced Heat/Mass Exchanger Technology for Geothermal and Renewable Energy Systems

Project 1 Final Report: Efficient Boiling Surfaces for Geothermal Power Cycles

R.A. Wirtz
Mechanical Engineering Department
University of Nevada, Reno
Reno, NV 89557

775-784-6714

rawirtz@unr.edu

October 10, 2013

Executive Summary

The evaporators (re-boilers) generally implemented in binary fluid geothermal power plants are of traditional steel tube-in-shell design with hot brine (tube-side fluid) evaporating a hydrocarbon (shell-side fluid).

A lamination of compressed, fine-filament screen provides an open-cell, structured-porous matrix with large specific surface area and very high pore density. Variation of wire diameter, wire pitch and laminate pitch allows for creation of monolithic structures having predetermined porosity, specific surface area, effective thermal conductivity and pore density. When deployed as a copper filament surface coating in sub-cooled, flow boiling of water at 0.2atm, we have shown that these structures can accommodate wall heat flux up to 4.5MW/m^2 (4500kW/m^2) with only moderate superheats because of the large surface area inherent to the media and very high density of open-cell, cusped-shaped pores (potential bubble nucleation sites). A typical sub-millimeter thickness surface coating consists of several layers of compressed, fine-filament screen that are diffusion-bonded together and to the heat transfer surface, producing a three-dimensional array of small interconnected pores. We believe the cusped-shape of the pores is responsible for the very high bubble nucleation site density that the surfaces produce.

The objective is to translate this scalable technology to the low-temperature geothermal energy environment where hydrocarbons such as pentane are the working fluids of the power cycle. A reduction in power cycle re-boiler (evaporator) tube wall superheat will lead to a reduction in entropy generation rate, and thus an improvement in power plant thermal efficiency.

Sub-cooled liquid, flow-boiling experiments with Isopentane and n-pentane at 3.0bar pressure assess the utility of copper- and steel-filament screen laminate surface coatings as effective bubble nucleation sites. Boiling performance characteristics are documented. High-speed video records the dynamics of the ebullition process.

High-speed video show that at high heat flux, ebullition is stable but periodic-unsteady. Isopentane and n-Pentane are found to produce nearly identical boiling characteristic curves. At the same applied heat flux, the sub-surface superheats of copper filament coatings are much smaller than the steel filament coating sub-surface superheats. This is attributable to the relatively small thermal conductivity of stainless steel, which gives rise to a relatively large temperature rise across the thickness of the steel coating.

Increased sub-cooling and flow intensity shift boiling performance curves upward; the most notable effect being an increase in Critical Heat Flux. CHF enhancement is found to be intrinsically linked to the surface area enhancement ratio (βδ), which has an optimum value for the present coating material and fluid of $\left(\beta\delta_{opt} \cong 11\right)$. Since this is essentially the same value obtained by Penley and Wirtz in their experiments with copper coatings boiling water, the implication is that the area enhancement factor is the dominate parameter in the determination of optimal surface performance. The fluid properties and coating material properties are of secondary importance.

Our best performing surface, a lamination of 200-mesh copper plain weave, can accommodate up to 0.91 MW/m^2 (910kW/m^2) with a superheat of only 9.4K. Thermodynamic analysis shows that its entropy generation rate is minimum when it boils normal pentane. Boiling Isopentane leads to a slightly higher entropy generation rate since it is a lower temperature process. If the coating is Stainless Steel, then at the same heat flux, there is a relatively large temperature increase across the thickness of the coating due to the smaller thermal conductivity of stainless steel. This gives rise to larger superheats of the sub-surface, so there is an approximate 45% increase in entropy generation rate. It is interesting to note that steel coatings can also accommodate up to 0.9MW/m^2.

These surfaces out-perform plain (un-enhanced) surfaces by a wide margin. At applied heat fluxes ranging up to 100kW/m^2 (0.1MW/m^2) surface performance is similar to that of other commercial (enhanced) surfaces. However, we suspect these surfaces can accommodate much greater heat fluxes with relatively small superheats than existing enhanced surfaces. Since Critical Heat Flux data for boiling pentane on commercial (enhanced) surfaces is not in the open literature, this issue is not resolved.

Recommendations

We developed a fabrication methodology (diffusion bonding cold rolled screen to form the lamination) that is suitable to the laboratory environment. It is not clear that this methodology is suitable to the large-scale manufacturing environment. Electric or ultrasonic welding could be a better methodology for large scale manufacture. These alternatives (and others) should be investigated.

Due to the relatively short duration of the project, we were unable to debug our apparatus and run tests on tubular surfaces. Follow-up experiments with tubular surfaces, in conjunction with an established re-boiler manufacturer should be undertaken. Experiments that back-to-back compare this technology to existing enhanced surfaces should be conducted.

Project 1 Final Report: Efficient Boiling Surfaces for Geothermal Power Cycles

R.A. Wirtz

Introduction

The evaporators (re-boilers) generally implemented in binary fluid geothermal power plants are of traditional steel tube-in-shell design with hot brine (tube-side fluid) evaporating a hydrocarbon (shell-side fluid). The objective is to develop a scalable re-boiler tube outer surface that will result in a 10-fold improvement in outer-surface boiling performance over current practice.

A lamination of compressed, fine-filament screen provides an open-cell, structured porous matrix with large specific surface area and very high pore density. Variation of wire diameter (d) [1], wire pitch (inverse of mesh number, M) and laminate pitch ($2dC_f$) allows for creation of monolithic structures having predetermined porosity (ε), specific surface area (β), effective thermal conductivity (ke) and pore density [1,2][2]. When deployed as a copper filament surface coating in sub-cooled, flow boiling of water at 0.2atm, we have shown that these structures can accommodate wall heat flux up to 4.5MW/m^2 with only moderate superheats because of the large surface area inherent to the media and very high density of open-cell, cusped-shaped pores (potential bubble nucleation sites) [3,4].

A typical sub-millimeter thickness surface coating consists of several layers of compressed, fine-filament screen that are diffusion-bonded together and to the heat transfer surface, producing a three-dimensional array of small interconnected pores. Steel-filament coatings have wetted specific surface areas that can range to 900cm^2/cm^3, and pore densities that can range to approximately 5 million pores per cm^2 plan-area (a 12-layer lamination of 500-mesh plain weave). Pore hydraulic diameters ($D_h = 4\varepsilon/\beta$) are typically 20µm - 45µm. We believe the cusped-shape of the pores is responsible for the very high bubble nucleation site density that the surfaces produce.

Project Objective

The objective is to translate this scalable technology to the low-temperature geothermal energy environment where hydrocarbons such as pentane are the working fluids of the power cycle. A reduction in power cycle re-boiler (evaporator) tube wall superheat will lead to a reduction in entropy generation rate, and thus an improvement in power plant thermal efficiency.

Technical Approach

Sub-cooled, (parallel) flow-boiling experiments with Isopentane and n-pentane at 3.0bar pressure assess the utility of copper- and steel-filament screen laminate surface coatings as effective bubble nucleation sites. Boiling performance characteristics are documented. High-speed video records the dynamics of the ebullition process. Two boiling geometries are studied:

1. A 10mm x 30mm plane surface in a 10mm x 50mm channel.
2. The inner surface of a 46cm long annular channel (tubular surfaces).

Period of Performance

September 20, 2010 – September 20, 2012 (24 months)

---

[1] See the list of Symbols at the end of Project 1 Final Report.

[2] See the list of Cited Work at the end of Project 1 Final Report

Personnel

Principal Investigator: 10/20/2010 – 12/31/2011
Research Consultant: 01/01/2012 – 10/20/2012

Richard A. Wirtz, Professor Emeritus
Mechanical Engineering Department
University of Nevada, Reno
Reno, NV 89557
(O): 775-784-6714
rawirtz@unr.edu

Post Doctoral Associate: 10/20/2010 – 12/31/2011
Principal Investigator: 01/01/2012 – 10/20/2012

Paul J. Laca, Research Assistant Prof.[3]
Mechanical Engineering Department
University of Nevada, Reno
Reno, NV 89557
(O): 775-682-8408
placa@unr.edu

Publications Stemming From This Work

Laca, P.J. and Wirtz, R.A., 2012, "Flow Boiling of Sub-Cooled Pentane On a Micro-Porous Coating", ASME 6th Conf. on Energy Sust., ESFuelCell2012-91316, July 23-26, 2012, San Diego, CA.

Relevant Literature

It is well understood that boiling enhancement can be achieved by proper selection of the boiling surface [5,6]. Boiling improvement on enhanced surfaces is commonly attributed to an increase in the number of active bubble nucleation sites, as well as increases to bubble departure frequency, and improved surface wettability. These effects all result in an increase in the time-averaged solid surface area that is in contact with rapidly moving thin film menisci of nucleating bubbles; and, consequently by transient thin film evaporation, which Ma and Peterson [7] show provides the major fraction of the phase change heat transfer. These enhancement mechanisms can be achieved by the creation of a large number of interconnected, re-entrant vapor-containing cavities ("pore and tunnel" surfaces, porous surfaces, etc.), and when appropriately selected, enhanced surfaces will provide a substantial decrease in wall superheat, as well as provide improvement in CHF [8].

Further increase in CHF can be achieved with the use of sub-cooling and flow boiling [9,10]. Early work quantifying the increase in CHF with sub-cooling was suggested by Zuber in 1961 [11, 12], when he proposed a semi-empirical modification to his well-known hydrodynamic model for CHF in pool boiling to include a linear effect of sub-cooling. Kandlikar [13] developed a theoretical model that also suggests a linear relationship between sub-cooling and CHF for pool boiling, and in other work Kandlikar discusses the current understanding of CHF within sub-cooled flow-boiling [14]. Hall and Mudawar [15] comment on the multitude of empirical and semi-empirical models for sub-cooled flow-boiling of water at pressures greater than 1atm; and, they propose a model of their own.

Kandlikar and co-workers [16] and Carey [17] note that increased sub-cooling leads to reduced bubble growth rates such that bubbles form within the heat transfer controlled regime instead of the inertial controlled regime. They also found that increased flow velocity increased the departure frequency, but caused larger cavities to stop nucleating. Okawa *and* coworkers [18] found that the trajectory of bubbles formed at low heat fluxes can slide along a vertical surface whereas at high heat fluxes, inertial effects of bubble formation can propel bubbles away from the surface with a significant velocity. Warrier, Basu, and Dhir [19] performed dimensional analysis to develop a heat transfer model for the condensation rate of vapor bubbles residing in sub-cooled water.

Porous Coatings

You et al.[20] discuss boiling enhancement of dielectric fluids on micro-porous surfaces consisting of silver particles, epoxy binder, and a volatile carrier. Thinner coatings provided better performance, and they found an optimal particle size of about 20μm. In addition, they noted that the enhanced surfaces decreased the bubble departure size and increased the bubble departure frequency, which is suspected to be due to channeling of exiting vapor into a relatively high speed vapor jet, which breaks off before coalescence with adjacent bubbles. In another fundamental study, El-Genk and Parker investigated

---

[3] Prof. Laca is no longer affiliated with the University.

boiling of HFE-7100 on open-cell porous graphite [21]. They found that porous graphite improved CHF, decreased incipient overshoot, and provided up to a 16-fold improvement in heat flux over an unenhanced copper surface at 10K superheat.

Afgan et al. [22] and Cieśliński [23] improved the boiling performance of water at atmospheric pressure utilizing metallic-particle porous surface enhancements. Afgan et al. used sintered porous coatings of 63-100μm Cr-Ni particles, which provided high heat transfer coefficients for a limited heat flux range. Cieśliński's surfaces included scored surfaces as well as metallic porous surfaces consisting of aluminum, copper, molybdenum, brass, and stainless steel. He found that good thermal contact of the coating was an important performance parameter, and that aluminum porous surfaces provided the best enhancement.

Screen-Laminate Coated Surfaces

Jakob [24] makes an early reference to the use of a screen bonded to a heat transfer surface to promote pool boiling. He attributed the observed performance enhancement to the increase in surface area that the screen provided. Vasil'Yev [25] and, Brautsch and Kew [26] investigated boiling on surfaces that have a wire mesh overlaying (but not bonded to) the heat transfer surface. The general finding is that covering a smooth surface with a mesh enhances boiling when the mesh "size" is similar to the bubble departure diameter.

More recently, Li and Peterson [27] obtained significant enhancement to atmospheric pressure, saturated pool boiling of water by diffusion-bonding multi-layer copper screen laminates directly onto a horizontal copper surface. Similar to Liter and Kaviany's [28] observation regarding capillary pumped liquid re-flood of porous cones, they observed that most of the ebullition occurred at the edges of their 8mm square test articles. Their "best" surface was able to accommodate up to 2.1MW/m^2 with a superheat of approximately 12K. Subsequently, Penley and Wirtz [29] utilized *compressed*, multi-layer screen laminates bonded to vertical copper surfaces in saturated pool boiling of water at atmospheric and sub-atmospheric pressure. Screen laminate disks, of 4cm^2 plan area (22.6mm diameter), were compressed to promote bonding of adjacent screens and establish a uniform porosity, $\varepsilon = 43\%$. They documented the performance of 12 screen laminate surfaces with lamination thickness, δ ranging from 190μm to 1300μm and specific surface area, β ranging from 10,000m^{-1} to 57,000m^{-1}. They found that saturated, pool boiling performance correlates with the area enhancement factor ($\beta\delta$ = wetted surface area/plan area), and their boiling heat transfer correlation shows that there is an optimum value of area enhancement factor ($\beta\delta = 18.8$) that maximizes pool boiling performance. Their "best" surface (a 420μm thick lamination of 145 mesh plain-weave) is shown to accommodate up to 2.1MW/m^2 with 9K superheat at a pressure of 1.0atm; and, 1.5MW/m^2 with 8K superheat at 0.2atm.

In more recent work, Penley and Wirtz [3, 4] documented the subcooled, *flow boiling* performance of ten 22.6mm diameter, disk shaped, compressed screen laminate surfaces in a 10mm x 30mm channel ($\varepsilon = 0.43$, $5 \le \beta\delta \le 37$, $2K \le \Delta T_{sub} \le 35K$). All experiments were conducted with water at 0.2atm pressure (T_{sat} = 60^{o}C). Heat flux of up to 4.5MW/m^2 is achieved at 35K sub-cooling at a channel Reynolds number of 6,000, which represents a 3.5-fold increase in Critical Heat Flux (CHF) over that of saturated pool boiling on the same surface. Results show that CHF is strongly correlated with sub-cooling; and the effect of sub-cooling is more pronounced as the channel Reynolds number is increased. High speed video imagery (up to 8100fps) and long range microscopy are used to document bubble dynamics. At small sub-cooling and Reynolds number, micro-bubbles ejected from the surface coalesce to form a vapor cloud that resides adjacent to the surface, inhibiting liquid re-flood of the surface. An increase in flow intensity (Reynolds number) displaces the cloud downstream, exposing the surface to more liquid re-flood with an associated increase in CHF. With large sub-cooling, ebullition is periodic-unsteady. It is shown that time intervals with little micro-bubble ejection cannot accommodate the applied heat flux, so the surface "heats up" (superheat increases) and more vigorous evaporation ensues, resulting in micro bubble ejection and coalescence, and a reduction in superheat. The vapor cloud eventually collapses and the cycle is repeated at approximately 6 – 10Hz rate. This surging of bubble growth and collapse is observed to very high heat fluxes until points just prior to CHF, where collapse of the bubble is never completed, and a persistent blanket of vapor is seen on the surface.

Screen-Laminate Coated Fins

Laca and Wirtz [30] conducted saturated, pool boiling experiments with tapered copper fins coated with compressed copper screen-laminations. They found that vertically oriented fins outperform horizontally oriented fins. They suggest that vapor bubbles that sweep the vertical surface result in a greater boiling heat transfer coefficient. Their “best” surface is shown to accommodate up to 1.4MW/m^2 fin-base heat flux. Subsequent saturated pool boiling experiments with a coated wavy wall showed ebullition to be periodic-unsteady with ~15Hz repetition rate [31]. Performance was similar to that of a coated plane-surface [29]

Screen-Laminate Flow-Through Fins

Holland and coworkers [32] studied flow boiling of a dielectric fluid (FC-72) in a porous (screen-laminate) fin. At high heat flux that is normally associated with the Critical Heat Flux Condition, they observed stable boiling with all four heat transfer regimes identified by Tung and Dhir [33] simultaneously operable (vapor-phase convection at the fin-root with nucleate boiling, transitional boiling and liquid-phase convection successively further out from the fin-root). Zhao and Wirtz [34] repeated Holland et al’s. experiments with isopentane at 3.0bar. They observed stable boiling with fin-root heat fluxes ranging to 0.6MW/m^2. Their calculations of entropy generation rate [35] showed that screen-laminate fins are more thermodynamically efficient than competing surface morphologies.

Table 1- 1 Properties of Screen Laminate Coatings

M x d [mm^{-1} x mm]	[in^{-1} x in]	material	Layers N	Thickness δ [mm]	Porosity ε	β [cm^{-1}]	Dh [μm]	($\beta\delta$) [-]
(5.7 x 0.056)	(145 x 0.0022)	316L SS	4	0.21	0.43	400	43	8
(7.9 x 0.051)	(200 x 0.0020)	Cu, 316L SS	4 4, 8	0.24 0.24, 0.47	0.43	440	39	11 11, 21
(19.7 x 0.025)	(500 x 0.0010)	316L SS	4	0.16	0.43	900	19	15

Research Results

Task 1.1.0 Establish Pentane-Based Pool Boiling Test Capability

Tasks 1.1.0 and 1.3.0 have been combined. Rather than develop and maintain separate pool-boiling and flow-boiling test facilities, we simulate the pool-boiling environment by running our flow-boiling facility at low Reynolds number, $Re_{ch} = V_o D_{ch}/\nu = 1{,}000$ where V_o is the sub-cooled liquid average velocity, D_{ch} is the test section hydraulic diameter and ν is the kinematic viscosity of liquid pentane. Visual observation of ebullition at this low flow rate confirm that buoyant convection is dominant.

Task 1.3.0 Establish Pentane-Based Flow Boiling Test Capability

Test Articles

Coatings consist of stacked and bonded layers of copper (Cu) or 316L stainless steel (SS) filament plain weave wire mesh. Each lamination is characterized by its mesh number, M (filaments per inch), the filament diameter (d), the number of layers that comprise the lamination (N), and resulting thickness (δ). Table 1-1 summarizes the characteristics of the screen laminates considered. The table lists the mesh geometry (M x d), the number of layers and the lamination thickness. Geometric equations [1] are used to quantify nominal properties of the screen laminate surfaces: porosity (ε), specific surface area (β), and pore hydraulic diameter, $D_h=4\varepsilon/\beta$, which is used as a metric of the relative pore size. The table also lists the surface area enhancement ratio (βδ=wetted surface area/plan area), which Penley and Wirtz [3, 4, 29] have shown to be an important parameter that links boiling performance to surface morphology.

We cold-roll the individual layers of the screen laminations to establish a constant porosity, ε= 0.43. The resulting laminations have specific surface area that ranges from 400 cm^2/cm^3 to 900 cm^2/cm^3; pore size (D_h) ranging from 19µm to 43µm; and, $8 \le \beta\delta \le 21$. In the following, screen-laminate test surfaces are identified using the following convention: **MA mmM-nnN-ε**, where **MA** is the material (Cu or SS), **mm** is the mesh number, M [in^{-1}], **nn** is the number of layers in the lamination and **ε** is the porosity.

The coating is formed by diffusion bonding the randomly placed weave stack directly to a larger, 125µm thick copper or steel foil. The foil is prepared by sanding the surface area that is directly under the $3cm^2$ lamination with #600 emery paper. The foil serves as a lamination sub-layer, its temperature is T_s. Diffusion bonding of the copper coating is in a 0.04CO/0.96Ar atmosphere; and the Stainless Steel coating bonding is in a $0.25H_2/0.75N_2$ atmosphere. The surface is fixed in a dense alumina form (Cu: dense graphite form) and the temperature is ramped at ~5K/min to approximately 1300°C (Cu: 1060°C) and held for 60min. Cool-down at ~5K/min to ambient takes approximately 4hrs. The bottom of the foil substrate is electro-plated with Nickel and then silver alloy-brazed to the test article assembly.

The lower view of Figure 1-1 shows a 118µm thick section of a 2-layer lamination of 200-mesh, copper, plain weave screen that has been compressed to a porosity of $\varepsilon = 0.43$. The wire filament diameter is 51µm, and wire pitch is 127µm. The lamination has a nominal specific surface area, $\beta = 440\, cm^2/cm^3$ and nominal pore hydraulic diameter, $D_h = \frac{4\varepsilon}{\beta} = 39\mu m$. The section view clearly shows a lack of bond lines indicating a monolithic structure. We can speculate that nucleation initiates in the cusped corners of the pores shown in Figure 1-1. The upper view of Figure 1-1 is an SEM of Surface 200M-4N-43. The surface provides ≈ 24,800 interconnected pores (potential vapor nucleation sites) per cm^2 plan area.

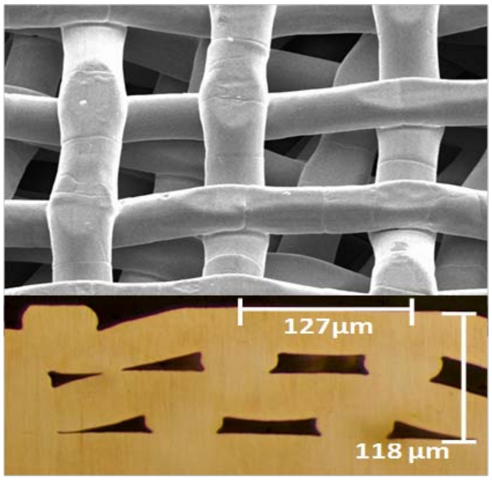

Fig. 1- 1 SEM of 200M4N-43 (top). Section of 200M2N-43 (bottom)

Test Article Assembly

Figure 1-2 is an exploded view rendering of the test article assembly, which is mounted to the back wall of the hydrocarbon test facility test section (thermocouples, tube compression fittings and O-rings are not shown). Each Test Article Assembly consists of the 10mm x 30mm test surface/foil sub-layer (1), a heater block/heat flux gage (5), and mounting ancillaries (2, 3, 4). The heat flux gage/heater block (5) is ASTM C10100, 99.99% (minimum) pure, oxygen-free copper, k = 391W/mK. The heater block portion of the element has provision for the interference fit of a 1000W cartridge heater (6). Four 0.5mm diameter holes are staggered along the centerline of the heat flux gage. Four 0.5mm diameter Type-T stainless steel sheathed, isolated junction thermocouples (not shown) are silver-brazed into these holes, allowing for the determination of heat flux and tip-temperature of the gage. Four 1/16" NPT stainless steel compression fittings (not shown) provide pass-through the stainless steel bulkhead (4) for the 4 heat flux gage thermocouples. The Teflon spacer (3) insulates the stainless steel wall adapter (2) and test surface (1) from the heater block/bulkhead (4, 5). It also provides lateral location to the heat flux gage/heater block so that the tip of the gage is in the plane of the back wall of the test channel. The adapter plate (2) seals the test article assembly to the test section. A pressure port in (4) is provided to pressurize the cavity surrounding the heat flux gage to system operating pressure (3bar). Items 2-6 are preassembled. Then, item 1 is silver-soldered to the tip of the heat flux gage and nickel plated sealing surface of the stainless steel adapter plate (2).

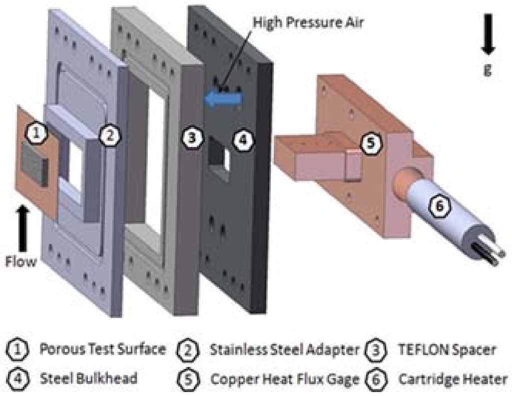

Fig. 1- 2 Test article assembly.

Figure 1-3 is a section view of the flow-boiling test facility test section assembly. It consists of a vertically oriented 10mm deep x 50mm wide x 340mm long stainless steel channel with a centrally located heat flux

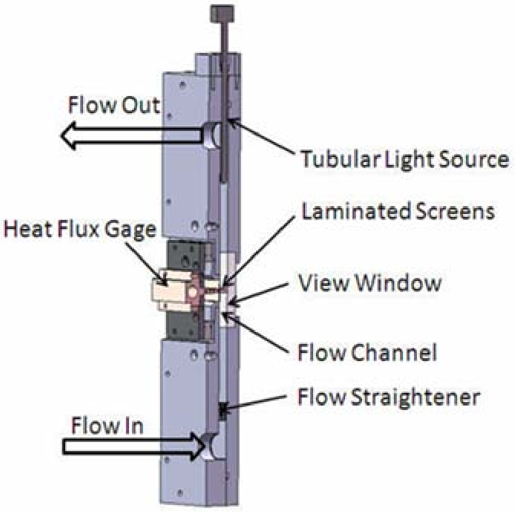

Fig. 1- 3 Test channel section view.

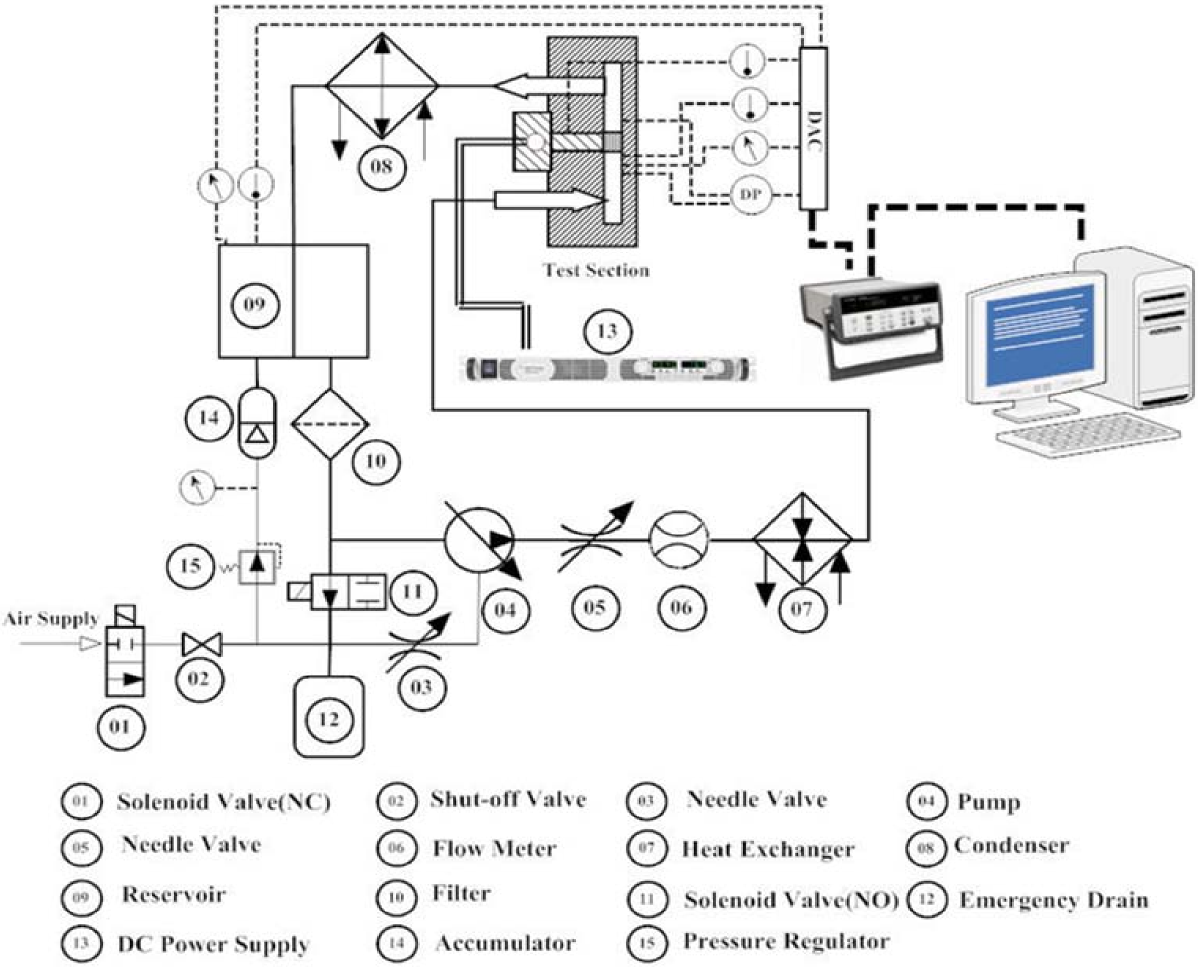

Fig. 1- 4 Flow loop schematic.

gage/screen laminate test article assembly. Flow is vertical, up-flow. A flow straightener is located upstream of the test article. Temperature and pressure sensors sense T_{in}, P_{in} (not shown in the figure). A viewing window allows for visual observation of the boiling phenomena.

Figure 1-4 is a layout schematic of the flow-boiling test facility with the vertical-flow channel test section in the middle of the figure. The test facility, which was originally built with DoE funding from an earlier project, consists of the test section, a dc-power supply, a data acquisition/control system (DAC), and a hydrocarbon storage and flow loop. An Agilent Technology N5770A power supply powers the test article. An HP 34970A data logger with 34901A and 34902A A/D cards monitors volumetric flow (Q); T_{in} and P_{in}; and the four type-T thermocouples embedded in the test article assembly heat flux gage. DAC is via LabView.

Liquid Isopentane is contained in a stainless steel reservoir (9) that is attached to a pressure controlled (15) accumulator (14). A magnetically coupled, air-driven pump (4) drives fluid from the reservoir through a 10µm filter (10), a flow control valve (5), a turbine flow meter (6) and a heat exchanger (7), to the test section inlet. The heat exchanger (7) is a two-fluid plate-fin heat exchanger, which is connected to a temperature-controlled hot water circulator that is set to bring the Isopentane temperature to the desired inlet temperature. Inside the test section/test channel, the fluid inlet pressure (P_{in}) and the inlet temperature (T_{in}) are measured. Upon exiting the test section, flow passes through a Propylene glycol-cooled condenser (8) to the reservoir.

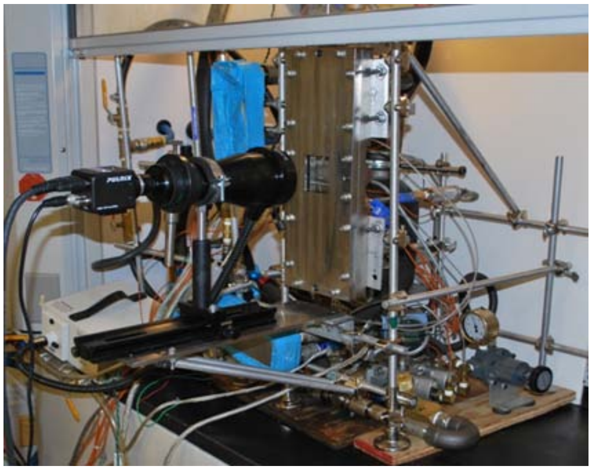

Fig. 1- 5 Hydrocarbon flow-boiling test rig.

Safety Provisions The experimental flow loop is put inside an externally vented laboratory hood, and instruments that could cause sparks are kept outside. The fluid is driven by a magnetically-coupled, air driven pump. All interfaces where pentane may escape from the test rig are Viton O-ring sealed. The wetted parts of pipes, fittings and hoses are either stainless steel, Buna-N, or TEFLON, all compatible with pentane. The system (see Fig. 1-4) has provision for emergency de-pressurization and evacuation (E/V) of fluid to a reservoir that is located remotely from the test facility (12). De-pressurization would also shut down the pump and power supply. E/V occurs if there is a fire or if preset temperature or pressure limits are exceeded.

Figure 1-5 is a view of the test section assembly installed with Pulnix high-speed video camera, 76mm Telecentric lens and ring-light in-place. The system provides up to 1000W to the 3cm^2 test surface. Experiments are conducted at 3bar with saturated or sub-cooled isopentane or n-pentane flowing at channel Reynolds number, $Re_{ch} = V_o D_{ch}/\nu$ ranging from 1,000 to 10,000, where V_o is the average flow velocity, $D_{ch} = 1.667cm$ is the 50mm x 10mm channel hydraulic diameter; and v is the kinematic viscosity of liquid pentane.

Task 1.2.0 Characterize Screen Laminate Enhanced Plane Surfaces in Sub-Cooled Pool Boiling

Task 1.2.0 has been combined with Task 1.4.0.

Task 1.4.0 Characterize Screen Laminate Enhanced Plane Surfaces in Sub-Cooled Flow Boiling

Procedure

Prior to installation in the test rig, the test surface is cleaned, oxides are chemically removed, and the surface is visually inspected. The test article is installed in the test section and pentane is pumped through the loop and the test section at 3.0bar absolute pressure, where the pentane is brought to saturation temperature and vigorously boiled for one hour for degassing. The reservoir is periodically "bled" to remove non-condensable gas.

Experiments are run at sequentially increasing power settings. The heater block power supply is set to a constant power level so that the heat flux through the test article reaches steady state. Once steady state operation is reached, raw data is collected for a period of five minutes at each power setting in 1 – 1.5 second intervals (approximately 250 data realizations). After this, a 1-second, 200 fps video is acquired at each power setting. The power setting is then advanced to the next increment, and the process is repeated until CHF is found, at which point the power is shut down, and the system cools to near ambient conditions. Flow rate or sub-cooling is then incremented, and the next boiling performance curve is generated. A complete data set has the surface boiling for approximately 30hrs, and we observe no shift in performance due to “ageing”.

Table 1- 2 95% Confidence Level Measurement Uncertainty.

Measured Quantity	Typical Values	2σ Uncertainty
Linear dimensions	5mm to 50mm	±0.125mm
Temperature, T	40 to 150°C	±0.25°C
Pressure, P	304kPa	± 1.9kPa
Volumetric Flow, Q	0.47 – 4.7L/min	± 0.1L/min

Table 1- 3 95% Confidence Level Calculated Quantity Uncertainty

Calculated Value	Typical Values	2σ Uncertainty
$\Delta T_{sat,b}$	10K	± 0.9K
q″	.94W/cm^2	±0.06W/cm^2
ΔT_{sub}	10K	± 0.5K
Re_L	6000	± 290
CHF	1.0MW/m^2	±0 .14MW/m^2

Data Management

A data “point” is the average of the 250 data realizations. A linear least-squares fit to the heat flux gage average (over 250 data realizations) temperature profile is used to determine the temperature distribution along the gage, yielding the temperature gradient and the temperature at the tip of the heat flux gauge, T_g. The heat transfer rate at the gage tip (q_g) is determined using Fourier’s Law. The solder joint between the heat flux gauge tip and the foil sub-surface is estimated to be 0.04mm thick ($k_{solder} = 53W/mK$), so the small gage tip-to-foil temperature drop is determined. Losses from the foil sub-surface are estimated and subtracted from the gage tip heat flux, q_g'' giving the boiling heat flux, q'' [36]. Losses from the un-coated surfaces of the steel foil are found to be less than 5% of q_g. Then, the small temperature drop across the foil sub-surface is determined, giving the boiling sub-surface temperature, T_s.

Direct measurement of pressure (P_{in}), and temperature (T_{in}) of the incoming flow to the test section is used to determine the saturation temperature, $T_{sat} \equiv T_{sat}(P_{in})$, which is then used to determine superheat, $\Delta T_{sat} \equiv (T_s - T_{sat})$, and subcooling $\Delta T_{sub} \equiv (T_{sat} - T_{in})$. The turbine meter volumetric flow rate (Q), is used to determine the channel Reynolds number, $Re_{ch} = \frac{4Q}{P_w \cdot \nu}$ where P_w = 12cm is the wetted perimeter of the channel, and the kinematic viscosity (ν) is evaluated at the inlet temperature. We believe the Reynolds number based on test article length (L = 10mm) is the appropriate flow characterization parameter, $Re_L = 0.6Re_{ch}$.

The complete data set (data points, videos and data reduction programs) is on-file at the Mechanical Engineering Department, University of Nevada, Reno. Contact RAWirtz@unr.edu .

Measurement Uncertainty

Table 1-2 shows the typical values of the measurements and our estimates of the associated 95% confidence level (2σ) uncertainties in the data for dimensions, temperatures, and pressure. Ninety-five percent level uncertainties in calculated results are calculated through a Monte Carlo uncertainty propagation simulation [37]. The results of the Monte Carlo simulation are listed in Table 1-3 where nominal values for the superheat, heat flux, sub-cooling and Reynolds number are used to calculate their uncertainty. The uncertainty in CHF is assumed to be one-half of the heater block power increment at near CHF operating conditions.

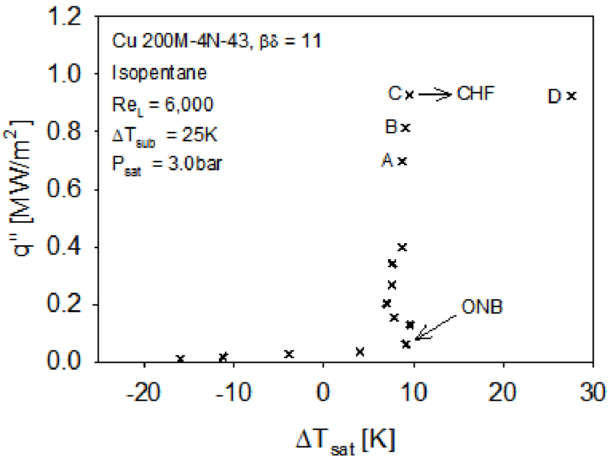

Fig. 1- 6 Typical boiling performance curve.

Boiling Performance Plots

The heater block power is the control variable. A boiling performance curve is constructed by incrementally increasing and holding constant the heater block power, and measuring (at steady state conditions) the boiling heat flux, q" and sub-surface superheat, $\Delta T_{sat} = T_s - T_{sat}$. Figure 1-6 shows a typical boiling performance curve where, as the heater block power is incrementally increased, successive data points are recorded. Steady, nucleate boiling is first observed at the point labeled "ONB" (Onset of Nucleate Boiling) followed by a steep rise in steady boiling heat flux to points A, B, C. A further increment in heater block power gives rise to a rapid temperature excursion and reduction in q" that is indicative of a reduction in surface heat transfer coefficient, since the critical heat flux has been exceeded and vapor phase heat transfer obtains (point D). In this case, some of the heater block power is diverted to sensible heating of the surface, resulting in a rapid transient increase in surface temperature, T_s and decrease in q" (point D rapidly moves down and to the right). The experiment control algorithm senses the decrease in q" and shuts down the system. We conservatively label the last stable boiling point (point C in Fig. 1-6) the Critical Heat Flux condition (CHF).

Plane Surface Cu/SS 200M-4L-43 Boiling Performance: Surface Material and Fluid Comparison

Penley and Wirtz [3, 4] have demonstrated the superior boiling performance of compressed laminations of fine filament *copper* screen ($k_{cu} \cong 400\, W/mK$ @ $100℃$), implemented as a thick-film coating. Their 200M-4L-43 surface demonstrated that it can accommodate up to 4.5MW/m^2 (CHF) with a superheat of only ~9K in 35K sub-cooled flow-boiling of *water* at 0.2atm ($T_{sat} = 60℃$). The current work looks at compressed laminations of fine filament copper and *316L stainless steel* screen, which has a considerably lower thermal conductivity ($k_{ss} \cong 16.3\, W/mK$ @ $100℃$).

Furthermore, the current work considers both Isopentane and n-pentane since either fluid is often the working fluid in a binary fluid plant. Table 1-4 compares relevant thermophysical properties of Isopentane and n-pentane (at 3bar) and water (at 0.2bar). The table shows that while n-pentane has a lower vapor pressure (higher "boiling point"), the other properties (with the exception of surface tension, σ_f) are quite close to each other. The surface tension of n-pentane is approximately 20% smaller than that of Isopentane. Surface tension is an important boiling parameter since it directly relates to the vapor bubble nucleation and growth process. Finally, the table shows that water (even at a reduced pressure of 0.2bar) is a vastly better heat transfer fluid (relative to pentane) with: a 5.6-fold higher surface tension, σ_f ; a 12.7 fold higher volumetric latent heat $(\rho_f h_{fg})$; a 2.8-fold fold higher liquid volumetric sensible heat $(\rho_f c_f)$; and, a 2.2-fold higher thermal diffusivity, $\left(\frac{k_f}{\rho_f c_f}\right)$.

A comprehensive series of experiments with surface 200M-4N-43 were completed ($Re_L = 600, 3000, 6000$, $\Delta T_{sub} = 2K,\ 10K,\ 25K$) which compare copper compressed laminates with steel laminates; and, Isopentane performance with n-pentane performance. Figure 1-7 ($Re_L = 6{,}000$, $\Delta T_{sub} = 25K$) is a typical result where the isopentane/n-pentane boiling performance curves overlay each other while the copper surface data traces are left-shifted relative to the stainless steel data traces.

Fluid Comparison n-pentane on stainless steel achieves a slightly higher CHF than isopentane on steel. We feel that this is not significant since the data traces are almost horizontal and heat flux is the control variable of the experiments. Apparently, surface 200M-4N-43 (copper or stainless steel) has a sufficiently large enough number of potential nucleation sites ($\sim 24{,}800\ per\ cm^2 plan\ area$) that the difference in surface tension is insignificant, and Isopentane and n-pentane boiling curves overlay each other.

Copper vs. Stainless Steel A comparison of the copper vs. stainless steel materials shows very different characteristic curves. The copper surface exhibits **O**nset of **N**ucleate **B**oiling (ONB)[4] with a few degrees superheat overshoot, while the stainless steel surface exhibits no overshoot, with ONB occurring at a very small heat flux. Both surfaces have ONB at 7K – 10K superheats. Similar to Penley and Wirtz's observations with water at 0.2atm [3, 4], the copper surface has an almost vertical performance curve (n-pentane data points overlay isopentane points), and very sudden onset of CHF, while the stainless steel surface performance curve trails off with increase in heat flux. This is similar to the function that is typical of other surfaces. The larger stainless steel superheats are easily explained in that the copper coating effective thermal conductivity is ~24x the stainless steel coating effective thermal conductivity [1, 38]. Consequently, there is a greater temperature drop across the stainless steel coating with increase in heat flux. Note, $\Delta T_{sat} \equiv (T_s - T_{sat})$ and $\Delta T_{sub} \equiv (T_{sat} - T_{in})$ are based on the sub-surface temperature, T_s.

Table 1- 4 Pentane Thermophysical Properties.

	i-C_5H_{12}	n-C_5H_{12}	H_2O
P_{sat}(bar)	3	3	0.2
T_{sat}(˚C)	63.5	72.2	60.2
h_{fg} (kJ/kg)	312	326	2357
ρ_f(kg/m^3)	573	571	982
ρ_g(kg/m^3)	8.56	8.31	0.132
k_f(W/m-K)	0.106	0.101	0.662
c_f(kJ/kg-K)	2.485	2.562	4.183
ν_f (m^2/s)×10^7	2.62	2.394	4.549
σ_f(dyne/cm)	13.1	10.5	66.0
Pr	3.89	3.46	3.05

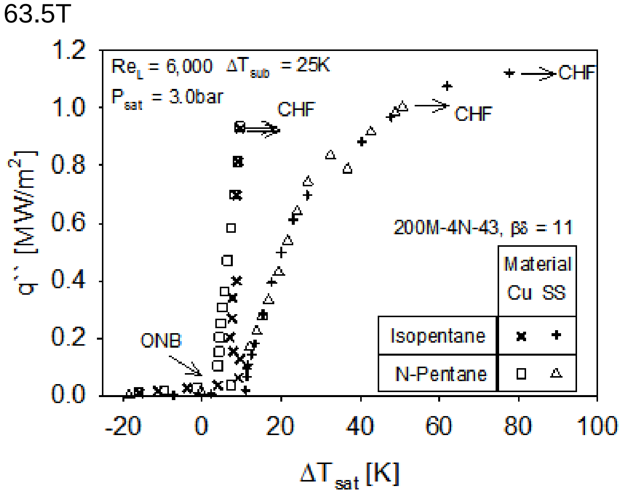

Fig. 1- 7 Boiling curves for Isopentane and n-pentane on stainless steel and copper surfaces.

---

[4] Our conservative criteria for ONB has micro-bubbles visible (but not necessarily departing from) the surface. This criterion over-estimates the heat flux and superheat at ONB. Since there is a temperature drop across the thickness of the coating, some nucleated vapor bubbles collapse before they reach the surface [4].

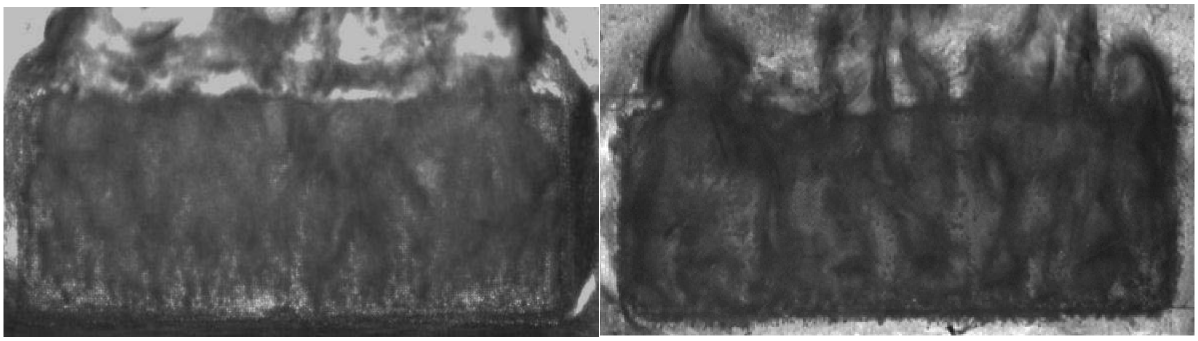

(a) copper (b) SS

Fig. 1- 8 Isopentane ebullition on Surface 200M-4N-43, Re_{ch}=10,000, ΔT_{sub}=25K.
(a) Copper laminate, q"=71W/cm^2, ΔT_{sat}=8.8K. (b) Stainless steel, q"=73W/cm^2, ΔT_{sat}=28K.

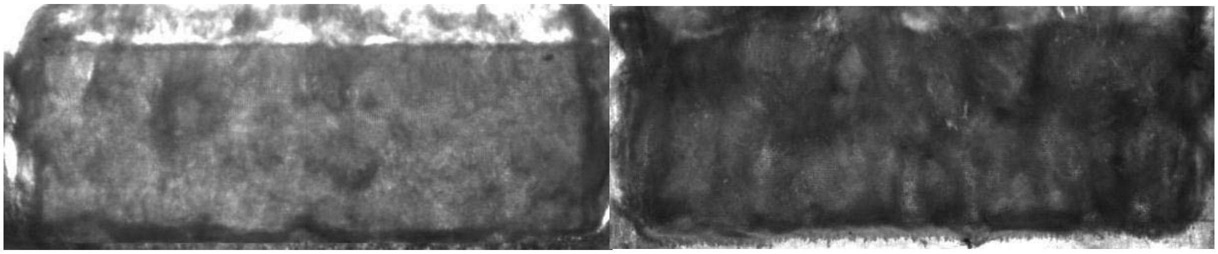

(a) copper (b) SS

Fig. 1- 9 Near CHF Isopentane ebullition on Surface 200M-4N-43, Re_{ch}=10,000, ΔT_{sub}=25K.
(a) Copper laminate, q"=94.5W/cm^2, ΔT_{sat}=9.7K. (b) Stainless steel, q"=113W/cm^2, ΔT_{sat}=92K.

Figure 1-8 are video still [5] images of ebullition of isopentane at approximately 72W/cm^2 on copper (a) and SS316L (b) Surfaces 200M-4N-43 (note the two similar data points of Fig. 1-7). At these moderate heat flux levels, ebullition on the two surfaces is similar. Micro-bubbles ejected from the surface quickly coalesce to form vapor columns, which are carried downstream. Liquid re-flood of the surface occurs between the vapor columns [39], with capillary pumping spreading the liquid laterally in the porous coating [34].

With increased heat flux, the vapor columns are known to thicken and become sinuous (a Helmholtz instability) so that they interact, inhibiting liquid re-flood of the surface and forcing transition to vapor-phase convection (CHF). Figure 1-9b [6] (ebullition on SS316L surface 200M-4N-43 at near CHF conditions) shows the merging vapor columns have almost totally obscured the surface. On the other hand, Figure 1-9a (ebullition on copper surface 200M-4N-43 at near CHF conditions) shows a vapor cloud that obscures the surface (the vapor columns are gone). In this case, high speed video shows the cloud pulsates at approximately 40Hz. The process appears to be similar to Penley and Wirtz's observations [4] of ***water*** ebullition on copper surface 200M-4N-43 where they have shown that, with

---

[5] Short (40 frame) videos of Figs. 1-8a and b, shot at 200fps, are found at http://wolfweb.unr.edu/~rawirtz/Fig8a.avi and http://wolfweb.unr.edu/~rawirtz/Fig8b.avi . Play-back at 30fps (standard video) results in a 7-fold time expansion. Down-load and play-back at 200fps is illuminating. We suggest use of "Image J" for playback.

[6] Short (40 frame) videos of the near CHF conditions, Figs. 9a and 9b, shot at 200fps, are found at http://wolfweb.unr.edu/~rawirtz/Fig9a.avi and http://wolfweb.unr.edu/~rawirtz/Fig9b.avi . Play-back at 10fps (use Image J) shows the cloud growth and collapse (Fig. 1-9a) and column interactions (Fig. 1-9b).

large sub-cooling, vapor cloud formation and collapse is periodic-unsteady. It is shown that time intervals with little micro-bubble ejection cannot accommodate the applied heat flux, so the surface “heats up” (local superheat increases) and more vigorous evaporation ensues, resulting in energetic micro bubble ejection and coalescence, and a reduction in local superheat. The vapor cloud eventually collapses and the cycle is repeated at approximately 6 – 10Hz rate. At CHF, the vapor cloud segments never totally collapse, totally obscuring the surface. Thus inhibiting liquid re-flood; resulting in vapor phase convection and a rapid temperature excursion that, at high heat flux of 0.5MW/m^2, usually results in damage to the surface. In the present, relatively lower heat flux case, micro-bubble ejection and coalescence is zonal (Fig. 1-9a). As CHF is approached, zones merge together, inhibiting liquid re-flood and forcing transition to vapor-phase convection and possible surface damage.

Parametric Effects on Boiling and Critical Heat Flux

Subcooling

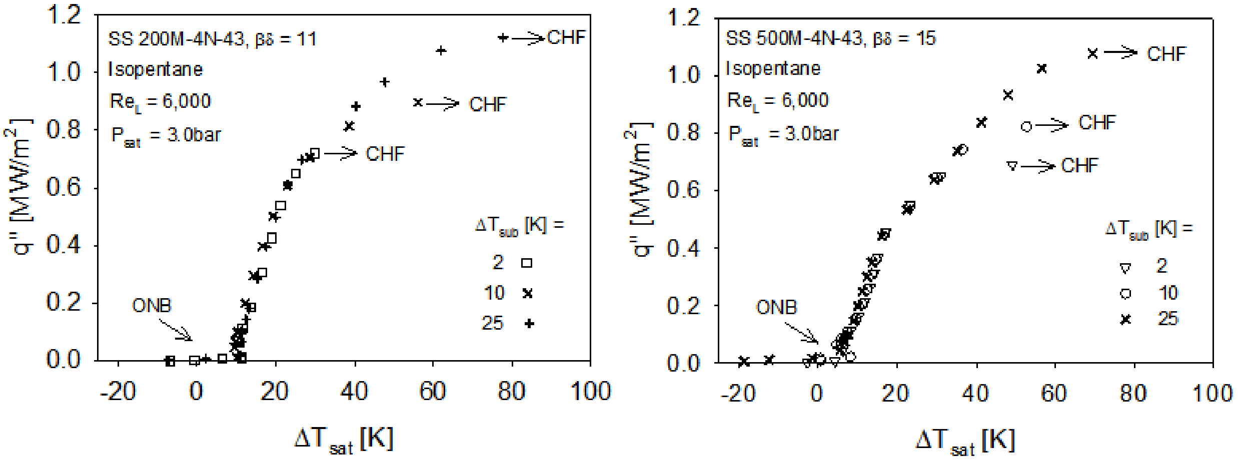

Fig. 1- 10 Sub-cooling effect on boiling performance curves: (a) surface SS 200M-4N-43, (b) surface SS 500M-4N-43.

Sub-cooling of the ambient liquid below saturation generally shifts the boiling performance curve upward [40]. Since the nucleate boiling component of the present curves are steeply sloped, the most noticeable effect is the increase in CHF. Figure 1-10 illustrates this for surfaces SS 200M-4N-43 and SS 500M-4N-43, where successively greater CHF (and superheat) is achieved with increase in superheat. Close inspection of the nucleate boiling component of the curves shows the high-sub-cooling data is also shifted (slightly) to the left, due to the increase in liquid-phase convection.

Flow Intensity (Reynolds number)

Similar to the sub-cooling effect, introduction of pressure gradient driven flow generally shifts the boiling performance curve upward [40]. The most noticeable effect is an increase in CHF with increase in flow intensity. Boiling curves are similar to those depicted in Figure 1-10. Figure 1-11 is a bar-graph showing a monotonic increase in CHF (left ordinate) and superheat at CHF (right ordinate) with flow intensity. This result is representative of all of the surfaces investigated.

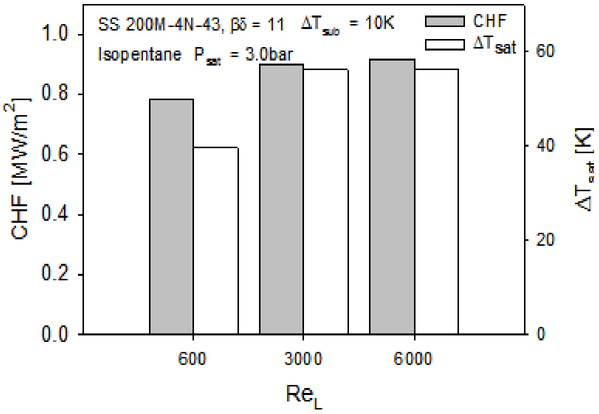

Fig. 1-11 Surface SS 200M-4N-43 CHF/ super-heat as a function of Re$_L$

Area Enhancement Ratio, (βδ)

Penley and Wirtz [29, 3, 4] have shown that CHF enhancement due to sub-cooling and channel Reynolds number is intrinsically linked to the surface area enhancement ratio (βδ), which has an optimum that depends on the degree of sub-cooling, and to a lesser extent on the Reynolds number. Their saturated pool boiling experiments with water at sub-atmospheric pressure had $(\beta\delta)_{opt} = 18.8$ [29]. Their sub-cooled flow boiling experiments with water at 0.2atm [3, 4] showed the optimum value to be a function of sub-cooling and flow intensity (Reynolds number), with the optimal value shifting to lower values with increased sub-cooling and flow intensity. Their best performing surface [Cu 200M-4N-43,$(\beta\delta) = 10.5$] achieved 4.5MW/m^2 with 8K superheat when 35K subcooling is employed with a channel Reynolds number of 6,000.

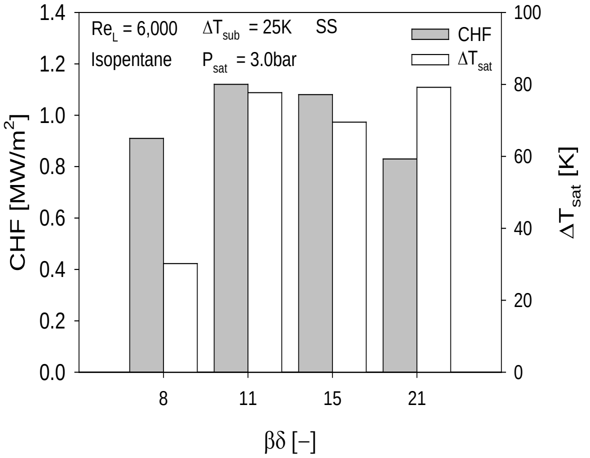

Figure 1-12 CHF as a function of Area Enhancement Ratio (βδ).

Figure 1-12 plots CHF (left ordinate) and superheat at CHF (right ordinate) for four surfaces boiling in Isopentane at 3bar: SS145M-4N, $(\beta\delta) = 8$; SS200M-4N-43, $(\beta\delta) = 11$; SS500M-4N-43, $(\beta\delta) = 15$; and SS200M-8N-43, $(\beta\delta) = 21$. The figure shows that, for the conditions: Re$_L$ = 6000, ΔT$_{sub}$ = 25K; $(\beta\delta)_{opt} \approx 11$ in agreement with the findings for boiling water on a copper surface. This indicates to us that the area enhancement factor is the dominate parameter in the determination of surface performance.

Boiling Surface Thermodynamic Efficiency

Bejan has promoted entropy generation minimization as a method to optimize the performance of finite-size thermal systems [41]. Zhao and Wirtz [35] show that, for flow boiling past a surface of face area LxW in a channel of cross section HxW, the entropy generation rate per unit face area, $\dot{S}''$ is given by

$$\dot{S}'' = q''\left(\frac{1}{T_{in}} - \frac{1}{T_S}\right) + \rho_o V_o \frac{H}{L}(S_{out} - S_{in}) \tag{1-1}$$

where H is the channel height (other terms previously defined). The first term on the rhs of Eq. 1-1 is the generation rate due to heat transfer across a finite temperature difference. The second term is the generation rate due to pressure drop in the streaming direction; it is of small magnitude for the present test configuration and it will be neglected.

While sub-cooling will allow for stable boiling at higher heat flux, Eq. 1-1 shows that sub-cooling (lower T$_{in}$) gives rise to a thermodynamically less efficient process. With saturated liquid (no sub-cooling) flow boiling ($T_{in} = T_{sat}$), and the first term on the rhs of Eq. 1-1 is minimized.

While our data show surface 200M-4N-34 is our best performer, Eq. (1-1) allows us to quantify its thermodynamic efficiency.

Table 1- 5 Boiling process entropy generation on Surface 200M-4N-43. $q'' = 0.75MW/m^2$, $P = 3bar$, $\Delta T_{sub} = 25K$, $Re = 6000$

Surface	**Fluid,** T_{sat} [℃]	T_{in} [℃]	ΔT_{sat} $[K]$	T_s [℃]	$T_s - T_{in}$ $[K]$	$\dot{S}''\left[\frac{W}{m^2K}\right]$
Cu	n-C_5H_{12}, 72.2	47.2	**9.1**	81.3	**34.1**	**225**
Cu	i-C_5H_{12}, 63.5	38.5	**9.8**	73.3	**34.8**	**242**
SS	n-C_5H_{12}, 72.2	47.2	**26.9**	99.1	**51.9**	**326**
SS	i-C_5H_{12}, 63.5	38.5	**31.0**	94.5	**56.0**	**367**
Flat Cu♣	n-C_5H_{12}, 72.2	47.2	**49.1**	121.3	**74.1**	**440**

♣ Stephan – Abdelsalam correlation [42] for hydrocarbon pool boiling on an unenhanced flat copper surface.

Table 1-5 lists observed temperatures when surface 200M-4N-43 is accommodating 0.75MW/m^2, boiling sub-cooled n-pentane and isopentane ($\Delta T_{sub} = 25K$, $Re = 6000$, see Fig. 1-7). The table lists the porous material (Copper or Stainless Steel), the fluid with its saturation temperature at 3bar, the fluid inlet temperature (T_{in}), the wall superheat (ΔT_{sat}), the resulting sub-surface temperature, T_s, the wall temperature increase relative to T_{in}, and the entropy generation rate (Eq. 1-1, $\dot{S}''$).

The first row shows that, at 0.75MW/m^2 (with n-C_5H_{12}) the wall superheat is only 9.1K, resulting in a 34.1K temperature rise of the sub-surface. Equation 1-1 gives the entropy generation rate as $\dot{S}'' = 225\left[\frac{W}{m^2K}\right]$.

The second row shows boiling i-C_5H_{12} under the same conditions gives a 2.1% larger temperature rise of the surface ($T_s - T_{in} = 34.8K$). However, Eq. 1-1 shows a 7.6% higher entropy generation rate ($\dot{S}'' = 242\left[\frac{W}{m^2K}\right]$). Of course, the lower temperature process (boiling i-C_5H_{12}) is thermodynamically less efficient.

The third and fourth rows of Table 1-5 show that Stainless Steel is not a very good boiling heat transfer surface. The relatively small thermal conductivity of stainless steel gives rise to a large temperature gradient across the coating, leading to higher subsurface temperature, T_s. Consequently, ($T_s - T_{in} = 51.9K$, and $\dot{S}'' = 326\left[\frac{W}{m^2K}\right]$, 45% greater than when the copper surface is the coating.

The fifth row of Table 1-5 uses the Stephan-Abdelsalam correlation [42] to estimate the superheat of sub-cooled normal-pentane boiling on an unenhanced, flat, copper surface[7]. The calculation gives super heat of the sub-surface, $\Delta T_{sat} = 49.1K$, and $T_s = 121.3$℃., so that, relative to the sub-cooled liquid, there is a 74.1K increase in system temperature. Equation 1-1 gives $\dot{S}'' = 440\left[\frac{W}{m^2K}\right]$. A comparison with row 1 of

---

[7] Sub-cooling and flow intensity extend CHF upward with only a small left-shift of the nucleate boiling part of the boiling curve [40].

the table shows the superheat of the unenhanced surface to be 5.4 times greater than that obtained with Surface Cu200M-4N-43 while the entropy generation rate is approximately twice that of the coated surface.[8]

Commercial (Enhanced) Surfaces

In recent years, attention has been focused on “tunnel and pore” surfaces. These surfaces are usually formed by mechanically deforming a finned surface to obtain an array of inter-connected reentrant cavities. Unfortunately, performance data for boiling pentane on commercial (enhanced) surfaces is apparently not available in the open literature.

However, a well known example of these Tunnel/Pore surfaces is Wolverine Tube’s Turbo-B surface [43], which is shown to outperform a plain surface by a factor of 8 (Fig. 9.16 of reference [43]) in terms of boiling heat transfer coefficient) when boiling the refrigerant R-123 over the heat flux range: 4KW/m^2 – 60kW/m^2. At heat flux 60kW/m^2 (0.06MW/m^2), the Turbo-B has approximately 4K superheat. This is comparable to the superheat of surface Cu-200M-43 (Fig. 1-7). Wolverine Tube does not report CHF limits for their tubes, so we do not know if their product can accommodate 0.75MW/m^2 (750kW/m^2), as shown in Table 1-5.

---

[8] This calculation is an extrapolation. The Zuber/Kutateladze equation [39] predicts CHF (plane surface in Pool boiling) = 0.34MW/m^2. Sub-cooling/forced convection would push this value upward, but we do not think to the 0.75MW/m^2 level.

Fig 1-13 Photograph of tubular test section

Tubular Surface Test Article and Test Section Design and Fabrication (P. J. Laca)

Figure 1-13 shows a photograph and Figure 1-14 shows a sketch of the tubular test section for the flow boiling test rig. It consists of a 1.5in inner diameter polycarbonate tube encasing a 0.75in steel tube. Inlet and outlet plenums on both ends create a seal with the polycarbonate tube. Steel plugs mounted to the plenums hold the test article in place and also feed through the test article heater and thermocouple wires. The outer surface of the steel tube is coated with the screen laminate. The tube is heated from the inside by a cartridge heater (Watlow pn# L18A36) that can supply up to 4.7kW of power over its 18in length. Fluid flow enters from the inlet plenum and flows vertically in the channel between the outer tube and the inner tube. A flow straightener is in the inlet plenum to ensure uniform flow approaches the test article. The tubes create a 3/8in wide annular channel where a channel Reynolds number of 10,000 can be achieved. Bulk fluid temperature is measured by 4 exposed junction thermocouples (x) placed in the flow that are distributed evenly along the length of the tube.

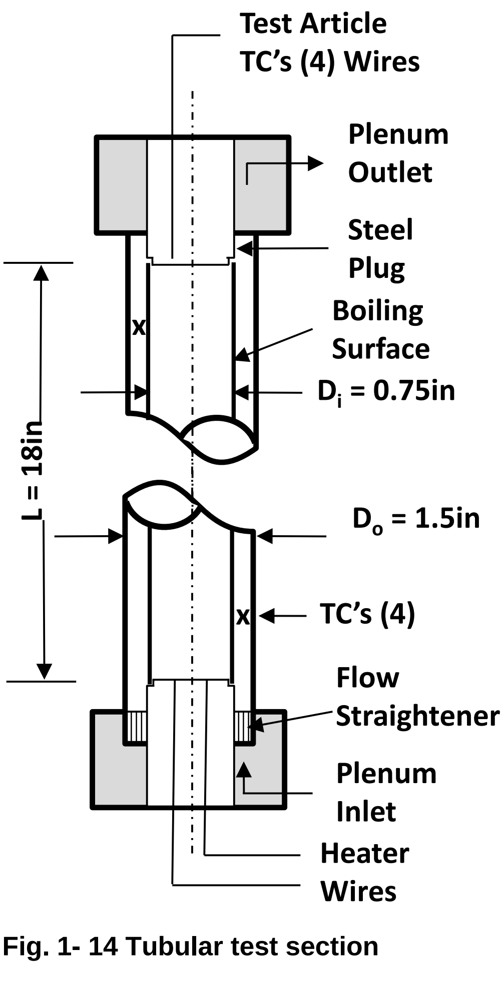

Fig. 1- 14 Tubular test section

Fig 1-15 Photograph of a section of the test article

Tubular Surface Test Article Design (P.J. Laca)

A photograph of a section of the test article where the surface has a Cu200M-4N-43 coating is shown in Ficure 1-15. Due to furnace and fixture limitations three of these tubes are soldered together to get an 18in test article. The three sections are then installed on a 4500W 5/8in diameter cartridge heater and instrumented with thermocouples. A cross section of the tubular test article can be seen in Figure 1-16. The outer surface of the test article will be made in three 6in sections. Each section's screen laminate surface will be diffusion bonded individually and the 6in sections will be silver soldered to each other when the test article is assembled. The cartridge heater seen in the center of fig. 1-14 is inserted into the tube with an interference fit. Four sheathed ungrounded thermocouples are placed in machined grooves in the inner surface of the tube at evenly spaced locations both azimuthally and vertically. The heat flux and the surface temperatures are calculated using the thermocouple temperatures and the heater power

Results

We were unable to get reliable performance data in the time span of this project.

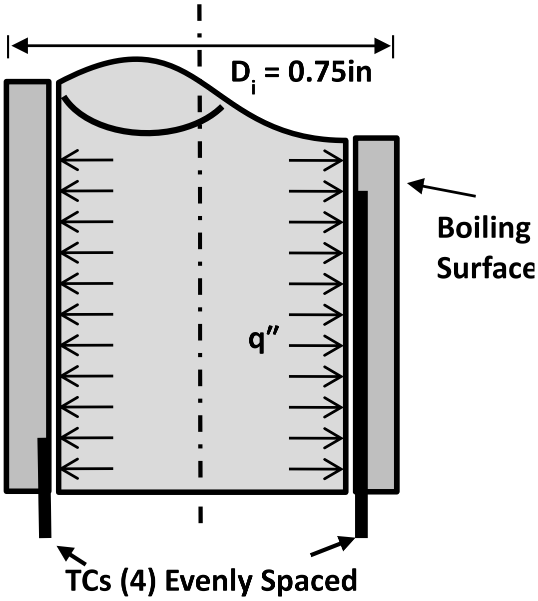

Fig. 1- 16 Test article cross section.

Conclusions

Flow boiling experiments with sub-cooled Isopentane and n-Pentane at 3.0bar pressure assess the utility of sub-millimeter thickness, compressed copper- and steel-filament screen laminate surface coatings as high performance boiling surfaces for these liquids. High-speed video show that at high heat flux, ebullition is stable but periodic unsteady. Isopentane and n-Pentane are found to produce nearly identical boiling characteristic curves. At the same applied heat flux, the sub-surface superheats of copper filament coatings are much smaller than the steel filament coating sub-surface superheats. This is attributable to the relatively small thermal conductivity of stainless steel, which gives rise to a relatively large temperature rise across the thickness of the steel coating.

Increased sub-cooling and flow intensity (Reynolds number) shift boiling performance curves upward; the most notable effect being an increase in Critical Heat Flux. CHF enhancement is found to be intrinsically linked to the surface area enhancement ratio (βδ), which has an optimum value for the present coating material and fluid of $\left(\beta\delta_{opt} \cong 11\right)$. Since this is essentially the same value obtained by Penley and Wirtz in their experiments with copper coatings boiling water, the implication is that the area enhancement factor is the dominate parameter in the determination of optimal surface performance. The fluid properties and coating material properties are of secondary importance.

Our best performing surface, Cu-200M-4N-43, can accommodate up to 0.91 MW/m^2 (910kW/m^2) with a superheat of only 9.4K. Thermodynamic analysis shows that its entropy generation rate is minimum when it boils normal pentane. Boiling Isopentane leads to a slightly higher entropy generation rate since it is a lower temperature process. If the coating is Stainless Steel, then at the same heat flux, there is a relatively large temperature increase across the thickness of the coating due to the smaller thermal conductivity of stainless steel. This gives rise to larger superheats of the sub-surface, so there is an approximate 45% increase in entropy generation rate.

These surfaces out-perform plain (un-enhanced) surfaces by a wide margin. At applied heat fluxes ranging up to 100kW/m^2 (0.1MW/m^2) surface performance is similar to that of other commercial (enhanced) surfaces. However, we suspect they can accommodate much higher heat fluxes with relatively small superheats than existing enhanced surfaces. Since Critical Heat Flux data for boiling pentane on commercial (enhanced) surfaces is not in the open literature, this issue is not resolved.

Recommendations

1. We developed a fabrication methodology (diffusion bonding cold rolled screen to form the lamination) that is suitable to the laboratory environment. It is not clear that this methodology is suitable to the large-scale manufacturing environment. Electric or ultrasonic welding could be a better methodology for large scale manufacture. These alternatives (and others) should be investigated.
2. Due to the relatively short duration of the project, we were unable to debug our apparatus and run tests on tubular surfaces. Follow-up experiments with tubular surfaces, in conjunction with an established re-boiler manufacturer should be undertaken. Experiments that back-to-back compare this technology to existing enhanced surfaces should be conducted.

Nomenclature

c_f	Liquid specific heat [j/Kg K]
C_f	Compression factor [$\delta/2^{Nd}$]
d	Filament diameter [mm]
D_h	Hydraulic diameter [mm]
h	Latent heat [j/kg}
H	Channel height [mm]
k	Thermal conductivity [W/m K]
ke	Effective thermal conductivity [W/m K]
M	Mesh number [in^{-1}]
N	Number of layers
P	Pressure [bar]
Pr	Prandtl number [-]
q	Heat Transfer Rate [W]
q”	Heat Flux [W/m^2]
Q	Volumetric flow [m^3/s]
Re	Reynolds number
S	Entropy [W/K]
T	Temperature [K]
V	Velocity [m/s]
W	Channel width [mm]
β	Specific surface area [cm^2/cm^3]
δ	Coating thickness [mm]
ε	Porosity [%]
ρ	Density [kg/m^3]
v	Kinematic viscosity [m^2/s]
Subscripts	
f	Liquid
g	Vapor
in	Inlet
out	Outlet
s	Sub-surface
sat	Saturation
sub	Sub-cooling

References

---

1 Xu, Jun and R.A. Wirtz (2003) "In-plane Effective Thermal Conductivity of Plane-Weave Screen Laminates", IEEE Trans. on Components and Packaging Tech, Vol. 25, #4, pp. 615 – 620.

2 Xu, J., and Wirtz, R. A. (2005) “In-Plane Effective Thermal Conductivity of Symmetric Diamond-Weave Screen Laminates”, ASME J. Electronic Packaging, Vol. 127, pp. 353 – 356.

3 Penley, S.J. and R.A. Wirtz, “Sub-Atmospheric Pressure, Sub-Cooled, Flow Boiling of Water on Screen-Laminate Enhanced Surfaces” Proc. Int. Heat Transfer Conf., Paper IHTC14-22741, Washington DC, USA.

4 Penley, S.J. and R.A. Wirtz (2012) “Mechanistic Study of Sub-Atmospheric Pressure, Sub-Cooled, Flow Boiling of Water on Structured-Porous Enhanced Surfaces”, ASME Journal of Heat Transfer, 134,112902.

5 Tong, L.S. and Y.S. Tang (1997) “Boiling Heat Transfer and Two-Phase Flow, 2nd Ed”, Taylor & Francis, Washington DC.

6 Webb, R.L. and Nae-Hyun Kim (2005) “Principles of Enhanced Heat Transfer, 2nd Ed.”, Taylor & Francis, Washington DC.

7 Ma, H.B., and Peterson, G.P., 1997, "Temperature variation and heat transfer in triangular grooves with an evaporating film," *J. Thermophysics and Heat Transfer*, **11**(1), pp. 90-97

8 Webb, R.L., 2004, “Donald Q. Kern Lecture Award Paper: Odyssey of the Enhanced Boiling Surface,” *ASME J. Heat Transfer*, **126**, pp. 1051-1059.

9 Mudawar, I., and Bowers, M.B., 1998, "Ultra-high critical heat flux (CHF) for sub-cooled water flow boiling-I: CHF data and parametric effects for small diameter tubes," *Int. J. Heat Mass Trans*. **42**, pp. 1405-1428

10 Kuo, C.J., and Peles, Y., 2008, "Critical Heat Flux of Water at Sub-atmospheric Pressures in Microchannels," *ASME J. Heat Transfer*, **130**, 072403.

11 Zuber, N., Tribus, M., and Westwater, J.W., 1961, "The Hydrodynamic Crisis in Pool Boiling of Saturated and Sub-cooled Liquids," Int. Developments in Heat Transfer, Part 2, ASME, pp. 230-236

12 Zuber, N., 1958, "Hydrodynamic aspects of boiling heat transfer," Report AECU-4439

13 Kandlikar, S.G., 2001a, “A Theoretical Model To Predict Pool Boiling CHF Incorporating Effects Of Contact Angle And Orientation,” *ASME J. Heat Transfer*, **123**, pp. 1071-1079.

14 Kandlikar, S.G., 2001, "Critical Heat Flux in Sub-cooled Flow Boiling- an Assessment of Current Understanding and Future Directions for Research," *Multiphase Science and Technology*, **13**(3), pp. 207-232

15 Hall, D.D., and Mudawar, I., 2000, "Critical heat flux (CHF) for Water Flow in Tubes-II. Sub-cooled CHF correlations," *Int. J. Heat and Mass Trans*, **43**, pp. 2605-2640

16 Kandlikar, S.G., Mizo, V.R., and Cartwright, M.D., 1995, "Investigation of bubble departure mechanism in Sub-cooled Flow Boiling of Water Using High-speed Photography," Proc. Convective Flow Boiling Conf., pp.161-166

17 Carey, V.P., 2008, Liquid-Vapor Phase Change Phenomena, 2nd Edition Taylor and Francis, pp. 227-228

18 Okawa, T., Ishida, T., Kataoka, I., and Mori, M., 2005, "Bubble rise characteristics after the departure from a nucleation site in vertical upflow boiling of sub-cooled water," Nuclear Engineering and Design **235**, pp. 1149-1161

19 Warrier, G.R., Basu, N., and Dhir, V.K., 2002, "Interfacial heat transfer during sub-cooled Flow Boiling," *Int. J. Heat and Mass Trans*, **45**, pp. 3947-3959

20 You, S.M., Rainey, K. N., and Ammerman, C. N., 2004, "A New Microporous Surface Coating for Enhancement of Pool and Flow Boiling Heat Transfer," *Advances in Heat Transfer*, **38**, pp. 73-142.

21 El-Genk, M. S., and Parker, J. L., 2005, " Enhanced boiling of HFE-7100 dielectric liquid on porous graphite," Energy Conversion and Management, 46, pp. 2455-2481.

22 Afgan, N.H., Jović, L.A., Kovalev, S.A., and Lenykov, V.A., 1985, “Boiling heat transfer from surfaces with porous layers,” International J. of Heat and Mass Transfer, 28(2), pp. 415-422

23 Cieśliński, J.T., 2002, “Nucleate pool boiling on porous metallic coatings,” Experimental Thermal and Fluid Science, 25, pp. 55-564

24 Jakob, M., (1949) Heat Transfer, John Wiley and Sons, pp 636-637.

25 A.A. Vasil'yev, “Heat transfer and Critical heat flux densities in boiling of water under a vacuum on walls covered with a single layer of mesh,” Heat Transfer Research, vol. 24, 1992, pp. 913-921.

26 Brautsch and P. Kew, “The effect of surface conditions on boiling heat transfer from mesh wicks,” Proceedings of the 11th International Heat Transfer Conference, 2002, p. 635–640.

27 Li, C., and Peterson, G.P., 2007, “Parametric Study of Pool Boiling on Horizontal Highly Conductive Microporous Coated Surfaces,” *ASME J. Heat Transfer*, **129**, pp. 1465-1475.

28 Liter, S. and M. Kaviany (2001) “Pool-boiling enhancement by modulated porous-layer coating: theory and experiment”, Int. JHMT, 44, 4287-4311.

29 Penley, S.J., and Wirtz, R.A., 2010, “Correlation of Sub-atmospheric Pressure, Saturated, Pool Boiling of Water on a Structured-Porous Surface,” *ASME J. Heat Transfer*, **133** 041501 (11 pgs)

30 Laca, P.J. and R.A. Wirtz (2009) “Sub-Atmospheric Pressure Pool Boiling of Water on a Screen Laminate-Enhanced ExtendedSurface”, Proc. 25th IEEE Semi-Therm Symposium, Paper 0-7803-xxxx-x/06.

31 Lace, P.J. and R.A. Wirtz (2010) “Sub-Atmospheric Pressure Pool Boiling of Water on a Screen Laminate-Enhanced, Wavy-Fin Array” Proc. ASME IMEC&E, Paper IMECE2010-40678

32 Holland, B. N. Ozman and R.A. Wirtz (2008) “Flow boiling of FC-72 from a screen-laminate extended surface matrix”, Microelectronics Journal**, 39**, pp. 1001 - 1007

33 Tung, VX Dhir VK, Force flow cooling studies of volumetrically heated porous layers. Proc Nuclear Reactor Thermal Hydraulics 1983 2:876-883.

34 Zhao, Zenghui and R.A. Wirtz (2012) Flow boiling of isopentane from a structured-porous copper fin” ASME J. Heat Transfer, 134, 071501; see alsoProc. Energy Sustainability 2009, paper ES2009-90384.

35 Zhao, Z. and R.A. Wirtz (2010) “High-Flux Boiling/Evaporation of Isopentane from a Structured-Porous Fin” Proc. GRC Annual Meeting, Paper 223.

36 Sloan, A.D., Penley, S.J., and Wirtz, R.A., 2009, “Sub-Atmospheric Pressure Pool Boiling of Water on a Screen-Laminate Enhanced surface,” 25th IEEE SEMI-THERM Symposium, pp. 246-253

37 Moffat, R.J., “Describing the Uncertainties in Experimental Results,” Experimental Thermal and Fluid Sciences, Vol 1, pp 3-17, 1988

38 Li, Chen and G.P. Peterson (2006) “The effective thermal conductivity of wire screen”, Int J. Heat Mass Trans., 49, 4095 - 4105

39 Lienhard IV, J.H. and J. H. Lienhard V (2003) “A Heat Transfer Textbook, 3ed”,Chapter 9, Phlogiston Press, Cambridge Massachusetts.

40 Carey, V (1992) “Liquid-Vapor Phase-Change Phenomena” Hemisphere Publishing Corp., Washington.

41 Bejan, A. (1998) “Entropy generation minimization: The method of thermodynamic optimization of finite-size systems and finite-time processes” CRC Press, NY

42 Stenhan, K. and Abdelsalam (1980) “Heat Transfer Correlations for Natural Convection Boiling”, Int. J. Heat Mass Trans, Vol. 23, pp. 73 – 87.

43 Throme, J.R. (2006) Chapter 9, Data Book III, Wolverine Tube Inc, http://www.wlv.com/products/databook/db3/DataBookIII.pdf

Advanced Heat/Mass Exchanger Technology for Geothermal and Renewable Energy Systems

Project 2 Final Report:
Heat and Mass Transfer in Membrane Contactor Processes

A.E. Childress and S.R. Hiibel
Civil and Environmental Engineering
University of Nevada, Reno
Reno, Nevada 89557

775 784-6942
amyec@unr.edu

775 327-2260
shiibel@unr.edu

December 16, 2014

Executive Summary

The objective of this project was to develop advanced understanding of microporous hydrophobic membrane performance for membrane distillation membranes. These membranes can be coupled with geothermal and solar renewable energy systems to produce high-quality potable water, particularly in distributed or remote applications. Fundamental surface characterization was performed to support experimental and analytical studies of mass transport in membrane distillation systems. *A priori* water flux prediction was enabled through the development of a simplified model that can be used to predict the relative magnitudes of water fluxes. A newly introduced structural parameter that contains non-coupled membrane properties but still carries physical meaning was determined by simple and reliable measurements using inexpensive analytical equipment. In addition to the new structural parameter and model, a detailed collection of membrane distillation membrane properties and their water flux values was also made available to the literature to assist others in membrane selection, development, and application. Low water flux in membrane distillation is a concern for full-scale application. In the past decades, attempts have been made to improve water flux, and vacuum-enhanced direct-contact membrane distillation has proven to be an effective configuration to achieve this. However, only qualitative assessments of the factors that might improve water flux have been reported in the literature. A mechanistic investigation of the factors attributing to higher water fluxes was performed. Less membrane compaction was identified as one dominant factor attributing to improved water flux as very little compaction occurred in the vacuum-enhanced configuration until tested at a high pressure-gradient. Lower air pressure inside the membrane pores was found to be the other dominant factor attributing to improved water flux. Pressure gradient, as is present in both vacuum- and pressure-enhanced configurations, was found to have a minimal effect on water flux. High water flux of MD is desirable when treating feed waters with low fouling potentials; however, low water flux of MD is desirable when treating feed waters with high fouling potentials. Waters with high fouling and scaling potentials are often encountered in remote applications and can result in significant loss of membrane performance or membrane lifetime. Experimental results suggested optimal membrane cleaning scenarios to remove scalants and not increase the likelihood of pore wetting, which necessitates the need for chemical or physical drying of the membrane.

Recommendations

Overall, the capability of MD to be powered by low-grade thermal energy (e.g., geothermal and solar renewable energy systems), the high contaminant rejection, and the small decrease of the driving force when treating hypersaline feed waters make it an attractive water treatment technology. Additionally, the flexibility of MD to operate at high water fluxes when treating waters with low fouling potential or at low water fluxes with high fouling potential waters makes it an attractive option for a wide range of applications. Because of the wide potential operating range, further development of *a priori* water flux prediction techniques that can span the entire range of membrane types and pore sizes would be beneficial. Standardized characterization and flux assessment techniques would be useful as more commercially available MD membranes enter the market. The low water flux of MD, especially in air gap MD that has been studied at the pilot scale, should be addressed through techniques such as vacuum enhancement. Increased water flux for these membranes would make MD competitive when treating feed waters with low fouling potentials, where pressure-driven membrane processes are commonly used. Studies not only on manufacturing MD membranes with high water fluxes but also modifying membranes and identifying ideal operating conditions are desirable. Membrane scaling and wetting during long-term operation of MD would also be improved. To make MD more competitive when treating feed waters with high fouling potentials, where pressure-driven membrane processes typically cannot be used, standardized cleaning protocols should be developed based on experimental studies such as the one in this report. Similar to membrane fouling being a significant concern in all membrane applications, membrane scaling and subsequent reduction or loss of membrane hydrophobicity must be mitigated to enhance applicability to extreme solution chemistries. From a broader perspective, system integration of the membrane distillation unit with a geothermal or solar energy unit needs to be performed. As part of this, the assessment to determine the range of conditions for which use of a reverse osmosis-organic Rankine cycle system may be preferable over membrane distillation should be continued.

Project 2 Final Report:
Heat and Mass Transfer in Membrane Contactor Processes

A.E. Childress and S.R. Hiibel

Project Objectives

The overall objective of this project was to develop advanced understanding of MD membrane performance to facilitate its application in treating a range of feed waters (those with high fouling potentials requiring low flux and those with low fouling potentials desiring high flux). Three sub-objectives were included. The first sub-objective targeted the development of a simplified flux prediction model to easily identify MD membranes with desirable water fluxes. To achieve this, a novel membrane structural parameter was proposed first, which was highly correlated with water flux, contained non-coupled membrane property parameters, and required simple and reliable laboratory measurements with low costs. Next, an empirical model based on the new structural parameter was also developed for flux prediction and the flux prediction performance was compared to the performance with the existing mass transfer models. At last, the application of this model to membranes with a wider range of pore sizes was explored. The second sub-objective was aimed at mechanistically evaluating the factors attributing to the improved water flux in VEDCMD in order to provide insight for water flux improvement. To achieve this, the traditional DCMD and pressure-enhanced DCMD (PEDCMD) were studied for comparison with VEDCMD. The dominant factors contributing to higher water flux in VEDCMD were first theoretically identified. Next, membrane compaction phenomena in all three DCMD systems was investigated. At last, the magnitude of the air pressure inside the membrane pores for each DCMD system was quantified. The third sub-objective focused on identifying effective membrane cleaning solutions for the removal of typical scalants ($CaCO_3$, $CaSO_4$, SiO_2, and NaCl) in DCMD in order to facilitate the application of DCMD in long-term operations when treating various feed waters. To achieve this, four feed solutions containing different scalants were collected or synthesized and tested in bench-scale DCMD systems. Membrane performances for each feed solution before and after membrane cleaning were compared to estimate the effectiveness of the cleaning solutions. The scaled membrane surface before membrane cleaning was analyzed using the scanning electron microscopy (SEM) coupled with energy dispersive spectrometry (EDS) to identify the components of the scalants. Membrane surface analysis after cleaning was also performed when necessary to identify the effectiveness of scale removal.

Technical Approach

Fundamental surface characterization was performed to support experimental and analytical studies of mass transport in membrane distillation systems. Statistical analyses and model development utilized data from a range of surface characterization and performance techniques. A bench-scale MD system with real-time system monitoring and data collection was constructed and used to evaluate flux enhancement and performance under a range of solution chemistries.

Period of Performance

September 20, 2010 – September 20, 2014

Personnel

Amy E. Childress
Professor
Civil and Environmental Engineering
University of Nevada, Reno
Reno, NV 89557
amyec@unr.edu

Sage R. Hiibel
Research Assistant Professor
Civil and Environmental Engineering
University of Nevada, Reno
Reno, NV 89557
shiibel@unr.edu

Andrea Achilli, Post-doctoral researcher

Guiying Rao, PhD student

Publications from this Work

Publications

1) Rao, G.Y., Gustafson, R, .Hiibel, S.R., Childress, A.E., "Desalination energy consumption using low-grade heat as energy source: membrane distillation vs. reverse osmosis with an organic Rankine cycle", in preparation.
2) Rao, G.Y., Childress, A.E., Hiibel, S.R., "Membrane fouling and cleaning in direct-contact membrane distillation (DCMD)", in preparation for submission January 2015.
3) Rao, G.Y., Hiibel, S.R., Childress, A.E., "Factors attributing to flux improvement in vacuum-enhanced direct contact membrane distillation", submitted.
4) Rao, G.Y., Hiibel, S.R., Childress, A.E., "Simplified flux prediction in direct-contact membrane distillation using a membrane structural parameter", Desalination, in press.
5) Rao, G.Y., Ph.D. Dissertation "Direct-Contact Membrane Distillation: Simplified Flux Prediction, Mass Transfer Mechanisms, and Membrane Cleaning", August 2014.
6) Cath, T.Y., Elimelech, M., McCutcheon, J.R., McGinnis, R.L., Achilli, A., Anastasio, D., Brady, A.R., Childress, A.E., Farr, I.V., Hancock, N.T., Lampi, J., Ngheim, L.D., Xie, M., Yip, N.Y., "Standard Methodology for Evaluating Membrane Performance in Osmotically Driven Membrane Processes", Desalination, Vol. 312 March 2013, pages 31-38.

Presentations

1) Rao, G.Y. "Direct-Contact Membrane Distillation: Simplified Flux Prediction, Mass Transfer Mechanisms, and Membrane Cleaning", Ph.D. Dissertation Defense. June 26, 2014, Reno, Nevada.
2) Rao, G. Y. "Direct-Contact Membrane Distillation: Simplified Flux Prediction, Mass Transfer Mechanisms, and Membrane Cleaning", University of Wisconsin, Milwaukee, June 2014.
3) Childress, A.E., "Membrane Systems for Wastewater Reclamation and Water Purification", American Chemical Society 246th National Meeting, September 8-12, 2013, Indianapolis, Indiana. (keynote speaker for symposium on Membranes for Water Purification)
3) Rao,G.Y*., Achilli, A., and Childress, A.E., "Factors Attributing to Flux Improvement in Vacuum-Enhanced Direct Contact Membrane Distillation", American Institute of Chemical Engineers 2012 Annual Meeting, October 28-November 2, 2012, Pittsburgh, Pennsylvania.
   * Awarded Best Presentation Award at AIChE 2012
4) Rao,G.Y., Achilli, A., Childress, A.E., "Effects of Membrane Characteristics on Performance in membrane distillation", CA-NV AWWA Annual Fall Conference 2011, October 17-20, 2011, Reno, Nevada.
5) Childress, A.E., Rao, G.Y., and Achilli, A. "Direct Contact Membrane Distillation: Effects of Membrane Pore Size Distribution and Support Layer on Mass Transfer", International Workshop on Membrane Distillation and Related Technologies, October 9-12, 2011, Ravello, Italy.

Introduction

Membrane distillation is a relatively new thermally driven desalination technology that that uses the temperature difference at the membrane surfaces as the driving force to separate contaminants from potable water. Membrane distillation has mostly been studied in bench-scale investigations [1]; very little pilot-scale research has been published. Membrane distillation has a simpler system configuration than traditional distillation and can utilize low-grade thermal energy, such as that from geothermal or solar energy. The capability of membrane distillation to be combined with low-grade thermal energies to generate temperature gradients makes it an attractive water treatment technology compared to the pressure-driven membrane processes, which typically utilize electricity as the power source. MD has been reported to have nearly 100% salt and non-volatile organic rejection regardless of feed-water salinity [2-4], and thus, can be used to treat feed waters with both high and low fouling potentials [5-8]. Its ability to treat highly saline waters with little decrease in driving force makes it particularly appealing for extreme salinity feed waters.

The overall objective of this project was to develop advanced understanding of MD membrane performance to facilitate its application in treating a range of feed waters (those with high fouling potentials requiring low flux and those with low fouling potentials desiring high flux)Three outputs were pursued. The first targeted the development of a simplified flux prediction model to easily identify MD membranes with desirable water fluxes. The second was aimed at mechanistically evaluating the factors attributing to the improved water flux in VEDCMD in order to provide insight for water flux improvement in all MD configurations. The third focused on identifying effective membrane cleaning solutions for the removal of typical scalants in MD in order to facilitate long-term operations when treating various feed waters.

References

[1] K.W. Lawson, D.R. Lloyd, Review: Membrane distillation, J. Membr. Sci. , 124 (1997) 1-25.
[2] K.W. Lawson, D.R. Lloyd, Membrane Distillation. II. Direct contact MD, J. Membr.Sci. , 120 (1996) 123-133.
[3] J.L. Cartinella, T.Y. Cath, M.T. Flynn, G.C. Miller, K.W. Hunter, A.E. Childress, Removal of natural steroid hormones from wastewater using membrane contactor processes, Environ. Sci. Technol., 40 (2006) 7381-7386.
[4] S. Lee, J. Choa, M. Elimelech, Influence of colloidal fouling and feed water recovery on salt rejection of RO and NF membranes, Desalination, 160 (2004) 1-12.
[5] Division of Water Resource Management, F.D.o.E. Protection, Desalination in Florida: A Brief Review of the Technology, Environmental Issues and its Implementation., in, Tallahassee, Florida, 2010.
[6] E. Curcio, E. Drioli, Membrane Distillation and Related Operations - A Review, Sep. Purif. Rev., 34 (2005) 35-86.
[7] M. Khayet, Membranes and theoretical modeling of membrane distillation: A review, Adv. Colloid Interface Sci., 164 (2011) 56-88.
[8] T.Y. Cath, Ph.D. Dissertation “Membrane Contactor Processes for Seawater Desalination and Wastewater Reclamation” Civil Engineering, University of Reno, Nevada. Reno, Nevada, 2003.

Research Output #1

Simplified Flux Prediction in Direct-Contact Membrane Distillation Membrane Distillation Using a Membrane Structural Parameter

Abstract

A priori water flux prediction is desirable when conducting membrane distillation (MD) studies, however existing models are complicated with inconsistent mass transfer mechanism assumptions. To develop a simplified model that can be used to predict the relative magnitudes of water fluxes for a group of MD membranes, correlation analyses were performed between water flux and 28 structural parameters. Four parameters were found to be highly correlated with water flux: ε/δ, $\varepsilon/\tau\delta$, $1/\tau\delta$, and C_m. C_m is a newly introduced structural parameter that contains non-coupled membrane properties but still carries the physical meaning of a relationship between δ and ε, and is determined by simple and reliable measurements using inexpensive analytical equipment. The correlation result between water flux and C_m suggests C_m is a good structural parameter for MD flux prediction. The flux prediction errors for membranes with pore sizes from 0.1 to 0.9 μm were generally smaller for the model developed with C_m than for the dusty gas model. In addition to the new structural parameter and model, this study also makes available to the literature a detailed collection of MD membrane properties and their water flux values that will assist others in membrane selection, development, and application.

1.1. Introduction

1.1.1. Membrane distillation

Membrane distillation (MD) is a thermally-driven process in which separation occurs through a phase change to produce clean water. The driving force in MD is the vapor pressure gradient, resulting from the temperature difference across the membrane. Among all types of MD, direct-contact MD (DCMD) is the most commonly used configuration in lab-scale research [1]. In DCMD, two solutions at different bulk temperatures are circulated on either side of a hydrophobic microporous membrane. Temperatures of the feed solution can range from 30-90 °C [2, 3], which makes it feasible to be combined with low-grade heat sources. DCMD has been used to treat feed waters with high fouling and scaling potentials, such as industrial wastewater [4, 5], water from salt lakes[6], RO brines[7, 8], and produced water from the oil and gas industry [9-11], because the driving force of DCMD does not decrease significantly with increasing water salinity. DCMD is also well suited to treat feed waters with low fouling and scaling potentials where targeted removal or polishing is desired because DCMD achieves near 100% salt and organic rejection [12, 13]. Examples include impaired water containing endocrine disrupting compounds [14]; brackish water contaminated with fluoride [15]; groundwater with heavy metals [16]; and feed waters with urine and hygiene wastewater [17]. In some DCMD applications (particularly with low fouling and scaling feedwaters) obtaining high water flux is desirable while in other applications (with high fouling and scaling feedwaters) it is not, thus *a priori* water flux prediction is desirable for membrane selection. Because MD water flux is affected by membrane properties, feed water properties, and operating conditions [18], if a group of MD membranes is operated on the same feedwater at specific operating conditions, only the membrane properties will affect the relative magnitude of water flux.

1.1.2. Existing mass transfer models for flux prediction in MD

Water flux (N_i) through an MD membrane is given as:

$$N_i = B\Delta P_i \qquad (1.1)$$

where B is the membrane mass transfer coefficient and ΔP_i is the water vapor pressure gradient across the membrane. Here, subscript i is used to represent water vapor and subscript j is used to represent air. Water vapor pressure (P_i) for both the feed stream and the distillate stream is expressed using the Antoine equation [19, 20]:

$$P_i = \exp(23.328 - \frac{3841}{T-45}) \qquad (1.2)$$

where T is the temperature of the respective stream. The dusty gas model is often used to estimate water flux in MD, where four mass transfer mechanisms (surface diffusion, Knudsen diffusion, molecular diffusion, and viscous flow) may occur; the thermal circuit representation is given in Fig. 1.1. The complete expression of the dusty gas model is complex, thus surface diffusion, which only occurs when membrane pore sizes are smaller than 0.02 μm [21], is typically not included so as to simplify MD flux prediction [2, 22]. MD water flux without consideration of surface diffusion is given as:

$$N_i = N_i^D + N_i^V \qquad (1.3)$$

where N_i^D and N_i^V are the diffusive (combined Knudsen and molecular) flux and viscous flux of water vapor, respectively. In its most general form, the dusty gas model applicable to MD is given by two equations [2]:

$$\frac{N_i^D}{\frac{2r\varepsilon}{3\tau\delta}(\frac{8RT_m}{\pi M_i})^{0.5}} + \sum_{j=1\neq i}^{n} \frac{P_j N_i^D - P_i N_j^D}{\frac{\varepsilon}{\tau\delta} PD_{ij}} = \frac{1}{RT}\Delta P_i \qquad (1.4)$$

$$N_i^V = \frac{P_i}{8RT_m \mu}\frac{r^2\varepsilon}{\tau\delta}\Delta P \qquad (1.5)$$

where r, ε, τ, and δ are the membrane pore radius, porosity, tortuosity, and thickness, respectively; R is the universal gas constant; T_m is the average temperature of the membrane; M_i is the molecular weight of water vapor; P_j is the air pressure inside the membrane pores; N_j^D is the diffusive flux of air; P is the total pressure; D_{ij} is the ordinary diffusion coefficient; μ is the fluid viscosity; and ΔP is the transmembrane pressure. Two equations for PD_{ij} are given in the literature [2, 12, 23]:

$$PD_{ij}\ (kPa\ m^2/s) = 4.46 \times 10^{-9} \times T_m^{2.334} \qquad (1.6)$$

and [22, 24]:

$$PD_{ij}\ (kPa\ m^2/s) = 1.895 \times 10^{-8} \times T_m^{2.072} \qquad (1.7)$$

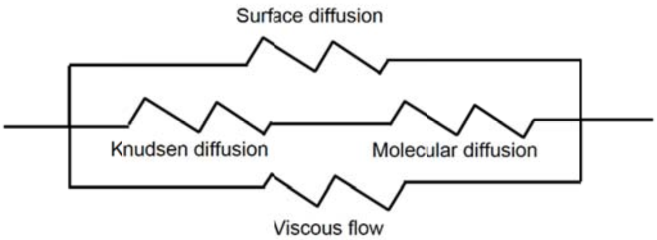

Figure 1.1 Thermal circuit of the dusty gas model [2].

Because of temperature polarization, the temperatures at the membrane surfaces (feed and distillate sides) are different from the bulk temperatures, thus the dynamic conditions inside the membrane module have to be considered (with hydraulic pressures, salinities, heat capacities, viscosities, and flow rates on both the feed and distillate sides, spacer properties if spacers are used, and membrane module dimensions) when determining the average membrane temperature (T_m) [19, 25-27]. Also, because hydraulic pressures always exist in flowing streams, membrane compaction may occur during MD testing, resulting in modified membrane properties (r, ε, τ, and δ) [28, 29]. Both temperature polarization and membrane compaction complicate the mass transfer equations. In seeking simplification of flux prediction, some investigations have assumed that viscous flow is negligible in DCMD due to the lack of a hydraulic pressure gradient [12, 22]; in these cases, only Eq. 1.4 is used to predict water flux. Other investigations assert that viscous flow cannot be neglected, especially for membranes with large (e.g., > 0.3 μm) pore sizes where the mean free path of water vapor in air is much greater than the membrane pore size [19, 30]. In these cases, a membrane pore size distribution instead of the average pore size has been used for mass transfer modeling [22, 31, 32]. The complicated model expressions and contradictory assumptions from the literature for the mass transfer mechanisms make prediction of water flux using the simplified dusty gas model cumbersome and ambiguous.

1.1.3. Existing membrane property parameters

If experimental operating conditions and solution chemistries are kept constant, then only the membrane properties will affect water flux. Considering this, further simplifications of the dusty gas model in the literature have used membrane property parameters (also referred to as membrane morphology parameters) to qualitatively analyze water flux. From Eqs. 1.4 and 1.5, membrane property parameters affecting water flux are $\varepsilon/\tau\delta$, $r\varepsilon/\tau\delta$, or $r^2\varepsilon/\tau\delta$ for molecular diffusion, Knudsen diffusion, and viscous flow, respectively. It is expected that membranes with greater $\varepsilon/\tau\delta$, $r\varepsilon/\tau\delta$, or $r^2\varepsilon/\tau\delta$ will have higher water fluxes [2, 24, 33-36]. It is also generally agreed that higher water fluxes occur for MD membranes with higher porosity [33, 37, 38] or lower tortuosity [23, 39].

It is unclear to what extent membrane pore size affects water flux since the role of membrane pore size is not the same in $\varepsilon/\tau\delta$, $r\varepsilon/\tau\delta$, and $r^2\varepsilon/\tau\delta$. Lawson et al. [37] found that water flux increased with increasing pore size. Mericq et al. [40] found that the Knudsen permeability ($B \propto r\varepsilon/\tau\delta$; r included) of the membrane strongly affected water flux. However, in a couple of observations, water flux was found to be highly sensitive to the characteristic parameter $\varepsilon/\tau\delta$ [27, 34] and only slightly sensitive to pore size [27]. Ali et al. [36] also observed no dramatic increase of the water flux with increasing pore size, especially when the pore size was smaller than 0.3 μm.

Although thickness is generally included in the membrane property parameters, some studies discounted its role and utilized ε/τ, $r\varepsilon/\tau$, and $r^2\varepsilon/\tau$. Lawson et al. [37] found that flux increased as the membrane parameter $\tau\delta$ increased. Bonyadi et al. [33] and El-Bourawi et al. [38] found that thickness was important because thinner membranes have reduced mass transfer resistance but they also found that flux did not monotonically increase with thickness reduction because of increased conductive heat loss through the membrane.

Although several membrane property parameters have been analyzed in the literature, there are contradictory observations about their effects on water flux (with the exception of porosity and tortuosity). Furthermore, only qualitative analyses between water flux and membrane property parameters were given; these enable the evaluation of trends but not the prediction of specific values of flux. Uniform terminology for the combinations of membrane property parameters also does not exist: membrane constant, membrane parameter, model parameter, structural parameter, morphology parameter, membrane factor, and characteristic parameter have all been used in the literature. The term membrane structural parameter will be used in this work and will refer to a single membrane-specific property or a combination of properties.

1.1.4. Concern of coupled membrane properties in structural parameters

Often, membrane structural parameters given in the literature ($\varepsilon/\tau\delta$, $r\varepsilon/\tau\delta$, $r^2\varepsilon/\tau\delta$, $r\varepsilon/\tau$, $r^2\varepsilon/\tau$, ε/τ, and $\tau\delta$) may have coupled membrane properties. For example, porosity may be calculated as a function of thickness [35, 37, 41, 42] and tortuosity is frequently calculated as a function of porosity [34, 35, 39, 43]. Thus, errors in the thickness measurement will be propagated into the porosity determination and then into the tortuosity determination. The presence of errors in measurements as straightforward as thickness measurements can be seen by comparing membrane thickness values for the same membrane from different sources (e.g., from [44, 47] for the GVHP and HVHP membranes). Although membrane structural parameters may be decoupled by evaluating more of the membrane properties experimentally, as has been done in some investigations (e.g., [33, 48, 49]), this comes with additional cost of time, effort, and equipment. Therefore, a membrane structural parameter that requires few laboratory measurements and does not include coupled membrane properties would be very useful to make a priori flux predictions.

1.1.5. Objective

Because low water flux is preferred when treating feedwaters with high fouling and scaling potentials and high water flux is preferred when treating less challenging feedwaters (Section 1.1.1), a simplified model that can predict the relative magnitudes of water fluxes for a group of MD membranes would be useful. Membrane structural parameters have been used to simplify mass transfer modeling in MD, however, no flux predictions with either absolute or relative magnitudes have been made using these parameters, and also, these parameters may contain coupled properties. In this work, a new membrane structural parameter is introduced to provide a priori assessment of the relative magnitude of water flux. First, a membrane structural parameter with no coupled parameters and requiring simple and reliable laboratory measurements was identified. Second, an empirical model based on the new structural parameter was developed to predict water flux for single-layer membranes and composite membranes. Predictions from this model were compared with flux predictions of existing mass transfer models. Third, flux predictions from this model were correlated with water fluxes for membranes with a range of pore sizes. This study also makes available to the literature a detailed collection of MD membrane properties and their water flux values that will assist others in membrane selection, development, and application.

1.2. Materials and methods

1.2.1. MD membrane water flux test

Membrane water flux was evaluated using a bench-scale DCMD configuration (Fig. 1.2). Four liters of double-distilled water were added to both the feed and distillate reservoirs. The feed stream was maintained at 60 ºC using a flow-through heater (STFT-1500-120, TruHeat, Allegan, MI). The distillate stream was held at 20 ºC using a recirculating chiller (NESLAB ThermoFlex 1400, Thermo Fisher Scientific, Newington, NH). Temperatures were monitored using four resistance temperature detectors (PRTF-10, Omega, Stamford, CT) coupled to a 4-channel analog input module (NI 9217, National Instruments, Austin, TX) at the inlet and outlet of the feed and distillate loops of the membrane module. The membrane module utilized a flat-sheet membrane with 118 cm^2 of effective membrane surface area. Two spacers were used, one on the feed side and one on the distillate side of the membrane, to generate turbulence and reduce polarization effects. The feed and distillate streams were circulated counter-currently on their respective sides of the membrane at 1.5 L/min. As water evaporated through the membrane, the excess water from the distillate reservoir overflowed into a beaker on an analytical balance and the overflow rate was used to calculate water flux. For each membrane, water fluxes of three membrane samples were measured and the average water flux was calculated.

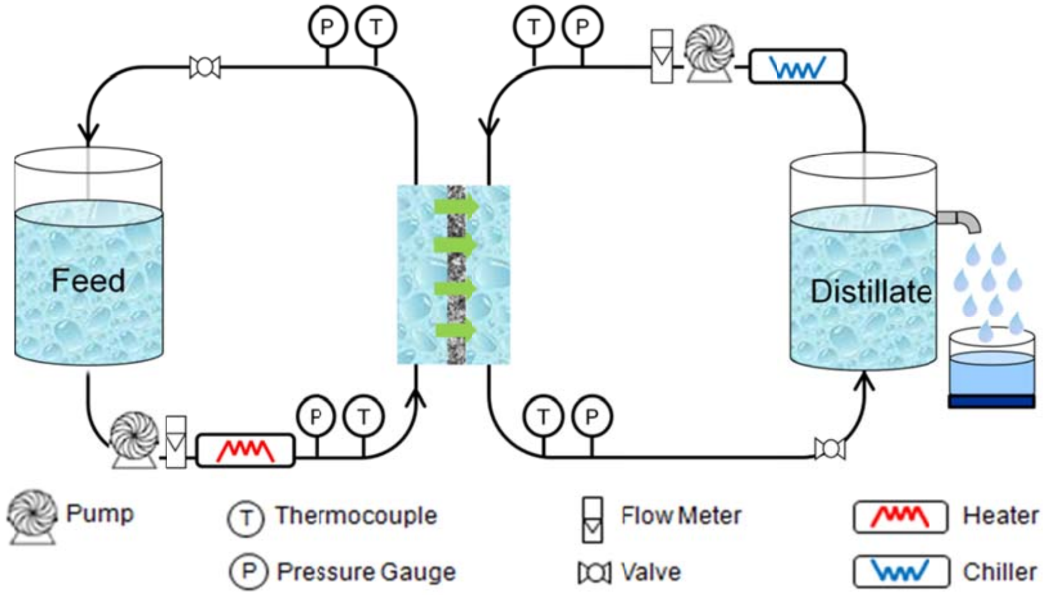

Figure 1.2: Schematic drawing of bench-scale DCMD system. The arrows in the membrane module indicate the direction of water vapor passing through the membrane.

1.2.2. Membrane characterization

A total of 19 flat-sheet membranes (10 single-layer, 9 composite) were tested. The membrane properties provided by the manufacturers are listed in Table 1.1 and the additional measurements performed to provide further membrane characterization are described below. The single-layer membranes were used directly for all characterization measurements. The composite membranes were used intact for all measurements except porosity, which required peeling of the active layer off the support layer. Care was taken to ensure as minimal disruption as possible to the peeled active and support layers.

Table 1.1: Membrane properties as reported by manufacturers. PTFE - polytetrafluorethylene; PP - polypropylene; PVDF - polyvinylidene fluoride.

Membrane	Nominal pore size (μm)	Thickness[a] (μm)	Porosity (%)	Active layer material	Support layer material
A	0.20	79	70	PTFE	--
B	0.22	--	--	PTFE	--
C	0.22	--	--	PP	--
D	0.80	75	76	PTFE	--
E	0.20	80	74	PTFE	--
F	0.10	76-154	--	PTFE	--
G	0.10	--	--	PTFE	--
H	0.50	75	78	PTFE	--
I	0.10	70	68	PTFE	--
J	0.45	--	83	PVDF	--
K	0.45	--	--	PTFE	PP
L	0.45	195	--	PTFE	PP
M	0.20	192	--	PTFE	PP
N	0.45	279	--	PTFE	PP
O	0.20	--	--	PTFE	PP
P	0.20	--	--	PTFE	PP
Q	0.20	130	72[b]	PTFE	PP
R	0.50	120	74[b]	PTFE	PP
S	0.45	190	--	PTFE	PP

[a] sum of the active layer thickness and support layer thickness for composite membranes
[b] refers to the percent open area of the membrane

1.2.2.1. *Average pore size measurement*

Intact membranes were used to determine the average pore size of the single-layer membranes and the active layers of the composite membranes using the gas permeation test with compressed air [50, 51]. The permeation flux of air through the dried membrane was measured at room temperature using transmembrane pressures from 10 to 100 kPa. Pore diameter (*d*) was then calculated as:

$$d = \frac{16}{3}\left(\frac{B_o}{K}\right)\left(\frac{2RT}{\pi M_j}\right)^{0.5} \qquad (1.8)$$

where B_o is the geometric factor of a membrane; K is the permeability coefficient; and M_j is the molecular weight of air [52].

1.2.2.2. *Porosity and tortuosity measurements*

The porosity (ε) of the single-layer membranes and peeled active and support layers of the composite membranes was determined by:

$$\varepsilon = 1 - \frac{\rho_m}{\rho_p} \qquad (1.9)$$

where ρ_m is the density of the membrane sample and ρ_p is the reported density of the polymer material [35]. The membrane sample density, ρ_m, for the single-layer membrane was calculated directly from the mass and dimensions of a membrane sample, excluding the pore space in the material. Values of ρ_p used were 2200 kg/m^3 for polytetrafluoroethylene (PTFE) [49, 53], 900 kg/m^3 for polypropylene (PP) [53], and 1780 kg/m^3 for polyvinylidene fluoride (PVDF) [54]. Although additives may be included during the membrane manufacturing proces [55], and could cause the actual density of the membrane material to be different from the reported polymer density, the difference is assumed negligible due to the very small additive amounts. Zhang et al. [35] used the reported polymer density in their porosity calculation and claimed a density error of less than 3%. Ruskowitz et al. [56] used energy dispersive spectrometry (EDS) surface analysis (0.3-0.5 wt% detection limit) on a virgin PTFE sample (Membrane D, Table 2.1), and detected only carbon and fluorine on the membrane sample.

The tortuosity (τ) of each single-layer membrane was calculated by [23, 57]:

$$\tau = \frac{(2-\varepsilon)^2}{\varepsilon} \qquad (1.10)$$

and the tortuosity of the active layer (τ_a) of the composite membrane was calculated by:

$$\tau_a = \frac{(2-\varepsilon_a)^2}{\varepsilon_a} \qquad (1.11)$$

where ε_a is the porosity of the active layer. Tortuosity of the non-woven support layer (τ_s) of the composite membrane was calculated by [43, 58]:

$$\tau_s = \frac{1}{\varepsilon_s} \qquad (1.12)$$

where ε_s is the porosity of the composite membrane support layer. The porosity-tortuosity relationship in Eq. 1.12 is different from Eqs. 1.10 and 1.11 because non-woven support layers are loosely packed, with structures similar to random spheres or clusters; while single-layer membranes and active layers of composite membranes are spongy, with structures similar to the interstices between closely packed spheres [43, 58]. Tortuosity of the scrim support layer of the composite membrane was assumed to be 1[59].

1.2.2.3. *Membrane thickness measurement*

The thickness (δ) of the single-layer membranes and the active layer and support layer of the composite membranes were measured from scanning electron micrographs of membrane cross-sections. Prior to measurement, the intact membranes were immersed in liquid nitrogen and cut with a razor blade. The thicknesses of the active layer and the support layer of the composite membranes were measured separately on the same scanning electron micrograph (no peeling was necessary). Each thickness was measured on three different sections of the membrane and the average thickness was calculated

1.2.2.4. Contact angle measurement

Contact angle (θ) was measured as an indication of membrane hydrophobicity. A commercial goniometer (Ramé-Hart, Mountain Lakes, NJ) was used to perform captive-bubble measurements on intact membranes to determine the contact angle of the single-layer membranes and composite membrane active layers. By immersing the membrane sample into a water solution and completely hydrating it, the contact angle measurement is less influenced by pores and swelling [60]. For each membrane, triplicate contact angles were measured on three samples, resulting in nine contact angles measured per membrane, and the average contact angle was calculated.

1.2.2.5. Liquid-entry pressure measurement

Liquid-entry pressure (LEP) is the pressure that must be applied to a water solution to penetrate into dry membrane pores. It is a function of the membrane properties and the liquid properties. The expression for LEP is:

$$P_l - P_j = \frac{2B_o \gamma_l \cos\theta}{r_{\max}} < LEP \qquad (1.13)$$

where P_l is the pressure of the liquid on the membrane surface; γ_l is the liquid surface tension; and r_{max} is the largest membrane pore radius [61]. The experimental apparatus reported by Smolders et al. [48] was used to perform LEP measurements on intact membranes to determine the LEP of single-layer membranes and composite membrane active layers. Each membrane was placed in a static stainless-steel cell filled with double-distilled water. The water pressure was increased in increments of 5 kPa and maintained for one minute at each pressure; the pressure at which continuous flow was observed on the distillate side was considered to be the membrane LEP.

1.2.2.6. Percent of open surface area of the support layer measurement

Scanning electron micrographs with 35x magnification were used to determine the percent of open surface area (POSA) of the support layers. The scrim support layer had a uniform pore structure (Fig. 1.3a), thus the POSA was calculated by dividing the total pore area (function of pore area and pore number) by the whole membrane sample area [34]. Because of the non-uniform pore structure of the non-woven support layer (Fig. 1.3b), the POSA was determined using the grid method with the scanning electron micrographs.

(a)

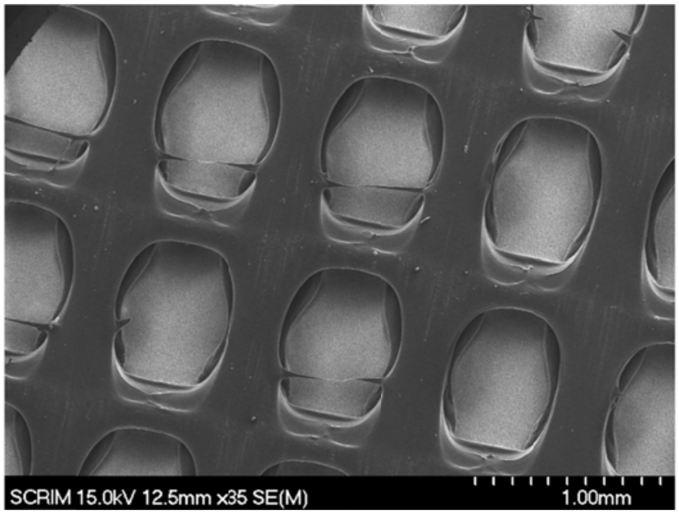

(b)

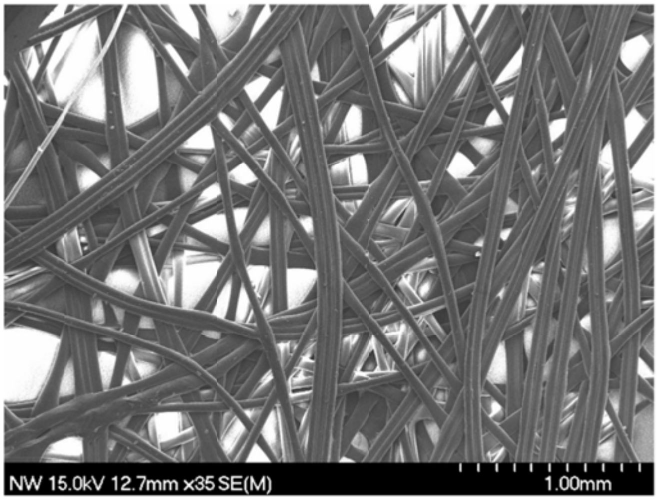

Figure 1.3: SEM images of (a) scrim support layer and (b) non-woven support layer.

1.2.3. Model development and validation for water flux prediction

Scatterplots and correlation matrices between water flux and the membrane structural parameters were developed and analyzed using Minitab® 15.1.0.0 with the goal of identifying the structural parameters with the strongest correlation with water flux. For selected structural parameters, a linear regression analysis was performed between water flux and the structural parameter to develop a water flux prediction model. To ensure the robustness of the model, the process was performed three times in total with membranes from Table 2.1 randomly selected each time for the linear regression. The single-layer membranes and the composite membranes were tested separately from each other.

The models developed above were validated both internally and externally. For internal validation, the sum of the estimated standard deviations of the regression coefficients (s{b_0} and s{b_1}), squared errors (SSE), mean squared error (MSE), adjusted R^2, and predicted residual sums of squares (PRESS) criteria were used[62]. All criteria were obtained from the Minitab® regression output. Typically, a model with small s{b_0}, s{b_1}, SSE, MSE, PRESS, and high adjusted R^2 will fit well and result in small errors between the predicted water flux and the measured water flux for the membranes used to develop the model. For external validation, the mean squared prediction error (MSPR) was used. If the MSPR to MSE ratio of a model is smaller than the critical F-test value ($p < 0.05$), the model is valid, and vice versa [63]. For a valid model, if the MSPR is much smaller than or fairly close to the MSE, the MSE will give an appropriate measure of the predictive capability of the model. If the MSPR is much greater than the MSE, then the MSPR should be used as an indicator of the predictive capability of the model [64]. A model with a smaller MSPR or MSE (depending on which one is used) is expected to have a better predictive capability [64].

1.3. Results and discussions

1.3.1. Membrane property characterization and flux test results

The properties of the single-layer membranes and the active layers of the composite membranes, along with the intact membrane water fluxes are given in Table 1.2. The average pore sizes of the single-layer membranes (0.1-0.5 μm excluding membrane D) and the composite membrane active layers (0.2-0.6 μm) are comparable and generally within the range reported in the literature (0.2-1 μm) [1, 35, 36]. Membrane porosities for the single-layer membranes (37-85%) and the composite membrane active layers (47-90%) are also comparable and generally within the range reported in the literature (30-85%) [38, 39]. It follows from Eq. 1.10 that the tortuosities are also comparable (1.58-4.02 for the single-layer membranes except Membrane I and 1.59-5.05 for the active layers of the composite membranes) and consistent with the literature (1.21-6.84) [43]. The thicknesses of the single-layer membranes (39 to 205 μm) are similar to those reported in the literature (40 to 250 μm) [1]; they span a broader range than the thicknesses of the composite membrane active layers (27-59 μm). This is because single-layer membranes must be thick enough to be mechanically strong and to minimize conductive heat loss but thin enough to minimize the mass transfer resistance, while composite membranes must have thin active layers to reduce the mass transfer resistance and the support layers will provide mechanical strength and reduce conductive heat loss. The contact angles of the single-layer membranes (109-131^{o}) and the composite membrane active layers (106-128^{o}) are similar and are comparable with what has been reported in the literature (110-165^{o} [58, 66]). The LEP values of the single-layer membranes (141-430 kPa) and the composite membrane active layers (95-438 kPa) are comparable and generally within the reported range (48-463 kPa) [39].

The single-layer membrane water fluxes (11-35 L/m^2 h) are within the reported flux range (4-42 L/m^2 h at feed-side temperatures near 40 °C and flow rates from 0.02 to 0.23 m/s for DCMD [39]); it should be noted that other experimental conditions including the distillate-side temperature and type of membrane spacers will also affect water flux. The lowest water flux occurs for Membrane I, which has the lowest porosity (37%) (hence, highest tortuosity (7.07)) and the smallest average pore size (0.1 μm). Membrane G has similar pore size (0.11 μm) as Membrane I, but the water flux is 54% higher than that of Membrane I, which is likely due to the much greater porosity (84%; hence, much lower tortuosity (1.60)). The composite membrane water fluxes fall within a more narrow range (22-28 L/m^2 h) with all but two membranes having a water flux above 25 L/m^2 h. The wide range of membrane properties and experimental water fluxes of the single-layer membranes is beneficial in developing the model to predict water fluxes.

Table 1.3 provides the characterization results of the composite membrane support layers. The thicknesses of the non-woven structural support layers (133-283 μm) are greater than the thicknesses of the scrim structural support layers (50-77 μm except Membrane O with a thickness of 255 μm). The porosities of the non-woven structural support layers (66-81%) are higher than the porosities of the scrim structural support layers (31-59%), while the POSA are generally an order of magnitude lower for the non-woven structural support layers than the scrim structural support layers. This phenomena has been reported previously [58]. Because the larger POSA of the scrim structure benefits the mass transfer while the lower porosity limits the mass transfer, the effect of these on flux is not obvious.

Table 1.2: Properties of the single-layer membrane and composite membrane active layer.

Membrane	Pore size (μm)	Porosity[b] (%)	Tortuosity[b]	Thickness (μm)	Contact angle (^{o})	Liquid entry pressure (kPa)	Flux[c] (L/m^2 h)
A	0.22±0.11	53.4	4.02	39±5	125±2	380±4	28.7±0.9
B	0.25±0.06	84.5	1.58	119±11	128±3	430±5	25.8±0.5
C	0.24±0.13	82.6	1.67	205±4	126±1	375±3	21.3±0.7
D	0.90±0.09	78.8	1.86	78±2	121±2	141±5	26.8±1.5
E	0.25±0.06	67.4	2.61	95±3	114±3	258±5	18.3±1.1
F	0.18±0.02	80.1	1.79	67±17	131±3	385±3	34.5±1.2
G	0.11±0.05	84.1	1.60	111±4	124±3	358±6	17.5±0.3
H	0.36±0.04	61.2	3.15	56±4	109±4	183±5	21.9±1.2
I	0.10±0.01	37.4	7.07	63±4	114±2	400±10	11.4±3.0
J	0.51±0.04	65.2	2.79	109±6	118±3	154±6	24.3±1.1
K[a]	0.34±0.19	56.1	3.68	31±5	120±5	415±10	28.1±0.3
L[a]	0.52±0.08	84.2	1.59	27±2	118±5	190±5	26.0±1.1
M[a]	0.19±0.11	46.6	5.05	31±4	106±6	290±5	25.3±1.2
N[a]	0.57±0.26	90.3	1.33	59±3	126±1	95±6	26.3±0.6
O[a]	0.23±0.04	81.1	1.74	58±18	125±2	380±5	24.5±1.0
P[a]	0.25±0.01	79.6	1.82	50±11	125±3	395±10	24.0±0.9
Q[a]	0.21±0.04	64.4	2.85	31±10	128±2	390±15	25.7±1.1
R[a]	0.50±0.15	71.3	2.32	47±4	120±2	438±5	25.8±0.2
S[a]	0.44±0.13	77.5	1.94	21±3	109±2	238±15	22.2±3.5

[a] active layer of the composite membrane
[b] calculated using the average membrane properties
[c] refers to the intact membrane flux

Table 1.3: Composite membrane support layer properties. A tortuosity of 1 is assumed for the scrim support layers [59].

Membrane	Membrane structure	Porosity^a (%)	Tortuosity^a	Thickness (μm)	POSA (%)
K^s	Scrim	58.6	1	77±14	43.2
L^s	Non-woven	72.8	1.37	283±9	3.76
M^s	Non-woven	80.9	1.20	171±8	4.09
N^s	Non-woven	70.6	1.42	230±10	3.97
O^s	Scrim	52.0	1	255±14	44.6
P^s	Non-woven	72.3	1.38	194±13	11.4
Q^s	Scrim	39.4	1	54±7	35.4
R^s	Scrim	30.5	1	50±6	37.4
S^s	Non-woven	65.5	1.53	133±11	3.21

^{s} support layer of the composite membrane
^{a} calculated using the average membrane properties

1.3.2. Model development and validation for single-layer membranes

1.3.2.1. Identification of structural parameters that have high correlations with water flux

As discussed in Section 1.1.3, pore size, porosity, tortuosity, and thickness may each affect water flux in MD. In this work, four characteristics (r, ε , $1/\tau$, $1/\delta$) were considered in various combinations ($r^n\varepsilon/\tau\delta$, $r^n\varepsilon/\delta$, $r^n\varepsilon/\tau$, $r^n/\tau\delta$, $r^n\varepsilon$, r^n/τ, r^n/δ, and r^n), where n is 0, 1, or 2. Additional membrane properties, including θ, 1/LEP, 1/thermal conductivity ($1/k_m$), and 1/heat transfer coefficient ($1/h_m$) were also investigated to ensure a comprehensive analysis of possible structural parameters (28 total parameter combinations were tested). Calculations of k_m and h_m were performed as reported in the literature [2, 12, 45]. Overall, the structural parameters were classified into three groups: 1) those already reported in the literature: $\varepsilon/\tau\delta$, $r\varepsilon/\tau\delta$, $r^2\varepsilon/\tau\delta$, ε/τ, $r\varepsilon/\tau$, $r^2\varepsilon/\tau$, $1/\tau\delta$. r, ε, and $1/\delta$; 2) basic membrane properties and their reciprocals that were not included in the first group: $1/\tau$, 1/LEP, $1/k_m$, and $1/h_m$; and 3) others: $r\varepsilon/\delta$, $r^2\varepsilon/\delta$, ε/δ, $r^2\varepsilon$, $r\varepsilon$, r^2/δ, r/δ, $r/\tau\delta$, $r^2/\tau\delta$, r/τ, r^2/τ, and r^2. Membrane contact angle, θ, was eventually removed from consideration as a structural parameter to predict water flux in this investigation because there was little range in the contact angle of the single-layer membranes (Table 1.2).

To identify the structural parameters that correlate well with water flux, a correlation analysis between water flux and each structural parameter was first performed for the ten single-layer membranes. Although investigations of the effects of membrane pore size, porosity, and inverse thickness on water flux have been discussed in the literature (Section 1.1.3), the correlation results in Table 1.4 (correlation coefficient, β, from 0.243 to 0.428) suggest that none of the parameters alone can be used to adequately estimate water flux. The structural parameters ε/δ, $\varepsilon/\tau\delta$, and $1/\tau\delta$ all correlate well with water flux (β from 0.638 to 0.781), and those correlation observations are also supported by the scatterplots in Appendix 1A; thus, these structural parameters may be used to predict water flux. Care should be taken, however, because the three structural parameters include membrane properties that may be coupled, which can lead to error propagation as discussed in Section 1.1.4.

To avoid the use of coupled membrane properties, a structural parameter that can be measured independently but maintains the physical meaning of those membrane properties that may affect water flux (e.g., thickness and porosity) is preferred. In this regard, membrane porosity (Eq. 1.9) can be expressed as [35]:

$$\varepsilon = 1 - \frac{m}{\rho_p \times l \times w \times \delta} \qquad (1.14)$$

where m, l, and w are the mass, length, and width, respectively, of the membrane sample. Eq. 1.14 can be used to decouple porosity and thickness by incorporating the constant membrane properties (m, l, w, and ρ_p) into a new structural parameter termed the membrane constant (C_m):

$$C_m = \frac{\rho_p \times l \times w}{m} \qquad (1.15)$$

The physical relationship between the membrane constant, porosity, and thickness can be seen by combining Eqs. 1.14 and 1.15:

$$C_m = \frac{1}{\delta(1-\varepsilon)} \tag{1.16}$$

The correlation analysis between water flux and Cm for the 10 single-layer membranes was performed and a correlation of β = 0.714 was observed (last row of Table 1.4), suggesting it was a good structural parameter for flux prediction.

Table 1.4: Correlation results between water flux and membrane structural parameters for single-layer membranes. Bold numbers indicate structural parameters having the highest correlations with water flux.

	Structural parameter	Correlation coefficient
Structural parameters reported in literature	$\varepsilon/\tau\delta$	**0.731**
	$r\varepsilon/\tau\delta$	0.399
	$r^2\varepsilon/\tau\delta$	0.251
	ε/τ	0.326
	$r\varepsilon/\tau$	0.336
	$r^2\varepsilon/\tau$	0.243
	$1/\tau\delta$	**0.781**
	r	0.303
	ε	0.428
	$1/\delta$	0.243
Basic membrane properties	$1/\tau$	0.357
	1/LEP	0.111
	$1/k_m$	0.168
	$1/h_m$	-0.080
Other structural parameters	$r\varepsilon/\delta$	0.402
	$r^2\varepsilon/\delta$	0.257
	ε/δ	**0.638**
	$r^2\varepsilon$	0.244
	$r\varepsilon$	0.329
	r^2/δ	0.261
	r/δ	0.376
	$r/\tau\delta$	0.405
	$r^2/\tau\delta$	0.253
	r/τ	0.336
	r^2/τ	0.244
	r^2	0.243
New structural parameter	C_m	**0.714**

Because C_m is not based on thickness or porosity measurements (Eq. 1.15), constant flux will be predicted during membrane compaction periods. To experimentally validate this, four randomly selected membranes were compacted under feed-side pressures up to 100 kPa in DCMD. No flux change was observed for the four membranes; similar phenomena have also been reported by Cath et al. [28]. Although membrane compaction may occur, it may not be significant enough to measurably decrease flux. If the membrane were to be highly compacted, flux decline would likely occur and would not be predicted by C_m, thus using C_m to estimate water flux does have practical limitations. It should also be noted that C_m can only be used to estimate the steady-state water flux and not dynamic water flux behavior such as that frequently observed in the initial stages of an MD flux test [67-69].

1.3.2.2. Model development and validation using the membrane constant

A simple linear regression model using C_m was used to predict water flux under the given experimental conditions. The model was expressed as:

$$\hat{N}_i = b_0 + b_1 C_m \tag{1.17}$$

where $\hat{N}_i$ is the predicted water flux and b_0 and b_1 are the regression constants. Because the pore sizes of a typical MD membrane range from 0.2 to 1.0 μm [1, 35, 65] and are recommended to be smaller than 0.6 μm to prevent wetting [39, 67, 70], only the seven single-layer membranes with pore sizes from 0.18 to 0.51 μm were used during model development. Three independent test sets were performed; each test set used five membranes randomly selected for model development and the remaining two for model validation. In Test Set 1, Membranes B and E were used to validate the model; in Test Set 2, Membranes H and J were used; and in Test Set 3, Membranes A and C were used. The linear regression model was also used to predict water flux based on the other three well correlated structural parameters ($\varepsilon/\tau\delta$, $1/\tau\delta$, and ε/δ) simply by replacing C_m in Eq. 1.17 with $\varepsilon/\tau\delta$, $1/\tau\delta$ and ε/δ, respectively. Results using ε/δ revealed a nonlinear relationship with water flux for all three tests ($p > 0.14$; results not shown) and was thus dropped from further model development. The linear regression results for C_m, $\varepsilon/\tau\delta$, and $1/\tau\delta$ are given in Table 1.5. Linear relationships are observed ($p \leq 0.1$) for all three. The residual plots (Appendix 1B) for each structural parameter suggest that it is reasonable to use the linear regression analysis.

In Table 1.5, the calculated MSPR to MSE ratios are smaller than the critical $F_{0.05}$ value (5.786) for all tests, thus the developed models are valid to predict water flux for the membranes in the model validation group. In Test Set 1, no single structural parameter is consistently better than the others for the model development considering all model criteria (i.e., none has a consistently lower s{b_0}, s{b_1}, SSE, PRESS, and MSE and a higher adjusted R^2); however, the model developed using C_m has a better predictive capability due to the smaller MSE. The MSE criterion was used because the MSPR was similar to the MSE for each structural parameter. In Test Set 2, the model developed using C_m has lower s{b_0}, s{b_1}, SSE, PRESS, and MSE and a higher adjusted R^2 than the models developed using $\varepsilon/\tau\delta$ and $1/\tau\delta$, indicating that C_m is a better structural parameter for the model development. It should be noted however, that the predictive capability of this model (MSPR of 20.71) is not as good as the one developed using $\varepsilon/\tau\delta$ (MSE of 12.58). The MSPR criterion was used for C_m because the MSPR was much greater than the MSE; while the MSE criterion was used for $\varepsilon/\tau\delta$ because the MSE was close to the MSPR. In Test Set 3, the structural parameter $\varepsilon/\tau\delta$ is identified as a better structural parameter for the model development (lower s{b_0}, s{b_1}, SSE, PRESS, and MSE and a higher adjusted R^2) and the model has a better predictive capability due to the smaller MSE. The MSE criterion was used because the MSE was close to or much larger than the MSPR for each structural parameter. Overall, the models developed using C_m and $\varepsilon/\tau\delta$ have better flux prediction performance than the model developed using $1/\tau\delta$. Because the characterization of the membrane constant requires only basic and independent measurements (mass, length, and width of the membrane sample) that can be obtained with inexpensive analytical equipment (a ruler and a balance), less cost is associated with the measurement as compared to $\varepsilon/\tau\delta$, where the thickness measurement must be determined using scanning electron micrographs. Additionally, the problem of coupled parameters may exist between porosity, tortuosity, and thickness with $\varepsilon/\tau\delta$.

Comparing the results of the three test sets using C_m, the model developed in Test Set 1 has the smallest MSE or MSPR (depending on which one is used) compared to the models developed in Test Sets 2 and 3. Therefore, this model has the smallest flux prediction errors for the membranes used in the model validation process. The model developed in Test Set 2 has the lowest s{b_0}, s{b_1}, SSE, PRESS, and MSE and the highest adjusted R^2 compared to the models developed in Test Sets 1 and 3, thus it has the smallest flux prediction errors for the membranes used in the model development process. Because five out of the seven membranes had better flux predictions using the model developed in Test Set 2, this model was taken as the final model for flux prediction under the current experimental conditions. The model is expressed as:

$$\hat{N}_i = 10.1 + 318 \times C_m \tag{1.18}$$

where the units of $\hat{N}_i$ and C_m are L/m^2 h and μm^{-1}, respectively.

Table 1.5: Regression results for candidate models based on the model development and validation data sets. The structural parameters all have units of 1/μm.

Statistics	Test 1			Test 2			Test 3		
	$C_m \times 10^3$	$\varepsilon/\tau\delta \times 10^4$	$1/\tau\delta \times 10^4$	$C_m \times 10^3$	$\varepsilon/\tau\delta \times 10^4$	$1/\tau\delta \times 10^4$	$C_m \times 10^3$	$\varepsilon/\tau\delta \times 10^4$	$1/\tau\delta \times 10^4$
p	0.053	0.062	0.073	0.010	0.052	0.019	0.079	0.058	0.102
b_0	15.13	16.60	15.10	10.10	13.04	10.41	12.67	13.46	11.53
$s\{b_0\}$[a]	3.802	3.593	4.348	2.863	4.363	3.513	4.991	4.147	6.054
b_1	0.239	0.263	0.208	0.318	0.323	0.285	0.262	0.295	0.252
$s\{b_1\}$[b]	0.077	0.091	0.077	0.006	0.103	0.061	0.100	0.099	0.108
SSE	28.87	31.96	35.27	13.36	37.75	19.83	44.50	36.76	52.13
PRESS	81.69	73.41	92.87	39.92	69.61	62.18	183.8	145.9	227.7
MSE	9.622	10.65	11.76	4.450	12.58	6.610	14.83	12.25	17.38
MSPR	13.01	18.57	13.60	20.71	12.16	21.19	2.031	13.83	3.450
MSPR:MSE	1.352	1.744	1.156	4.654	0.967	3.206	0.137	1.129	0.198
Adjusted R^2	68.4%	65.0%	61.4%	89.0%	68.8%	83.6%	59.5%	66.5%	52.5%

[a] estimated standard deviation of the regression coefficient b_0
[b] estimated standard deviation of the regression coefficient b_1

1.3.2.3. Flux prediction for membranes with pore sizes outside the typical range

The model (Eq. 1.18) was also used to predict water flux for membranes with pore sizes outside the range used for the model development ($d < 0.18$ or > 0.51 μm). The flux prediction errors, along with the errors for the membranes used to develop and validate the model, are given in Table 1.6. As expected, the water flux prediction errors for membranes used to develop the model are relatively small (≤ 11.5%). However, a relatively large flux prediction error (-23.9%) for one of the membranes used to validate the model (Membrane A) was observed. This is likely because of the relatively low porosity of this membrane (Table 1.2). As stated in Section 1.3.2., flux decline would likely occur for a highly compacted membrane and would not be predicted by C_m. Because a membrane with a low porosity is expected to be structurally similar to a highly compacted membrane, it follows that the flux prediction error using C_m for the low porosity membrane is also larger. This suggests the practical limitations of using C_m for flux prediction. The model predicts water flux well for the membrane with a large pore size (Membrane D; 0.9 μm) and one of the two membranes with very small pore size (Membrane G; ~ 0.1 μm). The error in flux prediction for Membrane I, which also has a very small pore size (0.1 μm), is nearly 60%. It is unclear whether the low porosity (37.4%) or the large variation of the experimental water flux (±3 L/m^2 h, twice the variation observed for other membranes) led to the large predicted flux error for Membrane I. Overall, it appears that the developed model can be used to predict the water flux of membranes with pore sizes from 0.10 to 0.9 μm, but may not be appropriate for membranes with very low porosities (e.g., Membrane I).

Table 1.6: Flux prediction error (%) between the measured water fluxes and the predicted water fluxes.

	Membrane	Current model[a] (%)	Dusty gas model v.1[b] (%)	Dusty gas model v.2[c] (%)
Model development	B	5.97	48.2	42.8
	C	-10.6	-2.61	-6.13
	E	11.5	28.0	23.4
	F	-1.59	36.9	32.5
	J	-3.84	-7.05	-11.2
Model validation	A	-23.9	-2.50	-5.86
	H	12.6	50.9	44.6
Pore size near 0.1μm	G	16.4	61.3	57.3
	I	59.3	-59.7	-60.7
Pore size of 0.9 μm	D	9.36	138	126

[a] Eq. 1.18
[b] Eq. 1.6 was used for PD_{ij} in Eq. 1.4 for flux prediction
[c] Eq. 1.7 was used for PD_{ij} in Eq. 1.4 for flux prediction

1.3.2.4. Performance comparison between the developed model and the simplified dusty gas model

The flux prediction performance using the simplified dusty gas model with two different PD_{ij} equations is also given in Table 1.6. Both PD_{ij} equations resulted in similar flux prediction. The simplified dusty gas model (Eq. 1.4) does not predict flux well for membranes with extremely small pore sizes (Membranes G and I) or large pore sizes (Membrane D). Because the dusty gas model neglects both surface diffusion and viscous flow when applied to DCMD, only Knudsen diffusion and molecular diffusion are considered as the mass transfer mechanisms. When the membrane pore size is comparable with the mean free path of water vapor in air (0.11 μm [22]), Knudsen diffusion is the dominant mass transfer mechanism. The addition of a molecular diffusion term may result in either over- or under-estimation of water flux depending on membrane properties and experimental conditions (Eq. 1.4). When the membrane pore size is much greater than the mean free path of water vapor in air, molecular diffusion is the dominant mass transfer mechanism. The addition of a Knudsen diffusion term likely led to the over-estimation of water flux for Membrane D (0.9 μm). Overall, the model developed using C_m has better flux prediction than the dusty gas model and can be used for membranes with a wider range of pore sizes.

1.3.3. Model development for the composite membranes

To investigate whether the membrane constant can be used to predict water flux for composite membranes, nine composite membranes were characterized and studied (Tables 1.2 and 1.3). The active layer membrane constant (C_{ma}) was used to represent the active layer properties since the membrane constant was already validated for single-layer membranes. The support layer properties investigated include support layer membrane constant (C_{ms}), thickness (δ_s), tortuosity (τ_s), porosity (ε_s), and POSA. Correlation results between composite membrane water flux and the membrane properties are given in Table 1.7, and it can be seen that none of the membrane properties alone correlate strongly with water flux. Although C_{ms} does not have the highest correlation coefficient with water flux, it's applicability for use with composite membranes alone and in conjunction with C_{ma} is evaluated here. Two linear regression models were tested based on: 1) a single composite membrane property (C_{ma} or C_{ms}), where the model was expressed the same as Eq. 1.17; and 2) the mass transfer in series theory, where the model was expressed as:

$$\frac{1}{\hat{N}_i} = b_0 + b_1 \frac{1}{C_{ma}} + b_2 \frac{1}{C_{ms}} \tag{1.19}$$

Linear regression tests were performed for both models and the absolute *p* values were found to be much greater than 0.316. Therefore, a nonlinear relationship exists between water flux and the membrane constant for the composite membranes. One possible reason is the narrow range of experimental water flux; membranes with a wider range of water flux should be tested to continue the model development for the composite membranes.

Table 1.7: Correlation results between water flux and membrane structural parameters for composite membranes.

Membrane property	Correlation coefficient
C_{ma}	-0.316
$1/\delta_s$	0.309
ε_s	-0.165
$1/\tau_s$	0.496
C_{ms}	0.318
POSA	0.448

1.4. Conclusions

A simplified water flux prediction model was developed to predict the water flux of DCMD membranes. The model uses a newly introduced structural parameter that does not contain coupled properties and can be measured independently while still carrying the physical meaning of a relationship with those membrane properties that may affect water flux (thickness and porosity). Compared to the simplified dusty gas model, the empirical model developed in the current investigation using C_m has the following advantages: 1) it can quantitatively analyze water flux with a less complicated expression using uncoupled membrane properties; 2) it has better flux prediction and can be used for membranes with a wide range of pore sizes (0.1-0.9 μm); and 3) C_m characterization can be carried out through simple and reliable measurements using inexpensive analytical equipment. However, using C_m for flux prediction does have limitations. It may not be valid for membranes with low porosities and it cannot adequately predict water flux for composite membranes when using the linear regression approach. Future efforts should be made to develop a non-linear prediction model for composite membranes.

1.5. Acknowledgments

The authors would like to thank the U.S. Department of Energy Geothermal Technologies Program (Grant No. DE-EE00003231) for the financial support of this work.

1.6. Nomenclature and units

$b_{(0,1,2)}$	Constants in the regression equation
B	Membrane mass transfer coefficient (L/m^2 Pa h)
B_o	Membrane geometric factor
C_m	Membrane constant (m^{-1})
$C_{m(a,s)}$	Membrane constant of the active layer (*a*) or support layer (*s*) (m^{-1})
d	Membrane pore size (m)
D_{ij}	Ordinary diffusion coefficient (m^2/s)
h_m	Heat transfer coefficient of the membrane (W/m^2 K)
k_m	Thermal conductivity of the membrane (W/m K)
K	Knudsen permeability coefficient (L/m^2 Pa h)
l	Membrane length (m)
m	Membrane mass (kg)
$M_{(i,j)}$	Molecular weight of vapor (*i*) or air (*j*) (kg/kmol)
n	Exponent of membrane pore size
N_i	Overall water flux (L/m^2 h)
$N_{(i,j)}^{D}$	Diffusive flux of vapor (*i*) or air (*j*) (L/m^2 h)
N_i^V	Viscous flux of vapor (L/m^2 h)
$\widehat{N}_i$	Predicted water flux (L/m^2 h)
p	Probability of obtaining a test statistic
P	Total pressure (Pa)
$P_{(i,j,l)}$	Pressure of vapor, air inside membrane pores, or liquid on membrane surface (Pa)
r	Membrane pore radius (m)
r_{max}	Largest membrane pore radius (m)
R	Universal gas constant (J/mol K)
T	Temperature (K)
T_m	Membrane temperature (K)
w	Membrane width (m)
β	Correlation coefficient
γ_l	Liquid surface tension (Pa m)
δ	Membrane thickness (m)
δ_s	Support layer thickness (m)
ΔP	Total pressure gradient (Pa)
ΔP_i	Vapor pressure gradient (Pa)
ε	Membrane porosity
$\varepsilon_{(a,s)}$	Porosity of the membrane active layer (*a*) or support layer (*s*)
θ	Contact angle (^{o})
μ	Fluid viscosity (kg/m s)
$\rho_{(m,p)}$	Density of the membrane (*m*) or membrane polymer (*p*) (kg/m^3)
τ	Membrane tortuosity
$\tau_{(a,s)}$	Tortuosity of the membrane active layer (*a*) or support layer (*s*)

1.7. References

[1] L.M. Camacho, L. Dumée, J. Zhang, J. Li, M. Duke, J. Gomez, S. Gray, Review: Advances in Membrane Distillation for Water Desalination and Purification Applications, Water, 5 (2013) 94-196.

[2] K.W. Lawson, D.R. Lloyd, Review: Membrane distillation, J. Membr. Sci. , 124 (1997) 1-25.
[3] A.M. Alklaibi, N. Lior, Transport analysis of air-gap membrane distillation, J. Membr. Sci. 255 (2005) 239-253.
[4] M. Gryta, Concentration of saline wastewater from the production of heparin, Desalination 129, (2000) 35-44.
[5] A. El-Abbassi, A. Hafidi, M.C. García-Payo, M. Khayet, Concentration of olive mill wastewater by membrane distillation for polyphenols recovery, Desalination 245, (2009) 670-674.
[6] P.P. Zolotarev, V.V. Ugrozov, I. B. Volkina, V.M. Nikulin, Treatment of waste water for removing heavy metals by membrane distillation, J. Hazard. Mater, 37 (1994) 77-82.
[7] C.R. Martinetti, A.E. Childress, T.Y. Cath, High recovery of concentrated RO brines using forward osmosis and membrane distillation, J. Membr. Sci., 331 (2009) 31-39.
[8] F. Edwie, T.S. Chung, Development of hollow fiber membranes for water and salt recovery from highly concentrated brine via direct contact membrane distillation and crystallization, J. Membr. Sci., 421-422 (2012) 111-123.
[9] C. M. Tun, A. G. Fane, J.T. Matheickal, R. Sheikholeslami, Membrane distillation crystallization of concentrated salts-flux and crystal formation, J. Membr. Sci., 257 (2005) 144-155.
[10] D. Singh, K.K. Sirkar, Desalination of brine and produced water by direct contact membrane distillation at high temperatures and pressures, J. Membr. Sci., 389 (2012) 380-388.
[11] A. Alkhudhiri, N. Darwish, N. Hilal, Produced water treatment: Application of Air Gap Membrane Distillation, Desalination 309, (2013) 46-51.
[12] K.W. Lawson, D.R. Lloyd, Membrane Distillation. II. Direct contact MD, J. Membr.Sci. , 120 (1996) 123-133.
[13] K. W. Lawson, D.R. Lloyd, Review: Membrane distillation, J. Membr. Sci. , 124 (1997) 1-25.
[14] J.L. Cartinella, T.Y. Cath, M.T. Flynn, G.C. Miller, K.W. Hunter, A.E. Childress, Removal of natural steroid hormones from wastewater using membrane contactor processes, Environ. Sci. Technol., 40 (2006) 7381-7386.
[15] J.W. D. Hou, C. Zhao, B. Wang, Z. Luan and X. Sun, Fluoride removal from brackish groundwater by direct contact membrane distillation, J. Environ. Sci., 22 (2010) 1860-1867.
[16] S. Yarlagadda, V.G. Gude, L.M. Camacho, S. Pinappu, S. Deng, Potable water recovery from As, U, and F contaminated ground waters by direct contact membrane distillation process, J. Hazard. Mater, 192 (2011) 1388-1394.
[17] T.Y. Cath, V.D. Adams, A.E. Childress, Membrane contactor processes for wastewater reclamation in space. II. Combined direct osmosis, osmotic distillation, and membrane distillation for treatment of metabolic wastewater, J. Membr. Sci., 257 (2005) 111-119.
[18] A.O. Imdakm, T. Matsuura, Simulation of heat and mass transfer in direct contact membrane distillation (MD): The effect of membrane physical properties, Journal of Membrane Science 262 (2005) 117-128.
[19] R.W. Schofield, A.G. Fane, C.J.D. Fell, Heat and mass transfer in membrane distillation, J. Membr. Sci., 33 (1987) 299-313.
[20] L. Mart´ınez-D´ıez, M.I. Vázquez-González, A method to evaluate coefficients affecting flux in membrane distillation, Journal of Membrane Science, 173 (2000) 225–234.
[21] A.O. Imdakm, T. Matsuura, A Monte Carlo simulation model for membrane distillation processes: direct contact (MD), J. Membr. Sci., 237 (2004) 51-59.
[22] J. Phattaranawik, R. Jiraratananon, A.G. Fane, Effect of pore size distribution and air flux on mass transport in direct contact membrane distillation, J. Membr. Sci., 215 (2003) 75-85.
[23] S. Srisurichan, R. Jiraratananon, A.G. Fane, Mass transfer mechanisms and transport resistances in direct contact membrane distillation process, J. Membr. Sci., 277 (2006) 186-194.
[24] M. Qtaishat, T. Matsuura, B. Kruczek, M. Khayet, Heat and mass transfer analysis in direct contact membrane distillation, Desalination 219, (2008) 272-292.
[25] A.R.D. Costa, A.G. Fane, D.E. Wiley, Spacer characterization and pressure drop modelling in spacer-filled channels for ultrafiltration, J. Membr. Sci., 87 (1994) 79-98.
[26] J. Phattaranawik, R. Jiraratananon, A.G. Fane, C. Halim, Mass flux enhancement using spacer filled channels in direct contact membrane distillation, J. Membr. Sci., 187 (2001) 193-201.
[27] L. Martínez, J.M. Rodríguez-Maroto, Characterization of membrane distillation modules and analysis of mass flux enhancement by channel spacers, J. Membr. Sci., 274 (2006) 123-137.

[28] T.Y. Cath, V.D. Adams, A.E. Childress, Experimental study of desalination using direct contact membrane distillation: a new approach to flux enhancement, J. Membr.Sci., 228 (2004) 5-16.
[29] J. Zhang, J. D. Li, S. Gray, Effect of applied pressure on performance of PTFE membrane in DCMD J. Membr. Sci., 369 (2011) 514-525.
[30] Z. Ding, R. Ma, A.G. Fane, A new model for mass transfer in direct contact membrane distillation, Desalination 151, (2002) 217-227.
[31] A. Hernfindez, J.I. Calvo, P. Prfidanos, F. Tejerina, Pore size distributions in microporous membranes: A critical analysis of the bubble point extended method, J. Membr. Sci., 112 (1996) 1-12.
[32] J. Woods, J. Pellegrino, J. Burch, Generalized guidance for considering pore-size distribution in membrane distillation, J. Membr. Sci., 368 (2011) 124-133.
[33] S. Bonyadi, T.S. Chung, Flux enhancement in membrane distillation by fabrication of dual layer hydrophilic–hydrophobic hollow fiber membranes, J. Membr. Sci., 306 (2007) 134–146.
[34] L. Martínez, J.M. Rodríguez-Maroto, Membrane thickness reduction effects on direct contact membrane distillation performance, J. Membr. Sci., 312 (2008) 143-156.
[35] J. Zhang, N. Dow, M. Duke, E. Ostarcevic, J. Li, S. Gray, Identification of material and physical features of membrane distillation membranes for high performance desalination, J. Membr. Sci. , 349 (2010) 295-303.
[36] M. I. Ali, E. K. Summers, H. A. Arafat, J.H. LienhardV, Effects of membrane properties on water production cost in small scale membrane distillation systems, Desalination 306, (2012) 60-71.
[37] K.W. Lawson, M.S. Hall, D.R. Lloyd, Compaction of microporous membranes used in membrane distillation. I. Effect on gas permeability, J. Membr. Sci., 101 (1995) 99-108.
[38] M.S. El-Bourawi, Z. Ding, R. Ma, M. Khayet, A framework for better understanding membrane distillation separation process, J. Membr. Sci., 285 (2006) 4-29.
[39] A. Alkhudhiri, N. Darwish, N. Hilal, Membrane distillation: A comprehensive review, Desalination 287, (2012) 2-18.
[40] J. Mericq, S. Laborie, C. Cabassud, Vacuum membrane distillation of seawater reverse osmosis brines, Water Res., 44 (2010) 5260-5273.
[41] D. Hou, G. Dai, J. Wang, H. Fan, L. Zhang, Z. Luan, Preparation and characterization of PVDF/nonwoven fabric flat-sheet composite membranes for desalination through direct contact membrane distillation, Sep. Purif. Technol. 101, (2012) 1-10.
[42] B.S. Lalia, E. Guillen-Burrieza, H.A. Arafat, R. Hashaikeh, Fabrication and characterization of polyvinylidenefluoride-co-hexafluoropropylene (PVDF-HFP) electrospun membranes for direct contact membrane distillation J. Membr. Sci. , 428 (2013) 104-115.
[43] S. B. Iversen, V. K. Bhatia, K .Dam-Johansen, G. Jonsson, Characterization of microporous membranes for use in membrane contactors, J. Membr. Sci., 130 (1997) 205-217.
[44] C. Fernández-Pineda, M.A. Izquierdo-Gil, M.C. Garcia-Payo, Gas permeation and direct contact membrane distillation experiments and their analysis using different models, J. Membr. Sci., 198 (2002) 33-49.
[45] J. Phattaranawik, R. Jiraratananon, A.G. Fane, Heat transport and membrane distillation coefficients in direct contact membrane distillation, J. Membr. Sci., 212 (2003) 177-193.
[46] M. Khayet, K.C. Khulbe, T. Matsuurab, Characterization of membranes for membrane distillation by atomic force microscopy and estimation of their water vapor transfer coefficients in vacuum membrane distillation process
J. Membr. Sci., 238 (2004) 199–211.
[47] M. Khayet, Membranes and theoretical modeling of membrane distillation: A review, Adv. Colloid Interface Sci., 164 (2011) 56-88.
[48] F.K. Smolders, Terminology for Membrane Distillation, Desalination 72, (1989) 249-262.
[49] Q. Huang, C. Xiao, X. Hu, X. Li, Study on the effects and properties of hydrophobic poly(tetrafluoroethylene) membrane, Desalination 277, (2011) 187-192.
[50] S. Nakao, Review: Determination of pore size and pore size distribution 3. Filtration membranes, J. Membr. Sci., 96 (1994) 131-165.
[51] M. Khayet, T. Matsuura, Determination of surface and bulk pore sizes of flat-sheet and hollow-fiber membranes by atomic force microscopy, gas permeation and solute transport methods, Desalination 158, (2003) 57-64.
[52] H.Yasuda, J.T.Tsai, Pore size of microporous polymer membranes, J. Appl. Polym. Sci., 18 (1974) 805-819.

[53] R. Mishra, S.P. Tripathy, D. Sinha, K.K. Dwivedi, S. Ghosh, D.T. Khathing, M. Muller, D. Fink, W.H. Chung, Optical and electrical properties of some electron and proton irradiated polymers, Nucl. Instrum. Methods Phys. Res., Sect. B 168, (2000) 59-64.

[54] Y. Luo, Y. Liu, Q. Yu, Influence of glow discharge plasma treatment on vapor-induced response of poly(vinylidene fluoride)-carbon black composite thin films, Thin Solid Films 515, (2007) 4016-4023.

[55] M. Mulder, Basic principles of membrane technology, Kluver Academic Publishers, Dordrecht, Netherlands, 1991.

[56] J. A. Ruskowitz, A.E. Childress, Salt-Gradient Solar Pond and Membrane Distillation System for Water Desalination Powered by Renewable Energy, in: Thesis, University of Nevada, Reno, Reno, Nevada, 2012.

[57] V.D. Alves, I.M. Coelhoso, Effect of membrane characteristics on mass and heat transfer in the osmotic evaporation process, J. Membr. Sci., 228 (2004) 159-167.

[58] S. Adnan, M. Hoang, H. Wang, Z. Xie, Commercial PTFE membranes for membrane distillation application: Effect of microstructure and support material, Desalination 284, (2012) 297-308.

[59] F. Meng, H. Zhang, F. Yang, S. Zhang, Y. Li, X. Zhang, Identification of activated sludge properties affecting membrane fouling in submerged membrane bioreactors, Sep. Purif. Technol., 51 (2006) 95-103.

[60] J.A. Brant, A.E. Childress, Assessing short-range membrane-colloid interactions using surface energetics, J. Membr. Sci., 203 (2002) 257-273.

[61] P.C. Carman, Flow of Gases Through Porous Media, Butterworth Scientific Publications, London, UK, 1956.

[62] M.H.Kutner, C.J.Nachtsheim, J. Neter, Applied Linear Regression Models 4th ed., McGraw-Hill/Irwin, New York, U.S.A, 2004.

[63] J. W. Stephens, J. A. Unruh, M. E. Dikeman, M. C. Hunt, T. E. Lawrence, T. M.Loughin, Mechanical probes can predict tenderness of cooked beef longissimus using uncooked measurements, J. Anim. Sci., 82 (2004) 2077-2086.

[64] R.L. Ott, M. Longnecker, An introduction to statistical methods and data analysis, fifth ed., Duxbury, California, 2001.

[65] A.M. Alklaibi, N. Lior, Membrane-distillation desalination: status and potential, Desalination, 171 (2004) 111-131.

[66] M. C. Garc ía-Payo, M. A. Izquierdo-Gil, C.F. ández-Pineda, Wetting Study of Hydrophobic Membranes via Liquid Entry Pressure Measurements with Aqueous Alcohol Solutions, J. Colloid Interface Sci., 230 (2000) 420-431.

[67] F. A. Banat, J. Simandl, Theoretical and experimental study in membrane distillation, Desalination 95, (1994) 39-52.

[68] A.M. Barbe, P.A. Hogan, R.A. Johnson, Surface morphology changes during initial usage of hydrophobic, microporous polypropylene membranes, J. Membr.Sci. , 172 (2000) 149-156.

[69] M. Gryta, Long-term performance of membrane distillation process, J. Membr.Sci., 265 (2005) 153-159.

[70] S. K, W. Hölz, R. Wollbeck, Membranes and modules for transmembrane distillation, J. Membr. Sci., 39(1) (1988) 25–42.

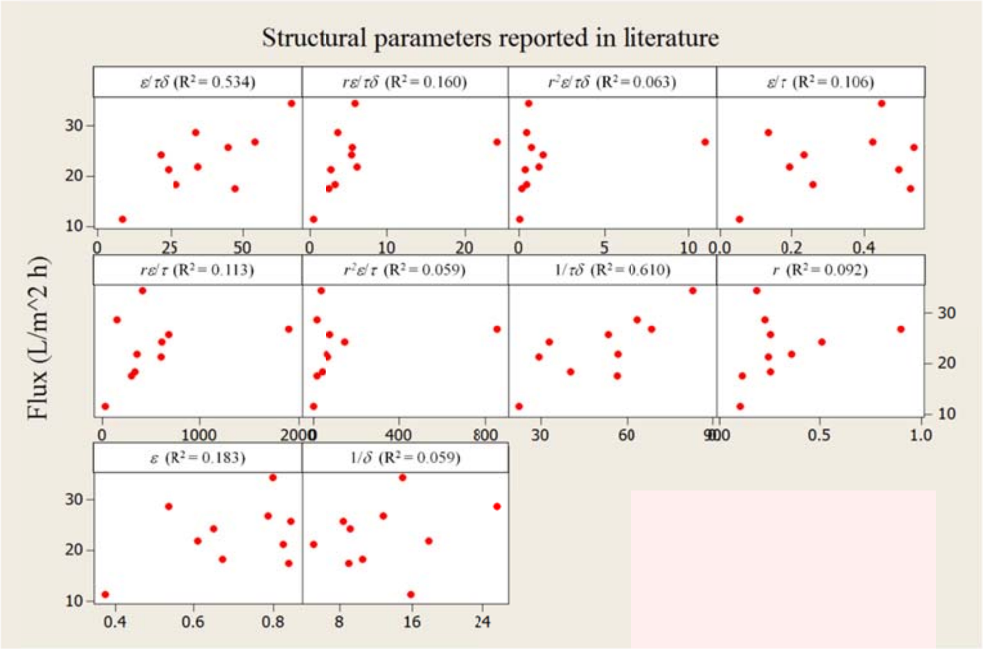
Structural parameters reported in literature
ε/τδ (R² = 0.534)
rε/τδ (R² = 0.160)
r²ε/τδ (R² = 0.063)
ε/τ (R² = 0.106)
rε/τ (R² = 0.113)
r²ε/τ (R² = 0.059)
1/τδ (R² = 0.610)
r (R² = 0.092)
ε (R² = 0.183)
1/δ (R² = 0.059)
Flux (L/m^2 h)
10
20
30
0
25
50
0
10
20
0
5
10
0.0
0.2
0.4
0
1000
2000
0
400
800
30
60
90
0.0
0.5
1.0
0.4
0.6
0.8
8
16
24

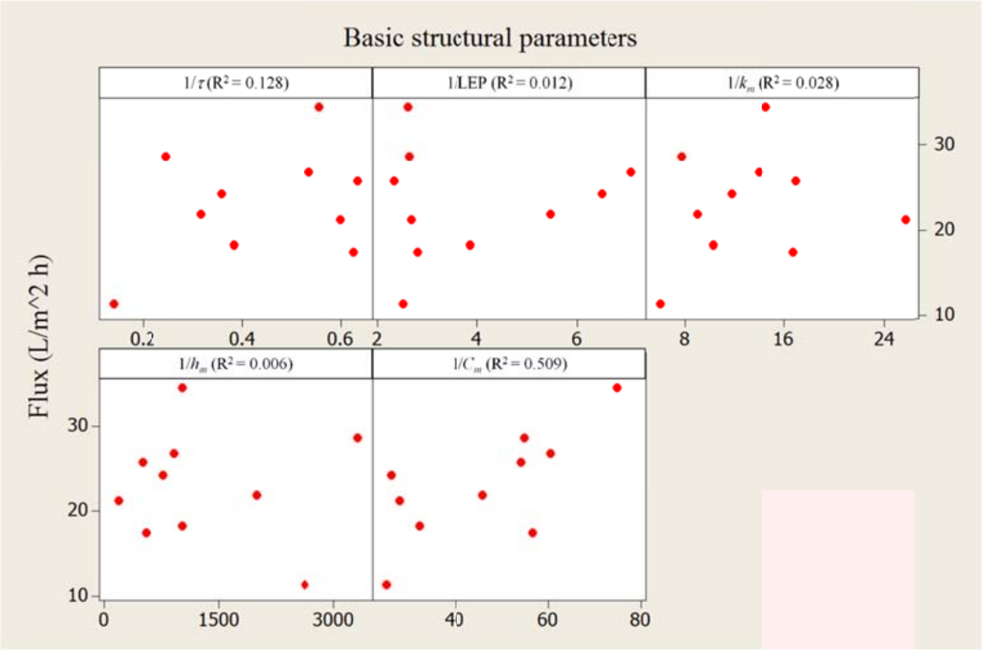
Basic structural parameters
1/τ (R² = 0.128)
1/LEP (R² = 0.012)
1/k_m (R² = 0.028)
1/h_m (R² = 0.006)
1/C_m (R² = 0.509)
Flux (L/m^2 h)
10
20
30
0.2
0.4
0.6
2
4
6
8
16
24
0
1500
3000
40
60
80

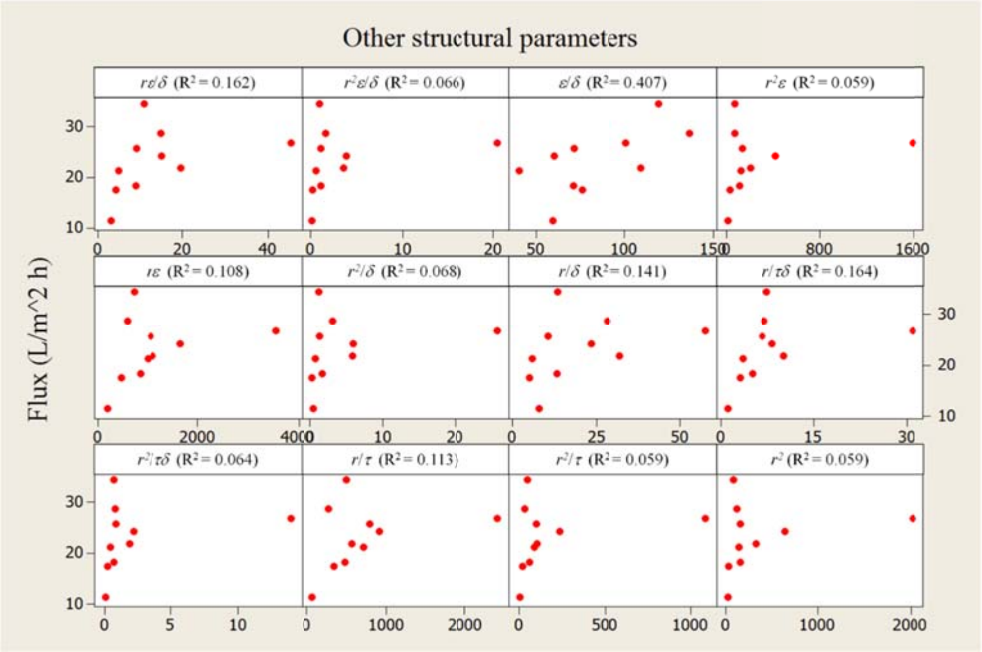

Appendix 1A: Scatterplots of water flux vs. membrane structural parameters for single-layer membranes used to identify the structural parameters that correlate well with water flux.

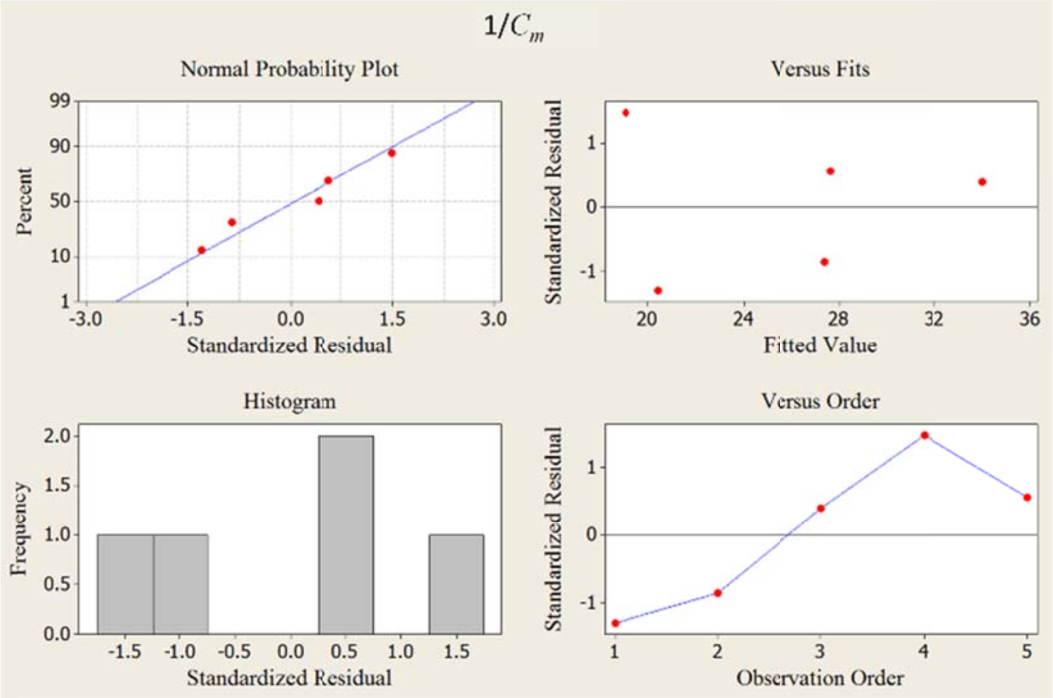

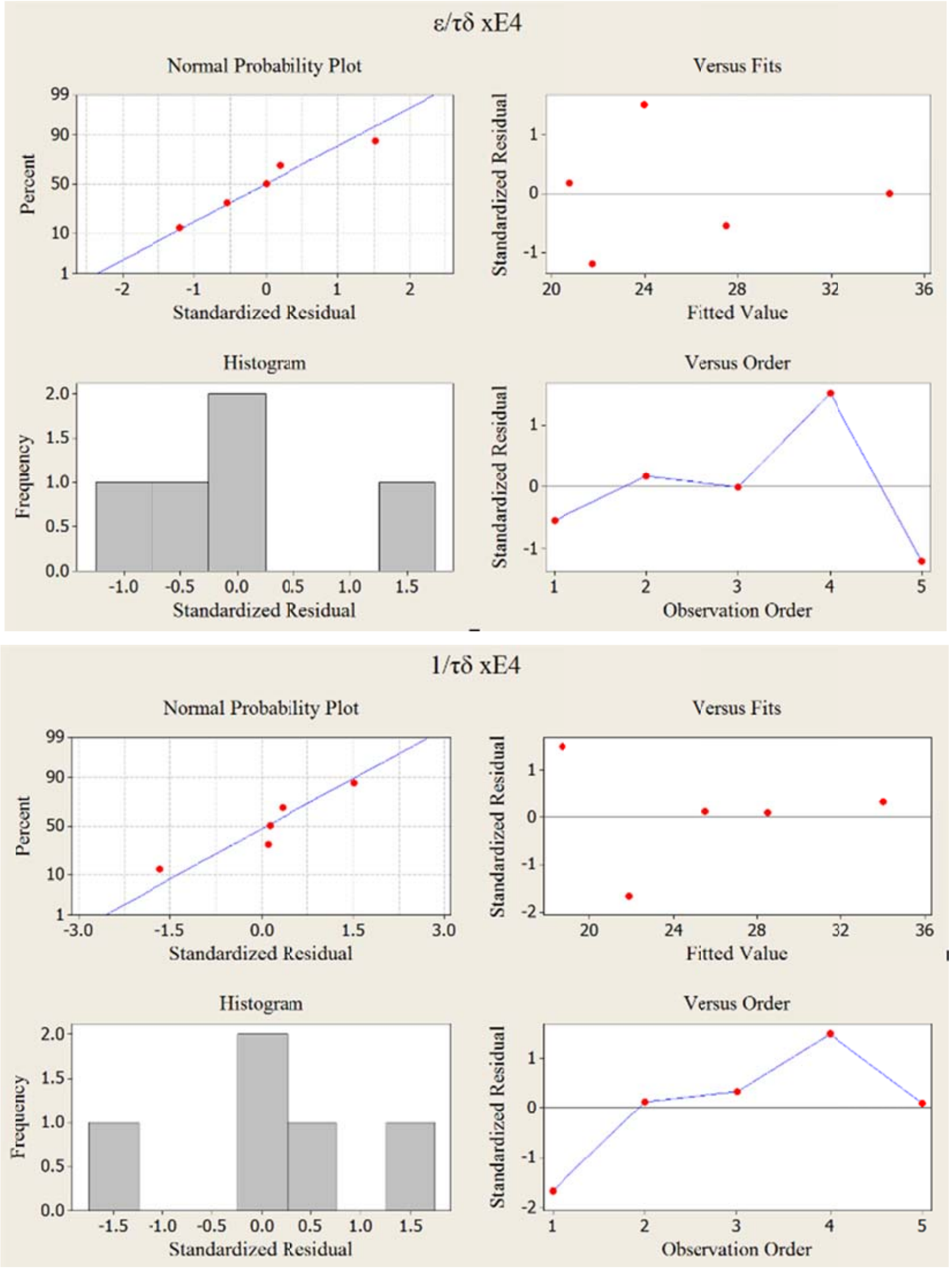

Appendix 1B: Residual plots used to validate the assumptions of the linear regression analysis.

Research Output #2

Factors Attributing to Flux Improvement in Vacuum-Enhanced Direct Contact Membrane Distillation

Abstract

Low water flux in membrane distillation (MD) is one of the major reasons limiting its full-scale application. In the past decades, attempts have been made to improve water flux of MD, and vacuum-enhanced direct-contact MD (VEDCMD) was proved a very effective configuration to achieve this purpose. However, only qualitative investigations about the factors that might affect water flux were reported in the literature. In this study, a mechanistic investigation of the factors attributing to higher water fluxes of VEDCMD was studied. Direct-contact MD (DCMD) and pressure-enhanced DCMD (PEDCMD) configurations were also investigated for comparison. Less membrane compaction was identified as one dominant factor attributing to improved water flux in VEDCMD as near no compaction occurred in VEDCMD until tested at a high pressure gradient, while little and sever compactions have occurred in DCMD and PEDCMD, respectively. Lower air pressure inside the membrane pores was found the other dominant factor attributing to improved water flux in VEDCMD and the magnitude of the air pressure was estimated near average of the feed and distillate pressures in VEDCMD and near the distillate-side pressure in DCMD and PEDCMD. Pressure gradient, as is present in both PEDCMD and VEDCMD, was found a minimal effect on water flux.

2.1. Introduction

2.1.1. Membrane distillation

Membrane distillation (MD) is a thermally-driven membrane process in which separation occurs through a phase change. The driving force in MD is the vapor pressure gradient resulting from the temperature difference across the membrane. Because of the high latent heat of evaporation of water, MD is an energy-intensive process [1]. However, it can be combined with low-grade (“waste”) heat to reduce energy costs [2-8]. The driving force of MD does not decrease significantly with increasing feed-water salinity; therefore, MD is well suited to treat feed waters with high salt concentrations. MD can achieve essentially 100% rejection of salts and non-volatile organics [3]; therefore, it is also well suited for use as a polishing step to remove low-molecular-weight contaminants (e.g., trace organic compounds) that may not be rejected well by other treatment methods such as reverse osmosis [9].

2.1.2. Methods to improve water flux in DCMD

When treating feed waters with relatively low fouling and scaling potentials such as seawater, obtaining high water flux is desirable [10]. Approaches to improve water flux have included developing novel membranes [11], deaerating feed waters [2, 12], and using vacuum in the membrane module [13, 14]. Schofield et al. [12] and Cath et al. [13] employed equal vacuum on both the feed and distillate sides of the membrane, and both studies observed higher fluxes compared to the traditional DCMD configuration (without hydraulic pressure or vacuum employed). Cath et al [12] also used vacuum only on the distillate side while keeping the feed side at atmospheric pressure and this led to even greater flux improvement [13]. This process, called vacuum-enhanced DCMD (VEDCMD), was patented in 2010 [15].

Increased flux with the application of vacuum has been attributed to decreased air pressure inside the membrane pores, decreased temperature polarization, decreased membrane conductive heat loss, and increased pressure gradient across the membrane [12-14]. However, the mechanisms for improved flux have not been systematically evaluated and the dominant factors affecting flux enhancement have not been clearly identified. It is possible that only one or two factors may explain flux improvement. Of these factors, mechanistic evaluations of air pressure inside the membrane pores have been inconclusive. In two different studies, one where vacuum was employed on the distillate side of the DCMD membrane [14] and the other where vacuum was employed on both the feed and distillate sides [12], the pore pressure (sum of air pressure and water vapor pressure inside the pores [16, 17]) was assumed to be equal to the vacuum pressure of the distillate stream. It is likely that the same assumption is not valid for both scenarios. Therefore, in determining the dominant factors affecting water flux in VEDCMD, analyses cannot rely on what has been done previously in the literature.

One study from the literature that employed hydraulic pressures of equal magnitude on the feed and distillate sides of the membrane observed flux reduction compared to traditional DCMD systems; membrane compaction was postulated to be the reason [18], especially for membranes with low porosities [19]. Another study that employed hydraulic pressure only on the feed side observed no flux change [13]. In this study, it was postulated that membrane compaction was one of the factors that increased water flux (opposite to [18]) , while other factors reduced water flux, leading to the near constant overall water flux.

2.1.3. Objectives

The overall objective of this study is to evaluate the dominant factors responsible for improved water flux when vacuum is employed in DCMD. Because employing vacuum only on the distillate side of the membrane (as in VEDCMD) leads to greater flux improvement than any other configuration, VEDCMD is the main focus of this study. To achieve the overall objective, first, the dominant factors attributing to higher water flux in VEDCMD are evaluated theoretically. Second, the magnitude of air pressure inside the membrane pores in VEDCMD is quantified and its effect on water flux is evaluated. Third, membrane compaction is measured and the effect of membrane compaction on water flux is evaluated. Results from this study will aid in better understanding of the factors leading to enhanced water flux in VEDCMD and in turn, facilitate application of VEDCMD especially in water polishing and other low fouling scenarios where high water fluxes are desirable.

2.1. Materials and methods

2.2.1. Experimental setup

Three DCMD configurations were evaluated: traditional DCMD without hydraulic pressures or vacuums applied; VEDCMD with vacuum applied on the distillate side; and pressure-enhanced DCMD (PEDCMD) with hydraulic pressure applied on the feed side. The PEDCMD configuration was used for comparative purposes by creating the same pressure gradient as VEDCMD. A bench-scale system with a modified acrylic membrane cell was used to study these configurations. DCMD and PEDCMD used the same setup (Fig. 2.1a) with a needle valve at the outlets of both the feed and distillate sides to adjust the pressure inside the membrane cell. In VEDCMD (Fig. 2.1b), the distillate-side pump is on the outlet of the membrane cell to create a vacuum on the distillate side by pulling water from the cell. The pressures on the feed and distillate sides were maintained at 20/20 (feed/distillate) kPa in DCMD; 60/20, 80/20, and 100/20 kPa in PEDCMD; and 20/-20, 20/-40, and 20/-60 kPa in VEDCMD. All pressures in the current study were reported as gauge pressures. All tests were performed using the same feed temperature (40 °C), distillate temperature (20 °C), and fluid flow rates (1.0 L/min) on both the feed and distillate sides. A 35 g/L NaCl solution was used as the feed solution and deionized (DI) water was used on the distillate side; the feed solution and the DI water were re-circulated counter-currently on their respective sides of the membrane cell. As water evaporated through the membrane, excess water from the distillate reservoir overflowed into a beaker on an analytical balance. The overflow rate was used to calculate the water flux. The test was stopped when the flux was stable for 30 min. To create turbulent flow and reduce temperature polarization, spacers were placed in the flow channels on both the feed and distillate sides. Temperatures, pressures, and dissolved oxygen (DO) concentrations were monitored using dual-channel digital thermometers, pressure gauges, and DO meters at the inlet and outlet of the membrane cell. Average DO values were calculated and used to investigate oxygen (i.e., air) transport across the membrane.

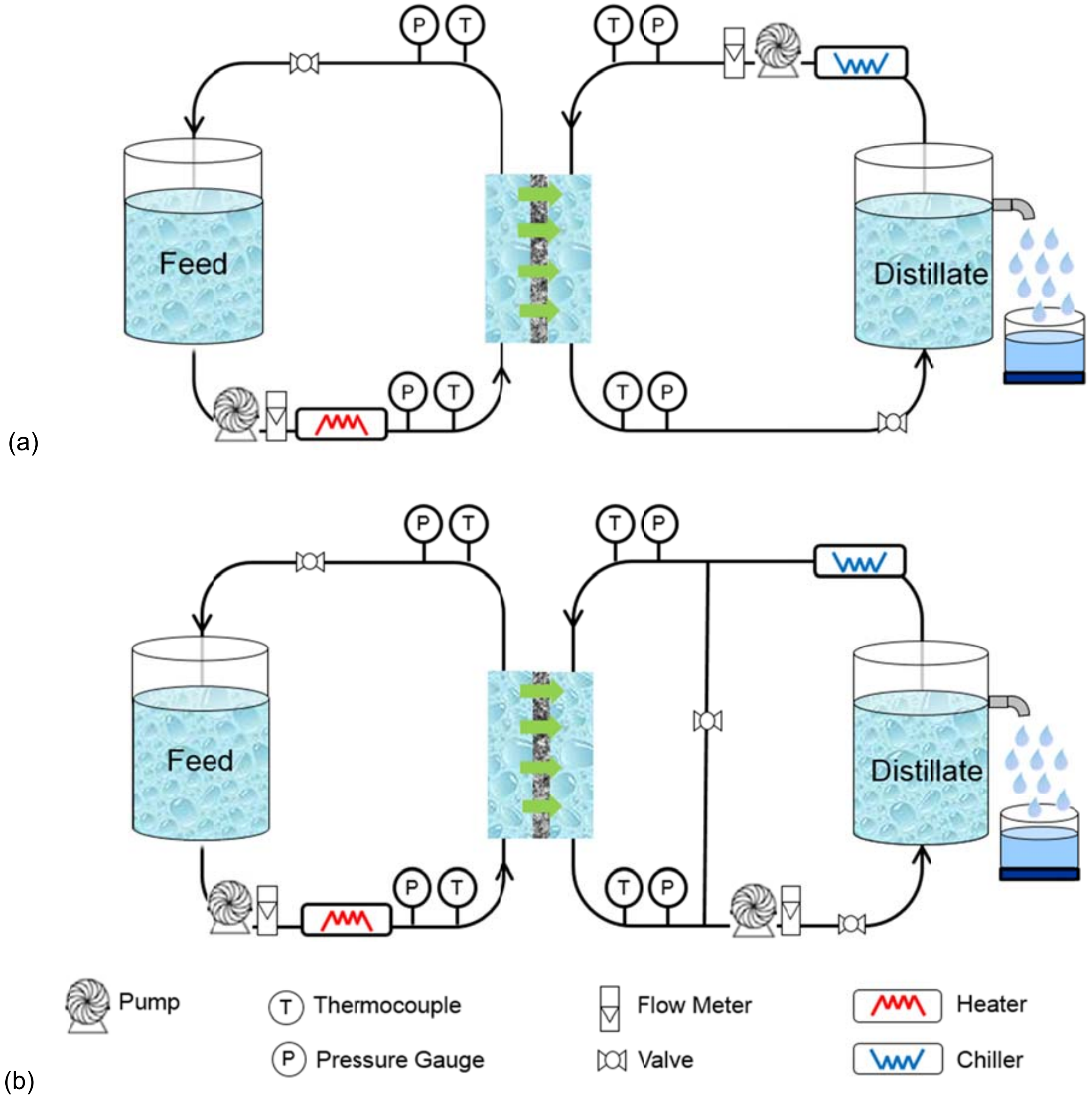

Figure 2.1: Schematic drawings of the bench-scale MD system configurations for (a) DCMD and PEDCMD and (b) VEDCMD.

2.2.2. Membrane characterization

A flat-sheet polytetrafluoroethylene membrane was used in this investigation. A new membrane coupon was used for each test. Membrane properties (thickness, porosity, tortuosity, and average pore size) were measured or calculated before and after each test as follows.

2.2.2.1. Membrane thickness measurement

Membrane thickness (δ) was measured from scanning electron micrographs of membrane cross- sections. A membrane coupon was frozen in liquid nitrogen and cut with a blade. The thickness of each membrane coupon was measured on three different sections and the average thickness was calculated.

2.2.2.2. Porosity and tortuosity measurements

Membrane porosity (ε) was determined by [20]:

$$\varepsilon = 1 - \frac{m}{\rho_p \times A \times \delta} \tag{2.1}$$

where m and A are the mass and surface area of the membrane coupon (assumed constant before and after flux testing); ρ_p is the reported density of the polymer material (2.2 g/cm^3 [21, 22]). Although additives may be included during the membrane manufacturing process, and could cause ρ_p to be different from 2.2 g/cm^3, additive effects are assumed negligible due to the very small amounts [23]. Energy dispersive spectrometry surface analysis (0.3-0.5 wt.% detection limit) on the membrane surface revealed only carbon and fluorine [24]. Furthermore, Zhang et al. [20] used the midpoint of the reported polymer densities in their porosity calculation and found an error less than 3%. Membrane tortuosity (τ) was calculated as [25, 26]:

$$\tau = \frac{(2-\varepsilon)^2}{\varepsilon} \tag{2.2}$$

2.2.2.3. Average pore size determination

Membrane average pore diameter (d) was determined by the gas permeation test with compressed air [27, 28]. The permeation flux of air through the dried membrane was measured at room temperature using transmembrane pressures from 10 to 100 kPa. Pore size was then calculated as:

$$d = \frac{16}{3}\left(\frac{B_o}{K}\right)\left(\frac{2RT}{\pi M_i}\right)^{0.5} \tag{2.3}$$

where B_o is the geometric factor of a membrane; K is the permeability coefficient; R is the universal gas constant; T is the ambient temperature; and M is the molecular weight [29]. Here, subscript i is used to represent air (subscript j will later be used to represent water vapor).

2.2.3. Statistical analysis of membrane compaction in DCMD, PEDCMD, and VEDCMD

The multiple regression analysis has been performed using Minitab® 17.1.0 to statistically investigate membrane compaction in DCMD, PEDCMD, and VEDCMD. All measured membrane thicknesses in DCMD, PEDCMD, and VEDCMD were set as the predictor, while the pressure scenario (e.g., 100/20, 80/20, as P_f/P_d) were set as the variables and coded as yes = 1 and no = 0. The unused membrane was used as control group. For each pressure scenario, if the p value obtained from the regression analysis results is smaller than 0.05, membrane compaction had occurred; if the p value is greater than 0.05, minimal membrane compaction has occurred [30].

2.2.4. Flux prediction using mass transfer models

In DCMD, viscous flow where the air and vapor mixture behaves as a continuous fluid [31] can be neglected because no pressure gradient exists [32]. Because of this, both the Schofield model (Fig. 2.2a) and the simplified dusty-gas model (surface diffusion neglected; Fig. 2.2b) become the same thermal circuit. In PEDCMD and VEDCMD, viscous flow must be included because a pressure gradient exists. Therefore, the simplified dusty-gas model and the Schofield model have unique thermal circuits that must include the term for viscous flow.

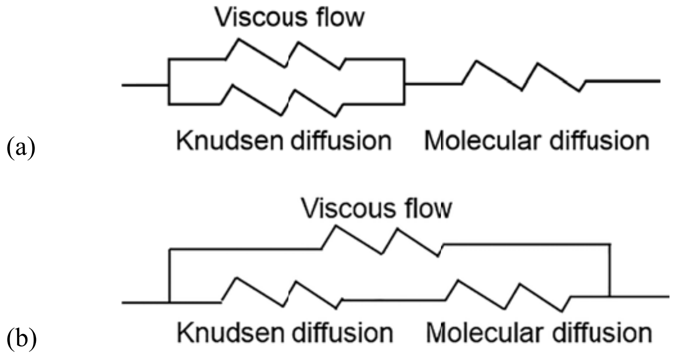

Figure 2.2: Thermal circuits of (a) the Schofield model and (b) the simplified dusty-gas model.

The flux attributed to Knudsen diffusion (N_k) was determined by [3]:

$$N_k = \frac{2}{3}\frac{r\varepsilon}{\tau\delta}\left(\frac{8M_j}{\pi R T_m}\right)^{0.5}\Delta P_i \qquad (2.4)$$

where r is membrane pore radius; T_m is the average temperature of the membrane surface on the feed (T_{mf}) and distillate (T_{md}) sides; and ΔP_i is the vapor pressure gradient across the membrane, which equals the feed-side vapor pressure (P_{if}) minus the distillate-side vapor pressure (P_{id}). P_{if} and P_{id} were determined by the Antoine equation [16, 17]:

$$P_{if} = \exp(23.328 - \frac{3841}{T_{mf} - 45})(1 - x_{NaCl})(1 - 0.5x_{NaCl} - 10x_{NaCl}^2) \qquad (2.5)$$

$$P_{id} = \exp(23.328 - \frac{3841}{T_{md} - 45})(1 - x_{NaCl})(1 - 0.5x_{NaCl} - 10x_{NaCl}^2) \qquad (2.6)$$

where x_{NaCl} is the molar fraction of NaCl inside the solution.
T_{mf} was determined by [17, 33, 34]:

$$T_{mf} = T_f - \frac{Q}{h_f} \qquad (2.7)$$

where T_f is the bulk temperature of the feed solution and h_f is the heat transfer coefficient in the boundary layer on the feed side. Q is the total heat input in the system, which was determined by:

$$Q = C_p \dot{m}(T_{dout} - T_{din}) \qquad (2.8)$$

where C_p and $\dot{m}$ are the heat capacity and fluid flow rate of the distillate; and T_{dout} and T_{din} are the distillate-side temperatures at the outlet and inlet of the membrane cell.
T_{md} was determined by [17, 33, 34]:

$$T_{md} = T_d + \frac{Q}{h_d} \qquad (2.9)$$

where T_d is the bulk temperature of the distillate and h_d is the heat transfer coefficient in the boundary layer on the distillate side.

The heat transfer coefficient (h; h_f in Eq. 2.7 and h_d in Eq. 2.9) was determined by:

$$h = \frac{Nu k_f}{d_h} \qquad (2.10)$$

where k_f is the thermal conductivity of the fluid and d_h is the hydraulic diameter of the flow channel on the feed or distillate side. Nu is the Nusselt number, which for a spacer-filled channel was determined by [35]:

$$Nu = 0.664 k_{dc} \,\mathrm{Re}^{0.5}\,\mathrm{Pr}^{0.33}\left(\frac{2d_h}{l_m}\right)^{0.5} \qquad (2.11)$$

where Re is the Reynolds number; P_r is the Prandtl number; and l_m is the mesh size of the spacer. k_{dc} was determined by [35, 36]:

$$k_{dc} = 1.654\left(\frac{d_f}{H}\right)^{-0.039}\varepsilon_s^{0.75}\left(\sin\frac{\theta_s}{2}\right)^{0.086} \qquad (2.12)$$

where d_f is the spacer filament size; H is the channel height; ε_s is the spacer porosity; and θ_s is the hydrodynamic angle of the spacer, which is the angle formed by the grids of the spacer.
The flux attributed to molecular diffusion (N_m) was determined by [3]:

$$N_m = \frac{\varepsilon}{\tau\delta}\frac{P_{pore}D}{RT_m}\frac{1}{|P_{air}|_{\ln}}\Delta P_i \qquad (2.13)$$

where P_{air} is the air pressure inside the membrane pores; P_{pore} is the membrane pore pressure, which equals the sum of P_{air} and P_i; and D is the diffusion coefficient.

$P_{pore}D$ was calculated as [17, 37]:

$$P_{pore}D = 1.895 \times 10^{-8} \times T_m^{2.072} \tag{2.14}$$

The flux attributed to viscous flow (N_v) was determined by [3]:

$$N_v = \frac{P_i}{8RT_m\mu}\frac{r^2\varepsilon}{\tau\delta}\Delta P \tag{2.15}$$

where μ is the vapor dynamic viscosity and ΔP is the pressure gradient across the membrane.

According to the structure of the thermal circuits (Fig. 2.2), the overall inverse flux (1/N) for the Schofield model is [31]:

$$\frac{1}{N} = \frac{1}{N_k + N_v} + \frac{1}{N_m} \tag{2.16}$$

and the overall flux (N) for the dusty-gas model (without surface diffusion) is [31]:

$$N = N_v + \frac{N_k N_m}{N_k + N_m} \tag{2.17}$$

In the discussion below, membrane thickness, δ, was chosen as a representative membrane property because the other three membrane properties (r, ε, and τ) depend on δ. This is easily seen in Eq. 2.1 for ε; Eq. 2.2 shows how τ depends on ε and the following Eq. shows how r depends on both τ and ε:

$$r = r_o\left(\frac{\rho_p A\delta - m}{\rho_p A\delta + m}\right)\sqrt{\frac{\tau_o}{\varepsilon_o}} \tag{2.18}$$

where r_o ε_o, and τ_o are the pore radius, porosity, and tortuosity of an unused membrane. Eq. 2.18 was derived by combing Eqs. 2.1, 2.2, and the expressions of membrane porosity before and after membrane compaction [18]:

$$\varepsilon_o = N_{pore}\frac{\pi r_o^2\tau_o}{A} \tag{2.19}$$

$$\varepsilon = N_{pore}\frac{\pi r^2\tau}{A} \tag{2.20}$$

where N_{pore} is the membrane pore number, which was assumed constant during membrane compaction [18].

According to the mass transfer models, factors that may affect membrane flux include temperature, feed concentration, fluid flow rate, ΔP, P_{air}, and membrane properties (which may be altered by ΔP). Because DCMD, PEDCMD, and VEDCMD were all tested under the same experimental conditions except the liquid pressures on the feed and distillate sides, ΔP, P_{air}, and changes in membrane properties (r, ε, τ, and δ) due to membrane compaction are the only factors that may affect water flux.

2.3.1. Pressure difference across the membrane

Flux test results are shown in Table 2.1 for DCMD, PEDCMD, and VEDCMD. Based on the results, two observations can be made. First, DCMD and PEDCMD had similar fluxes (12-13 L/m^2-hr) despite the ΔP that exists in PEDCMD. Second, VEDCMD had higher fluxes (16-21 L/m^2-hr) than PEDCMD although the same ΔP values of 40, 60, and 80 kPa were used in both. Similar observations were also reported by Cath et al. [13]. The different flux results in the presence of the same ΔP suggest that the enhanced flux in VEDCMD cannot simply be attributed to pressure gradient as will be discussed in the following sections.

Table 2.1: Flux test results for DCMD, PEDCMD, and VEDCMD (T_f: 40 °C, T_d: 20 °C, flow rate: 1.0 L/min).

Configuration	Feed/distillate pressure (kPa)	Pressure gradient (kPa)	Flux (L/m^2 h)
DCMD	20/20	0	12.1±0.6
PEDCMD	60/20	40	12.3±1.1
	80/20	60	12.1±1.1
	100/20	80	13.1±1.5
VEDCMD	20/-20	40	16.4±0.5
	20/-40	60	17.6±0.5
	20/-60	80	20.8±0.7

2.3.2. Changes in membrane properties

Membrane properties before and after flux testing are shown in Fig. 2.3. The new (unused) membrane has a thickness of 67±10 μm and porosity of 80%. By comparing the thickness data for the unused membrane with the membrane after testing in VEDCMD, it can be seen that although the membrane thickness has a relatively large variability, minimal thickness reduction (thus membrane compaction) occurs in VEDCMD. It also can be seen that the thickness is reduced (thus, the membrane is compacted) slightly less after testing in DCMD but still comparable to VEDCMD. Similar thickness reduction (10-33%) in DCMD has also been observed by Zhang et al. [18]. However, near 53% thickness reduction is observed for membranes tested in PEDCMD. Lawson et al. [37] also reported 13-20% membrane thickness reductions for different membranes when the membrane surface was pressurized to 35 kPa (similar to PEDCMD with a ΔP of 35 kPa). Statistical significance data for membrane thickness before and after testing in DCMD, PEDCMD and VEDCMD are given in Table 2.2. As can be seen, the *p* value (0.026) for the DCMD test is smaller than 0.05, suggesting the membrane thickness after tested in DCMD is statistically (at 95% confidence interval) different from the thickness of the unused membrane, thus membrane compaction had occurred. However, membrane compaction in DCMD is not statistically significant comparing to membrane compaction in PEDCMD, which have *p* values of 0.000 for all the tests. The *p* values for all the VEDCMD tests are much greater than 0.05, thus minimal membrane compaction had occurred. Data for membrane porosity and tortuosity are not shown but follow the thickness data. There was no significant change in membrane pore size before and after testing. Based on membrane compaction alone (Fig. 2.3), it is postulated that DCMD flux should be similar to VEDCMD flux and greater than the PEDCMD flux, which was not what was observed experimentally (Table 2.1). Thus, it is likely that other factors, in addition to membrane compaction, account for the higher water flux in VEDCMD.

Table 2.2: Statistical analysis for membrane thickness comparison after tested in PEDCMD and VEDCMD

Configuration	Feed/distillate pressure (kPa)	*p* value
DCMD	20/20	0.026
PEDCMD	60/20	0.000
	80/20	0.000
	100/20	0.000
VEDCMD	20/-20	0.813
	20/-40	0.251
	20/-60	0.235

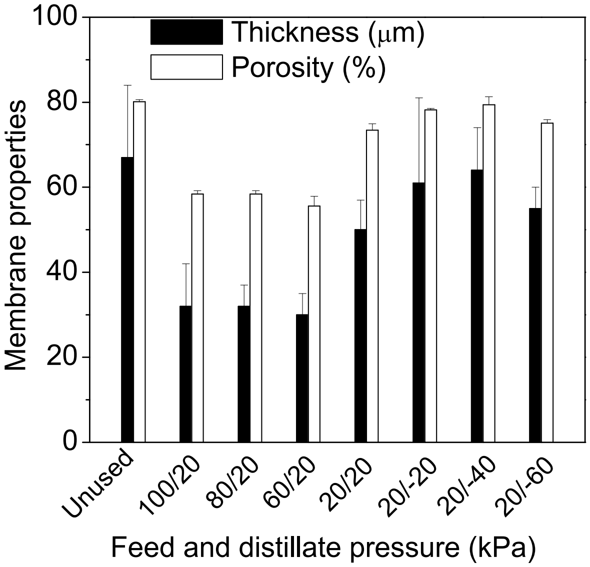

Figure 2.3: Membrane thickness and porosity before and after testing in DCMD, PEDCMD, and VEDCMD.

2.3.3. Air pressure inside the membrane pores

2.3.3.1. Estimation of P_{air} based on literature

Because P_{air} cannot be measured directly, P_{air} must be estimated. Zhang et al. [18] studied DCMD systems that employed equal magnitudes of hydraulic pressures on both the feed and distillate sides of the membrane. It was assumed that the air inside the membrane pores was stagnant and that the ideal gas law could be used to calculate P_{pore} (sum of P_{air} and P_i). For the PEDCMD and VEDCMD configurations, it is likely that the stagnant air assumption is not valid due to the existence of a pressure gradient.

To better understand the air pressure inside the membrane pores, the DO concentrations of the feed and distillate streams were evaluated. As can be seen in Fig. 2.4, the DO concentrations in DCMD (triangle symbols) and PEDCMD (star symbols) were relatively constant; however, in VEDCMD, the concentration of DO decreased with time – more for the distillate (open circle symbols) than for the feed (solid circle symbols). Results for the VEDCMD distillate were opposite to what was expected but easily explainable. In VEDCMD, both the feed and distillate streams might be degassed when the distillate stream was pulled out of membrane module by the pump - this was confirmed by the decreasing DOs in both streams and the observation of air bubbles in the distillate loop in VECDMD, but not in DCMD or PEDCMD.

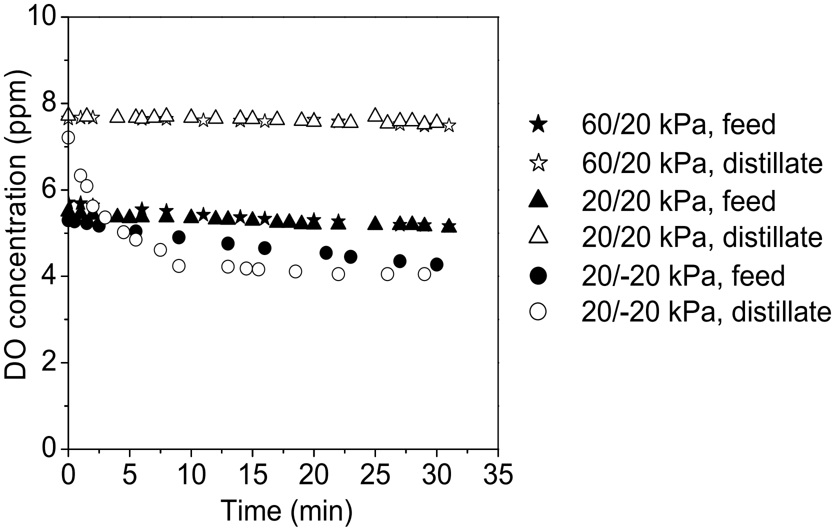

Figure 2.4: Dissolved oxygen concentration inside the feed and distillate streams in DCMD, PEDCMD, and VEDCMD.

Based on the above observations, the assumption of stagnant air inside the pores for DCMD and PEDCMD may be used as a first estimate for P_{air} in DCMD and PEDCMD, but not for VEDCMD. In VEDCMD, the bubbling of air out from the membrane pores suggests that setting P_{pore} equal to P_d (as was done by Zhang et al. [14]) or, since a pressure gradient is likely present inside the membrane pores under VEDCMD conditions, setting P_{pore} equal to the average pressure of the feed and distillate-side pressures ($P_{pore} = (P_f+P_d)/2$). Modeled results using these two assumptions in VEDCMD will be given in Section 2.3.3.

Modeled water fluxes for DCMD and PEDCMD using the ideal gas law assumption are given in Fig. 2.5. Only the Schofield model was used for flux prediction because both the Schofield and dusty-gas models predicted similar water fluxes (results not shown) due to the fact that water flux was only minimally affected by ΔP (Appendix A), which is the driving force for viscous flow. As can be seen from Fig. 2.2, it is the different connection modes of viscous flow that led to the two different mass transfer models - Schofield model and dusty-gas model.

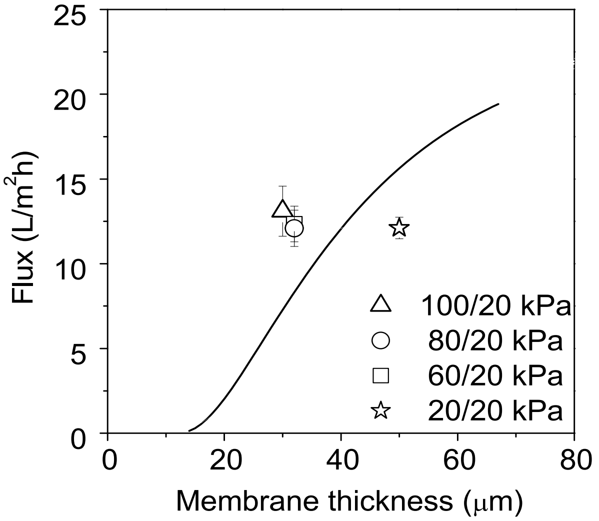

Figure 2.5: Tested and modeled water fluxes as a function of membrane thickness using the ideal gas law assumption for DCMD and PEDCMD (line: modeled fluxes for DCMD and PEDCMD; symbol: tested fluxes).

For PEDCMD, comparing predicted water fluxes (given by the line) with measured water fluxes (given by symbols) at a thickness near 30 μm (the membrane thickness after the PEDCMD test; Fig. 2.3), the model underpredicts water flux by approximately 44%. For DCMD, comparing the predicted water flux to the measured water flux at a thickness of 50 μm (the membrane thickness after the DCMD test; Fig. 2.3), the model over-predicts water flux by approximately 29%. Thus, using the ideal gas law to estimate P_{air} does not lead to good flux predictions in DCMD and PEDCMD; estimation of P_{air} using force balance analysis was then considered.

2.3.3.2. Estimation of P_{air} for DCMD and PEDCMD using force balance analysis

Force balance analysis at the pore surface

According to the force balance analysis, the following relationship exists [38, 39]:

$$P_{fluid} - P_{pore} = \frac{2\sigma\cos\theta}{r} \tag{2.21}$$

where σ is the surface tension of the liquid and θ is the angle formed among the liquid, membrane material, and gas inside the membrane pores under the applied hydraulic pressure (θ_f was used at the feed side and θ_d at the distillate side). If the θ values are known, P_{pore} (sum of P_{air} and P_i) can be calculated, thus P_{air} can also be estimated as P_i can be calculated using Eq. 2.3.

To estimate θ at steady-state for DCMD and PEDCMD, the movement of air inside the membrane pores and the structure of the liquid-gas interface were considered. In DCMD, membrane compaction has been identified, leading to a P_{pore} (near 100 kPa estimated using the ideal gas law) greater than P_f and P_d (20 kPa), thus the liquid-gas interface on the feed and distillate sides may convey into the respective liquid stream. Because of the shear stress of the flowing liquid, the air conveyed into the liquid may be removed, leading to a near flat liquid-gas interface, where θ_f and θ_d reach near 90° (Fig. 2.6a) and P_{pore} is close to P_f and P_d (Eq. 2.21). PEDCMD may follow the same process as DCMD until steady-state is reached at the distillate side, where P_{pore} is also close to P_d and θ_d reaches near 90° (Fig. 2.6b). Because $P_f > P_{pore}$, the feed water may infiltrate into membrane pores, leading to θ_f smaller than 90° (Fig. 2.6b) to maintain equilibrium at the feed side. Therefore, the same conclusion ($P_{pore} = P_d$) may be reached for both DCMD and PEDCMD.

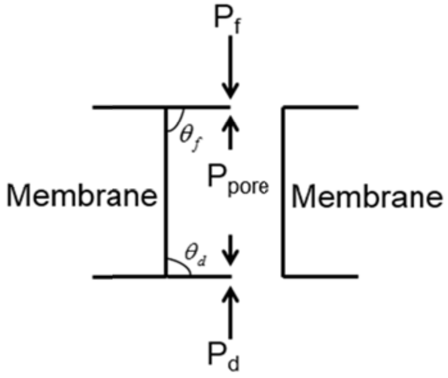

(a)

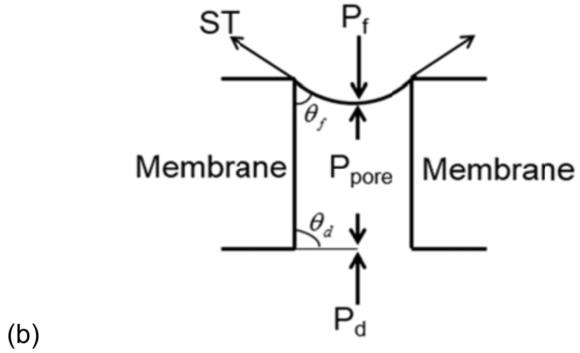

Figure 2.6: Force balance at the liquid-gas interface in: (a) DCMD; (b) PEDCMD (ST: surface tension).

Estimation of P_{air} for DCMD and PEDCMD using the $P_{pore} = P_d$ assumption

The modeled water fluxes for DCMD and PEDCMD using the $P_{pore} = P_d$ assumption are given in Fig. 2.7. Modeled fluxes are shown for a ΔP of 60 kPa. Comparing the measured water fluxes in PEDCMD to the predicted water fluxes at a thickness near 30 µm, it can be seen that the Schofield model gives an excellent fit for PEDCMD water flux and 28% over-prediction of water flux for DCMD. Therefore, the $P_{pore} = P_d$ assumption was identified as a reasonable assumption to estimate the magnitudes of P_{air} for both DCMD and PEDCMD. Because P_d can be controlled experimentally and the magnitude can be measured easily, the current identification that $P_{pore} = P_d$ may attribute to a fast and reliable estimation of P_{air} for both DCMD and PEDCMD.

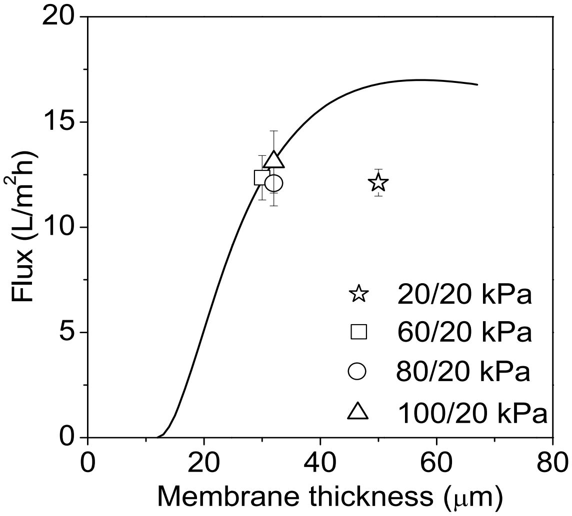

Figure 2.7: Tested and modeled water fluxes as a function of membrane thickness using $P_{pore} = P_d$ assumption for DCMD and PEDCMD (line: modeled fluxes; symbol: tested fluxes).

2.3.3.3. *Estimation of P_{air} in VEDCMD*

Modeled fluxes for VEDCMD using the $P_{pore} = P_d$ assumption are given in Fig. 2.8. As can be seen, the predicted water fluxes at thicknesses from 55-65 µm (membrane thickness after the VEDCMD test; Fig. 2.3) overestimate the measured water fluxes by 40-70%. Therefore, it is likely that actual P_{air} is greater than P_d (so to lower the predicted water flux) in VEDCMD. Combining this assumption with the air flow observations described in Fig. 2.4, a pressure gradient is likely present inside the membrane pores under VEDCMD conditions, thus P_{pore} more likely equals the average pressure of the feed and distillate-side pressures ($P_{pore} = (P_f+P_d)/2$).

Using this assumption ($P_{pore} = (P_f+P_d)/2$), lower flux prediction errors (<20%) were obtained at the thicknesses of 55-65 µm (Fig. 2.8). Therefore, once the hydraulic pressures and vacuums on the feed and distillate sides are known, P_{air} in VEDCMD can be determined accordingly. Because the calculated

P_{air} using the $P_{pore} = (P_f+P_d)/2$ assumption for VEDCMD is smaller than the calculated P_{air} using the $P_{pore} = P_d$ assumption for DCMD and PEDCMD, the lower P_{air} was identified as another dominant factor (besides less membrane compaction) attributing to the improved water flux in VEDCMD.

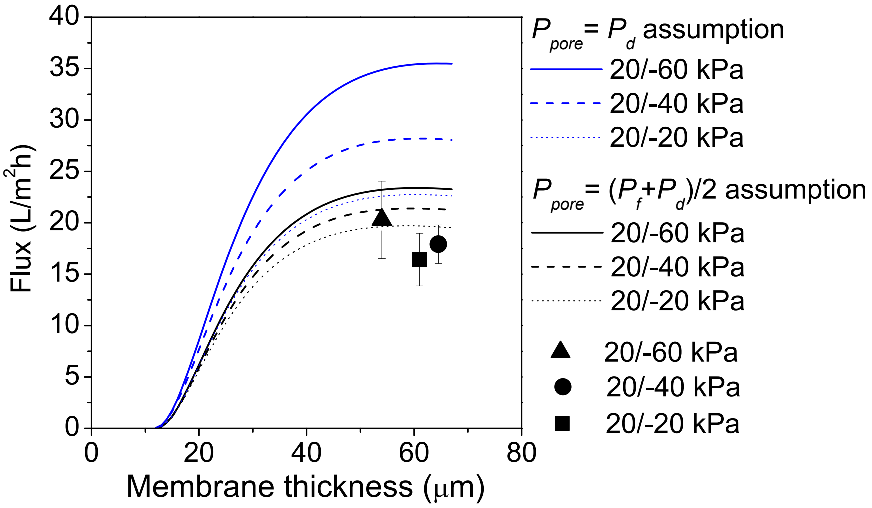

Figure 2.8: Tested and modeled water fluxes as a function of membrane thickness using the $P_{pore} = P_d$ and pressure gradient assumptions for VEDCMD (line: modeled fluxes; symbol: tested fluxes).

2.4. Conclusion

VEDCMD offers opportunities for higher fluxes than traditional DCMD, which may be particularly useful for water polishing and other low fouling applications. Pressure gradient was ruled out as providing significant contribution to the higher flux. The factors that were found to result in the higher water flux in VEDCMD were less membrane compaction and lower air pressure inside the membrane pores. Therefore, approaches to reduce air pressure inside the membrane pores (e.g., reducing the feed or distillate-side pressure) may provide opportunities for further flux enhancement in the VEDCMD process.

2.5. Acknowledgments

The authors would like to thank the U.S. Department of Energy Geothermal Technologies Program (Grant No. DE-EE00003231) for the financial support of this work.

2.6. References

[1] L.M. Camacho, L. Dumée, J. Zhang, J. Li, M. Duke, J. Gomez, S. Gray, *Review:* Advances in Membrane Distillation for Water Desalination and Purification Applications, Water, 5 (2013) 94-196.
[2] A.G. Fane, R.W. Schofield, C.J.D. Fell, The efficient use of energy in membrane distillation, Desalination, 64 (1987) 231-243.
[3] K. W. Lawson, D.R. Lloyd, Review: Membrane distillation, J. Membr. Sci., 124 (1997) 1-25.
[4] J. Walton, H. Lu, C. Tumer, S. Solis, H. Hein, Solar and waste heat desalination by membrane distillation, in: Desalination and Water Purification Research and Development Program Report No. 81, College of Engineering, University of Texas at El Paso, El Paso, Texas, 2004.
[5] S. Al-Obaidani, E. Curcio, F. Macedonio, G. Di Profio, H. Al-Hinai, E. Drioli, Potential of membrane distillation in seawater desalination: Thermal efficiency, sensitivity study and cost estimation, J. Membr. Sci., 323 (2008) 85-98.
[6] G. Zuo, R. Wang, R. Field, A.G. Fane, Energy efficiency evaluation and economic analyses of direct contact membrane distillation system using Aspen Plus, Desalination, 283 (2011) 237-244.
[7] H. Susanto, Review: Towards practical implementations of membrane distillation, Chem. Eng. Process. , 50 (2011) 139-150.
[8] M. Khayet, Membranes and theoretical modeling of membrane distillation: A review, Adv. Colloid Interface Sci., 164 (2011) 56-88.
[9] J.L. Cartinella, T.Y. Cath, M.T. Flynn, G.C. Miller, K.W. Hunter, A.E. Childress, Removal of natural steroid hormones from wastewater using membrane contactor processes, Environ. Sci. Technol., 40 (2006) 7381-7386.

[10] G. Rao, S.R. Hiibel, A.E. Childress, Simplified flux prediction in direct-contact membrane distillation using a membrane structural parameter, Desalination (In press)

[11] S. Bonyadi, T.S. Chung, Flux enhancement in membrane distillation by fabrication of dual layer hydrophilic–hydrophobic hollow fiber membranes, J. Membr. Sci., 306 (2007) 134–146.

[12] R.W.Schofield, G. A, Fane,, C.J.D. Fell, Gas and vapour transport through microporous membranes. II. Membrane distillation, Journal of Membrane Science, 53 (1990) 173-185.

[13] T.Y. Cath, V.D. Adams, A.E. Childress, Experimental study of desalination using direct contact membrane distillation: a new approach to flux enhancement, J. Membr.Sci., 228 (2004) 5-16.

[14] J. Zhang, J. D. Li, M. Duke, Z. Xie, S. Gray, Performance of asymmetric hollow fiber membranes in membrane distillation under various configurations and vacuum enhancement, J. Membr.Sci., (2010) 517-528.

[15] T.Y. Cath, V.D. Adams, A.E.Childress, Vacuum enhanced direct contact membrane distillation, U.S. Patent 20,100,089,830, (Apr 15, 2010).

[16] S. Adnan, M. Hoang, H. Wang, Z. Xie, Commercial PTFE membranes for membrane distillation application: Effect of microstructure and support material, Desalination 284, (2012) 297-308.

[17] M. Qtaishat, T. Matsuura, B. Kruczek, M. Khayet, Heat and mass transfer analysis in direct contact membrane distillation, Desalination 219, (2008) 272-292.

[18] J. Zhang, J. D. Li, S. Gray, Effect of applied pressure on performance of PTFE membrane in DCMD J. Membr. Sci., 369 (2011) 514-525.

[19] K.W. Lawson, M.S. Hall, D.R. Lloyd, Compaction of microporous membranes used in membrane distillation. I. Effect on gas permeability, J. Membr. Sci., 101 (1995) 99-108.

[20] J. Zhang, N. Dow, M. Duke, E. Ostarcevic, J. Li, S. Gray, Identification of material and physical features of membrane distillation membranes for high performance desalination, J. Membr. Sci. , 349 (2010) 295-303.

[21] R. Mishra, S.P. Tripathy, D. Sinha, K.K. Dwivedi, S. Ghosh, D.T. Khathing, M. Muller, D. Fink, W.H. Chung, Optical and electrical properties of some electron and proton irradiated polymers, Nucl. Instrum. Methods Phys. Res., Sect. B 168, (2000) 59-64.

[22] Qing-lin Huang, Chang-fa Xiao, Xiao-yu Hu, X.-f. Li, Study on the effects and properties of hydrophobic poly(tetrafluoroethylene) membrane, Desalination, 277 (2011) 187-192.

[23] M. Mulder, Basic principles of membrane technology, Kluver Academic Publishers, Dordrecht, Netherlands, 1991.

[24] J. A. Ruskowitz, A.E. Childress, Salt-Gradient Solar Pond and Membrane Distillation System for Water Desalination Powered by Renewable Energy, in: Thesis, University of Nevada, Reno, Reno, Nevada, 2012.

[25] V.D. Alves, I.M. Coelhoso, Effect of membrane characteristics on mass and heat transfer in the osmotic evaporation process, J. Membr. Sci., 228 (2004) 159-167.

[26] S. Srisurichan, R. Jiraratananon, A.G. Fane, Mass transfer mechanisms and transport resistances in direct contact membrane distillation process, J. Membr. Sci., 277 (2006) 186-194.

[27] S. Nakao, Review: Determination of pore size and pore size distribution 3. Filtration membranes, J. Membr. Sci., 96 (1994) 131-165.

[28] M. Khayet, T. Matsuura, Determination of surface and bulk pore sizes of flat-sheet and hollow-fiber membranes by atomic force microscopy, gas permeation and solute transport methods, Desalination 158, (2003) 57-64.

[29] H.Yasuda, J.T.Tsai, Pore size of microporous polymer membranes, J. Appl. Polym. Sci., 18 (1974) 805-819.

[30] J. Cohen, P. Cohen, S.G. West, L.S. Aiken, Applied Multiple Regression-Correlation Analysis for the Behavioral Sciences, Lawrnc rlbaum Asaociats, Inc, 2003.

[31] Z. Ding, R. Ma, A.G. Fane, A new model for mass transfer in direct contact membrane distillation, Desalination 151, (2002) 217-227.

[32] K.W. Lawson, D.R. Lloyd, Membrane Distillation. II. Direct contact MD, J. Membr.Sci. , 120 (1996) 123-133.

[33] R.W.Schofield, A.G.Fane, C.J.D.Fell, Heat and mass transfer in membrane distillation, Journal of Membrane Science, 33 (1987) 299-313.

[34] J. Phattaranawik, R. Jiraratananon, Direct contact membrane distillation: effect of mass transfer on heat transfer, J. Membr. Sci., 188 (2001) 137-143.

[35] J. Phattaranawik, R. Jiraratananon, A.G. Fane, C. Halim, Mass flux enhancement using spacer filled channels in direct contact membrane distillation, J. Membr. Sci., 187 (2001) 193-201.
[36] A.R.D. Costa, A.G. Fane, D.E. Wiley, Spacer characterization and pressure drop modelling in spacer-filled channels for ultrafiltration, J. Membr. Sci., 87 (1994) 79-98.
[37] J. Phattaranawik, R. Jiraratananon, A.G. Fane, Effect of pore size distribution and air flux on mass transport in direct contact membrane distillation, J. Membr. Sci., 215 (2003) 75-85.
[38] V. P.Carey, Liquid-vapor phase-change phenomena: an introduction to the thermophysics of vaporization and condensation processes in heat transfer equipment second ed., Taylor and Francis Group, LLC, New York, USA, 2008.
[39] P.C. Carman, Flow of Gases Through Porous Media, Butterworth Scientific Publications, London, UK, 1956.

2.7. Nomenclature and Units

A	Membrane surface area (m^2)
d	Membrane average pore size (m)
d_f	Spacer filament size (m)
d_h	Hydraulic diameter of the flow channel (m)
dZ_i/dt	Velocity of the liquid-gas interface at the normal direction (m/s)
h	Heat transfer coefficient (W/m^2 K)
$h_{(f,d)}$	Heat transfer coefficient in the boundary layer on the feed or distillate side (W/m^2 K)
H	Channel height (m)
k_{dc}	Parameter in Eq. 17
k_f	Thermal conductivity of the fluid (W/m K)
l_m	Mesh size of the spacer (m)
m	Mass of membrane sample (kg)
M	Molecular weight of vapor (kg/kmol)
N	Overall flux (L/m^2 h)
$N_{(k,m,v)}$	Water flux due to Knudsen diffusion, Molecular diffusion, or viscous flow (L/m^2 h)
N_{pore}	Membrane pore number
Nu	Nusselt number
P_{air}	Air pressure inside the membrane pores (Pa)
P_{fluid}	Hydraulic pressure of the liquid stream (Pa)
P_i	Water vapor pressure (Pa)
P_{pore}	Sum of P_{air} and P_i (Pa)
Pr	Prandtl number
Q_{cond}	Membrane conductive heat loss (W/m^2)
r	Membrane pore radius (m)
r_o	Original membrane pore radius (m)
R	Universal gas constant (J/mol K)
Re	Reynolds number
$R_{(1,2)}$	Curvature surface radius on the liquid or gas side (m)
$T_{(dout,\ din)}$	Distillate-side temperature at the outlet or inlet of the membrane cell (K)
$T_{(f,d)}$	Bulk temperature of the feed or distillate solution (K)
T_m	Average membrane temperature (K)
$T_{(mf,\ md)}$	Membrane surface temperature on the feed or distillate side (K)
x_{NaCl}	Molar fraction of NaCl inside the solution
δ	Membrane thickness (m)
ΔP	Pressure gradient (Pa)
ε	Membrane porosity
ε_o	Original membrane porosity
ε_s	Spacer porosity
θ	Angle formed among liquid, membrane material, and gas inside the membrane pores (°)
$_{(f,d)}$	θ at the feed or distillate side (°)
θ_s	Hydrodynamic angle of the spacer (°)
μ	Vapor dynamic viscosity (kg/m s)

$\dot{m}$	Fluid flow rate (L/min)
$\rho_{(\mathrm{l,\,p,\,v})}$	Density of liquid, polymer material, and vapor density (kg/m^3)
σ	Surface tension between liquid and gas at the pore entrance (N/m)
τ	Membrane tortuosity
τ_o	Original membrane tortuosity
$\omega_{(l,n,\ v,n)}$	Velocity of the liquid or vapor at the normal direction of the liquid-vapor interface (m/s)

Research Output #3

Membrane fouling and cleaning in direct-contact membrane distillation (DCMD)

Abstract

Membrane fouling has been recognized as a main obstacle that impedes the implementation of full-scale direct-contact membrane distillation (DCMD). Typical foulants in DCMD include $CaCO_3$, $CaSO_4$, SiO_2, and NaCl. The $CaCO_3$ scalant is commonly removed with HCl solutions in DCMD but the volatile property of HCl may increase the distillate conductivity. Thus, membrane cleaning using citric acid and Na_2EDTA solutions were investigated when treating the Walker Lake water, which has $CaCO_3$ as the major scalant. The citric acid solution was found to be able to completely restore membrane performance. The $CaSO_4$ scalant was successfully removed when treating the synthetic calcium sulfate solution by deionized water (DI water), which is different from the cleaning solutions reported in the literature. Membrane cleaning specifically focused on SiO_2 removal in DCMD has not been investigated; therefore, five cleaning solutions (DI water and NaOH solutions (62.5, 125, 250 mM at ambient temperature and 125 mM at 40 °C)) and a two-stage cleaning process (125 mM NaOH at 40 °C followed by 26.8 mM Na_2EDTA at ambient temperature) were tested for SiO_2 removal when treating the synthetic silica feed solution. It was found that the two-stage cleaning process completely restored membrane performance. The 2 wt.% HCl solution was used to remove the scalants (mainly NaCl) when treating the hypersaline solution; however, severe membrane wetting occurred after membrane cleaning. After membrane drying, the maximum water flux (94%) and the water recovery (90%) were restored.

3.1. Introduction

3.1.1. Membrane distillation

Membrane distillation (MD) is a thermally driven process that produces potable water via separation through a phase change process. The driving force of MD is the vapor pressure gradient across a membrane that results from the temperature difference across the membrane. The heat required to maintain the temperature (30-90 °C [1, 2]) of the feed solution can be supplied directly from low-grade thermal energies (low-temperature heat from solar system, geothermal heat, and industrial waste heat), which has led to an increase in interest in MD in recent years. Of all types of MD, direct-contact MD (DCMD) is the most commonly used configuration in lab-scale research [3]. DCMD is operated under atmospheric pressure with two solutions at different bulk temperatures circulated on either side of a hydrophobic membrane [1, 2]. DCMD membranes are typically made of polyvinylidenefluoride, polypropylene, or polytetrafluoroethylene with pore sizes from 0.2 to 1.0 μm [3-5]. Because the driving force of DCMD does not decrease significantly with increasing feed-water salinity, DCMD has been used to treat various feed waters [1, 6-8], and has near 100% salt and organic rejection [1, 9, 10]. However, membrane fouling has been recognized as a main obstacle impeding the implementation of full-scale DCMD [11, 12].

3.1.2. Membrane fouling and cleaning in DCMD

Membrane fouling is defined as the accumulation of foulants (organics, inorganics and microorganisms) at the membrane surface or inside the pores of a membrane [13]. Membrane fouling caused by inorganics is also called membrane scaling [13] and the inorganics are named scales [13, 14] or scalants [14]. Most reports in the literature concerning membrane fouling deal with pressure-driven membrane processes that are operated under hydraulic pressures using different membranes and feed waters than are used with DCMD. Thus, pressure-driven membrane processes are expected to have different fouling phenomena than DCMD processes. Membrane fouling in DCMD has been observed when treating tap water [15], ground water [16], reverse osmosis brines [17, 18], and saline solution produced while processing animal intestines [19]. Foulans on the membrane surface may alter the membrane's surface properties (e.g., hydrophobicity) and pore structures, hinder water transport to the membrane surface, and add an additional thermal resistance factor that in turn lowers the temperature at the membrane surface [12, 20, 21]. Membrane fouling caused by organics does not lead to significant flux decline in DCMD and organic foulants were found to be loosely packed on the membrane surface [22]. Inorganics, such as iron and manganese, also have minimal effects on water flux [18, 23]. Sparingly soluble salts, such as calcium carbonate ($CaCO_3$), calcium sulfate ($CaSO_4$), and silica (SiO_2) were frequently observed as major scalants leading to flux decline and ultimately lower water recovery [12, 13, 18, 24]. When treating hypersaline solutions, sodium chloride (NaCl) was observed as the major scalant [12].

3.1.2.1. Calcium carbonate

Although different forms of calcium carbonate ($CaCO_3$) exist in nature, the major scalant in DCMD has been recognized as calcite [25]. Calcite has a compact and hexagonal structure with a sticky property [18]. It mainly accumulates on the membrane surface rather than penetrating into the membrane pores [20]. Because the solubility of $CaCO_3$ decreases with increasing temperature [18], $CaCO_3$ is also often observed in the feed container and on the connecting tubes that have higher temperatures than the membrane module [18]. The $CaCO_3$ scalant can be alleviated by pretreatment processes such as softening and coagulation [16, 21], or by acidifying the feed solution to a pH near 4 [11, 18, 21]. The pretreatment process require large amounts of chemicals, yet scalants were still observed on the membrane surface after chemical coagulation followed by sand filtration or microfiltration [21]. Although acidification of the feed water limited the formation of $CaCO_3$, membrane scaling caused by other compounds (e.g., silica) may still be observed [20]. To clean the membrane scaled by $CaCO_3$, 2-5 wt.% hydrochloride acid (HCl) solutions have been used in DCMD systems [15, 18, 20, 21], but a slight increase in the distillate conductivity was observed in some reports due to pore wetting [18], or passing of the volatile HCl to the distillate side [15, 20, 21]. Both acidic solutions and metal chelating agents (e.g., ethylenediaminetetraacetic acid (EDTA) and citric acid) are frequently used for $CaCO_3$ removal in pressure-driven membrane processes [26, 27], but only HCl solutions were used for membrane cleaning in DCMD and no relevant reports investigating these metal chelating agents and DCMD membrane performance are currently available in the literature to the best of the authors' knowledge.

3.1.2.2. Calcium sulfate

Calcium sulfate ($CaSO_4$) was found to be a more severe scaling problem than $CaCO_3$ in DCMD based on the sharp flux decline when $CaSO_4$ was formed [24]. The major form of $CaSO_4$ scalants has been recognized as gypsum [25], which can have needle-shaped crystal structures [18, 28] and may penetrate into membrane pores after depositing on the membrane surface [20]. Gypsum scalants in the pores of a DCMD membrane may dissolve into the cleaning solution, leading to membrane wetting and even passing of the feed solution to the distillate side when performing DCMD tests [20]. Membrane breaks caused by $CaSO_4$ crystals were also observed in some reports [11, 24]. Control of $CaSO_4$ is a major challenge in both pressure-driven membrane processes and MD because the formation of $CaSO_4$ is not pH sensitive, thus cannot be prevented by acidifying the feed solution [28]. Both metal chelating agents [17] and NaCl solutions [29, 30] have been reported to effectively clean the membrane scaled by $CaSO_4$ in DCMD. Considering the relatively high solubility (2-2.5 g/L at 25 °C [31]) of $CaSO_4$, pure water may also serve as an effective and economical cleaning solution.

3.1.2.3. Silica

Silica (SiO_2) is abundant in natural waters, and membrane scaling has been observed with both high and low silica concentrations of feed solutions. Silica scaling can result in rapid flux decline and may irreversibly deteriorate the membrane material [32, 33]. The types of silica scalants are strongly pH dependent with colloidal silica (an accumulation of silicic acid) dominating at low pH and silicates (e.g., Mg_2SiO_4, Ca_2SiO_4) being precedent at high pH (> 8) [18, 33]. Silica can also adsorb onto the surface of insoluble metal compounds (e.g., $Mg(OH)_2$, $MgCO_3$) in alkaline conditions and sever the membrane scaling phenomenon[18]. Aggregates of opaque milky-to-white films were observed for colloidal silica scalants [33]. Silica scalants are very difficult to remove through chemical cleaning [32, 34]. In pressure-driven membrane processes, the addition of anti-scalants to inhibit silica scalant formation [32, 33, 35] and the use of pretreatment processes to reduce silica concentrations before the membrane processes

[33, 36] have been reported to mitigate the silica scaling phenomenon, but a proper type of anti-scalant or coagulant and an optimal dosage are needed, which make the membrane processes difficult to control [32, 35]. Although sonification was successfully used to remove silica scalants from microfiltration membranes [37], increased solute permeation was observed and the effectiveness of sonification was strongly affected by the intensity and direction of the irradiation [38]. No specific study has been carried out on silica removal in DCMD. Although a HCl solution was used to remove a mixture of calcium scaling and colloidal silica [18], and an EDTA solution was used to remove a mixture of $CaSO_4$ and SiO_2 scalants [17], no full recovery of water flux was obtained in each study after membrane cleaning.

3.1.2.4. Sodium chloride

Sodium chloride (NaCl) has been reported to cause rapid flux decline when homogeneous precipitation of NaCl crystals on the membrane surface occurred [12]. Due to the high solubility of NaCl in water (360 g/L at 25 °C [39]), precipitation of NaCl only occurs when the feed solution has been highly concentrated during a water treatment process or is originally a hypersaline solution. The NaCl scalant in DCMD has been recognized as halite [25], which has a cubic crystal structure. To prevent membrane scaling, crystallizers have been incorporated into the DCMD system to collect the crystals that will otherwise deposit on membrane surface [11, 40]. However, proper operation conditions have to be identified to prevent deposition of crystals in the membrane module or connecting tubes instead of the crystallizer [40]. No investigation of chemical cleaning of the NaCl scaled membrane in DCMD is currently available according to the author’s knowledge. Although DCMD is believed to be advantageous than pressure-driven membrane processes when treating hypersaline feed waters (driving force of DCMD does not decrease significantly with feed-water salinity [6-8, 41]), the performance of a cleaned MD membrane after treating the hypersaline feed waters is still unknown.

3.1.3. Objective

Due to the various problems and uncertainties associated with cleaning scaled membranes in DCMD systems, the main objective of this study is to identify effective cleaning solutions for typical scalant ($CaCO_3$, $CaSO_4$, SiO_2, and NaCl) removal in DCMD. To achieve this objective, four feed solutions containing different scalants were tested in bench-scale DCMD systems. The membrane performance of each feed solution before and after membrane cleaning was compared to estimate the effectiveness of each cleaning solution.

3.2. Materials and methods

3.2.1. Feed solutions

Four feed solutions were investigated in the study: the Walker Lake water, calcium sulfate solution, silica solution, and synthetic Great Salt Lake water. The Walker Lake (Nevada, U.S.A) water was collected onsite while the other solutions were synthesized using deionized water (DI water) and reagent grade salts. Compositions of each feed solution are given in Table 3.1. The calcium sulfate solution was prepared with the concentrations of SO_4 and Ca four times the concentrations in the well water as reported by the Eastern Municipal Water District of California, U.S.A [42] and NaCl was used to adjust the ionic strength of the calcium sulfate solution to be consistent with four times the ionic strength of the well water. The concentration of Si in the silica solution was four times the concentration in the same well water and the ionic strength was adjusted using NaCl and $MgCl_2$ to keep it four times the ionic strength of the well water. The pH of the silica solution was adjusted using the HCl solution (12.1 N). The Great Salt Lake water was synthesized according to the reported ion compositions by Encyclopaedia Britannica [43].

Table 3.1: Composition of feed solutions.

	Composition		TDS (g/L)	pH
	Salt	Concentration (g/L)		
Walker Lake* water [45]	Na^+	5.04	16.07	9.4
	K^+	0.270		
	Ca^{2+}	0.0103		
	Mg^{2+}	0.189		
	Cl^-	3.53		
	SO_4^{2-}	3.57		
	alkalinity	3.46		
Calcium sulfate solution	$CaCl_2.2H_2O$	5.12	8.125	6.7
	Na_2SO_4	2.70		
	NaCl	0.270		
Silica solution	$Na_2SiO_3.9H_2O$	2.55	13.75	6.0
	$MgCl_2.6H_2O$	3.85		
	NaCl	6.80		
	HCl	0.548		
Great Salt Lake water	NaCl	213	289.1	7.4
	$MgSO_4.7H_2O$	42.1		
	$MgCl_2.6H_2O$	25.4		
	KCl	7.75		
	$NaHCO_3$	0.345		
	$CaCl_2.2H_2O$	0.884		

3.2.2. DCMD experiments

A bench-scale DCMD system was used in the study. Vacuum (near -20 kPa as gauge pressure) was introduced to the distillate side of the membrane to expedite membrane scaling when treating the calcium sulfate solution and the silica solution. The system schematics are given in the literature [44]. Four liters of the feed solution and DI water were circulated counter-currently on the respective membrane surfaces at 1.5 L/min. The feed stream of each Walker Lake, calcium sulfate, and silica solutions was maintained at 40-45 °C using a hot bath (Model 280, Precision Scientific, Winchester, VA) and the distillate stream was held at 20-25 °C using a re-circulating chiller (Model M-33, Thermo-electron, Newington, NH), while the Great Salt Lake water was tested at 60 °C and 40 °C on the feed and distillate sides of the membrane, respectively, to achieve a temperature difference of 20 °C across the membrane for all four tests. Temperatures were monitored using dual-channel digital thermometers (DigiSense DualLog R, Cole-Parmer, Vernon Hills, IL) with thermocouples located at the inlets and outlets of the membrane module, which had an effective surface area of 118 cm^2. As water vapor passed through the membrane from the feed to the distillate, the excess water from the distillate reservoir overflowed into a beaker on an analytical balance and the overflow rate was used to calculate water flux. A conductivity meter (Jenway 4320, Jenway Ltd., U.K) was used in the distillate tank to monitor distillate conductivity. Flat-sheet polytetrafluoroethylene membranes from GE Osmonics (Minnetonka, MN) were used in the tests. The membranes are compatible with strong acids and aggressive solutions according to the manufacturer. The scalant analysis on the membrane surface was performed using scanning electron microscopy (SEM; S-3000N, HITACHI, Japan) coupled with energy dispersive spectrometry (EDS; Genesis, EDAX, USA). The OLI Stream Analyzer 9.0 (OLI Systems Inc., Morris Plains, NJ) was used to estimate the salts that may precipitate out of the feed solution during the DCMD test. The aqueous thermodynamic model based on published data and the Helgeson equation of state were used in the analyzer for polynomial fits [45].

3.2.3. Cleaning experiments

The membrane cleaning experiments were performed after the water flux dropped below 3 L/m^2-hr (more than 75% of flux decline). The cleaning procedure included first circulating 2 L of the cleaning solution on the feed side of the membrane at a flow rate of 2 L/min for 30 min; next, the membrane was flushed using ~10 L of DI water for each Walker Lake, calcium sulfate, and silica solutions, and a 2 hr tap water flushing of the membrane was used for the Great Salt Lake water. Two cleaning solutions were tested to clean the membrane scaled by the Walker Lake water: 1) a citric acid solution (240 mM) and 2) a disodium ethylenediamine tetraacetate solution (Na_2EDTA; 29 mM) combined with 58 mM NaOH. DI water was also tested to clean the membranes scaled by the calcium sulfate solution. Cleaning of the silica scaled membranes was tested with DI water, NaOH solutions (62.5, 125, and 250 mM at ambient temperature and 125 mM at 40 °C) and a two-stage procedure of NaOH (125 mM at 40 °C) followed by an Na_2EDTA solution (26.8 mM combined with 62.3 mM NaOH). A 2 wt.% HCl solution was used to clean the membrane scaled by the Great Salt Lake water. Membrane performance parameters (water flux and batch recovery) were evaluated before and after each cleaning cycle.

3.3. Results and discussions

3.3.1. Walker Lake water

The simulation results using the OLI Stream Analyzer predicted that $CaCO_3$ would become oversaturated first in the feed solution, followed by Hydromagnesite ($Mg_5(CO_3)_4(OH)_2 \cdot 4H_2O$), which reached saturation at a water recovery near 90%. The SEM-EDS results further confirmed the elements of the two scalants. Therefore, it is highly likely that $CaCO_3$ is the major scalant that caused flux decline at the low water recoveries.

Water flux and batch recovery before membrane cleaning are given in Fig. 3.1. The slight differences between the two runs are attributed to slight differences between membrane batches and Walker Lake water batches. Minimal flux decline was observed during the first 10 hrs, indicating that little membrane scaling occurred during this period. After 10 hr of operation, gradual flux declines were observed during the following tens of hours until a stable flux of ~ 2 LMH was reached. It is likely that calcite nucleation occurred near 10 hr of operation, and then the gradual flux decline was due to membrane scaling caused by gradual depositions of the $CaCO_3$ scalant on the membranes surface. It was also noted that $CaCO_3$ was prone to precipitate in the feed bulk solution rather than on the membrane surface, a phenomenon observed by others [21]. The sticky property of $CaCO_3$ prevented $CaCO_3$ from moving to the membrane surface, thus led to a gradual (instead of rapid) deposition of $CaCO_3$ on the membranes surface. This may be the reason that a gradual flux decline (instead of a sharp flux decline) was observed. Similar phenomenon has also been observed in the literature [18]. At the end of each test prior to membrane cleaning, a water recovery of near 50% was achieved.

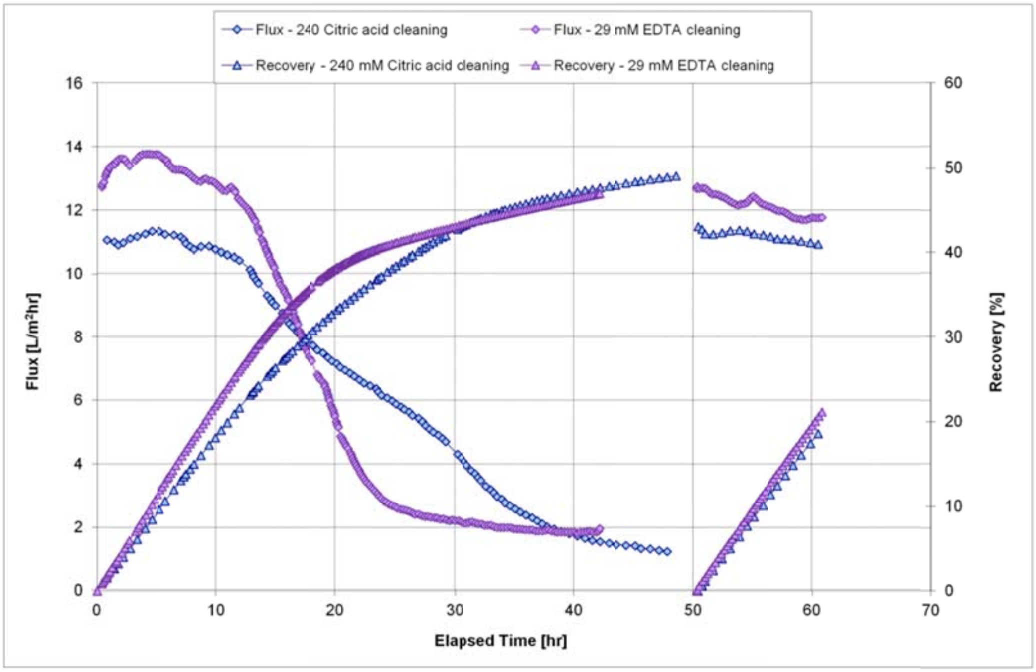

Figure 3.1: Membrane performances before and after membrane cleaning for Walker Lake water.

The maximum water flux was fully restored after the membrane cleaning with the citric acid solution, while only 90% flux restoration was observed with the Na_2EDTA solution (Fig. 3.1). One possible explanation for this was that the citric acid solution was at a much higher concentration (240 mM) of citric acid than Na_2EDTA (29 mM), thus more scalants could be removed by the citric acid solution. SEM images of the virgin membrane surfaces compared to after cleaning with both solutions are shown in Fig. 3.2. A small amount of scalants were observed on the surface of the Na_2EDTA cleaned membrane (Fig. 3.2c), while the membrane surface cleaned with the citric acid solution appears free of scalants. EDS analysis further confirmed less scalant on the citric acid-cleaned membrane. It should be noted that the membrane polymeric structure after cleaning with the Na_2EDTA solution is quite similar to the structure of the virgin membrane, while the polymeric structure of the citric acid-cleaned membrane surface has a noticeably different appearance. However, the observed physical differences of the membrane surfaces do not appear to negatively impact the membrane performance, considering the full restoration of the maximum water flux after cleaning with the citric acid solution. Because citric acid is non-volatile, there is less of a risk for citric acid to pass through the membrane compared to the membrane cleaning using the HCl solutions. Membrane samples treated with multiple citric acid cleaning cycles were able to maintain 99.9% salt rejection. Therefore, the 240 mM citric acid solution is recommended for $CaCO_3$ scalant removal in the future.

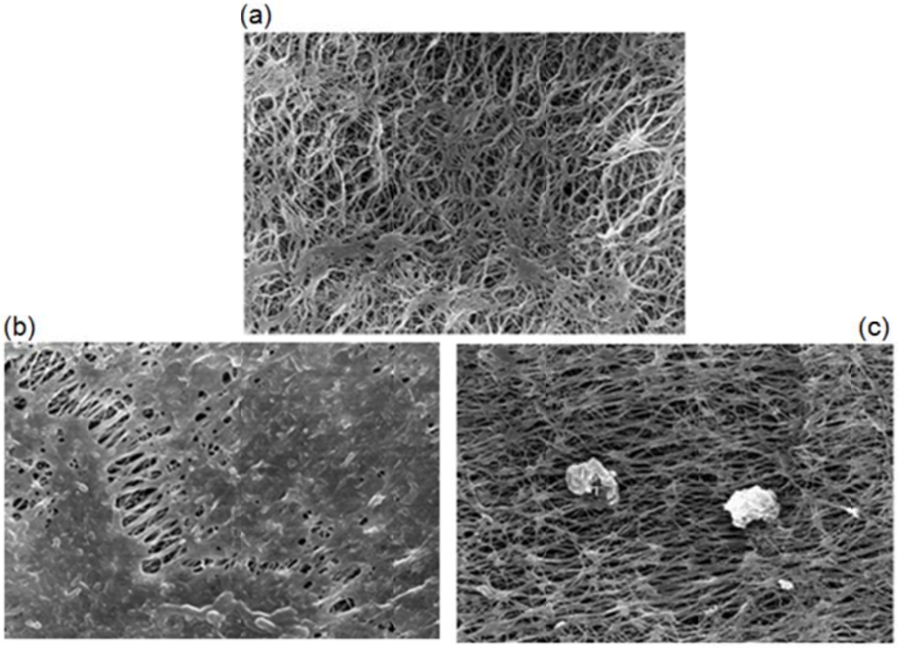

Figure 3.2: SEM images of virgin membrane and membranes cleaned using citric acid solution (240 mM) and Na_2EDTA solution (29 mM).

3.3.2. Calcium sulfate solution

Results from the OLI software suggest that gypsum was oversaturated in the feed solution before beginning the DCMD test with the $CaSO_4$ solution. It also suggested that anhydrous calcium sulfate had a scaling tendency of 0.93 (a scaling tendency of 1.0 is considered saturated) before the test. Due to concentration polarization effects, it is highly likely that the concentration of anhydrous calcium sulfate on the membrane surface will be greater than the concentration in the bulk solution, thus anhydrous calcium sulfate may also be saturated at the membranes surface at the beginning of the test. Typical calcium sulfate structure was observed on the membrane surface based on the SEM image and the SEM-EDS analysis results revealed only Ca, S and O elements on the membrane surface, indicating that $CaSO_4$ scalants had fully covered the membrane surface by the end of the test.

During the DCMD test but prior to membrane cleaning, the feed solution remained clear during the first hour, at which time precipitates were observed as the feed solution was further concentrated. A constant water flux was observed during the first 4 hr of the test (Fig. 3.3), suggesting that no membrane scaling had occurred during this period. Instead, the 4 hr period is likely the induction time for the nucleation of $CaSO_4$ scalants. A long induction time for the nucleation of $CaSO_4$ scalants has also been reported by Nghiem et al. [24]. After that, formation of $CaSO_4$ scalants caused a rapid flux decline that is consistent with what has been reported in the literature [24]. After 6 hr, the water flux was less than 2 L/m^2-hr and the flux began to decrease slowly; the water recovery reached 25-30% by the end of the test. After membrane cleaning using DI water, the membrane performance was completely restored (Fig. 3.3). Preliminary tests achieved similar membrane performances using NaOH (50 and 100 mM) and Na_2EDTA (29 and 58 mM) solutions for membrane cleaning. The distillate conductivity was stable at 2 µS/cm before and after membrane cleaning, suggesting a good salt rejection of the DCMD test with no pore wetting occurring. Therefore, DI water without additional chemicals is sufficient for $CaSO_4$ removal, which differs from cleaning solutions reportedly used in the literature [29, 30]. However, this result is not surprised considering the high solubility of $CaSO_4$ (e.g., 2-2.5 g/L at 25 °C [31]).

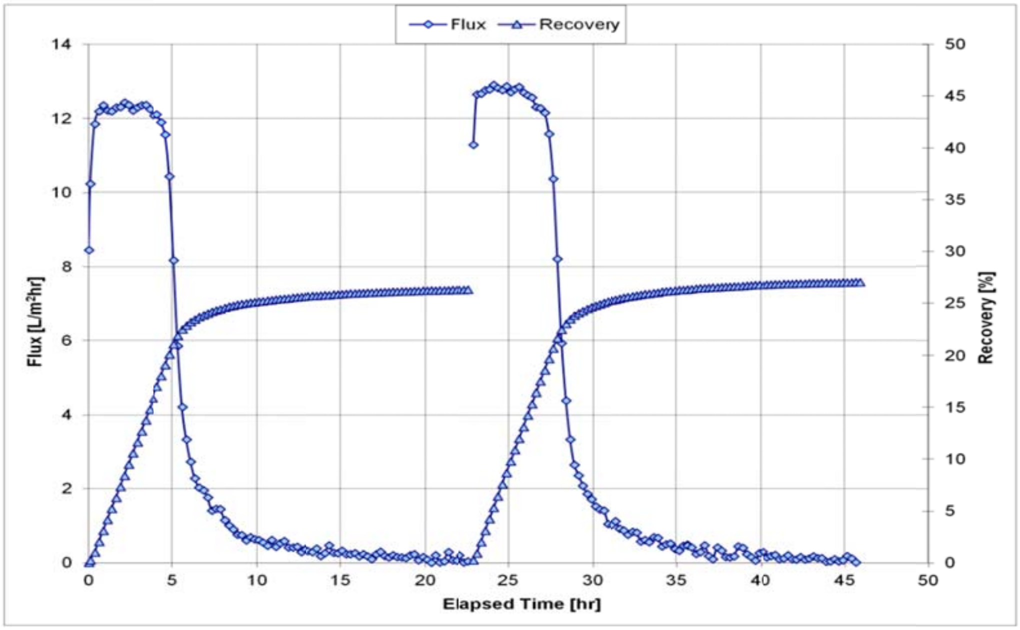

Figure 3.3: Membrane performances before and after membrane cleaning using DI water for calcium sulfate scalant removal.

3.3.3. Silica feed solution

Results from the OLI software suggested that SiO_2 was oversaturated in the feed solution during the test and was also the only scalant that was saturated. The SEM-EDS analysis revealed a compact layer of scalants on the membrane surface that had a typical structure of SiO_2 and contained only Si and O elements. In addition, magnesium scalant was also detected. Therefore, the membrane surface was fully covered by the SiO_2 scalant at the end of the test.

3.3.3.1. DI water cleaning

Water flux and batch recovery before and after membrane cleaning using DI water are given in Fig. 3.4. Slow flux declines were observed in both tests, which differs from what has been reported in the literature for reverse osmosis membrane processes, where rapid flux decline occurred [32, 33]. The faster flux decline caused by the SiO_2 scalant in RO is likely because RO membranes have much smaller pore sizes than MD membranes, thus membrane pore blockage may easily occur in RO but not in MD. The high applied pressure in RO may also attribute to the faster rate of membrane scaling. After membrane cleaning, the maximum water flux reached 5 L/m^2-hr, which is only 42% of the maximum water flux before cleaning. Also, the batch recovery reached only 19% after membrane cleaning, which is much lower than the batch recovery before membrane cleaning (60%). Therefore, DI water is not effective for the SiO_2 scalant removal.

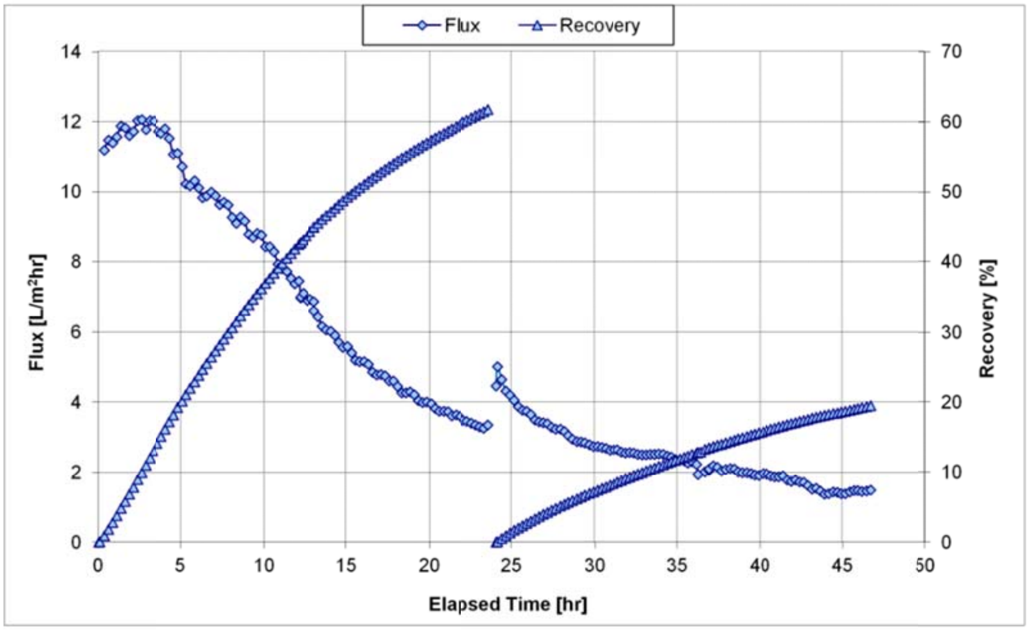

Figure 3.4: Membrane performances before and after membrane cleaning using DI water for silica scalant removal.

3.3.3.2. NaOH solution cleaning

Figure 3.5 gives the membrane performances before and after membrane cleaning using NaOH solutions. The membrane cleaned by the NaOH solution with the lowest concentration (62.5 mM) has only 20% of water recovery, and the membrane performance is quite similar to the membrane performance after cleaning using DI water (Fig. 3.4). Therefore, the addition of 62.5 mM NaOH did not improve membrane cleaning compared to DI water itself. Increasing the NaOH concentration to 125 mM led to the maximum water flux of 7 L/m^2-hr and a water recovery of 22% after membrane cleaning, compared to the maximum water flux of 12 L/m^2-hr and a water recovery of 55% before cleaning. Although the 125 mM NaOH solution also did not fully remove the SiO_2 scalant on the membrane surface, a better membrane performance after cleaning was achieved compared to the membrane performance after cleaning using DI water or 62.5 mM NaOH solution. The membrane cleaned by 250 mM NaOH solution had a continuous increasing of the distillate conductivity until 2 mS/cm during the test. Posterior inspection of the membrane revealed surface damage due to chemical reaction between the cleaning solution and membrane material. Therefore, the most effective solution among the three NaOH solutions for the SiO_2 scalant removal was the 125 mM NaOH solution and this solution was used for further analysis.

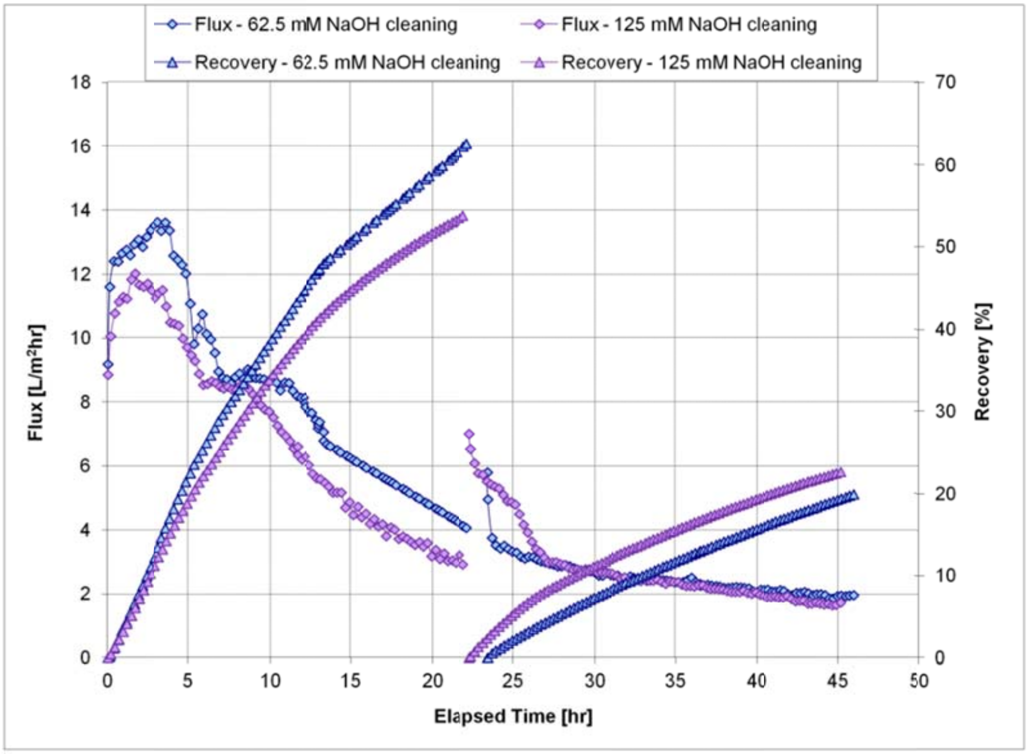

Figure 3.5: Membrane performances before and after membrane cleaning using NaOH solution (62.5 and 125 mM) for silica scalant removal.

3.3.3.3. NaOH solution cleaning at elevated temperature

Water flux and batch recovery before and after membrane cleaning using only NaOH solution (125 mM) at 40 °C and a two-stage cleaning process with NaOH solution (125 mM) at 40 °C followed by Na_2EDTA solution (26.8 mM combined with 62.3 mM NaOH) at ambient temperature are given in Fig. 3.6. Unlike the cleaning solutions investigated previously, the maximum water fluxes were fully restored after cleaning with both solutions, thus the increase in temperature seems to improve cleaning. It is likely that the chemical reaction between NaOH and SiO_2 was facilitated at elevated temperatures. However, after membrane cleaning using only the NaOH solution, there was an immediate onset of flux decline, leading to a water recovery of 35%, which is lower than the water recovery of a virgin membrane (52%). The fast drop of water flux is likely because of the fast formation of the SiO_2 scalant on the membrane surface. It is likely that the majority of the SiO_2 scalant was removed from the membrane following cleaning, thus restoring water flux to its initial level; however, the residual scalant that did remain on the membrane most likely provided sites for crystallization, leading to more rapid scalant formation and earlier onset of flux decline after cleaning.

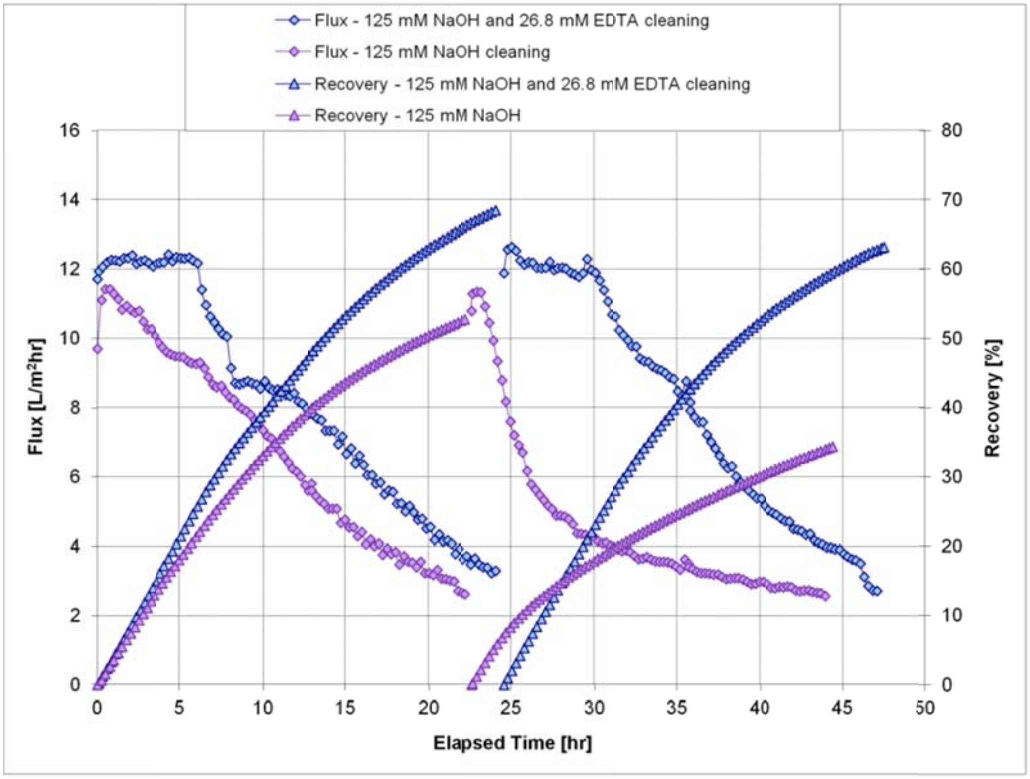

Figure 3.6: Membrane performances before and after membrane cleaning using NaOH solution (125 mM at 40°C) and the two-stage cleaning for silica scalant removal.

In comparison, the membrane performance after cleaning using the two-stage cleaning process is quite similar to that before cleaning with both water recoveries at approximately 65%. Therefore, the two-stage cleaning process improved membrane cleaning in comparison with only NaOH solution. The improved cleaning is likely attributed to the NaOH (62.5 mM) contained in the Na_2EDTA solution. It is likely that NaOH reacted with the SiO_2 residuals on the membrane surface after the first-stage cleaning and fully removed the SiO_2 residuals. Although Fig. 3.5 suggests the 62.5 mM NaOH solution did not improve membrane cleaning compared to DI water, it is likely that the 62.5 mM NaOH solution removed a small portion of the SiO_2 scalant, but this removal was not significant enough to lead to obvious improvements of water recovery and the maximum water flux. The possibility of Na_2EDTA reacting with SiO_2 is quite small since complicated procedures involving high temperatures (up to 200 °C) and extensive amounts of time (> 40 hr) have been used to couple silica with EDTA in the literature [46]. However, Na_2EDTA may attribute to the removal of the magnesium scalants on the membrane through the metal chelating process. After all, it is very unlikely that the NaOH solutions will help to remove the magnesium scalant, although magnesium scalant was detected using the SEM-EDS analysis (Section 3.3).

3.3.4. Great Salt Lake water

Results from the OLI software suggested that both NaCl and $CaSO_4$ salts reached saturation in the Great Salt Lake water at a water recovery of 4%. Because more NaCl is present in the feed solution, the NaCl scalant is expected to have a more significant effect on membrane performance than the $CaSO_4$ scalant. The SEM-EDS analysis revealed that the membrane surface was fully covered by salt scalants. Na, Cl were observed as the major scalant elements, followed by small quantities of Ca, Mg, K, and S. To completely remove all the scalants, the 2 wt.% HCl solution was used for membrane cleaning. HCl is commonly used for Ca and Mg scalant removal [16, 18]; as 98 wt. % of the HCl solution contains properties of water, it was hypothesized that the HCl solution would effectively remove the NaCl scalant based on the high solubility of NaCl.

Water flux and batch recovery before and after membrane cleaning are given in Fig. 3.7. With a virgin membrane, the water flux dropped immediately at the beginning of the test, indicating the onset of membrane scaling at a TDS of 250 g/L of the feed solution. This is consistent with previous reports in the literature [12]. After 3.5 hrs of the DCMD test, a rapid flux decline was observed, which is likely caused by the homogeneous precipitation of NaCl crystals on the membrane surface [12]. The feed solution had a TDS of 330 g/L at the beginning of the rapid flux decline, which is comparable to reported results from the literature [12]. Only 67% of the maximum water flux was restored after the first membrane cleaning and only 39% restoration after the second membrane cleaning, which is lower than the performance of the virgin membrane. To investigate whether the lower maximum water fluxes were because of ineffective membrane cleaning, the membrane surfaces after cleaning were investigated through the SEM-EDS analysis. Results suggested that the membrane surfaces were free of scalants with exception of few Si elements, which likely came from the environment (air or tap water) since no silica was used in the feed water preparation. Therefore, the 2 wt.% HCl solution effectively removed the scalants on the membrane surface, and determined that other factors led to the incomplete restoration of the maximum water flux. Because membrane wetting has been observed after cycles of membrane cleaning for the calcium carbonate scalant removal, leading to decreased water flux and lower flux restoration [15, 20, 21, 47], it is likely that membrane wetting also occurred in the current study. The increased distillate conductivity after each cycle of membrane cleaning also suggests that membrane wetting may have occurred during membrane cleaning.

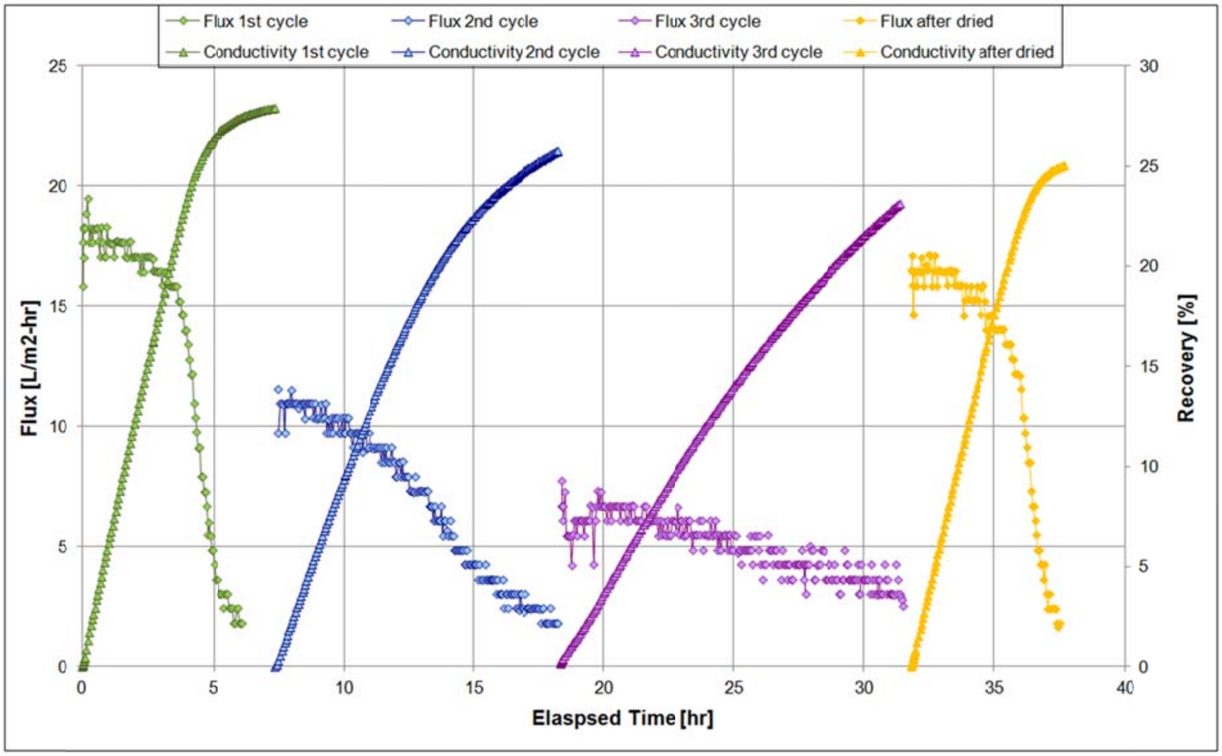

Figure 3.7: Membrane performances before and after membrane cleaning and after membrane drying when treating the synthetic Great Salt Lake water.

As scalants fully covered the membrane surface at the end of the DCMD test, the scalants such as the NaCl crystals may have entered into the pores at the upper layer of the membrane. Penetration of the salt scalants into the interior membrane pores up to a depth of 100 μm has been observed by others [20]. Therefore, the scalants deposited inside the upper layer of the membrane may readily dissolve into the cleaning solution, leading to severe membrane wetting of the membrane surface during membrane cleaning. The wetted membrane layer was suspected to act as an additional boundary layer, which reduced the heat transfer from the feed bulk solution to the evaporation surface of the water vapor, and thus lowered the evaporation temperature and ultimately water flux. To eliminate membrane wetting, the membrane after cleaning was dried inside an oven at 105 °C until the mass of the membrane sample remained constant. The non-wetted membrane was tested again using a new batch of the feed solution, and 94% of the maximum water flux was restored after membrane drying (Fig. 3.7). Therefore, the hypothesis of membrane wetting leading to the decreased maximum water flux was supported. Batch recoveries of 26% and 23% were achieved, respectively, after the first and second membrane cleaning, which were comparable and slightly lower than the water recovery before membrane cleaning (28%). This was likely because the lower maximum water flux led to a lower rate of membrane fouling, and longer operation time before membrane cleaning was needed. After membrane drying, water recovery of 25% was achieved, corresponding to 90% of the water recovery before membrane cleaning.

It should be noted that a dramatic increase of the distillate conductivity (up to 90 μS/cm) was observed at the beginning of the test after membrane drying, followed by a decrease to a constant ~70 μS/cm during the DCMD test. The early increase of the distillate conductivity is likely due to the wetting of the largest pores, leading to less salt rejection compared to the salt rejection before membrane drying. Membrane drying may enlarge the membrane pore size, making the new largest pores more easily wetted. However, although relatively higher distillate conductivity was observed after membrane drying, the salt rejection of the DCMD test still reached near 100%.

3.4. Conclusion

Membrane cleaning in DCMD when treating feed solutions containing typical scalants (calcium sulfate, calcium carbonate, silica, and sodium chloride) was investigated in this study. The 240 mM citric acid solution was found to effectively remove the $CaCO_3$ scalant and completely restored the membrane performance. The $CaSO_4$ scalant was easily removed using only DI water without need for additional chemicals. The SiO_2 scalant was difficult to remove, and a two-stage cleaning process using 125 mM NaOH solution at 40 °C and 26.8 mM Na_2EDTA solution was used to fully remove the SiO_2 scalant and restore the membrane performance. NaCl was observed as the major scalant when treating the hypersaline solution from the synthetic Great Salt Lake water, and was effectively removed by the HCl solution, however, severe membrane wetting occurred after cleaning, leading to reduced maximum water flux. After membrane drying, a 94% of the maximum water flux and 90% of water recovery were achieved.

3.5. Acknowledgments

The authors acknowledge the financial supports of California Department of Water Resources (Grant NO. 46-7446-R-08) and U.S. Department of Energy Geothermal Technologies Program (Grant No. DE-EE00003231).

3.6. References

[1] K.W. Lawson, D.R. Lloyd, Review: Membrane distillation, J. Membr. Sci. , 124 (1997) 1-25.
[2] A.M. Alklaibi, N. Lior, Transport analysis of air-gap membrane distillation, J. Membr. Sci. 255 (2005) 239-253.
[3] L.M. Camacho, L. Dumée, J. Zhang, J. Li, M. Duke, J. Gomez, S. Gray, *Review:* Advances in Membrane Distillation for Water Desalination and Purification Applications, Water, 5 (2013) 94-196.
[4] A.M. Alklaibi, N. Lior, Membrane-distillation desalination: status and potential, Desalination, 171 (2004) 111-131.
[5] J. Zhang, N. Dow, M. Duke, E. Ostarcevic, J. Li, S. Gray, Identification of material and physical features of membrane distillation membranes for high performance desalination, J. Membr. Sci. , 349 (2010) 295-303.
[6] S. Lee, J. Choa, M. Elimelech, Influence of colloidal fouling and feed water recovery on salt rejection of RO and NF membranes, Desalination, 160 (2004) 1-12.
[7] E. Curcio, E. Drioli, Membrane Distillation and Related Operations - A Review, Sep. Purif. Rev., 34 (2005) 35-86.
[8] M. Khayet, Membranes and theoretical modeling of membrane distillation: A review, Adv. Colloid Interface Sci., 164 (2011) 56-88.
[9] K.W. Lawson, D.R. Lloyd, Membrane Distillation. II. Direct contact MD, J. Membr.Sci. , 120 (1996) 123-133.

[10] J.L. Cartinella, T.Y. Cath, M.T. Flynn, G.C. Miller, K.W. Hunter, A.E. Childress, Removal of natural steroid hormones from wastewater using membrane contactor processes, Environ. Sci. Technol., 40 (2006) 7381-7386.
[11] M. Gryta, M. Tomaszewska, K. Karakulski, Wastewater treatment by membrane distillation, Desalination, 198 (2006) 67-73.
[12] K.L. Hickenbottom, T.Y. Cath, Sustainable operation of membrane distillation for enhancement of mineral recovery from hypersaline solutions, J.M.Sci, 454 (2014) 426-435.
[13] S. Shirazi, C. Lin, D. Chen, Inorganic fouling of pressure-driven membrane processes - A critical review, Desalination, 250 (2010) 236-248.
[14] H.L Yang, C. Huang, J.R. Pan, Characteristics of RO foulants in a brackish water desalination plant, Desalination, 220 (2008) 353-358.
[15] M. Gryta, Long-term performance of membrane distillation process, J. Membr.Sci., 265 (2005) 153-159.
[16] M. Gryta, Pretreatment of feed water for membrane distillation, Chemical Papers, 62 (2008) 100-105.
[17] C.R. Martinetti, A.E. Childress, T.Y. Cath, High recovery of concentrated RO brines using forward osmosis and membrane distillation, J. Membr. Sci., 331 (2009) 31-39.
[18] D. Qu, J. Wang, B. Fan, Z. Luan, D. Hou, Study on concentrating primary reverse osmosis retentate by direct contact membrane distillation, Desalination, 247 (2009) 540-550.
[19] M.T. M. Gryta, J. Grzechulska, A.W. Morawski, Membrane distillation of NaCl solution containing natural organic matter, Journal of Membrane Science, 2001 (2001) 279-287.
[20] M. Gryta, Fouling in direct contact membrane distillation process, J. Membr. Sci., 325 (2008) 383-394.
[21] M. Gryta, Desalination of thermally softened water by membrane distillation process, Desalination, 257 (2010) 30-35.
[22] R.J. Surapit Srisurichan, A.G. Fane, Humic acid fouling in the membrane distillation process, Desalination, 174 (2005) 63-72.
[23] M. Gryta, Effect of iron oxides scaling on the MD process performance, Desalination, 216 (2007) 88-102.
[24] L.D. Nghiem, T. Cath, A scaling mitigation approach during direct contact membrane distillation, Sep. Purif. Technol., 80 (2011) 315-322.
[25] J. Mericq, S. Laborie, C. Cabassud, Vacuum membrane distillation of seawater reverse osmosis brines, Water Res., 44 (2010) 5260-5273.
[26] L. Mo, X. Huang, Fouling characteristics and cleaning strategies in a coagulation-microfiltration combination process for water purification Desalination, 159 (2003) 1-9.
[27] A Maskooki, T. Kobayashi, S.A. Mortazavi, A. Maskooki, Effect of low frequencies and mixed wave of ultrasound and EDTA on flux recovery and cleaning of microfiltration membranes, Sep. Purif. Technol., 59 (2008) 67-73.
[28] Y.A. Le Gouellec, M. Elimelech, Calcium sulfate (gypsum) scaling in nanofiltration of agricultural drainage water, J. Membr. Sci., 205 (2002) 279-291.
[29] F. He, J. Gilron, H. Lee, L. Song, K. Sirkar, Potential for scaling by sparingly soluble salts in crossflow DCMD, in, 2008, pp. 68-80.
[30] F He, K.K.Sirkar, J. Gilron, Studies on scaling of membranes in desalination by direct contact membrane distillation: CaCO3 andmixedCaCO3/CaSO4 systems Chem. Eng. Sci., 64 (2009) 1844-1859.
[31] E. Bock, On the solubility of anhydrous calcium sulphate and of gypsum in concentrated solutions of sodium chloride at 25 °C, 30 °C, 40 °C, and 50 °C, Canadian J. Chemistry, 39 (9) (1961) 1746-1751.
[32] D. Lisitsin, D. Hasson, R. Semiat, Critical flux detection in a silica scaling RO system, Desalination, 186 (2005) 311-318.
[33] W. Den, C. Wang, Removal of silica from brackish water by electrocoagulation pretreatment to prevent fouling of reverse osmosis membranes, Sep. Purif. Technol., 59 (2008) 318-325.
[34] T. Koo, Y.J. Lee, R. Sheikholeslami, Silica fouling and cleaning of reverse osmosis membranes Desalination, 139 (2001) 43-56.
[35] G. Braun, W. Hater, C. zum Kolk, C. Dupoiron, T. Harrer, T. Götz, Investigations of silica scaling on reverse osmosis membranes, Desalination, 250 (2010) 982-984.
[36] R. Sheikholeslami, I.S. Al-Mutaz, S. Tan, S.D. Tan, Some aspects of silica polymerization and fouling and its pretreatment by sodium aluminate, lime and soda ash, Desalination, 150 (2002) 85-92.

[37] S. Kang, K. Choo, Use of submerged microfiltration membranes for glass industry wastewater reclamation: pilot-scale testing and membrane cleaning, Desalination, 189 (2006) 170-180.
[38] T. Tran, S. Gray, B Bolto, T.D. Farmer, T.F. Collings, Ultrasound enhancement of microfiltration performance for natural organic matter removal, Organic Geochemistry, 38 (2007) 1091-1096.
[39] J. Burgess, Metal ions in solution, Halsted Press, New York: Ellis Horwood, 1978.
[40] G. Chen, Y. Lu, W.B. Krantz, R. Wang, A.G. Fane, Optimization of operating conditions for a continuous membrane distillation crystallization process with zero salty water discharge, J. Membr. Sci., 450 (2014) 1-11.
[41] K. W. Lawson, D.R. Lloyd, Review: Membrane distillation, J. Membr. Sci. , 124 (1997) 1-25.
[42] E.M.W. District, Your Water Quality Consumer Confidence Report for 2004 http://www.emwd.org/modules/showdocument.aspx?documentid=1125, in, 2005.
[43] F.T. Mackenzie, "Hydrosphere." Encyclopaedia Britannica Encyclopaedia Britannica Online Academic Edition ed., Encyclopaedia Britannica Inc., 2014.
[44] T.Y. Cath, V.D. Adams, A.E. Childress, Experimental study of desalination using direct contact membrane distillation: a new approach to flux enhancement, J. Membr.Sci., 228 (2004) 5-16.
[45] J. A. Ruskowitz, A.E. Childress, Salt-Gradient Solar Pond and Membrane Distillation System for Water Desalination Powered by Renewable Energy, in: Thesis, University of Nevada, Reno, Reno, Nevada, 2012.
[46] E. Repo, T.A. Kurniawan, J.K. Warchol, M.E.T. Sillanpää, Removal of Co(II) and Ni(II) ions from contaminated water using silica gel functionalized with EDTA and/or DTPA as chelating agents, J. Hazard. Mater., 171 (2009) 1071-1080.
[47] J. Ge, Y. Peng, Z. Li, P. Chen, S. Wang, Membrane fouling and wetting in a DCMD process for RO brine concentration, Desalination, 344 (2014) 97-107.

Advanced Heat/Mass Exchanger Technology for Geothermal and Renewable Energy Systems

Project 3 Final report: Enhanced Single Phase Heat Transfer in Intermittently-Grooved Channels

M. Greiner
Mechanical Engineering Department
University of Nevada, Reno

775-784-4873

greiner@unr.edu

December 2014

Project 3 Enhanced Single Phase Heat Transfer in Intermittently-Grooved Channels

M. Greiner

Introduction

Direct dry-cooled condensers used in geothermal power plants (and numerous other industrial heat exchangers) are cooled by air. Blowers are used to force air though passages that are brazed to the outer surface of tubes carrying the fluid that is being condensed. The low thermal conductivity, specific heat and density of the air inhibit its ability to remove heat from the passage walls, as compared to water. As a result, the air-side of these heat exchangers can limit the overall performance of power plants.

Earlier experimental and computational research shows that forming transverse grooves into passage walls triggers flow instabilities that lead to three-dimensional mixing, even at flow rates and Reynolds numbers (Re) associated with laminar flow. At a given Reynolds number this mixing enhances heat transfer compared to a flat passage, but also increases drag. For a given blower power, the flow rate is lower in a grooved channel than in a flat-walled passage, but the heat transfer is higher. These studies were conducted for *fully-developed* flows that are far from the channel entrance. Moreover, the comparisons were made with a flat passage whose wall-to-wall spacing is the same as the *minimum* spacing in a grooved passage. The computational fluid dynamics (CFD) simulations were conducted using the spectral element method because it is less diffusive than methods used in commercial CFD simulation packages. This work also shows that for moderately high Reynolds numbers, three-dimensional simulations were required for agreement with measured data.

These results suggest that forming grooves into the air passages walls of direct dry cooled condensers has the potential to increase the condenser performance and/or reduce its size. Moreover, three-dimensional spectral element simulations have the ability to accurately predict flow performance in these highly unsteady flows.

Earlier experimental and computational results also show that heat transfer in a flat passage downstream from a grooved channel remains high for a significant distance, but the drag drops back to the flat passage level in a much shorter distance. This suggests that *intermittently*-grooved passages, in which grooved sections are separated by flat regions, may offer even higher levels of heat transfer augmentation than continuously-grooved passages.

Project objective

In our original proposal we planned to quantify the performance of *fully-developed* intermittently grooved passages using simulations, and experimentally benchmark the results in a limited number of channel configurations. However, during the course of this work we have become aware that the air passage length in direct dry cooled condensers is of the order of 100 times the wall center-to-center spacing, and the wall thickness is of the order of 20% of the wall-to-wall spacing. This indicates to us that *developing* flow is important in these passages, and the flow experiences significant acceleration at the channel entrance (due to the wall thickness and shape) and deceleration at its exit. Moreover, these devices use arrays of parallel passages and the interaction of the entrance and exit region of neighboring grooved passages must be examined.

We have therefore changed the focus of this work to quantify the performance of finite-length continuously-grooved passage arrays, including the accelerating and decelerating flows entering and exiting arrays of parallel passages, and the development regions within the passages. The performance of grooved channel arrays will be compared to that of flat passage arrays with the same mean wall center-to-center spacing.

Period of Performance

September 20, 2010 – September 17, 2014

Personnel

The Principal Investigator, Professor Miles Greiner, has performed experimental and computational research on grooved channel heat transfer augmentation since 1984, and supervises all aspects of this work. Dr. Aleksandr Obabko from Argonne National Laboratories provides technical support for the Nek5000 spectral-element computational fluid dynamics (CFD) code, which is being used to simulate grooved channel flow and heat transfer. Dr. Paul Fischer, who is the creator of the Nek5000 spectral element computational fluid dynamics code, originally planned to collaborate on this work has had to withdraw due to personal reasons.

Graduate Research Assistant John Akerley was a master's degree candidate who performed CFD simulations for this project beginning in September 2010. He received financial support as a recipient of a University of Nevada, Reno Fellowship for Materials and Thermal Science for Nuclear Power, and so was not financially supported by the current project. Mr. Akerley performed an internship at Argonne working directly with Dr. Obabko during summer of 2011. Mr. Akerley completed all course work and research required for his MS degree, and defended his MS theses in August 2012. He is currently working at Ormat Technologies, Inc. (http://www.ormat.com/), in Reno, Nevada as a Resource Engineer, working on computational studies geothermal power plants.

Graduate Research Assistant Austin Thibault began constructing an experimental grooved channel test facility in June 2011 with support from the current grant. He completed all course work and research required for his MS degree, and defended his MS theses in December 2013. Mr. Thibault was hired for the month of January 2014 to design and acquire materials to make some modification on the apparatus to better quantify heat losses. He is currently working at Naval Air Systems Command (NAVAIR) as a mechanical engineer in the Engineer/Scientist Development Program, which is the company's developmental program for recent graduates.

Postdoctoral research associate, Dr. Mustafa Hadj-Nacer, began working on the project part time in January 2014, and received training from Mr. Thibault to become familiar with the experimental apparatus, and its operation.

Two undergraduate students, Mr. Blake McCoy and Mr. Joshua McGuire, were hired in May 2014 to work with Dr. Hadj-Nacer on the construction of the heat flux gages and guard heaters and performed preliminary experiment tests. The appointment of Mr. McCoy and Mr. McGuire ended on August, 2014. Dr. Hadj Nacer continued troubleshooting the experimental apparatus.

Publications Stemming From This Work

Akerley, J., Obabko, A., Fischer, P., and Greiner, M., 2012, "Flow Destabilization and Heat Transfer Augmentation in an Array of Grooved passages with Developing Flow," HT2012-58528, to appear in the Proceeding of the ASME 2012 Summer Heat Transfer Conference, HT2012, July 8-12, 2012, Rio Grande, Puerto Rico

Akerley, J., 2012, "Flow Destabilization and Heat Transfer Augmentation in an Array of Grooved Passages with Developing Flow," MS Thesis, Mechanical Engineering Department, University of Nevada, Reno.

Thibault, A., 2013, "Design, Construction, and Qualification of an Open Loop Wind Tunnel Facility to Quantify Enhanced Heat Transfer/Pumping Power Performance in Isothermal Rectangular-Cross Section Passages," MS Thesis, Mechanical Engineering Department, University of Nevada, Reno.

Summary of Work

1. Tasks 3.1 and 3.2 Numerical Simulation

In the past, a number of researchers have considered passage configurations that enhance mixing and heat transfer by triggering flow instabilities. Transversely grooved channels, passages with eddy promoters, and communicating channels all contain features whose sizes are roughly half the channel wall to wall spacing. These structures excite normally damped Tollmien-Schlichting waves at moderately low Reynolds numbers.

The Principal Investigator has presented a series of studies on flow destabilization in rectangular cross section channels with transverse grooves cut into the walls. Visualizations in a range of passage geometry show that the critical Reynolds number Re_c where two-dimensional waves first appear decreases as the spacing between grooves decreased. For a sawtooth-shaped wall with no spacing between grooves, two-dimensional waves first appear in a fully-developed flow at $Re_c = 350$, followed by a rapid transition to three-dimensional mixing.

These previous numerical and experimental investigations using air in a fully-developed flow show that both the Nusselt number and friction factor are greater than the corresponding values for a flat channel with the same minimum wall to wall spacing. Three-dimensional numerical simulations for $Re \le 2000$ give results that are in good agreement with experimental measurements. Furthermore, two-dimensional simulations were inadequate of capturing the transport processes in these configurations for Reynolds numbers greater than $Re = 570$.

The current work is a numerical investigation of heat and momentum transport in an array of finite-length continuously grooved passages with developing flow. Although these simulations use a two-dimensional domain, the results will be used as an initial condition for the three-dimensional simulations.

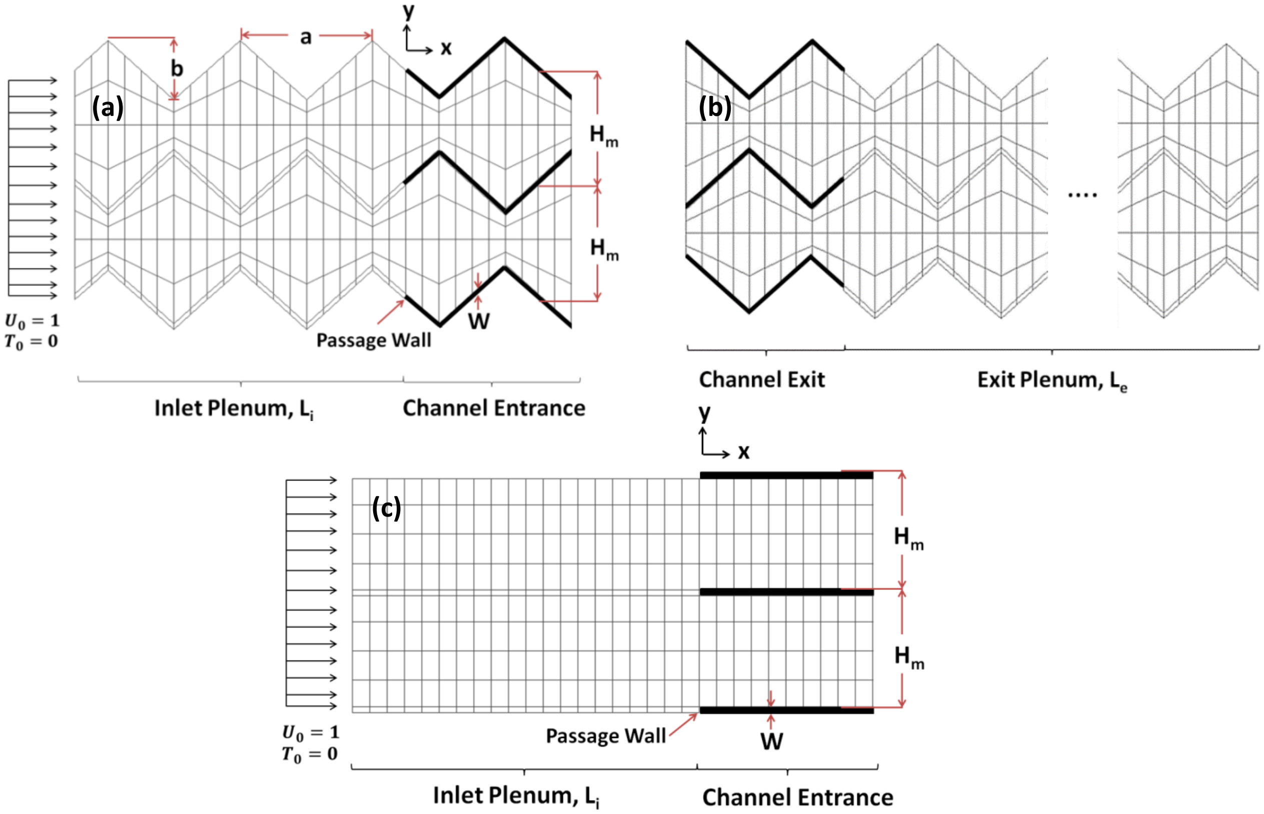

Figure 1.1: (a) Inlet plenum and channel entrance. (b) Channel exit and exit plenum computational regions for grooved channels. (c) Inlet plenum and channel entrance computational region for a flat channel. The spacing between the centers of the walls is the same as mean center-to-center spacing used for the grooved passage.

Two-Dimensional Simulations

Array Model

Computational Domain. Figure 1.1 shows the two-dimensional spectral element mesh used in the current work to study an array of grooved passages. Figure 1.1a shows the inlet plenum with channel entrance on the left, a pair of grooved channels (one above the other and each containing thirty grooves on each wall). Figure 1.1b shows the channel exit with exit plenum on the right. Figure 1.1c shows the inlet plenum with channel entrance for flat passages. In Figs. 1.1a and 1.1b the groove depth normal the flow direction is b, length in the flow direction is a, the wall thickness normal to the flow direction is w, the mean center-to-center wall spacing is H_m, and the minimum wall-to-wall spacing within the grooved channel is $H_{min} = 0.77$. The dimensionless geometric parameters are $a/b = 2$, $a/H_m = 0.925$, $b/H_m = 0.465$, $a/H_{min} = 2.4$, and $w/H_m = 0.150$. Previous studies have shown that the ratio $a/H_{min} = 2.4$ is compatible with the most slowly decaying Tollmien-Schlichting wave. The length of the inlet plenum, channel, and exit plenum are, respectively, $L_i = 2.5a$, $L = 30a$, and $L_e = 25a$. There are 32 spectral elements in each groove length.

Air with a Prandtl number of 0.7 enters the left side of the entrance plenum with a uniform dimensionless axial speed of $U_0 = 1$ and dimensionless temperature of $T_0 = 0$. Periodic boundary conditions are applied to the top and bottom edges of the inlet plenum to model an infinite number of channels stacked above and below the computational domain (the zigzag shape of the plenum boundaries are used for convenience, but flat boundaries would be equivalent).

Figure 1.1a shows the fluid entering the inlet plenum. The x-axis is parallel to the flow direction, and its origin is at the channel array entrance. The y-axis is also shown. Due to the passage walls, the cross section available for flow within the channels is smaller than that in the plenum. The upper passage begins in a converging portion of a groove while the lower one starts with a diverging section. The passages are an integer number of grooves lengths long (30), so Fig. 1.1b shows the upper passage ending in a converging section, while the lower ends with a diverging section. In this work the walls are modeled using no slip conditions and a uniform dimensionless temperature of $T_W = 1$. The flow enters the exit plenum from the channel array and exits the domain using outflow boundary conditions in the last vertical layer of elements. The upper and lower edges of the exit plenum are also modeled using periodic boundary conditions to model an infinite array of channels stacked on top of each other. The exit plenum is long to allow the unsteady flow exiting from the grooved channel to decay to a steady flow before it exits the domain. This allows the pressure recovery that takes place as the air decelerates (diffuses) outside the channel array to be calculated.

Figure 1.1c shows inlet plenum region of a flat passage array used as a comparison to the grooved channel. The center-to-center wall spacing of these channels H_m is the same as the mean spacing of the grooved passage. The wall thickness in the direction normal to the flow direction w, is also the same. The volume of the walls for the two configurations is also the same.

Spectral Element Method. In the spectral element method, the velocity, data, and geometry are expressed as tensor-product polynomials of degree N in each of K quadrilateral spectral element, corresponding to a total grid point count of roughly KN^2. Numerical convergence is achieved by increasing the spectral order N. The present calculations were carried out at a base resolution of K = 4120, N = 8 (Fig. 1.1 shows some spectral elements but not the KN^2 grid points). Resolution tests were performed for Re = 1000 and Re = 3000 at N = 8 and N = 12. The present simulations use consistent approximation spaces for velocity and pressure, with pressure represented as polynomials of degree N-2. The momentum equations are advanced by first computing the convection term, followed by a linear Stokes solve for the viscous and pressure terms. The decoupling allows for convective Courant numbers greater than unity while maintaining second-order accuracy in time.

Results

In this work we define the hydraulic diameter as

$$D_H = \frac{4\,VOL}{A_p} = \frac{4LM(2H_m)}{4LM} = 2H_m$$

In this expression, VOL is the passage volume, and A_P is the projected wetted parameter, and M is the length of the domain in the direction normal to the plane (x,y). Reynolds number is defined as:

$$Re = \frac{u_0(2H_m)}{v} = \frac{2}{v}\int_B^T u\,dy$$

In this expression, ν is the fluid kinematic viscosity and u is the axial component of the velocity. The integration is performed at a given x-location, from the bottom (B) to the top (T) of the domain. Since the flow is steady and incompressible the integral is the same at all axial locations x and times t.

Figure 1.2 shows contour plots fluid vorticity that are intended to help visualize the flow field. Figure 1.2a shows the entire computational domain for a flat passage array at Re = 3000. Figures 1.2b and c show a blow up focusing on the grooved channel arrays at Re = 1000 and 3000, respectively. Each contour is at an instant in time after the simulation has reached steady state conditions. In the flat passages the vorticity contours are essentially parallel with the walls for all Reynolds numbers, indicating the flow is essentially parallel to the walls and is steady (the current two-dimensional simulations are not capable of modeling the three-dimensional instabilities that lead to turbulent flow in flat passages at Re > 2300). Figure 1.2b shows that at Re = 1000, unsteadiness appears near the end of the grooved channels, roughly 24 groove lengths from the entrance in the upper channel and 26 groove lengths from the entrance in the lower channel. Figure 1.2c shows that at Re = 3000, unsteadiness appears near the channel entrance, roughly 2 groove lengths from the entrance in the upper channel and 3 groove lengths from the entrance in the lower channel. Arrows indicate these locations in Figures 1.2b and c. This onset location of oscillatory flow is generally different for all Reynolds numbers and moves upstream with an increase in Reynolds number.

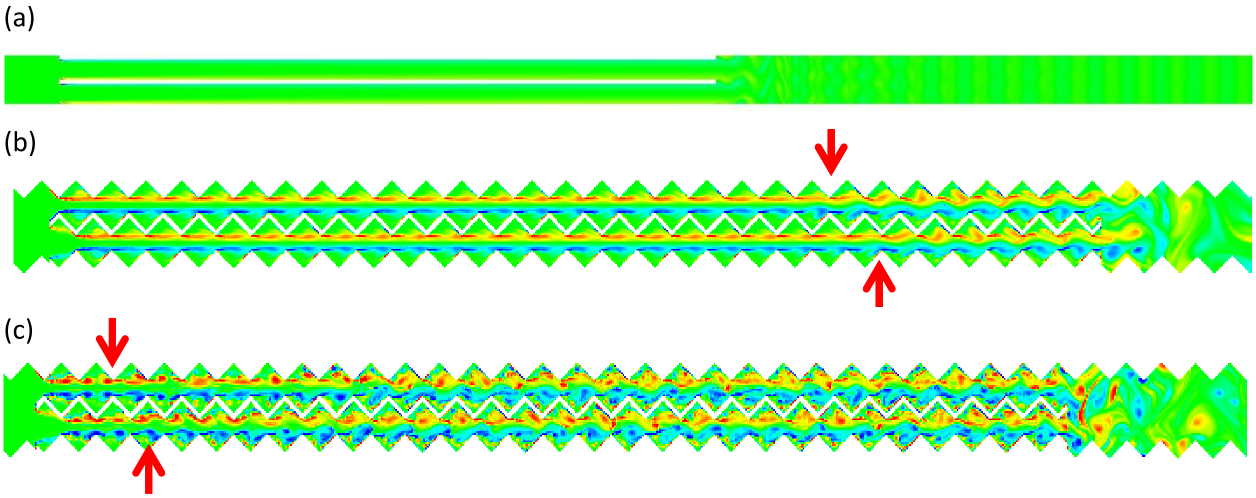

Figure 1.2: Flow vorticity visualizations for (a) full domain flat passage at Re=3000, (b) channel array at Re=1000, and (c) channel array at Re=3000. Arrows point to the observed onset location of oscillatory flow.

Figure 1.3 shows the observed onset location of oscillatory flow versus x/D_h for the simulations. For a comparison, the onset location determined from experimental flow visualization data from a passage with one grooved and one flat wall are included [Greiner et al., 1990]. These onset locations are highly qualitative and were determined based on observed changes in the data. The diamond marker indicates the observed onset location for oscillatory flow based on the current vorticity plots. Bars are included to indicate the difference in onset location between the upper and lower channels. Only the simulation at Re = 2200 had the same axial onset location for the upper and lower channels. The onset location moves upstream with an increase in Reynolds number. These results agree with experimental data at Re =1000. That data also shows the onset location moves upstream with increasing Reynolds numbers. However, for Re > 1000 the experimental onset locations are further upstream than those from the current simulations. This may be due to the inadequacy of two-dimensional simulations at relatively high Reynolds numbers.

In this work we defined the average Nusselt number (dimensionless average heat transfer coefficient h_x) for a region between the inlet of a channel array and an axial location x as

$$Nu_x = \frac{h_x x}{k} = \frac{\bar{Q}(x)}{A_{px}(T_w - T_0)}\frac{x}{k} = \frac{\rho c_p M \int_B^T (\overline{uT})_x \, dy}{4Mx(T_w - T_0)}\frac{x}{k}$$

$$= \frac{\int_B^T (\overline{uT})_x dy}{4\alpha}$$

The over bar $\overline{}$ denotes an average over time after the system has reached steady state, and the subscript $()_x$ indicates a value at the axial location x. In this definition, $\bar{Q}$(x) is the total heat transfer from all walls to the fluid between the entrance to location x, A_{Px} = 4xM is the total *projected* surface area for both sides of the two walls from the entrance to x, and the temperature difference between the inlet gas and uniform temperature walls is $T_w - T_0 = 1 - 0 = 1$. The fluid specific heat, density, thermal conductivity and thermal diffusivity are, respectively, c_P, ρ, k and $\alpha = k/\rho\, c_P$.

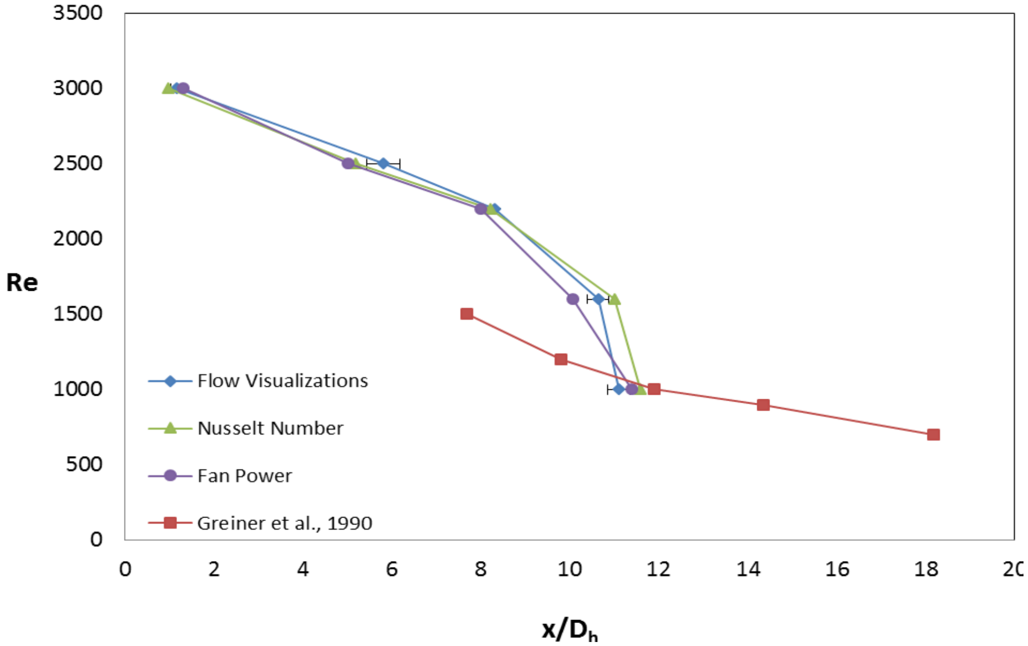

Figure 1.3: Observed onset location of oscillatory flow. Observations from flow visualizations, Nusselt number plots, and fan power plots are compared to experimental data from Greiner et al 1990. Bars are shown for the flow visualizations indicating the different onset location in the upper and lower channels.

The full channel average Nusselt number, Nu_L is the value of Nu_X at N_G = 30, and it characterizes the total heat transfer to the gas. Figure 1.4 shows Nu_L versus Reynolds number for both the grooved, $Nu_{L,G}$, and flat passages, $Nu_{L,F}$, versus Reynolds number. The heat transfer enhancement for a grooved array over a flat array increases with Reynolds number from approximately a 42% increase at Re = 1000 to approximately a 175% increase at Re = 3000. The surface area of the grooved channel is $\sqrt{2}$ times larger than that of the flat passage. The dashed line marked $\sqrt{2}$ $Nu_{L,F}$ shows the level of enhanced heat transfer that would be expected due to the area increase alone. We see that most all of the enhancement is due to area increase at Re = 1000, and this is consistent with the onset of unsteady flow being near the channel exit at that Reynolds number (Fig. 1.2a). This shows that enhancement due to instabilities increases for Reynolds numbers greater than 1000.

The dimensionless flow work or power required to accelerate the gas or move it against drag in the channel from its entrance at x = 0 to another x-location is

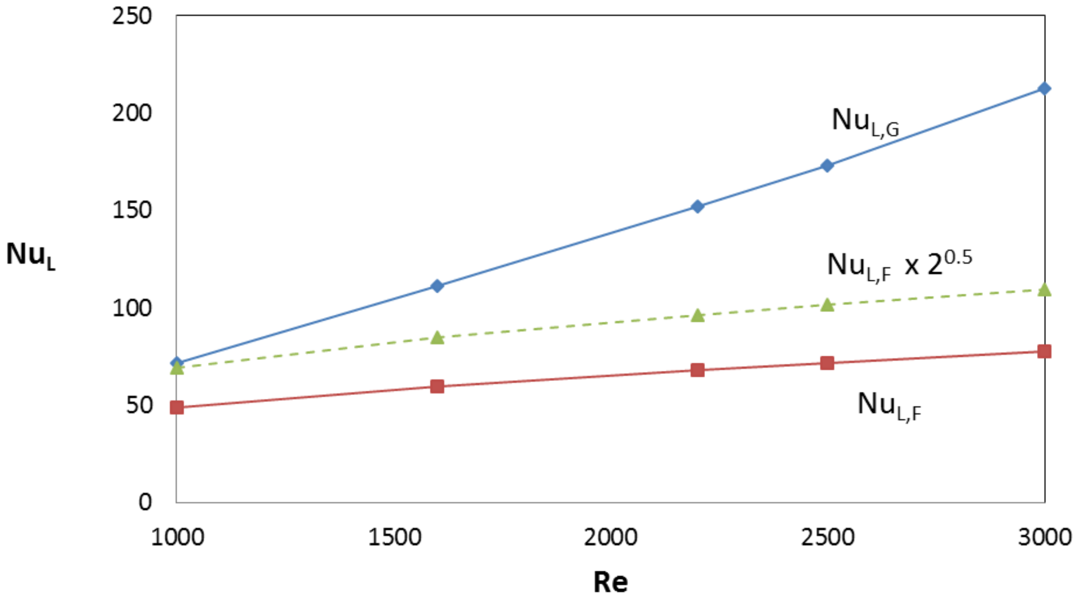

Figure 1.4: Average full channel Nusselt number at NG = 50 versus Reynolds number for grooved and flat passages.

$$\Phi_x = \frac{1}{\rho u_0^2 v}\left[\int_B^T (\overline{uP})_{x=0} dy - \int_B^T (\overline{uP})_x dy\right]$$

In this expression P is the pressure. This quantity acts as a velocity weighted average pressure drop between pressure at x = 0 and the pressure at an axial location x.

Figure 1.5 shows the non-dimensional fan power versus N_G for Re = 1000, 1600, 2200, 2500 and 3000 for both grooved and flat passages (on the scale of this plot the flat passage fan powers are very close to each other and only the ones for Re = 1000 and 3000 are marked). For all locations and Reynolds numbers the grooved passage flows require significantly higher fan power than in the flat channel. For the groove array at Re = 3000, the fan power exhibits a sharp increase at the channel entrance where the flow accelerates into the channel array. This acceleration is caused by blockage from the grooved wall thickness and shape. The air must accelerate around this blockage as it enters the passage. Some of the pressure is recovered in the first few grooves as the velocity field becomes established. Further downstream the fan power continues to increase due to drag within the channels. The fan power within the channel array oscillates as the flow accelerates and decelerates in the converging and diverging sections of the channel. The fan power decreases as the flow decelerates into the exit plenum where the pressure increases. The fan power and pressure reach their final values at roughly N_G = 45, which is 15 groove lengths downstream of the channel exit.

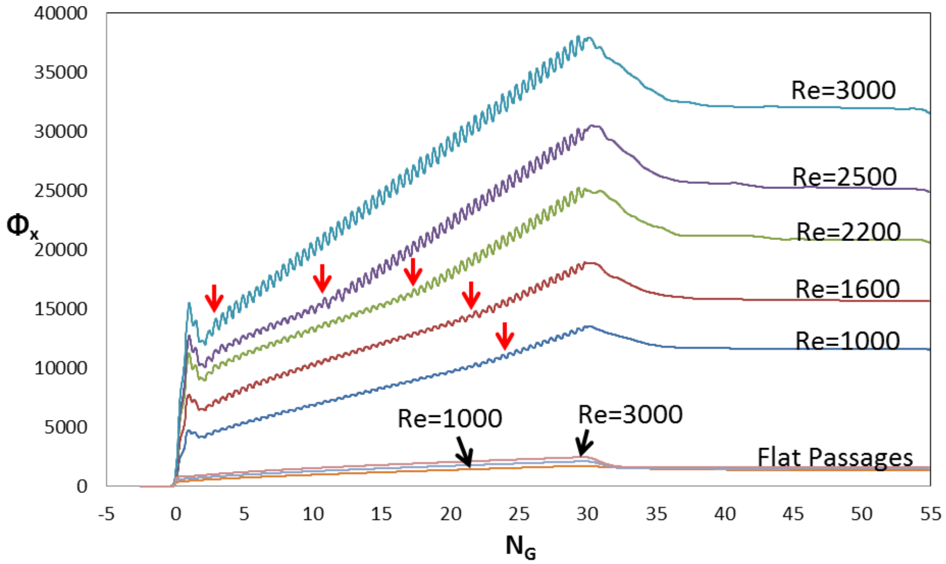

Figure 1.5: Non-dimensional fan power versus groove number for Re=1000, 1600, 2200, 2500 and 3000 for both grooved and flat passages. Arrows on the grooved wall plots point to observed onset location of oscillatory flow. The arrows on the flat passage plots indicate the Reynolds number.

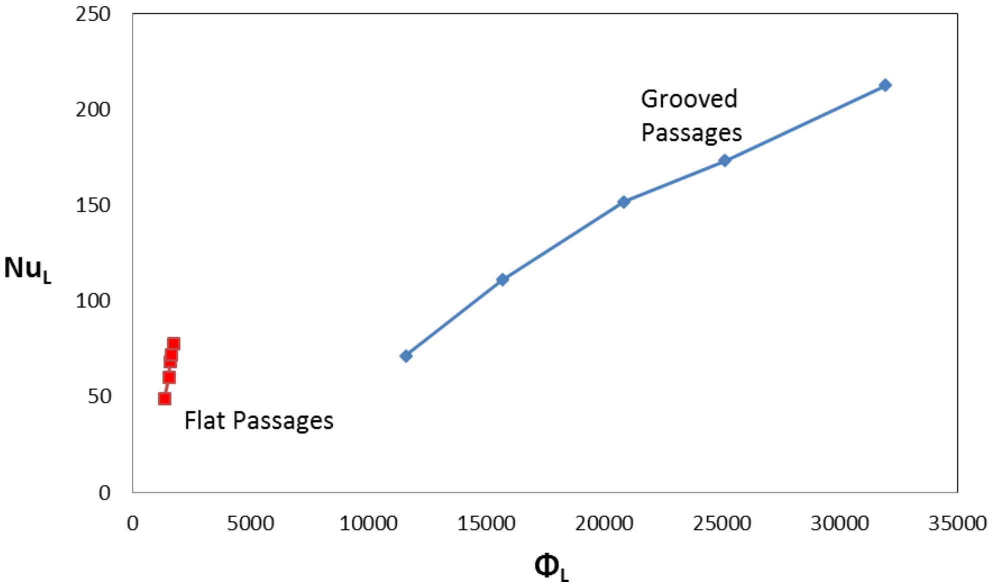

Figure 1.6: Full channel average Nusselt number versus non-dimensional fan power for both grooved and flat passage channels. The values are taken at an x-location near the end of the exit plenum.

Figure 1.6 shows Nu_L versus Φ_L for both grooved and flat passage arrays at Re = 1000, 1600, 2200, 2500 and 3000. Heat transfer augmentation can be achieved using grooved passage arrays but only with a significant increase in the required fan power. At lower Reynolds numbers, the fan power exhibits a similar behavior with a sharp increase at the channel entrance, small recovery, increase due to drag within the channel array, and decrease in the exit plenum. However, at the lower Reynolds numbers the amplitude of the oscillations and its slope are small in a region near the inlet. Further downstream the amplitude and slope both increase significantly. This location is marked by an arrow for each Reynolds number and these locations are shown as Fan Power data points in Figure 1.3 (circles). These locations move upstream with an increase in Reynolds number and are in good agreement with the locations of the onset of flow unsteadiness and location where the Nusselt number exhibits a change in curvature. This suggests that the increase in amplitude and slope are caused by the onset of unsteady flow. The flat passage fan power curves in Fig. 1.5 exhibit a slight increase in the flat passage arrays, and a slight decrease at the exit. These changes are much smaller than those of the grooved channels because the flat passage blockage is much smaller. Fan power is significantly greater in the grooved passage arrays than in the flat passage arrays.

Summary

The addition of transverse grooves to the parallel passage arrays introduces unsteadiness a number of grooves downstream of the channel entrance. This onset location moves closer to the channel entrance as the Reynolds number increases. The unsteadiness improves the overall heat transfer compared to a flat passage array of equal mean channel height by a factor of 1.42 at Re = 1000 and a factor of 2.75 at Re = 3000. The grooves also cause an increase in the required fan power by a factor of 8.6 at Re = 1000 and a factor of 18 at Re = 3000. However, these two-dimensional results may not adequately capture the entire instability and mixing structures that have been seen in three-dimensional simulations and experiments. These results will be used as an initial condition for the three-dimensional simulations.

Single Channel Model

Due to the large size of the two-dimensional model array model, it was determined that a smaller domain should be used to analyze developing flow in a passage with transverse surface grooves in three dimensions. However, prior to building a three-dimensional, single channel mesh, a two-dimensional, single channel mesh was designed to be compared with the two-dimensional array models. Figure 1.7 shows the two-dimensional, single channel mesh that was used as a comparison to the array model. Flow with a Prandtl number of 0.7 (air) enters the left side of a shorter inlet plenum L_I = 0.6a and then encounters a single grooved channel. The channel entrance height is the maximum flow area, H_M+2b, so that periodic boundary conditions could be applied to the upper and lower edges of the inlet and exit regions. The channel has a finite wall thickness, w, that is still $0.15H_A$. The length of the channel is L = 30a and the dimensionless groups defining the groove dimensions (length a and depth b) are the same as with the array model. Because there are an integer number of grooves, the channel begins with a converging section and ends with a diverging section. The flow exits the channel into an exit region (L_E=14.8x_G) where flow unsteadiness decays to steady flow before exiting the domain using the same special outflow conditions as was used in the array model. There are 896 elements in the single channel model as compared to the 4120 in the array model. The polynomial degree for the spectral element method is N = 7.

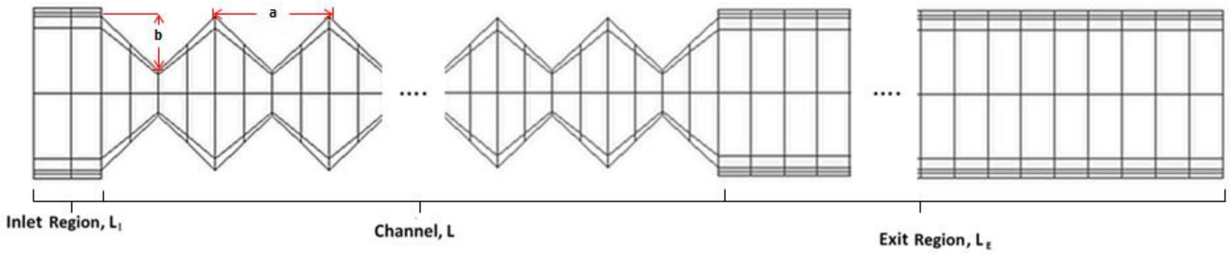

Figure 1.7: Two-dimensional, single channel mesh.

The two-dimensional, single channel model was investigated at Re=1000, 1600, 2200, 2500 and 3000. Once the simulations had reached steady-state conditions, the average Nusselt number and dimensionless Fan Power were calculated and compared with the two-dimensional array results. Figure 1.8 shows the total average Nusselt number (average Nusselt number at channel exit) versus time. Once the lowest Reynolds number (1000) reaches steady-state conditions, the final result is used as an initial condition for the subsequent Reynolds number. This method is used achieve results in shorter wall-clock time.

The average Nusselt number is calculated in a similar method as with the array model. However, since only two heat transfer surfaces are present in the single channel model as opposed to the four heat transfer surfaces in the array model, an adjustment was made to the calculation to reflect this difference. Figure 1.9 shows the average Nusselt number versus groove coordinate comparing the single channel and array channel models for Re=1000.

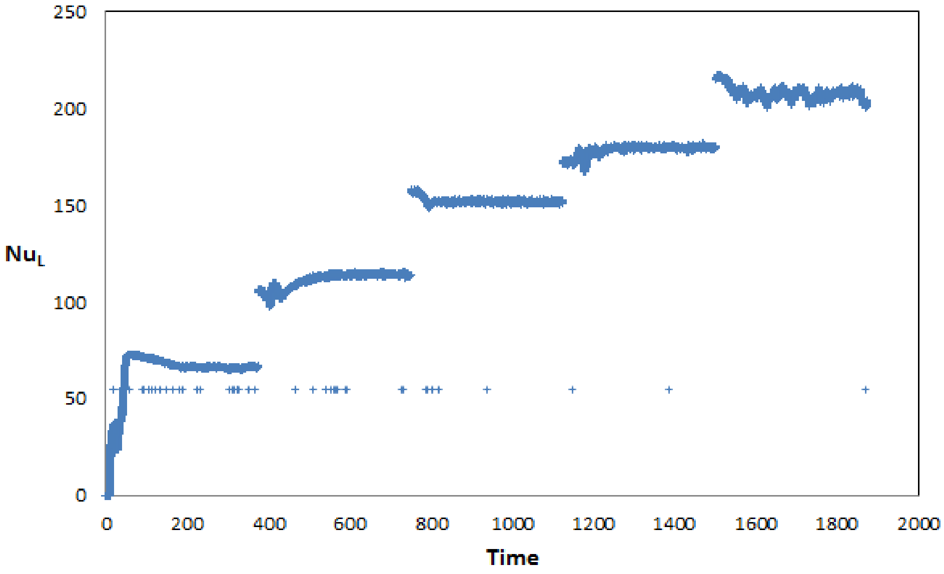

Figure 1.8: Total average Nusselt number versus time.

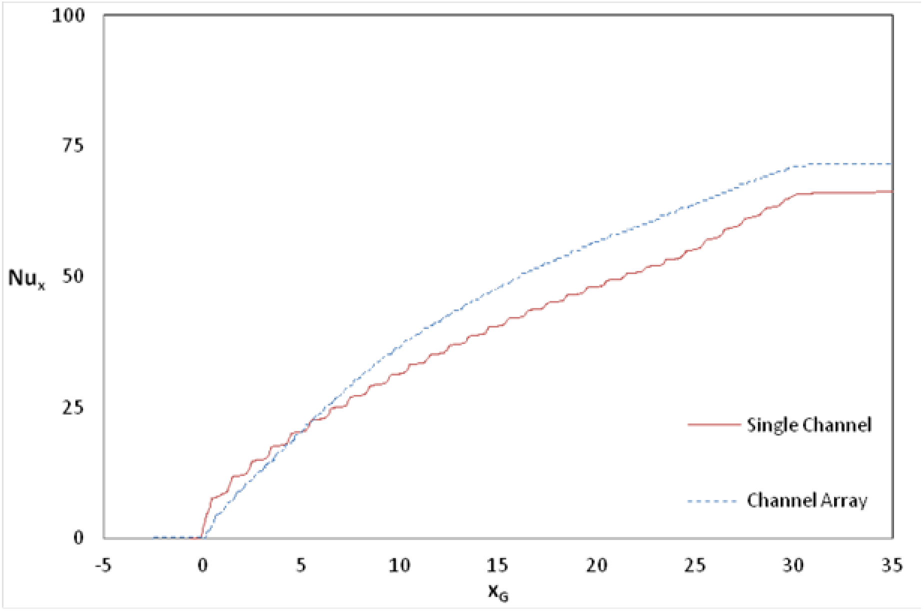

Figure 1.9: Average Nusselt number array and single channel comparison Re = 1000.

Figure 1.9 shows that the average Nusselt number in the single channel is greater at the channel inlet, and this is typical for all Reynolds numbers investigated. This is likely due to the greater surface area at the channel inlet in the single channel, which contains a full converging section rather than a half converging section in the array model. The average Nusselt number exhibits a similar behavior in the single channel as in the array model. However, the change in curvature that was pointed out in previous reports for the array models is more pronounced in these single channel results. Although the results are not identical, the difference was expected due to the slight difference in passage geometry. The percent difference between the results can be seen in Table 1.1.

Table 1.1: Single channel and channel array average Nusselt number percent difference

Re	Percent Difference
1000	8.01%
1600	2.27%
2200	0.93%
2500	3.48%
3000	2.12%

The percent difference was calculated at x_G=30, or at the total average Nusselt number. The differences are small enough that this model can be used a basis for the three-dimensional simulations.

The dimensionless fan power results from the single grooved channel model were also compared with the results from the grooved channel array model. The dimensionless fan power is calculated in the same method as with the array model. Figure 1.10 shows the dimensionless fan power versus groove coordinate comparing the single channel and array channel models at Re=1000. The plot contains the single channel result (red), the channel array result (blue), and one half the channel array result (dashed blue). The channel array result is multiplied by one half to reflect the reduction in the number of passages from two to one.

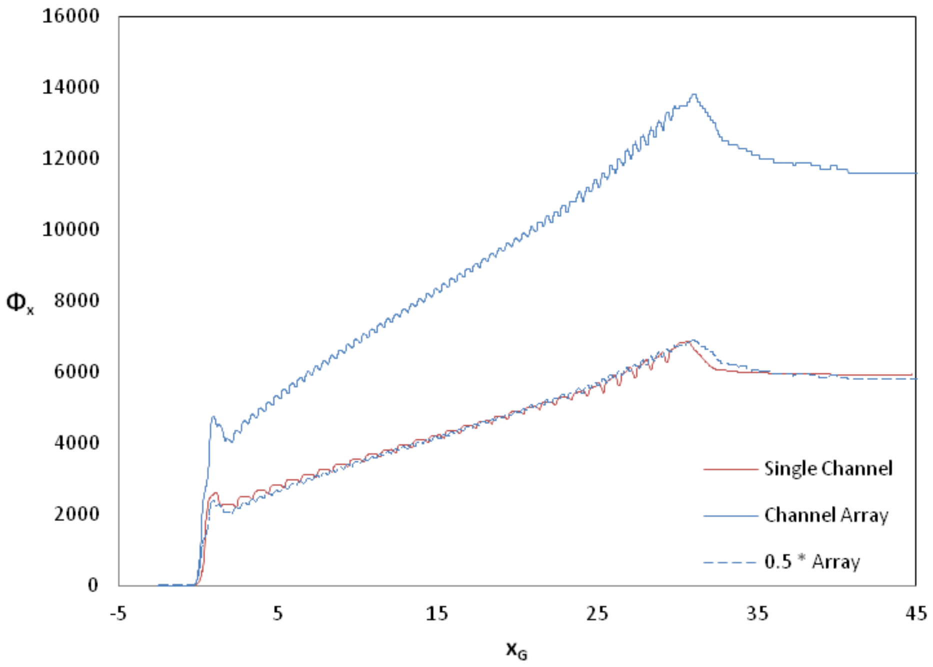

Figure 1.10: Non-dimensional fan power array and single channel comparison Re = 1000.

As expected, the non-dimensional fan power result from the grooved channel array is roughly twice that of the single channel model at each Reynolds number investigated. However, the single channel result is consistently greater than half the channel array results for each Reynolds number. Table 1.2 shows the percent difference between the single channel full channel non-dimensional fan power (evaluated at x_G=45) and channel array full channel non-dimensional fan power.

Table 1.2: Single channel and channel array non-dimensional fan power percent difference

Re	Percent Difference
1000	2.17%
1600	18.82%
2200	13.74%
2500	15.69%
3000	8.45%

The percent difference for the total non-dimensional fan power is generally greater than for the total average Nusselt number. This indicates that the added effect of multiple channels could play a role in the pressure recovery in the exit region.

Three-Dimensional Simulations

A three-dimensional spectral element mesh used to study the three-dimensional instabilities that were seen in previous experiments was constructed using the two-dimensional, single channel mesh shown in Figure 1.7. Using a Nek5000 program, the mesh was extruded in the z-direction using six equal elements in that span-wise direction. Periodic boundary conditions were also applied in the z-direction. Figure 1.11 shows an isometric view of the three-dimensional, single channel model.

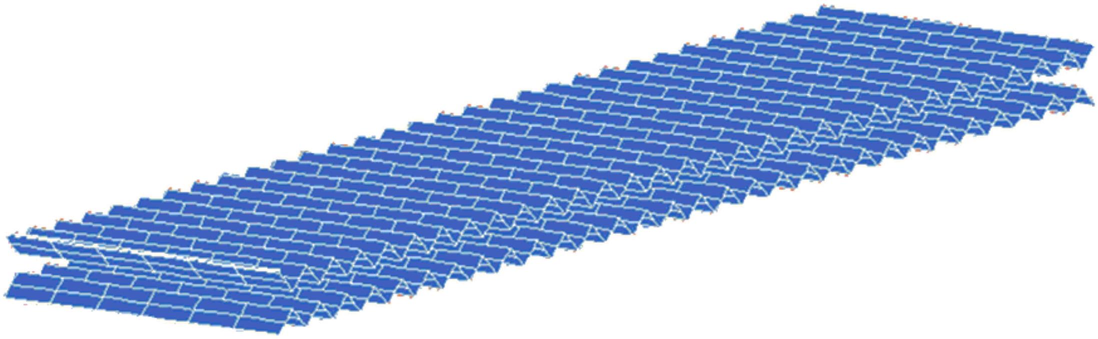

Figure 1.11 Isometric view of three-dimensional, single channel mesh boundary.

This figure only shows the upper and lower boundaries of the three-dimensional computational domain so that the domain is easier to see. Figure 1.11 shows the six equally-spaced elements in the span-wise direction. Furthermore, the exit region that can be seen in Figure 1.7 was removed from the three-dimensional domain due to the inconsistencies in fan power results for the single channel and to speed up the computational time. Fluid with a Prandtl number of 0.7 enters an inlet region from the left side of the domain with a uniform, non-dimensional temperature and velocity. The length of the inlet region is still 0.6a. Like the single channel model in Figure 1.7, the three-dimensional model has thirty grooves with the upper and lower walls modeled using no-slip boundary conditions and a constant wall temperature. The fluid exits the channel (and the domain) using the same special outflow boundary condition that was used in both the channel array model and the two-dimensional single channel model.

The collaboration with Dr. Paul Fischer ended on the second year of the project, therefore, the three-dimensional simulations were not completed.

2. Task 3.3 Design and Construction of Experimental Heat Transfer Facility

Objective

The objective of this work is to measure the heat transfer and pumping power performance in the developing region of a grooved passage for Reynolds numbers between 400 and 4000. The grooved passage is designed to trigger two-dimensional Tollmein-Schliching waves at Reynolds numbers as low as 350, which become three-dimensional when the Reynolds number exceeds 750. Earlier experimental and computational work has shown that triggering these instabilities increases the heat transfer in fully-developed grooved passages for a given pumping power compared to fully-developed flat passages. These experimental results will be compared to computational simulations that use the spectral element technique.

In this work a flat channel test section was constructed and used to acquire preliminary data. The flat passage was used so that the heat transfer and pressure drop data can be compared with correlations in literature, and use to assess the quality of the experimental technique. Once the measurement techniques were assessed, a grooved passage was constructed. The heat transfer and pumping power performance of the grooved passage are compared with flat channel results.

Method

This work is completed in two parts. First, a smooth flat plate channel is constructed and compared to analytical solutions for laminar flow in a flat duct. By comparing experimental data with a known analytical solution, the overall performance of the apparatus is evaluated. Second, a grooved channel apparatus is constructed using similar methods and geometry.

For a plate heat exchanger of this type, there are two parameters which play a factor in the efficiency of the exchanger. The first is the heat transfer (in this case the Nusselt number) and the second is the power required to pump the air through the exchanger. It is the goal of this work to increase the heat transfer in a given passage without increasing the pumping power required by a corresponding amount.

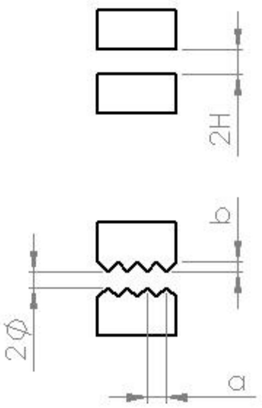

Figure 2.1: A small cross section of the apparatus. The mean wall to wall spacing is given for the flat passage by 2H and for the grooved array by 2φ+b/2.

Experimental Method

The boundary condition most representative of the real world application for a flat plate heat exchanger is the constant wall temperature condition. A large amount of working fluid is consistently flowing into the apparatus, and when this system approaches steady state the walls will all be at the same temperature. So the experiment was designed around having the constant wall temperature condition. The first step of this experiment was to decide on overall dimensions for the apparatus based upon the quantities that needed to be measured. For this design, it was the pressure drop as a function of length that designated the channel size. According to the analytical calculations for pressure in the channel, the pressure difference would not be accurately measureable if the channel became any larger. The corresponding dimensions of the grooved channel were then calculated. To make the channels as similar as possible, it was determined that the mean wall to wall spacing would be the same for each channel. For the flat plate channel this simply corresponds to the distance between plates, but for the grooved experiment this is the averaged distance between plates. Figure 2.1 illustrates the difference.

The ideal mean wall spacing was found to be 0.333 Inch. At this distance, the base of each groove (dimension "a" on figure 2.1) is exactly 0.25 Inches in length. The length of the array was originally intended to be one meter, however since the grooves were .25 inches wide and the heaters (to be discussed later) were exactly one inch wide, it became easier to make the apparatus just over a meter long (40 inches). Lastly, the width of the channel was chosen. Analytically the problem is considered to be two parallel plates without sides, so a large aspect ratio was required to make the experimental results as close as possible to the analytical ones. Based on the selection of the channel height and length, the selection of an economical heater resulted in a width of 9.125 Inches, which provided an aspect ratio of approximately 27. This is sufficiently large to assume infinite parallel plates.

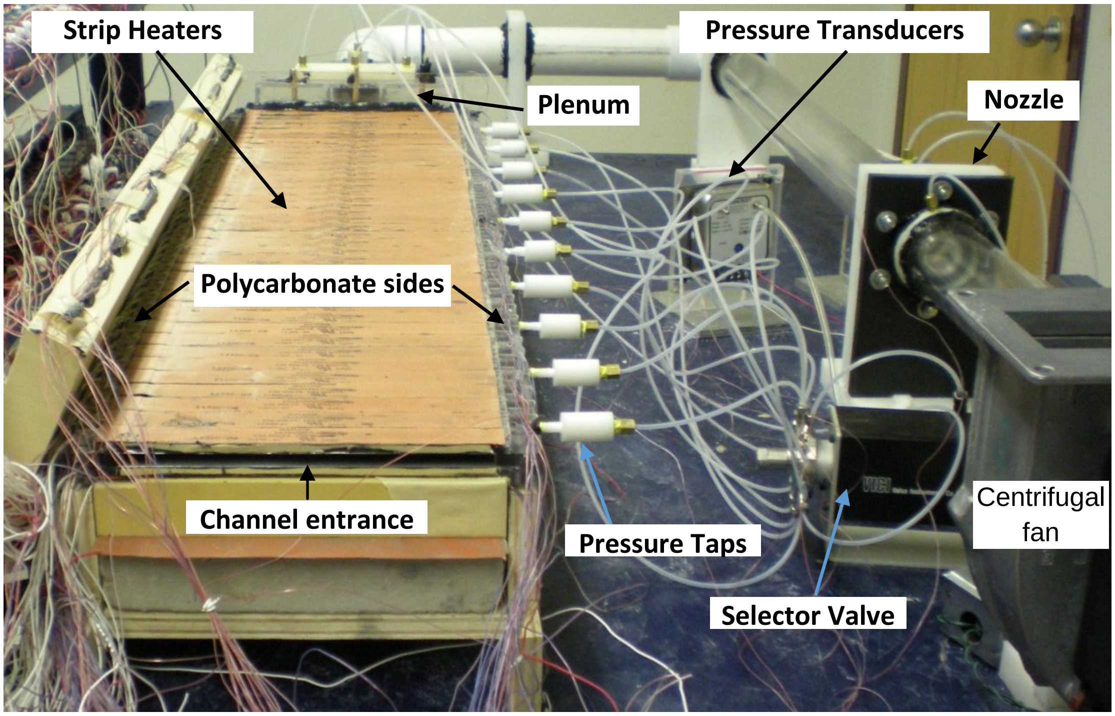

Figure 2.2: Experimental apparatus.

Experimental Apparatus

Figure 2.2 shows a computer rendering of the experimental apparatus. The first and most important part of the experiment is the channel. Initially, the entrance to the channel was exposed directly to the laboratory air, and was kept as a square entry. Due to the design of the channel, the air encountered a square-edge orifice as it flowed into the test section. As a result, the flow separates from the wall and reattaches some distance away from the channel entrance. To overcome this problem, a rounded channel entrance nozzle (not shown) was installed in an effort to reduce flow separation, so that the channel entrance condition is better defined. The channel is constructed to the dimensions specified by the analytical estimations, (0.333 inches x 9.125 inches x 40 inches), the top and bottom plates were made from cast aluminum. The heaters are attached to the aluminum, and the air flow we are interested in flows between the two plates. Several other configurations were considered, such as placing the heaters inside the channel, but were dismissed to keep the flow as uninterrupted as possible. Therefore the chosen material had to be easy to machine so grooves could be cut into it, and it also needed to have a high thermal conductivity so the heat could easily get from the heaters to the air. This is how cast aluminum was chosen. The sides of the channel are made from polycarbonate, which was chosen for its low thermal conductivity and its machinability.

To measure the temperature of the interior surface, thermocouples are pressed into the aluminum on the side exposed to air. This is done by drilling a small hole (slightly less than 1mm) through the plate. The 30 AWG thermocouple wire is then threaded through this hole, soldered, and then pressed back into the hole. The solder bead is kept as small as possible, and when the bead is pressed back into the aluminum, it creates a press fit, holding the weld bead slightly below the surface of the aluminum.

The first concern with this type of fixturing is that the actual bead is not on the surface of the aluminum. It is actually slightly below the surface. However the high conductivity of the metal causes the temperature difference between the actual surface and the location of the weld bead much too small to be accurately measured by a thermocouple. The second concern is the introduction of a third metal to the thermocouple circuit. Thermocouple usage states that it is a temperature difference across the metals that contribute to the voltage signal produced. If the solder bead is too large, then there could theoretically be a temperature difference from one end of the bead to the next, which would throw off the temperature measurement. By making the bead small, and realizing that for steady state the whole junction will be at the same temperature, this no longer becomes a concern.

The Nusselt number as well as the pressure drop are needed as a function of location throughout the experimental apparatus. To calculate the Nusselt number, the temperature difference between the wall and the air had to be known. However, there were no good ways to measure the temperature of the air without interrupting the flow. Therefore the plan is to calculate the bulk air temperature using the mass flow rate and the heat put into the air. The mass flow rate is calculated by knowing the velocity in the channel (to be discussed later) and the heat put into the channel by the heaters. The difficulty here is in maintaining a constant wall temperature. As air flows through the channel and warms up, the temperature difference between the air and the wall will decrease, leading to a decreased heat transfer coefficient as the channel end is approached. This prompted the use of many individual heaters. Ideally, an individual heat flux would be applied at every point along the channel. However there is currently no good way to do this, no heaters that are designed this way. If only one heater was used per plate, an average heat flux would have to be chosen, and it would be grossly inaccurate at the front and rear of the plate. The “resolution” would be very poor. In this work 40 individual heaters are used on each plate to provide a more accurate estimate of the required heat flux (see Fig. 2.2). The heaters are controlled by solid state relays which can only turn the heaters on or off at full power. Therefore a time averaged approach is necessary. The first 27 heaters on each side are each controlled by an individual relay, the next 12 heaters are connected in pairs to a relay, and the last heater is connected to its own relay. This is permissible because the largest change in heat flux needed to maintain a constant wall temperature occur at the beginning of the channel, where the heat transfer required is theoretically infinite. However as the end of the channel is approached, the heat flux required doesn’t change much. Heat losses from the end of the channel are significant enough to affect the temperature of the channel at the last thermocouple location, which is why the last heater is controlled individually. This allows the 40 heaters on each side to be controlled with 34 relays for a total of 80 heaters controlled by 66 relays. To keep this control accurate, each heater has a thermocouple embedded in the plate at its center, meaning each plate as a total of 40 thermocouples axially and centered width-wise. Additional thermocouples are located in the plates to measure the change in temperature across the width and ensure it is the same as the center temperature as expected. This results in a total of 50 thermocouples in each plate.

Plate design iteration

In the initial design, the plates were one continuous piece. It was thought that because they were thin compared to their length (0.5” to 40”) that the flux applied by the heaters would act primarily through the plate. Unfortunately, as early tests illustrated, the axial conduction of this design was so great that several heaters were not needed. A re-design of this channel resulted in segmented plate design illustrated in figure 2.3.

The solid plate was broken up into 40 separate ~1 Inch pieces. A small piece of highly insulative foam was then placed in between them and the resulting surface (on the side exposed to the air) was sanded smooth. Simulations (and now experimental results) show that the low thermal conductivity of the foam prevents axial conduction from altering the results. The only downside is the experiment must run longer to allow the foam to reach the desired steady state temperature. Figure 2.3b shows a side view of the resulting assembly.

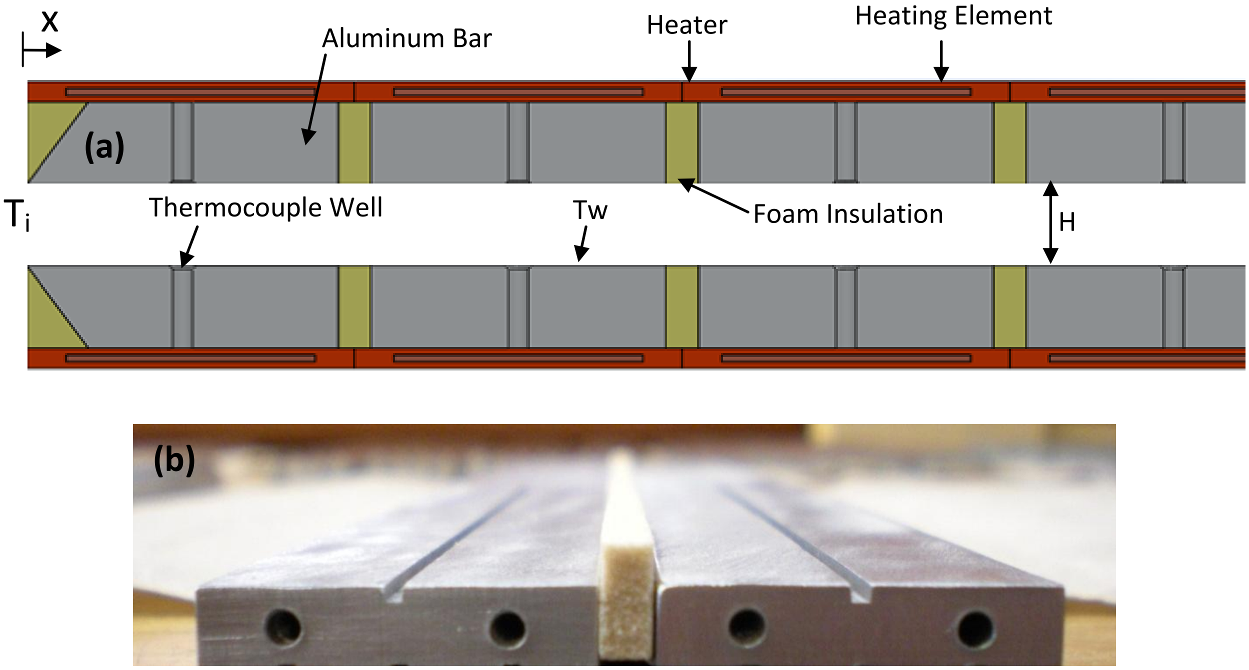

Figure 2.3: (a) Axial Slice Schematic of Flat Heat Transfer Passage. (b) Insulating foam placed between plates to prevent axial conduction.

Channel end

The polycarbonate sides (Figure 2.2) are designed to hold the plates at the proper wall to wall spacing. The actual width of the aluminum is slightly longer than the 9.125” that comprises the channel width. This allows the aluminum to slightly overlap the polycarbonate, which is machined to the ideal wall-to-wall spacing. To measure the pressure at multiple locations throughout the channel, threaded holes are machined into one of the sides of polycarbonate. These then allow the fittings to be connected to the channel. There are 10 holes located at 4 inch intervals throughout the entire length of the channel. This will be illustrated later when the pressure measurement system is outlined.

The air exits the passage into a plenum. The plenum allows the air flow from a rectangular channel to enter the circular tubing while ensuring the air comes out of the channel at uniform velocity. It consists of a square cross section channel, with soda straws packed into its downstream end (see Figure 2.4). It is placed between the channel exit and the converging section. Additionally, pressure taps are located in the plenum to experimentally verify the uniform flow assumption. Thermocouples are also placed in and around the plenum to quantify the heat lost by conduction as well as measure the temperature of the air exiting the apparatus. This plenum is constructed from 1/8 Inch polycarbonate. The air then flows through PVC tubing. The air makes a U-turn (see Figure 2.2). This is done to conserve space in the lab. After making both turns the air flows through an ASME long-radius flow nozzle. The pressure drop on either side of the nozzle is measured and used to calculate the airspeed in the channel. The air then flows toward the centrifugal fan through a flow straightener. The centrifugal fan works by making a rotary motion whose cross product is parallel with the pipe. This can cause vortices in front of the fan and may affect the reading of the pressure transducer, which is the reason for the flow straightener. Distances from the corners to the flow element as well as the location of the pressure taps on either side of the nozzle are all specified by the ASME standards.

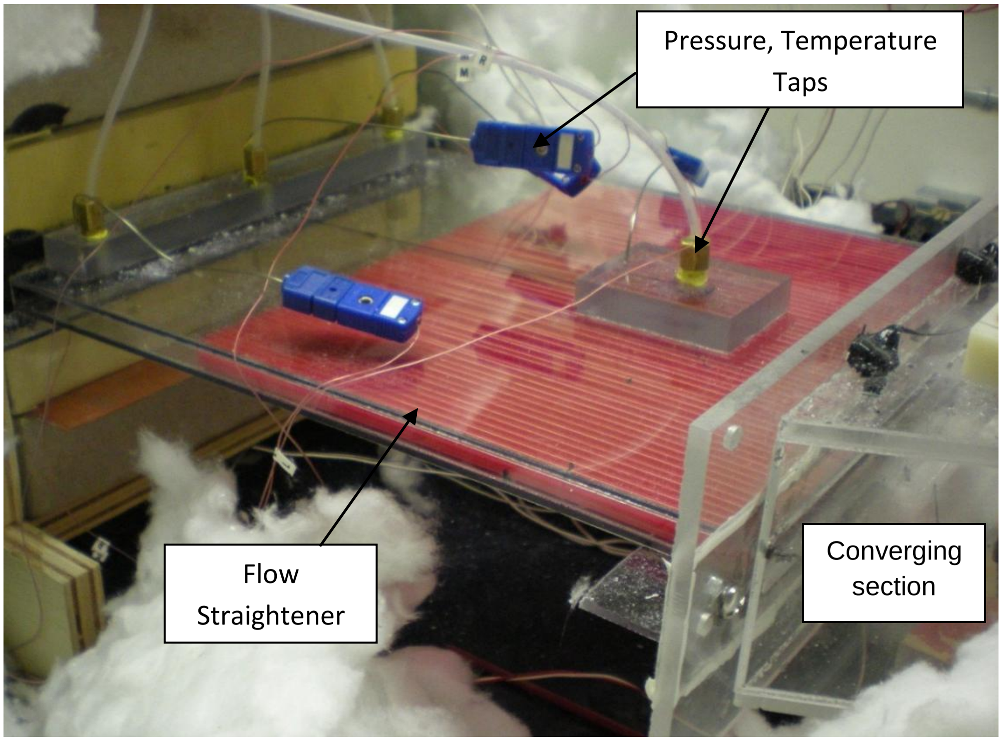

Figure 2.4: Exit geometry with a flow straightener (red straws) and pressure/temperature taps.

Heater System

As previously mentioned, 40 rubber encapsulated strip heaters, with nominal room temperature resistance of 144 ohms, are fastened to both outer surfaces of the channel to get an accurate idea of the heat flux at each axial location of the channel. The first 27 on each side and the last one are in series with a solid state relay. The other twelve on each side are grouped into pairs. Each pair is connected in parallel, and the parallel heaters are connected to a relay. All the heater/relay circuits are connected in parallel with regulated DC power supply whose output voltage is V_{PS}= 40 V. The heaters can either be "on" or "off" in state. This means that the heaters can either be applying full power or turned completely off. Most locations do not require full heater power, so a time averaged approach is applied. Each heater has a corresponding thermocouple embedded at its axial center. The temperature at this thermocouple use used to control that heater. A DaQ system records the temperature, compares it to the set temperature, at then runs the difference through a proportional-integral control loop to develop a Fraction of Time On (FTO). This a fraction of a set time is the period in which the heater will be on. A common time is three seconds. The PI specifies a desired wall temperature, T_D, and the program adjusts the FTO for each heater until the associated thermocouple reading, T_W, is the desired value. The experiment will run for many minutes, and the fraction of time on for each set time will be averaged into the time-averaged fraction of time on. This value is then multiplied by the total heater output (the wattage put out when the heater is fully on) to provide the heat flux at each one-inch location.

Pressure System

Pressure taps are used to connect to the tapped holes in the primary channel. Figure 2.5 shows 10 pressure taps that are drilled into one of the polycarbonate side walls at x = 5.08, 15.24, 25.4, 35.56, 45.72, 55.88, 66.04, 76.2, 86.36, and 96.52 cm. Three additional taps are drilled into the top of the plenum at x = 104.14 cm, and one more at x = 106.68 cm. These pressure taps are constructed from acetal, which is easy to machine and has a low thermal conductivity. Their purpose is to reduce the conduction heat loss through the pressure tap. Brass compression fittings connect to the standoffs and then plastic tubing runs to a multi-selector valve. This valve has a rotating component which is computer controlled. As it turns it allows a different pressure tap to be connected to a pressure gage. That gage measures the pressure difference between the taps and the external atmosphere. The elevation of the lab (in Reno, Nevada) is 1300 m, where the average atmospheric pressure is 86 kPa. The value of the pressure is then sent to the computer via a DaQ. After the pressure is read, the computer rotates the valve and the process is started over again.

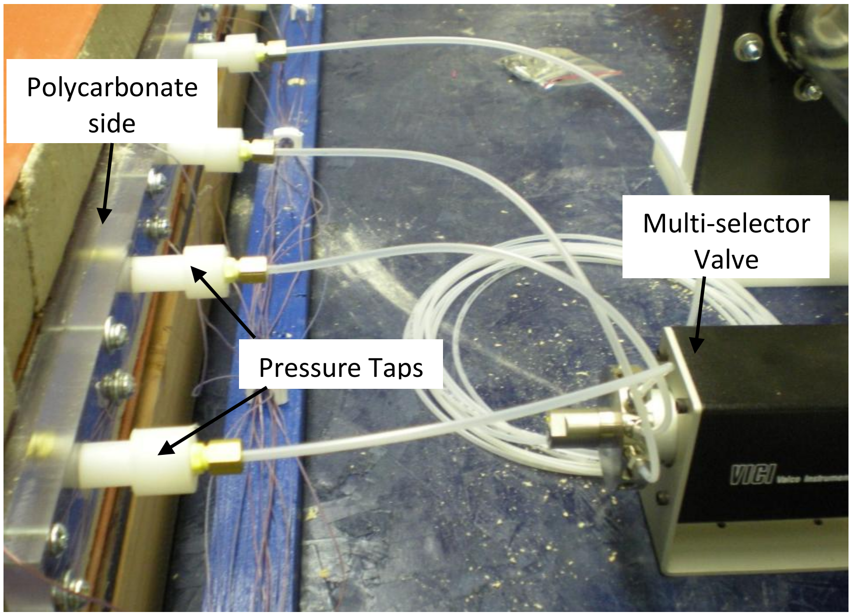

Figure 2.5: Pressure standoffs in the channel sidewall.

Speed System

The centrifugal fan is controlled by a Pulse-Width Modulated (PWM) signal from the computer via the DaQ. This creates an airflow which creates a pressure differential across the flow nozzle. This pressure difference is measured by a pressure transducer and sent to the computer for processing. The computer takes the differential pressure and then calculates the channel Reynolds number from that value. There is no feedback loop for the fan control. The fan is initiated, and then the Reynolds number is dialed in by manually adjusting the computer control of the PWM signal.

Insulation

The channel is insulated on the top, bottom and side surfaces to reduce heat loss to the ambient air. The upper insulation layer is removed in Figure 2.2 to expose the strip heaters that are fastened to the passage upper surface. Low thermal conductivity foam was chosen for its ease of machinability. To quantify the heat lost to the ambient air through the foam, thermocouples are placed in the foam and the heat flux is calculated using the difference between temperatures. Figure 3.6 illustrates where the heat flux loss is calculated for each insulation piece.

Results

The experiments are performed for a set of wall temperature Tw and Reynolds numbers Re. After steady state conditions are reached a nine minute period of time is examined at each hour and is used to create a data point. The experimental results shown below are for the flat channel passage.

Figure 2.6 shows the measured thermocouple temperature versus axial location on the top and bottom surfaces for three different desired wall temperature Tw=50, 60 and 70 °C, after the system reached steady state conditions. For all air flow rates, and inlet and desired wall temperatures, the maximum difference between the measured and desired wall temperature is less than 0.4°C. The measured average wall temperature T_W is roughly 0.5°C lower than the desired value.

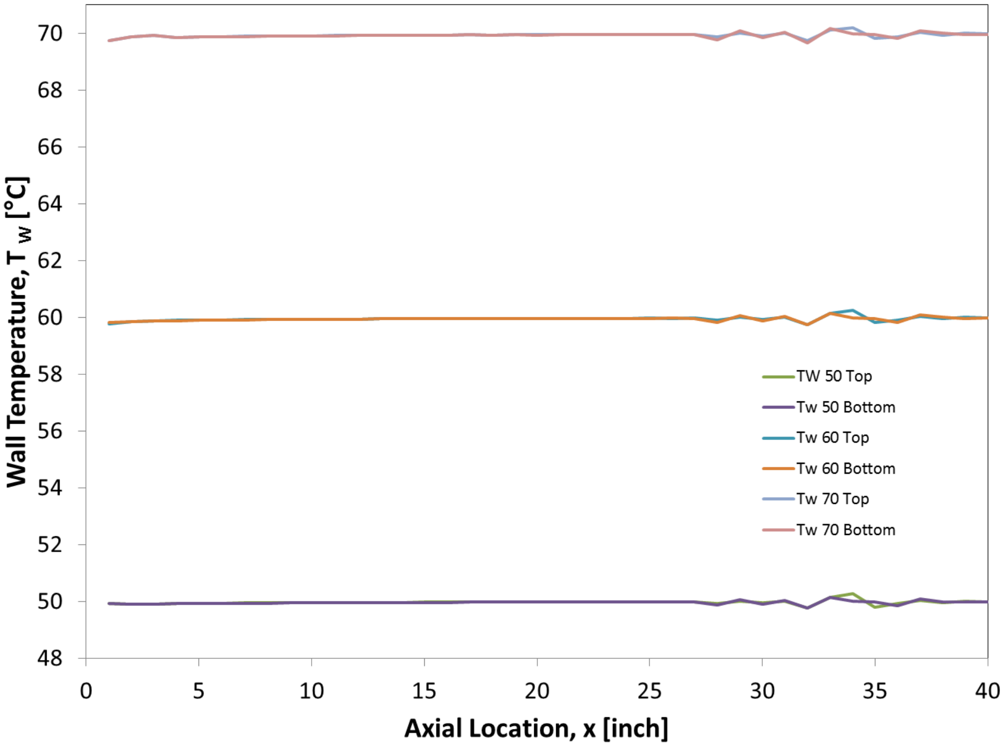

Figure 2.6: Measured axial variation of upper and lower wall temperature for desired values of 50, 60 and 70°C. Results are similar for all inlet temperatures and air flow rates.

The definition of the local dimensionless bulk temperature θ_x means it equals 1 when the bulk fluid temperature reaches the wall temperature. At this point heat transfer ceases, meaning the value of θ_x will never exceed 1. A calculation of θ_x using the experimental heat input results and assuming no heat losses ($Q_{x,loss} = 0$) and is plotted in Figure 2.7 using below equations, once for each combination of T_w and Re as a function of number of hydraulic diameters.

$$T_{b,x} - T_{b,x-1} = \frac{Q_x - Q_{loss,x}}{mc_p}$$

$$\theta_x = \frac{T_{b,x} - T_0}{T_w - T_0}$$

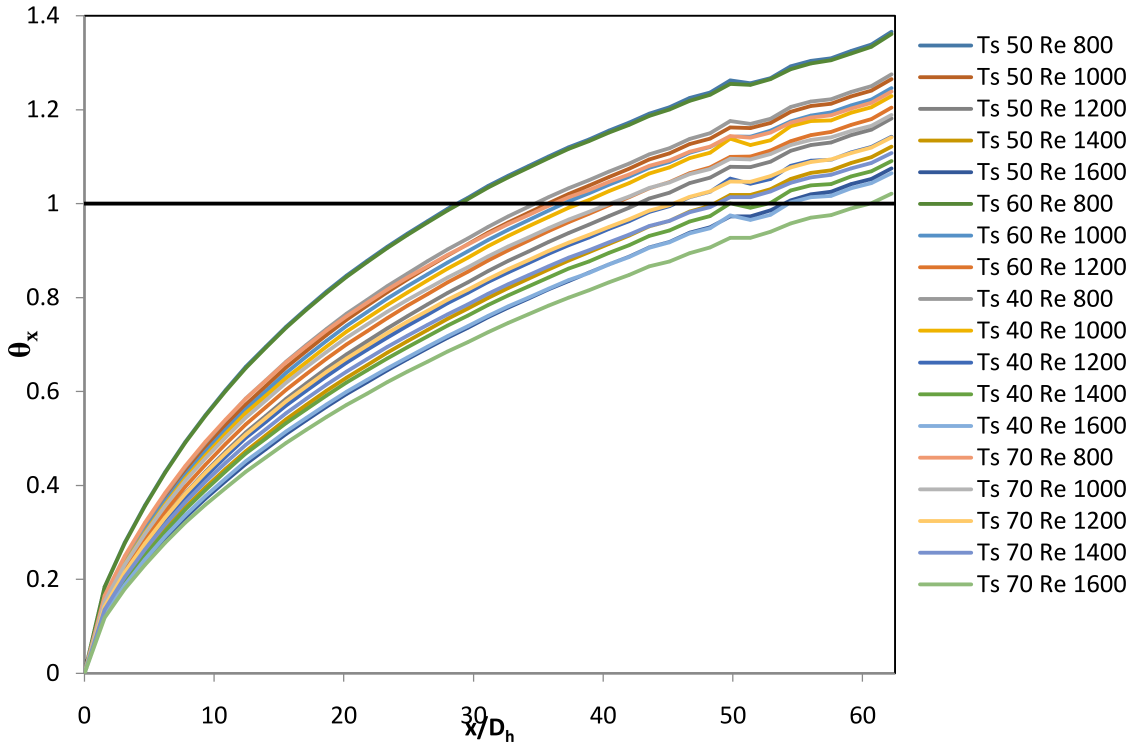

Figure 2.7: Calculated dimensionless temperature as a function of hydraulic diameters.

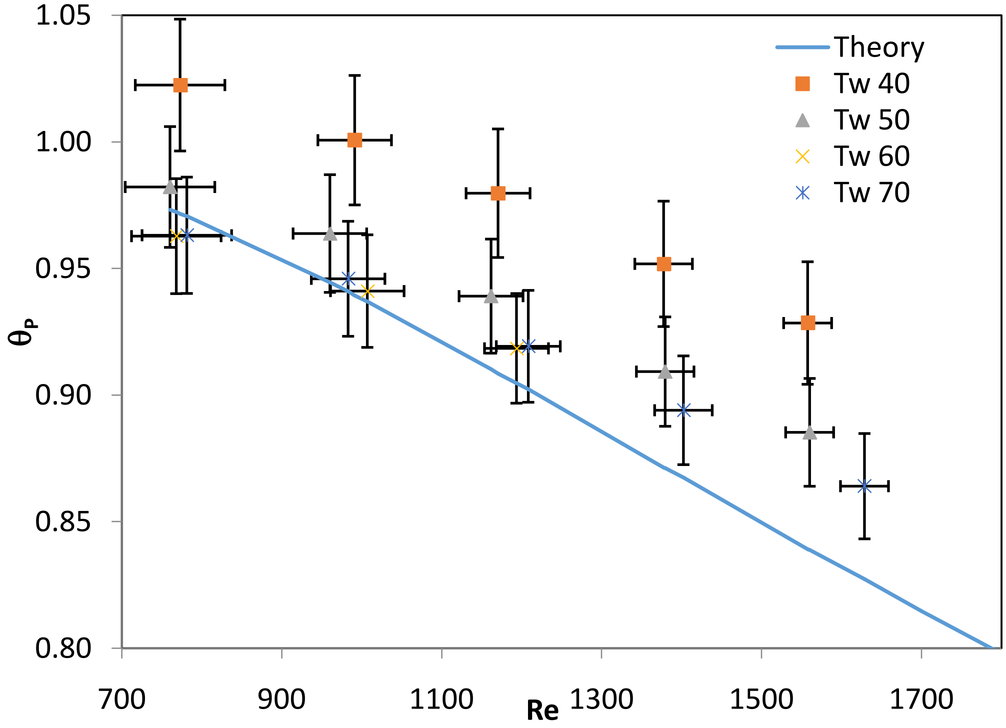

Figure 2.8: Plenum exit temperature as a function of Re for different T_w for the ideal case and the average measured values.

Physically the bulk mean temperature cannot exceed the wall temperature, which suggests the profiles in Figure 2.7 are inaccurate. The dimensionless temperature at the end of the experiment can be calculated for the experimental values using the readings from the thermocouples in the plenum. Figure 2.8 illustrates the average measured plenum temperature non-dimensionalized and plotted as a function of average Re for different wall temperatures. The theoretical value of the exit temperature is also plotted for comparison.

The mean bulk temperature is an average temperature based on the velocity and temperature profiles in the channel. A measured temperature value represents a data point for a certain velocity and temperature which may not be representative of the average temperature. While this means the measured values used in Figure 2.8 are not the true bulk temperature measurements, they do provide a general indication of the fluid temperature. The physically measured values in Figure 2.8 are significantly lower than the calculated values of Figure 2.7, which means the presence of heat loss.

The method used to estimate the input heat employs the plenum temperature $T_{b,L}$, the mass flow rate, specific heat and inlet temperature, as illustrated by following equation:

$$Q_{in} = mc_p(T_{b,L} - T_0)$$

Figure 2.9 shows the calculated total heat generation rate Qin versus the Reynolds number for different wall temperature. The heat generation rates from the top and bottom surface are nearly the same, which indicates that natural convection does not play a strong role under these conditions. The heat generation rate increases with the Reynolds number.

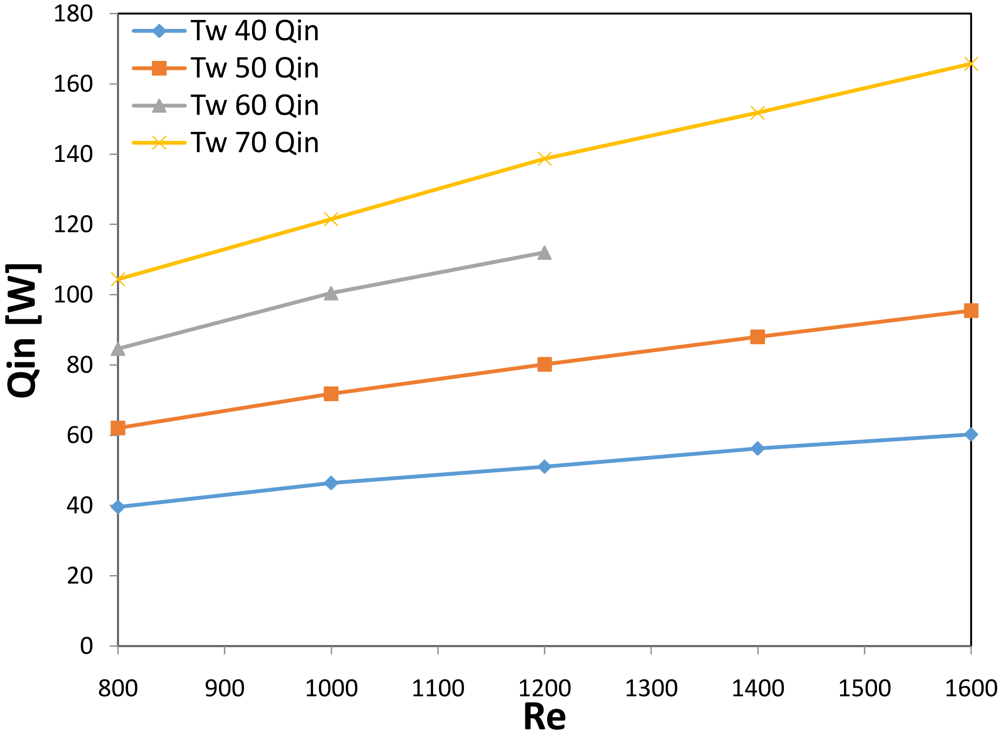

Figure 2.9: Total heat input into the system as function of the Reynolds number for different wall temperature.

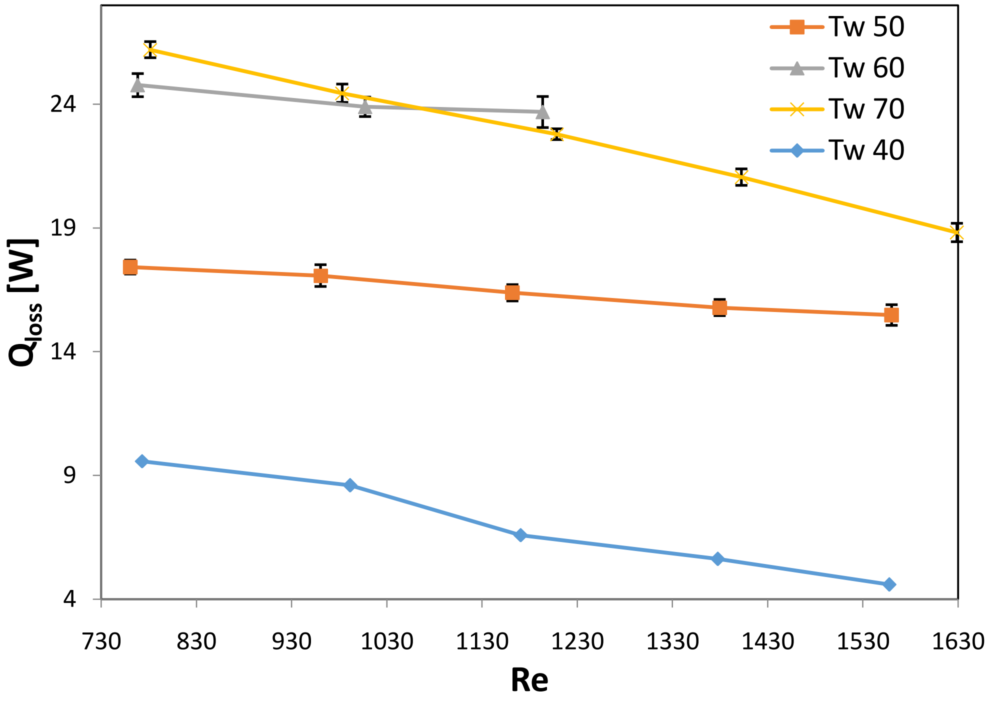

Figure 2.10: Heat loss Q_{loss} as a function of Reynolds number for different wall temperature.

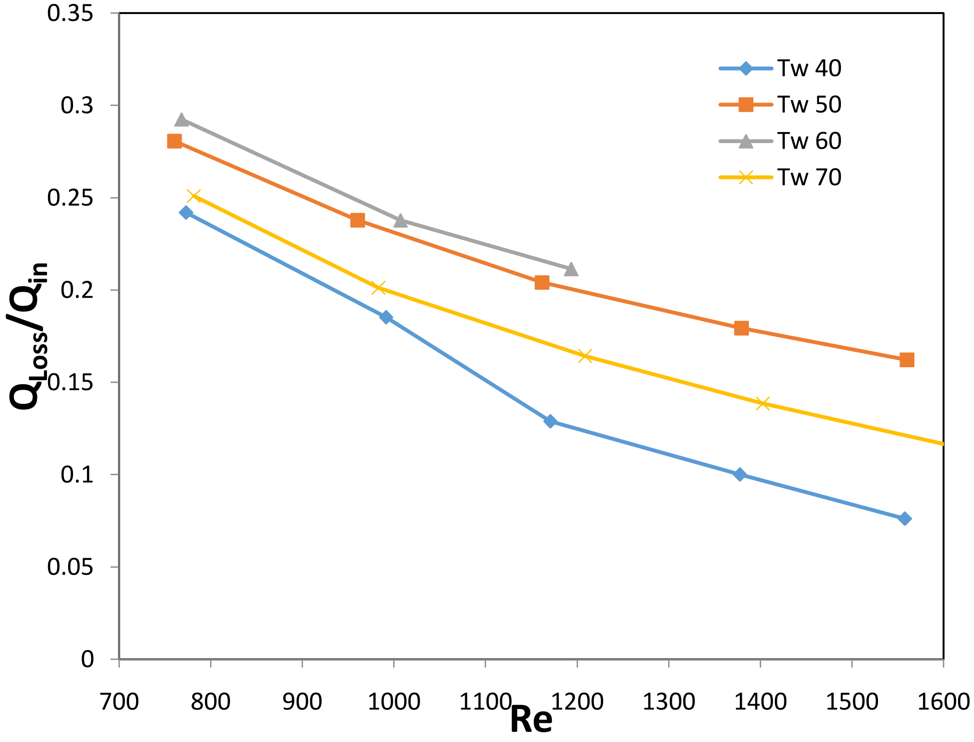

Figure 2.11: Ratio Q_{loss}/Q_{in} as a function of Reynolds number for different wall temperature.

To estimate the heat loss the energy balance method is used. This method allows for a calculation of total heat into the system by measuring the temperature in the exit plenum. This value is then subtracted from the measured heat input resulting in a total system heat loss by this method Qloss. The total heat loss calculated is then applied systematically as Qloss,x to calculate the mean bulk temperature. The heat loss calculated by this method is plotted as a function of Reynolds number for different wall temperatures in Figure 2.10,

Figure 2.11 shows the ratio Qloss/Qin as a function of Reynolds number for various wall temperatures. The heat loss estimated by the energy balance method is between 10 and 30% of the total heat input.

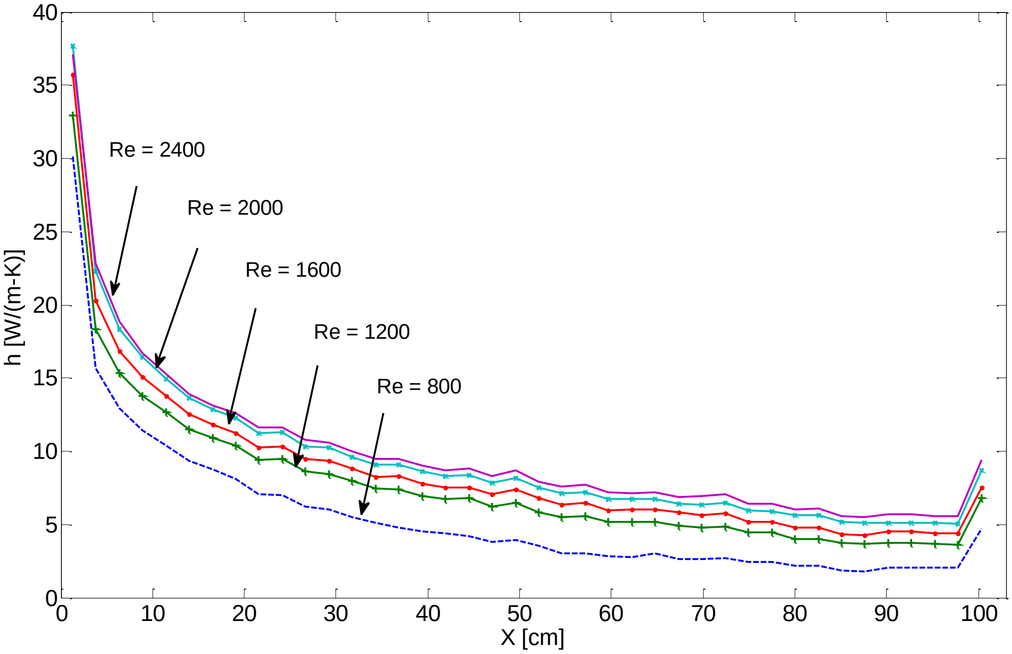

Figure 2.12: Combined power output as a function of axial position for a range of Reynolds numbers.

Figure 2.12 shows the measured heat transfer coefficient versus axial location for four experiments. The heat transfer coefficient plotted in this figure is based on the wall-to-inlet temperature difference, $h = Q/[A(T_w - T_i)]$, where A is the sum of the surface areas one aluminum bar plus one foam spacer. It shows that the local values consistently increase with Re.

Figure 2.13 shows the area-averaged heat transfer coefficient for the entire channel versus Reynolds number from 16 experiments. The average heat transfer coefficient increases roughly linearly with Reynolds number for Re < 1600, but more slowly at higher Reynolds numbers.

Figure 2.14 shows the measured passage pressure below atmospheric pressure, Patm – P, versus axial location. The measurements for x >100 cm are in the exit plenum. The pressure drop decreases slightly in the plenum due to the lower speed in the plenum compared with the channel. These data are for Re = 800, 1200, 1600 and 2000. The local pressure drop consistently increases with Re.

Summary

The experimental apparatus maintains a uniform wall temperature within the equipment error for a range of wall temperatures and Reynolds numbers. However the calculated temperature profiles indicate a bulk mean temperature above the wall temperature, which is a physical impossibility. This suggests a systematic heat loss. To quantify the heat loss a heat flux gage is constructed and described in the next section.

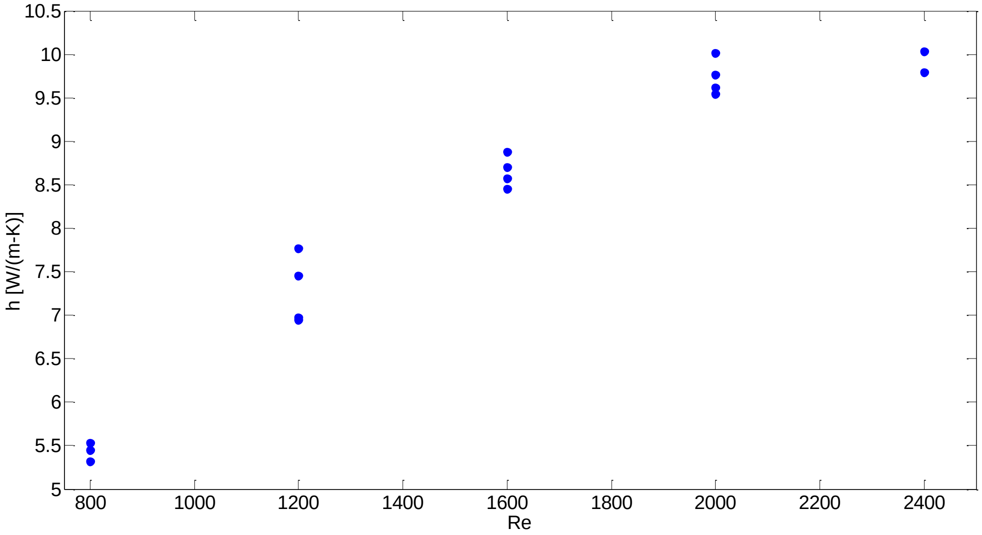

Figure 2.13: Experimental mean convection coefficient for a range of Reynolds numbers.

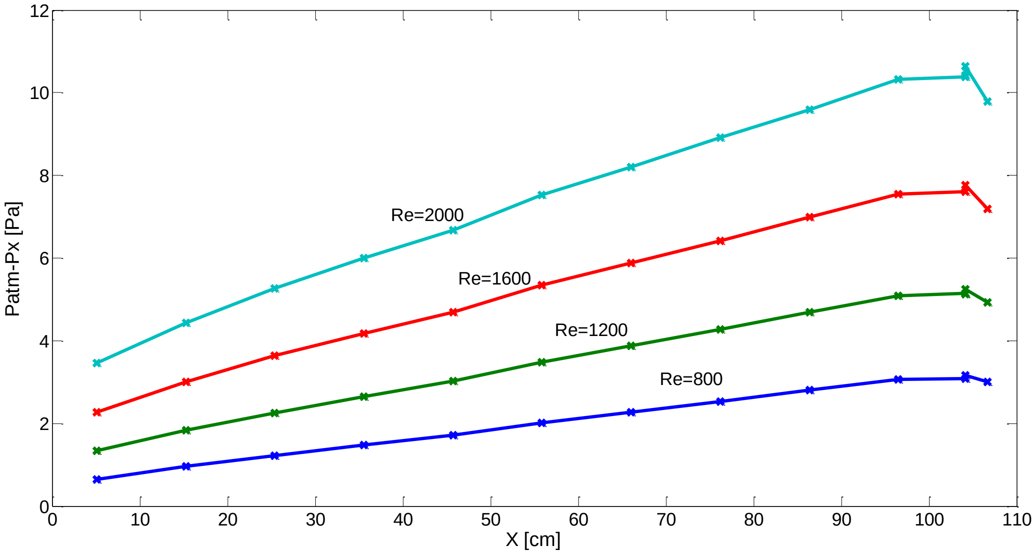

Figure 2.14: Pressure drop as a function of axial position for a range of Reynolds numbers.

Heat flux gage assembly construction

In order to estimate the heat loss from the backside of the silicone rubber heaters a heat flux gage assembly is placed on the top and bottom of the channels. Figure 2.15 shows a side-view schematic of upper and lower channel surfaces and the air passage between them. Each channel surface bar is backed by a strip heater. Each channel heater is backed by a heat-flux-gage subassembly, consisting of top and bottom aluminum bars with insulation between them. The bars are separated from the ones upstream and downstream from them by a 0.1-inch long air-filled gap. Each bar has channels cut into one of their surfaces. A thermocouple probe is placed in the center channel of each bar. The thermocouple sensing bead is midway between the two channels sidewalls, and the lead wires lie inside the groove.

Between the aluminum gage bars are dense foam simulation blocks that are 1 inch long in the flow direction, 9.75 inch in the transverse direction, and 0.75 inch thick. The thermocouples in the gage bars measure the temperature on either side of the insulation. The heat flux leaving the back side of each heater is determined by measuring the temperature difference between the top and bottom bars, and knowing the insulation thickness, its area, and thermal conductivity. Using the following expression the heat flux through the gage can be calculated.

$$q_x" = \frac{(\Delta T)}{L_i/k}$$

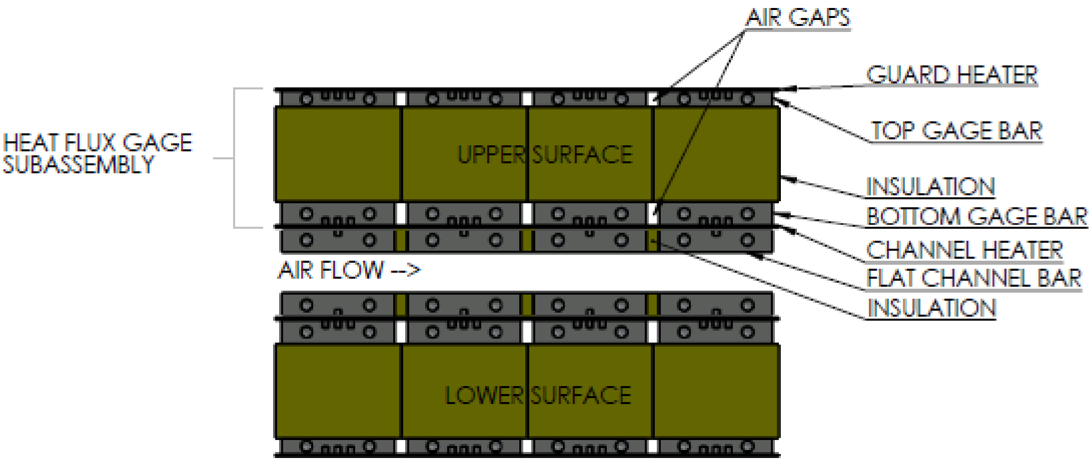

Figure 2.15: Side-view schematic of the upper and lower flat channel surfaces and the air passage between them.

Each heat flux gage subassembly is backed by a guard heater. Dense foam insulation is placed on the back side of the guard heaters to reduce losses to the surroundings. Each guard heater is connected in series with a digital relay, and this circuit is wired in parallel to a DC power supply. A signal to the relay controls the fraction of time the heater is turned on. The fraction of time on is controlled using a LabVIEW program to minimize the temperature difference between the top and bottom gage bars (and the heat flux leaving the back side of each wall). A proportional/integral feedback control methodology is employed to drive this temperature difference and the back side heat flux rate to zero.

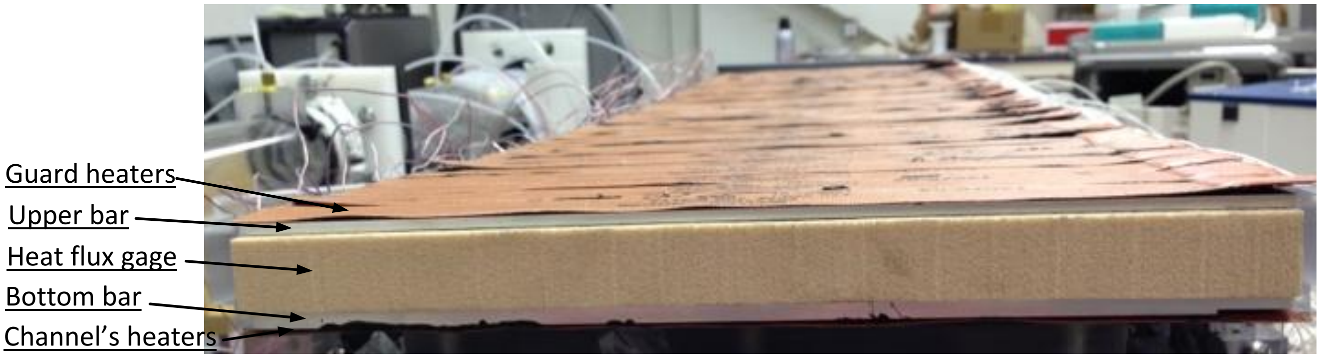

Figure 2.16: End view photograph of the Channel-heater/Heat-Flux-Gage/Guard-Heater Assembly.

Figure 2.16 shows an end-view photograph of the upper surface's channel-heater/heat-flux-gage/guard-heater assembly. The lower and upper gage bars and foam insulation are visible. Guard heater on the back side of the flux gage subassembly is also visible. These heaters are bonded to the upper gage bars using room temperature vulcanizing rubber cement. However, due to the heater surface shape, the heaters do not lie flat on the upper gage bars.

Future Work

In 2013, two research proposals were submitted to continue this work. Those proposals employed the computational results and experimental facility that were developed in this work. Those proposals were submitted to the National Science Foundation and the Nevada NASA EPSCoR program, but were not funded.

The Nevada NASA EPSCoR proposal is currently being revised and will be resubmitted in December 2014. .

Advanced Heat/Mass Exchanger Technology for Geothermal and Renewable Energy Systems

Project 4: Final Report: Reinforced Super-hydrophobic Surfaces for High-Performance Condensers

K. J. Kim
Mechanical Engineering Department
University of Nevada, Reno
Reno, NV 89557

775-784-6931

kwangkim@unr.edu

December 10, 2014

Executive Summary

The objective of this project is to develop a material-engineered, long-term, and performance-effective technique to enhance heat transfer rates in steam condensation, which can dramatically reduce footprints and manufacturing costs of industrial condensers. Condensation is a critical heat transfer mechanism in numerous industrial processes and there have been many efforts to promote “dropwise” condensation which shows a higher heat transfer rate than that of a conventional “filmwise” condensation. The main expected outcome of the proposed work is to craft a unique technique to promote dropwise condensation.

The emphasis of the current endeavor is to conduct engineered materials process development via. condensate drop dynamic modeling and subsequent experimental work. Experimental techniques were done in laboratory scale. With certain treatments, robust and sustained dropwise condensation was achieved. Also, it is important to gain a fundamental understanding of wetting characteristics of textured surfaces having different geometric configurations. This can be accomplished by studying how a single droplet behaves on a given surface. Drop dynamics are affected by surface energies of different interfacial surfaces and surface morphologies. Contact angle hysteresis (CAH) – which is the difference between advancing and receding angles – can be estimated by utilizing concepts of surface-energy minimization. This is essential in heat transfer applications, as CAH determines such parameters as drop sizes and distribution in condensation heat transfer. The upshots of the project can be summarized as follows:

1) The framework for a drop dynamic model was conducted to estimate CAH on different surface geometries and degrees of wetting. Drop dynamics was shown to have direct impact with condensation heat transfer.
2) A number of promising surface coatings/modifications in connection with a drop dynamic model developed from this work, were conducted. The resulting surface morphologies were investigated by microscopic images, and the wetting characteristics were obtained by measuring the water contact angle to find key parameters for promoting a dropwise condensation mode.
3) Steam condensation tests with visual observations were conducted to evaluate the heat transfer performance. From visual observations, the hydrophobic surfaces could promote dropwise condensation modes effectively by limiting the growth of large condensate drops.

Recommendations

1) In order to further gain the fundamental knowledge about dropwise condensation, future works need to work on detailed studies on drop population group behavior both mathematically and experimentally.
2) There is a need to develop industry acceptable, low-cost and long-term performing dropwise condensation promoter.

Project 4: Final Report: Reinforced Super-hydrophobic Surfaces for High-Performance Condensers

K. J. Kim

Project Objective

With proper promotion, dropwise condensation produces much higher heat transfer rates than filmwise condensation. However, the enhancement significantly drops with time due mainly to the degradation of organic promoters. The objective is to develop a material-engineered and long-term performance-effective technique for enhancing heat transfer rate in steam condensation which would dramatically reduce the footprint and manufacturing cost of condensers. The main expected outcome of the proposed work is to craft a unique technique for promoting dropwise condensation.

Technical Approach

1-Engineered Materials Process Development: We explored the controllable surface wettability by building up multi-scale roughness, so called “tertiary roughness” on hierarchical substrates. It ascertained the limit of the perfect hydrophobic/philic surface with low surface energy coatings and hydrogen bondings, respectively. Both modeling and experimental work are described.

2-Surface Characterization: Water contact angles were measured for the engineered heat exchanger to assess the characteristics of heat transfer surface. A contact angle measurement apparatus was used to measure the contact angles of liquids on the heat transfer surface for determining the hydrophobic/hydrophilic nature of the surface.

3-Steam Condensation Testing: The existing multi-functional condensation facility was used for simulating industrial steam condensers. The heat transfer coefficients for a number of treated condensing surfaces have been documented. Throughout the testing, the condensation mode and the condensing surface structure were visually monitored and their images were recorded.

Period of Performance

September 20, 2010 – September 20, 2014

Personnel

Kwang J. Kim, Principal Investigator
Foundation Professor and Chair:
10/20/2010-06/30/2012
Mechanical Engineering Department
University of Nevada, Reno
Reno, NV 89557 / kwangkim@unr.edu

Southwest Gas Professor of Energy and Matter:
07/01/2012-09/20/2014
Mechanical Engineering Department
University of Nevada, Las Vegas
Las Vegas, NV 89154 / kwang.kim@unlv.edu

Publications Stemming From This Work

1. B. J. Zhang, J. Park, K. J. Kim and H. Yoon, “Biologically inspired tunable hydrophilic/hydrophobic surfaces: a copper oxide self-assembly multitier approach,” *Bioinspir. Biomim.* (2012) **7,** 036011: doi:10.1088/1748-3182/7/3/036011.
2. S. Lee, H. Yoon, K. J. Kim, S. Kim, M. Kennedy, and B. J. Zhang, “A dropwise condensation model using a nano-scale, pin structured surface,” *International Journal of Heat and Mass Transfer* (2013) **60,** 664–671: http://dx.doi.org/10.1016/j.ijheatmasstransfer.2013.01.032.
3. B. J. Zhang, K. J. Kim, and D. Y. Lee, “Nanosphere-decorated tunable anatase titania conic self-Assemblies, “*J Nanopart Res* (2013) **15**, 1837: DOI 10.1007/s11051-013-1837-5.
4. R. Enright, N. Miljkovic, J. L. Alvarado, K. J. Kim, and J. W. Rose, “Dropwise Condensation on Micro- and Nanostructures Surfaces,” *Nanoscale and Microscale Thermophysical Engineering* (2014) **18**(3), 223-250, DOI: 10.1080/15567265.2013.862889.
5. K. Cheng and K. J. Kim, “Contact angle hysteresis using surface-energy-minimization method,” under preparation.

Task 4.1 Conduct Engineered Materials Process Development

➢ *Condensate Drop Dynamic Modeling*

Theoretical and experimental approaches were conducted in drop dynamics in relationship with surface energy. In recent years, advances in nanomaterials research have enabled super-hydrophobic and other interesting wetting properties [1-13]. Non-homogeneous surfaces often are presented in studies on super-hydrophobic surfaces and other complex morphologies that produce complex wetting characteristics. In early studies of wetting properties, such as contact angles, researchers began incorporating the notion of roughness.

It is important to understand how a single drop on a surface behaves. Wetting properties of a single droplet strongly influence the drop-size distribution in condensation heat transfer [14, 15]. Thermodynamics of such a droplet on the surfaces need to be understood [16]. Gibbs free energy, *E*, provides a relationship between surface energies in terms of interfacial contact areas and their respective surface energies, as shown in Equation (4-1),

$$E = A_{LG}\gamma_{LG} + A_{SL}\gamma_{SL} + A_{SG}\gamma_{SG} \tag{4-1}$$

where A_{LG}, A_{SL}, and A_{SG} are liquid/gas, solid/liquid, and solid/gas interfacial areas, respectively; and γ_{LG}, γ_{SL}, and γ_{SG} are the corresponding surface energies per unit area.

According to Young [17], the shape of a liquid droplet is determined by surface tensions of the interfacial forces. Liquid droplets attempt to spread through evenly on the wetting surface, and the act of spreading stops when all interfacial tension forces are balanced, i.e., liquid/solid, solid/gas, or liquid/gas. A liquid droplet forms a unique angle with the solid surface, as shown in Figure 4-1.

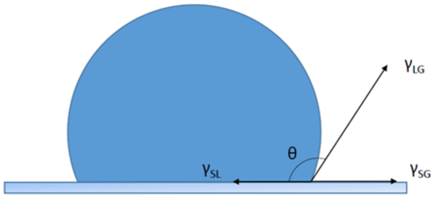

Fig. 4-1. Surface tension and contact angle of a liquid droplet

Young's equation for contact angles is obtained by the force balance, as given in Equation (4-2):

$$\gamma_{LG}\cos\theta = \gamma_{SG} - \gamma_{SL} \tag{4-2}$$

Similarly, Equation (4-2) can be obtained by minimizing surface energies with respect to the interfacial area given in Equation (4-1) and seen in Equation (4-3):

$$dE = 0 = dA_{LG}\gamma_{LG} + dA_{SL}\gamma_{SL} + dA_{SG}\gamma_{SG}\,. \tag{4-3}$$

Young's equation gives an important insight on how a droplet behaves on a static homogeneous surface. However, it does not give information on how a droplet behaves under an external influence or the shape of the droplet in a non-homogeneous surface [18]. While Young's equation gives insight only on basic information on wetting for flat surfaces, it has been the basis of wetting models [10, 12, 19-22]. Notably, Wenzel [21] was one of the first to examine wetting on rough surfaces. Wenzel established the relationship between the roughness ratio, which is the area of a rough surface to the area of the projected flat surface, and contact angles. This researcher established the following equation under homogeneous wetting conditions:

$$\cos\theta_W = r_f\cos\theta_0\,, \tag{4-4}$$

where r_f, θ_W, and θ_0 are the roughness ratio, the Wenzel contact angle, and Young's flat surface contact angle, respectively. Later, Cassie and Baxter [20] established contact angles in relationship with the non-homogeneous condition to take into account the weighted average of various contact angles for different components:

$$\cos\theta_{CB} = \phi\cos\theta_1 + (1-\phi)\cos\theta_2 \, , \tag{4-5}$$

where θ_1 and θ_2 are the contact angles for Component 1 and Component 2, respectively and ϕ is the fraction of the solid/liquid contact area. Both the Wenzel and Cassie models give some insights on wetting characteristics of rough surfaces. However, they do not fully encompass how wetting characteristics change under external influences, i.e., external forces.

Regarding drop dynamics, contact angle hysteresis (CAH) should be the first topic studied. For example, several researchers have proposed models to explain how wetting changes with respect to CAH. As explained by Gao and McCarthy et al. [23], in order to initiate the motion of drop on a surface, the movement of a droplet is caused by external forces from the environment. An external force deforms the shape of a droplet and causes an observable difference in contact-angle measurement. Contact angle hysteresis (CAH) can be defined as the difference between the maximum and minimum contact angles. CAH can be caused by an addition or subtraction of droplet masses, or by tilting the contact surface at an angle. It is very important to understand how the CAH process is initiated for incorporation into an application such as the condensation process. CAH is measured experimentally in several ways [24]. One of the most common methods involves adding and drawing the liquid droplet mass in order to measure immediate advancing and receding angles. A second common method involves measuring the advancing and receding angles of a droplet on a titled surface. Even so, these methods may have large variations, and do not always represent accurate operating conditions on rough surfaces. Additionally, CAH has been the subject of research with both experimental and theoretical models. Johnson [16] first explained the relationship between CAH and surface roughness. Over the past decade, experiments have advanced an understanding of the relationship between CAH and surface structure [11, 23, 25, 26]. For example, in experimental studies, micro-structured surfaces often are fabricated using known contact angles on flat surfaces [25]. Forsberg et al. [25] fabricated a micro-structured surface using various polymers with known flat-surface contact angles; they found that the cosine of CAH that resulted with these structured surfaces is linearly correlated with aspect ratios and fin densities. Forsberg [25] found that CAH increased with surface having higher fin heights and increased roughness. Quere et al. [27] reviewed how roughness was related to surface energies and wetting characteristics. This group reviewed and adapted Young's equation and the associated equation for Gibbs energy to different roughnesses and geometries. Since wetting dynamics depends on the concepts of surface tension and surface energy, Gibbs energy continues to be used in various wetting dynamic models, especially in CAH. Most recently, Hejazi et al. [28] proposed a multi-phase model to describe contact angle hysteresis for systems having multiple wetting components. Similar to the Wenzel and Cassie-Baxter models, this group described wetting under conditions of multi-phase surface energies. Rough surfaces were idealized as a flat surface having various components with different wetting properties. The model took into consideration several geometric factors, such as component spacing. The results of modeling for CAH were found to agree well with solid/water/air systems and solid/water/oil systems.

Since contact angle hysteresis is caused by additional energy applied to the system, Adam and Jessop [29] proposed that the additional energy is proportional to the forces with CAH,

$$F = \gamma(\cos\theta_{red} - \cos\theta_{adv}) \, . \tag{4-6}$$

Similar models [30, 31] have explored contact angles and CAH in relation to roughness contribution. Xu and Wang et al. [32] modified the Cassie-Baster Equation and simulated contact line movements with different patterns of wetting components arrangements. It was found that the classic Cassie-Baxter Equation works relatively well when different components are homogenously dispersed. However, contact line movement and CAH is highly dependent on wetting components arrangements. Moradi et al. [11] examined geometry effect on spreading and CAH. They modeled the surface as parabolic cones and modeled how a drop would spread on the surface, depending on geometries of the cones. It was found that CAH was largest with cones having high pillars. Other models [10, 28, 32-35] continued to modify the Wenzel and Cassie-Baxter drop models. McHale et al. [10] examined the limitations of these two models. In most cases, they both were good at describing trends of surface wetting. However, such factors as geometries potentially might be ignored in these models, and therefore could not be used above certain ranges, e.g., the Wenzel model on a super-hydrophobic surface.

Recent studies have found that geometric factors, along with local wetting properties in surface morphologies are very important. Wettability could be tuned by changing surface geometries having the same materials [1, 11, 36-39]. In studies of nano-structured surface morphologies, relationships between wettability and geometrical factors continued to be of interest with regard to drop dynamics.

The goal of this work was to provide a fundamental framework of the relationship between surface energy and geometry through mathematical modeling. CAH, which could be estimated, provided a design tool for tuning the surface wettability.

For a liquid droplet to be stable on the surface, surface energies of interfaces between solid, liquid, and gas are minimized with the respective interfacial areas [17]:

$$E = A_{LG}\gamma_{LG} + A_{SL}\gamma_{SL} + A_{SG}\gamma_{SG} \tag{4-7}$$

$$dE = 0 = dA_{LG}\gamma_{LG} + dA_{SL}\gamma_{SL} + dA_{SG}\gamma_{SG}\ , \tag{4-8}$$

where E is the surface energy of all the interfaces. A_{LG}, A_{SL}, and A_{SG} are the liquid/gas, solid/liquid, and solid/gas interfacial areas and γ_{LG}, γ_{SL}, and γ_{SG} are the corresponding surface energies per unit area. Figure 4-2 illustrates the surface energies of a drop on a surface.

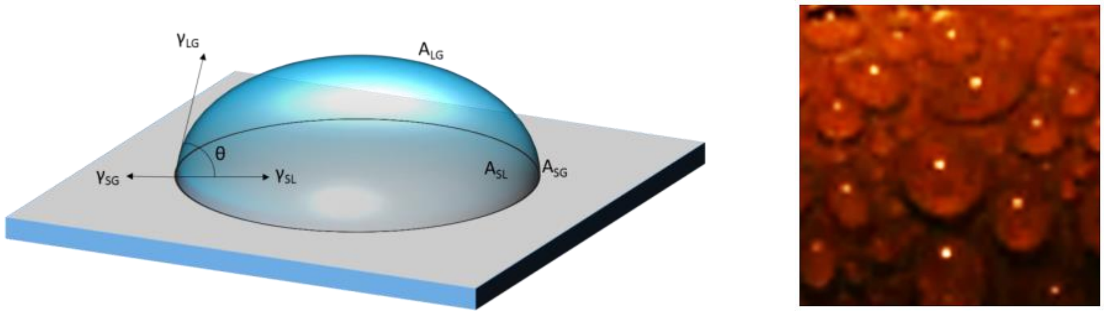

Fig. 4-2. (left)-Surface energies of a single drop and (right)-Typical water condensation on a sub-cooled copper surface

Assume that a droplet resting on a surface is a spherical cap with drop radius R and a contact angle θ. The drop volume, V (assuming a constant drop volume) and the cap surface area, A_C, are given as:

$$V = \frac{\pi}{3}R^3[2 - 3\cos\theta + \cos^3\theta] \tag{4-9}$$

$$A_C = A_{LG} = 2\pi R^2(1 - \cos\theta)\ . \tag{4-10}$$

Solid/gas surface energy, γ_{SG}, is responsible for spreading the drop, and solid/liquid energy, γ_{SL}, is responsible for holding the drop together. The area of both interfaces should be the same, except with opposite signs, i.e., $A_{SL} = -A_{SG}$. The projected base area, A_P, is given by:

$$A_P = A_{SL} = -A_{SG} = \pi R^2\sin^2\theta\ . \tag{4-11}$$

Equations (4-7) and (4-8) could be rewritten as:

$$E = A_{LG}\gamma_{LG} + A_{SL}(\gamma_{SL} - \gamma_{SG}) \tag{4-12}$$

$$dE = 0 = \frac{dA_{LG}}{dA_{SL}}\gamma_{LG} + (\gamma_{SL} - \gamma_{SG}) \tag{4-13}$$

Applying conditions from Equations (4-9) to (4-13), Young's equation is obtained by minimizing the surface energy with respect to contact areas for a flat surface with Young's contact angle, θ_0:

$$\gamma_{SG} = \gamma_{SL} + \gamma_{LG}\cos\theta_0\ . \tag{4-14}$$

As a result, Young's equation states that the forces act in equilibrium on the contact line of the triple interfaces of solid, liquid, and gas. Assuming a constant volume, the drop radius R could be written in terms of V and θ so that the surface energy depends only on the contact angle. If so, the surface energy for a flat surface becomes:

$$E = \gamma(A_C - \cos\theta_o \, A_p) \tag{4-15}$$

For convenience, the solid/liquid interfacial area and the liquid/gas surface energy are equivalent to the surface tension of a liquid, γ_{LG}, and are replaced simply with γ. The liquid/gas interfacial area, A_{LG}, is replaced with A_C. The A_{SL} of a flat surface is projected by a flat surface area of the cap, A_P, for any contact angle θ.

In case of textured surfaces, additional parameters are needed to describe the surface geometries during wetting. The roughness parameters, r_f and ϕ, are introduced for rough surfaces, where r_f is the ratio of the actual area to the projection area and ϕ is the ratio of the top surface area to the projection area. An idealized situation, where rough surface is pillars extending from the surface, is shown in Figure 4-3.

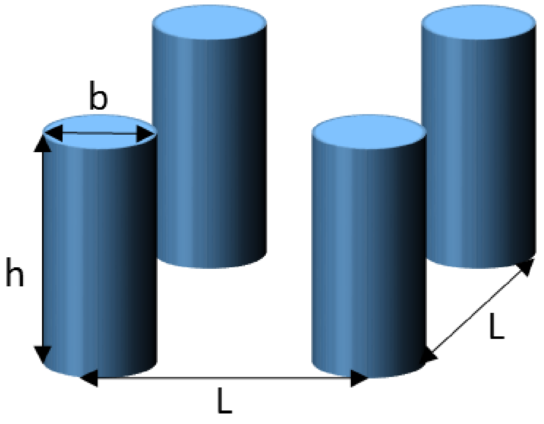

Fig. 4-3. Idealized representation of surface roughness, where *b* is the diameter, *h* is the height, and *L* is the center-to-center separation distance

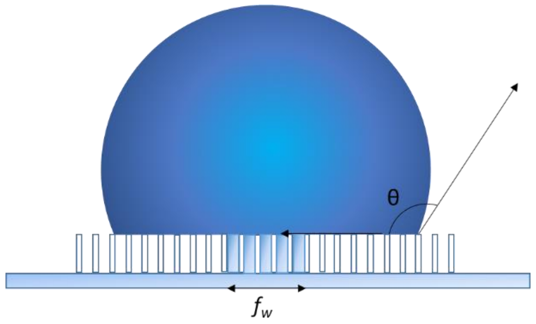

Fig. 4-4. Wetting on a textured surface

L, b, and h represent pillar-to-pillar distance, diameter of the cylinder top, and the height of the pillars, respectively. In this representation, r_f and ϕ can be presented as follows:

$$r_f = 1 + \frac{\pi b h}{L^2} \tag{4-16}$$

$$\phi = \frac{\pi b^2}{4L^2} \tag{4-17}$$

For evaluating an equilibrium contact angle in textured surface, the surface energy of a droplet can be found, as shown in Figure 4-4. A fraction of the liquid could penetrate the spaces between the pillars when liquid droplet rests on the rough surface and starts to spread.

A way to represent this phenomenon is needed in order to represent all wetting conditions on a rough surface. Therefore, f_w is introduced as the projected area fraction for a wetting space, where the fraction is between 0 and 1. The Cassie-Baxter state is achieved if f_w is 0, and the Wenzel state is achieved if f_w is 1, as shown in Figure 4-5.

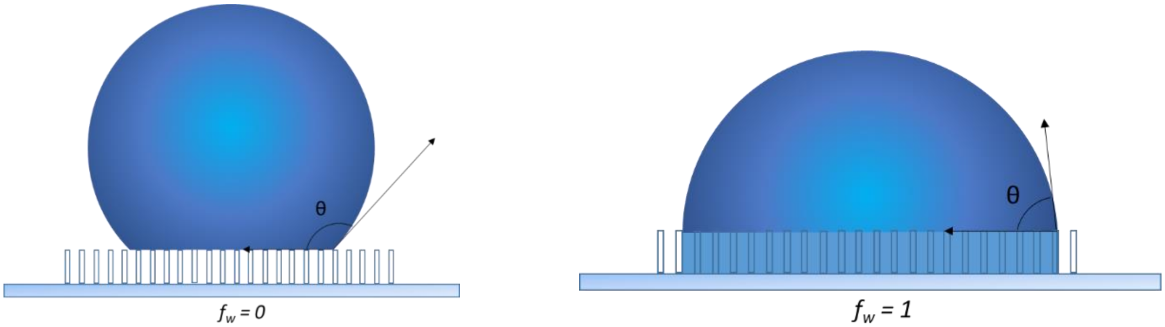

(a) (b)

Fig. 4-5. Droplet with different wetting conditions for (a) the Cassie-Baxter state and (b) the Wenzel state

Interfacial areas for liquid/gas, solid/liquid, and solid/gas should be found in order to determine the surface energy for a partially wetted textured surface. The liquid/gas area, A_{LG}, the solid/liquid area, A_{SL}, and the solid/gas area, A_{SG}, with given geometry parameters, are expressed in Equations (4-18) and (4-19):

$$A_{LG} = 2\pi R^2(1-\cos\theta) + (1-f_w)(1-\phi)\pi R^2 \sin^2\theta \qquad (4\text{-}18)$$

$$A_{SG} = -A_{SL} = \left[r_f f_w + \phi(1-f_w)\right](\pi R^2 \sin^2\theta)\ . \qquad (4\text{-}19)$$

Substitute Equations (4-10) and (4-11) for the droplet cap and projection area, A_C and A_P, respectively, into Equations (4-20) and (4-21):

$$A_{LG} = A_C + (1-f_w)(1-\phi)A_P \qquad (4\text{-}20)$$

$$A_{SG} = -A_{SL} = \left[r_f f_w + \phi(1-f_w)\right]A_P \qquad (4\text{-}21)$$

When substituting Equations (4-18) and (4-19) into Equation (4-12), the surface energy becomes:

$$E = \left[A_C + (1-f_w)(1-\phi)A_P\right]\gamma_{LG} + \left\{\left[r_f f_w + \phi(1-f_w)\right]A_P\right\}(\gamma_{SL} - \gamma_{SG}) \qquad (4\text{-}22)$$

Using results for Young's contact angle from Equation (4-15) and substituting into Equation (4-22):

$$E = \gamma\left[A_C - A_P\left(\left[r_f f_w + \phi(1-f_w)\right]\cos\theta_0 - (1-f_w)(1-\phi)\right)\right] \qquad (4\text{-}23)$$

where $A_C = 2\pi R^2(1-\cos\theta)$ and $A_P = \pi R^2 \sin^2\theta$.

An equilibrium contact angle can be achieved when the surface energy is minimized and the differential of energy with respect to the contact angle is zero:

$$\frac{dE}{d\theta} = 0 = \gamma\left[\frac{dA_C}{d\theta} - \frac{dA_P}{d\theta}\left(\left[r_f f_w + \phi(1-f_w)\right]\cos\theta_0 - (1-f_w)(1-\phi)\right)\right] \qquad (4\text{-}24)$$

When both sides are divided by γ and $dA_P/d\theta$, Equation (4-24) becomes:

$$\left(\frac{dA_C}{d\theta}\right)\Big/\left(\frac{dA_P}{d\theta}\right) = \left[r_f f_w + \phi(1-f_w)\right]\cos\theta_0 - (1-f_w)(1-\phi) \qquad (4\text{-}25)$$

By simplifying left-hand side of Equation (4-25), equilibrium angle, θ_E, for a partially wetted textured surface is given as:

$$\cos\theta_E = \left[r_f f_w + \phi(1-f_w)\right]\cos\theta_0 - (1-f_w)(1-\phi). \qquad (4\text{-}26)$$

If no liquid penetrates into the spaces between the structures, then $f_w = 0$, and the Cassie-Baxter equation is extracted from Equation (4-26):

$$\cos\theta_E = \phi\cos\theta_0 - (1-\phi) \tag{4-27}$$

If spaces between structures are fully wetted, then $f_w = 1$ and Wenzel's equation can be extracted from Equation (4-26):

$$\cos\theta_E = r_f\cos\theta_0. \tag{4-28}$$

The equilibrium angle on a textured surface can be found with the given geometries, the contact angle on a flat surface, and the degree of wetting on a rough surface from Equation (4-26).

Contact angle hysteresis occurs while an external force acts on a droplet. This could be viewed as extra energy acting on the system. This extra energy is included as an additional term in the surface energy equation:

$$E = E_{drop} + E_{hys} \tag{4-29}$$

Hysteresis energy, E_{hys}, acts on the triple-phase contact line between solid, liquid, and gas, as shown in Figure 4-6.

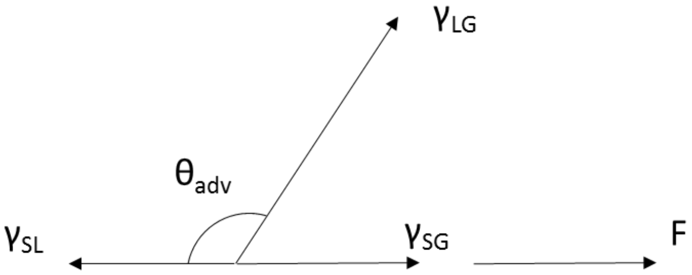

Fig.4-6. Hysteresis energy acts on the triple-phase contact line

It is assumed that line force *F* acts in parallel to the wetting surface, and should be a minimum force that is required in order for the triple-phase contact line to move. Line force *F* is proportional to the difference between the equilibrium angle and the advancing or receding angle. In case of an advancing angle, it should be written as:

$$F = \gamma(\cos\theta_E - \cos\theta) \tag{4-30}$$

Hysteresis energy acts on solid/gas and solid/liquid interfacial areas in order for a contact line to move parallel to the wetting surface. The hysteresis energy could be written as:

$$E_{hys} = \gamma(\cos\theta_E - \cos\theta)\left[r_f f_w + \phi(1-f_w)\right]A_P = F * T_2 \tag{4-31}$$

where:

$$F = \gamma(\cos\theta_E - \cos\theta)$$

$$T_2 = \left[r_f f_w + \phi(1-f_w)\right]A_P\,.$$

F represents the line force with differences on the cosine of the equilibrium and maximum contact angles. T_2 represents contact areas underneath the drop. Substitute Equations (4-23) and (4-31) into Equation (4-29) to get:

$$E = \gamma\{A_C - A_P D_1\} \tag{4-32}$$

where:

$$D_1 = \left[r_f f_w + \phi(1-f_w)\right]\left(\cos\theta_0 + (\cos\theta_E - \cos\theta)\right) - (1-f_w)(1-\phi).$$

Take *dE/dθ = 0* in Equation (4-32) to find max/min angles:

$$\frac{dE}{d\theta} = 0 = \gamma \left\{ \frac{dA_C}{d\theta} - \left(\frac{dA_P}{d\theta} \right) K - A_p \left(\frac{dK}{d\theta} \right) \right\} \tag{4-33}$$

where:

$$K_1 = \left[r_f f_w + \phi(1 - f_w) \right] \left(\cos\theta_0 + (\cos\theta_E - \cos\theta) \right) - (1 - f_w)(1 - \phi)$$

Divide Equation (4-33) by $dA_P/d\theta$ and γ to get:

$$0 = \frac{dA_C/d\theta}{dA_P/d\theta} - K_1 - \frac{A_P}{dA_P/d\theta} \left(\frac{dK_1}{d\theta} \right) \tag{4-34}$$

$$\frac{dA_C/d\theta}{dA_p/d\theta} = \cos\theta$$

$$K_1 = \left[r_f f_w + \phi(1 - f_w) \right] (\cos\theta_0 + (\cos\theta_E - \cos\theta)) - (1 - f_w)(1 - \phi)$$

$$A_P = \pi R^2 \sin^2\theta , \frac{dA_P}{d\theta} = 2\pi R \left(\frac{dR}{d\theta} \right) \sin^2\theta + 2\pi R^2 \sin\theta \cos\theta$$

$$= 2\pi R \sin\theta \left(\frac{dR}{d\theta} \sin\theta + R\cos\theta \right)$$

$$R = \left(\frac{3V}{\pi} \right)^{\frac{1}{3}} [2 - 3\cos\theta + \cos^3\theta]^{-\frac{1}{3}}, \frac{dR}{d\theta} = -\left(\frac{3V}{\pi} \right)^{\frac{1}{3}} \sin^3\theta \, (2 - 3\cos\theta + \cos^3\theta)^{-\frac{4}{3}}$$

$$\frac{dK_1}{d\theta} = 2\left[r_f f_w + \phi(1 - f_w) \right] \sin\theta \, .$$

Simplify Equation (4-34) to obtain:

$$\cos\theta = \left(f_w \left(r_f - \phi \right) + \phi \right) C_1 - (1 - f_w)(1 - \phi) \tag{4-35}$$

where:

$$C_1 = \cos\theta_0 + \cos\theta_E - \cos\theta + \frac{1}{2} \sin^2\theta \, (\cos\theta + 2).$$

Thus, max/min angles can be solved with Equation (4-35) for known surface geometries and Young's contact angle.

For study in a model, from Equations (4-16) and (4-17), the roughness factor, r_f, and the top-area projection factor, ϕ, are idealized as cylinders on a flat surface. The surface energy profile given in Equation (4-23) can change with varying pillar geometries and spacing. Changes in surface energy profiles in relation to varying contact angles are shown in Figure 4-7 for Young's contact angle, θ_0 = 60°, θ_0 = 90°, and θ_0 = 120° for different f_w values; surface geometries are set at b = 1μm, h = 2 μm, and L = 3 μm. CAH can be affected by surface geometry factors as well as the ratio of a fully wetted area. Figure 4-8 demonstrates how CAH can be changed by varying the ratio of the fully wetted projected area with different pillar heights (h = 0.5 μm, 1 μm, and 2 μm), while b and L are fixed at 1 μm and 3 μm, respectively. Figure 4-9 shows how CAH depends on changing the local flat-surface contact angle under varying wetting conditions. Surface geometries are fixed at b = 1 μm, h = 2 μm, and L = 3 μm.

An increase in pillar height increases surface roughness and Figure 4-9 shows that CAH increases as roughness increases at θ_0 = 90° across all values of wetting area ratio, f_w. CAH increases in θ_0 = 60° for $f_w \leq 0.7$ but decreases for $f_w \geq 0.7$ as surface roughness increases. In the case of θ_0 = 120°, CAH decreases as roughness increases in all f_w values. At θ_0 = 90°, increases on CAH with increasing roughness ratio could be explained as more liquid/solid contact area is presented for the same value of f_w. Therefore, higher roughness ratio increases CAH. With a hydrophilic surface for $\theta_0 \leq$ 90°, the contact angle is decreased as roughness increases; therefore, CAH increases with roughness. However, the contact angle decreases at a faster rate as f_w increases. As shown in Figure 4-7, the droplet approaches filmwise at a faster rate as the wetting area increases, and CAH decreases at a higher value of f_w. The equilibrium contact angle increases on a hydrophobic surface at a high value of the roughness ratio, as shown in Equation (4-26). The equilibrium contact angle increases at a faster rate at an increasing roughness ratio than the contact angle during the hysteresis state. Therefore, CAH decreases with an increased roughness ratio.

In a different roughness profile, CAH trends remain similar with respect to the projected wetting ratio, f_w, for each corresponding local Young's contact angle, θ_0. Peak values are shown in Figure 4-7 for θ_0 = 60°. This was explained earlier that as wetting area increases, CAH increases accordingly; at a high wetting ratio, f_w, as the contact angle approaches zero, CAH also decreases. At θ_0 = 90°, CAH increases as f_w increases; however, the rate of increase slows at higher values of f_w. For intermediate Young's contact angles, an increasing solid/liquid contact area increases the surface energy; as a result, CAH increases. However, values for the equilibrium contact angle remain similar at higher values of f_w; therefore, CAH remains flat at high wetting-area ratios. In cases of θ_0 = 120°, CAH increases with increasing f_w. This is due to a higher contact area of solid/liquid. When the drop spreads into spaces between the pillars, more and more energy is required to move contact line of the drop. When the liquid is trapped inside the spaces between the gaps in a textured hydrophobic surface, it does not tend to spread to other areas very easily. The liquid stagnates inside the gaps, thus more energy is required to induce movement on the contact line of a drop. CAH would increase with increasing values of f_w as a result. With fixed surface geometries, CAH increased with increasing wetted areas in hydrophobic surface for $\theta_0 \geq 90°$, as shown in Figure 4-9. In a hydrophilic surface with $\theta_0 \leq 90°$, aside from a non-wetted surface where f_w = 0, CAH values are lower at $f_w > 0.75$; this phenomenon is more apparent when values for θ_0 decrease. Figure 4-9 shows that CAH values are at a peak with f_w = 0.5 if the surface is hydrophilic. These phenomena are explained earlier for individual cases with regard to hydrophobic and hydrophilic textured surfaces. At f_w = 0, CAH remains flat and small with varying Young's contact angles. A minimum solid/liquid contact area is maintained; thus, little energy is required to move droplet contact line. At f_w = 0.25, CAH decreases with increasing θ_0. The droplet starts to spread out and the solid/liquid contact area increases. Since the contact line requires more energy to move in hydrophilic surfaces than hydrophobic surfaces, the CAH tends to be higher with lower values of θ_0. At f_w = 0.5, a similar trend is seen in the case for CAH vs. θ_0. The peak at CAH starts to form with θ_0. Since the contact area for solid/liquid is increased, more energy is needed to move contact line in hydrophilic surface. At lower values of θ_0, the drop starts to spread out and approach film-wise, and the CAH starts to decrease. In cases of f_w = 0.75 and f_w = 1, there are clear maximum values of CAH with respect to Young's contact angle. The droplet spreads out to be closer to the film at a higher value of f_w as θ_0 decreases; thus, the CAH is lower as a result. As θ_0 increases, the equilibrium angle also increases; however, the maximum angle increases at a slower rate at the same time, as indicated in Equations (4-29) and (4-35).

In a single-drop dynamic model, contact angle hysteresis can be estimated using theories of surface energies. Roughness and the projected top-area ratios affect the surface energy profile with fixed Young's contact angles. Differences between surface energies in equilibrium states and the hysteresis state generally increase as the wetted solid/liquid area increases. However, differences in surface energies decrease in hydrophilic surfaces with increased wetted areas and roughness ratios. This indicates that the CAH can be lower when droplet is in Wenzel's state than in partially wetted states. Differences in surface energies at low and high contact angles remain small in all wetting conditions. Results indicate that the CAH remains low when Young's angle is either super-hydrophilic or super-hydrophobic ($\theta_0 \approx 0$ or $\theta_0 \geq 150°$). It was found that CAH remains low with any Young's contact angle when the ratio for the totally wetted surface area is small. Further, CAH increases with increased roughness, in general. However, CAH was shown to have an optimum value with varying the wetted area ratio when the surface is hydrophilic. Moreover, CAH was shown to be lower with a higher roughness ratio when the wetting ratio is high ($f_w > 0.7$). Generally, CAH values increased when comparing CAH against various Young's contact angles. In addition, peak values of CAH started to form with Young's contact angles with increased wetting. CAH decreased with increasing Young's contact angles at $f_w < 0.5$. Low values of CAH were shown to be either super-hydrophilic or super-hydrophobic ($\theta_0 \approx 0$ or $\theta_0 \geq 150°$), as previously indicated. Droplet sizes in condensation often are determined when the contact line starts to move.

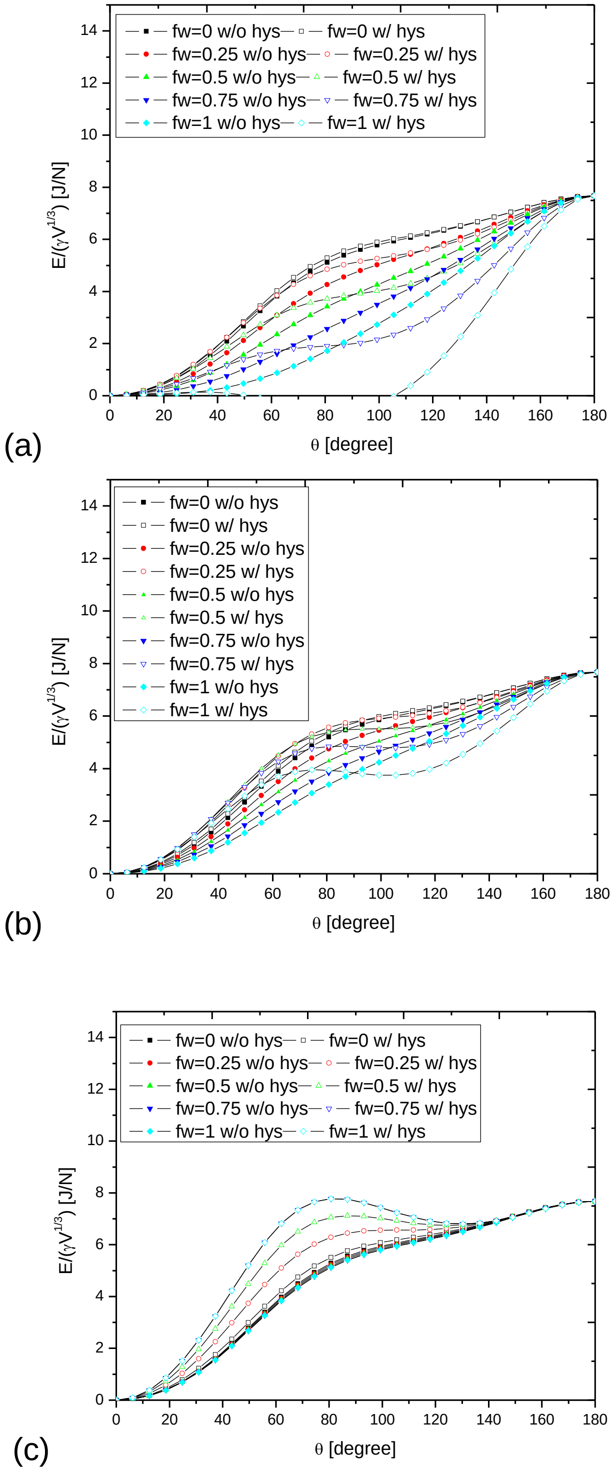

Fig.4-7 Surface energy profiles vs. contact angles for (a) θ_0 = 60°, (b) θ_0 = 90°, and (c) θ_0 = 120°, where *b* = 1 µm, *h* = 2 µm, and *L* = 3 µm

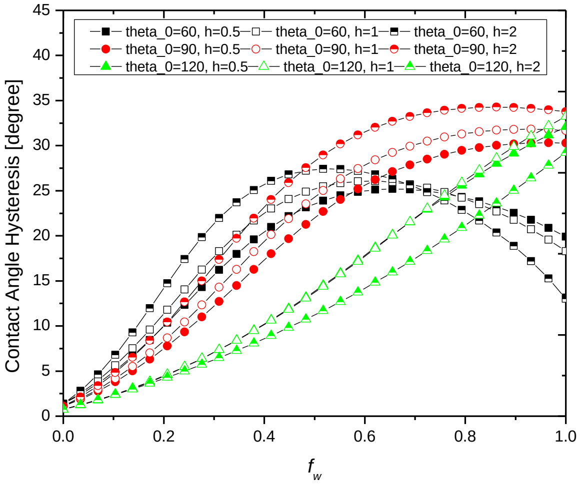

Fig. 4-8 Contact angle hysteresis vs. fully wetted projection-area ratio, *b* = 1 µm and *L* = 3 µm

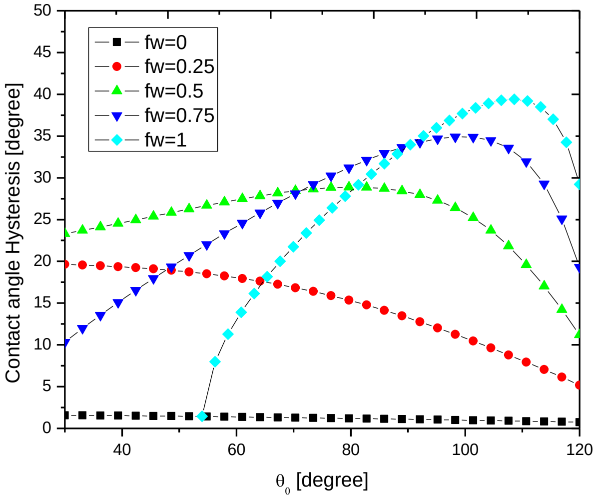

Fig. 4-9 Contact angle hysteresis vs. Young's contact angles, *b* = 1 µm, *h* = 2 µm, and *L* = 3 µm

- ***Experiments***

Experiments were designed to determine the degree of wetting based on the relationship between pressure conditions and contact angle. Common methods to promote the "dropwise" condensation are surface treatments on condensing surfaces using hydrophobic coatings, which can shift condensation modes from filmwise (FWC) to the dropwise (DWC). It is also important that super- or ultrahydrophobicity-induced water droplet rolling off motions (called *self-cleaning*) can increase condenser performance by increasing the rate of refreshing the surfaces.

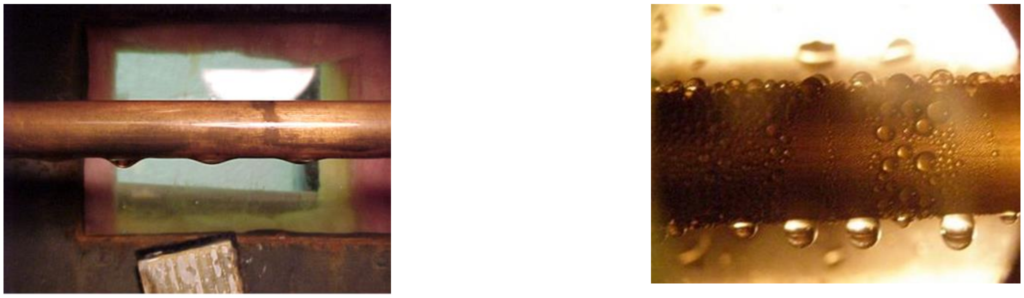

Fig. 4-10 Example photographs of filmwise (left) and dropwise (right) condensation

Excellent examples of hydrophobic surfaces can be found in bio-inspired design such as rose petals and water strider, which utilize hierarchical cell-structures to achieve superhydrophobicity. Biologically inspired hybrid structures were prepared by using Copper Oxide Self-Assembly (COSA). As shown in Figure 4-11, COSA shows different morphologies, which are controlled by thermodynamically and/or kinetically controlled oxidation condition. At poor oxidation condition (lower concentration and/or shorter reaction time), single tier structure with low aspect ratio is shown in Figure 4-11(a). At good oxidation condition (higher concentration and/or longer reaction time), micro- and nano-hybridized double tier structure is shown in Figure 4-11(b). Hydrophobic coated COSA can effectively prevent water droplets from impinging on a surface by entrapping gas within the micro- and nano-grooves.

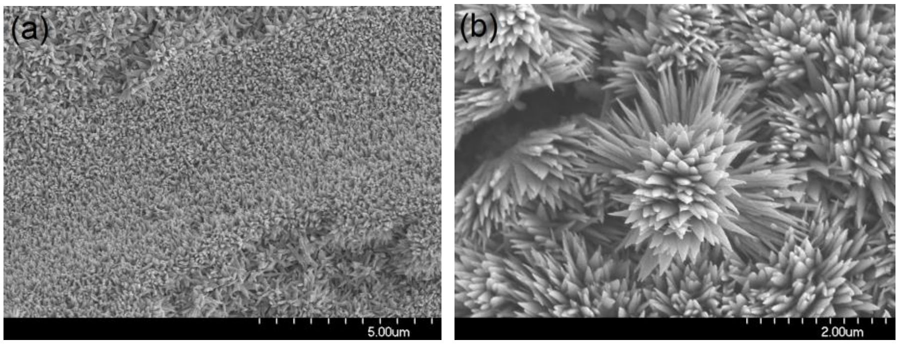

Fig. 4-11 FE-SEM images of COSA with different morphologies: (a) Single tier structure (x10,000) (b) Double tier structure (× 20,000)

The chemical interaction of the COSA in aqueous base solution can be summarized as

$$Cu_2^+ + 2OH^- \rightarrow Cu(OH)_2 \rightarrow CuO + H_2O \qquad (4\text{-}36)$$

Highly fluorinated polymers with low surface energy such as PTFE and PVDF have been widely used to make a hydrophobic surface. Their hydrophobicity can be utilized for water impingement applications such as water proofing and DWC.

Polyphenylene sulfide (PPS) would be another approach to make a hydrophobic coating. Since PPS is widely used in diverse engineering fields due to its hydrophobicity as well as durability, it can be a good candidate for condensation surface materials for heavy duty industrial applications. In spite of hydrophobicity of PPS coating, its low thermal conductivity might be detrimental to heat transfer performance. In order to overcome the thermal conductivity issue, carbon nanotubes (CNTs) were added. The CNTs in the PPS coating play a role in increasing thermal conductivity as well as hydrophobicity.

The preparation of multiple-tiered COSA was followed by previous methods described elsewhere [40]. In order to introduce polymeric coatings on the condensing substrate (copper), the following methods were used:

The substrates for testing surfaces are copper alloy 122 tubes with an outside diameter of 15.9 mm, a wall thickness of 0.813 mm, and a length of 914 mm. First, the substrate surfaces were prepared by polishing with a 150 grid sand-paper and then cleaned with ethanol and acetone solutions before applying coatings and etching. Two types of coating solutions were prepared for the polymer-based coatings which were solutions of PPS with CNT and Polytetrafluoro ethylene (PTFE). For PTFE coatings, PEG (Polyethlylene glycol) is used as a binder solution mixed in $(NH_4)_2CO_3$ solution, so that a nano-porous network can be formed on the condenser surfaces during the melting process of PPS compounds in an oven at 340°C for four hours with decomposing of the solution $(NH_4)_2CO_3$ into CO_2 and NH_3 and forming escaping gases from the coatings. The compositions of PPS based coating are summarized and listed in Table 4-1.

Table 4-1 Composition of other coatings

Composition	PPS	PTFE	SiC	$(NH_4)_2CO_3$	PEG	CNT
PPS coating	36 g	20g	4g	20 g	1 g	3 g

PTFE compounds obtained from DuPont were used for the test surfaces which were prepared by following the procedure offered by DuPont. It is a two-step procedure for applying a primary coating (DuPont, 850G-204) and a top coating (DuPont 852N-201).

Another type of surface of interest is nano-conic structure. This effort was done by looking at TiO_2 nanostructures. In particular, we prepared TiO_2 nano-conic structure. Titanium foil was obtained from Sigma-Aldrich (99.7 %, 0.127 mm thick) and used as it was received without further surface treatment. The Ti foil was cut into 1 cm x 4 cm and chemically cleaned in acetone and ethanol (1:1 by vol) under ultrasonication for ten minutes. Aqueous 1.0 M H_3PO_4 with 0.5 wt % NH_4F electrolytes were prepared. After the addition of the fluoride source to the solution, the mixture was stirred for two hours to fully dissolve the salt at room temperature. The Ti specimen was then anodized in potentiostatic mode (10–100 V) at room temperature in the electrolytes. An Agilent N5771A DC power supply was used for all tests. After anodization, specimens were thoroughly rinsed with ethanol followed by de-ionized water. Individual specimens were fully dried in the oven at 95 ºC overnight. Figure 4-12 shows titania nano cone that was produced by anodizing technique.

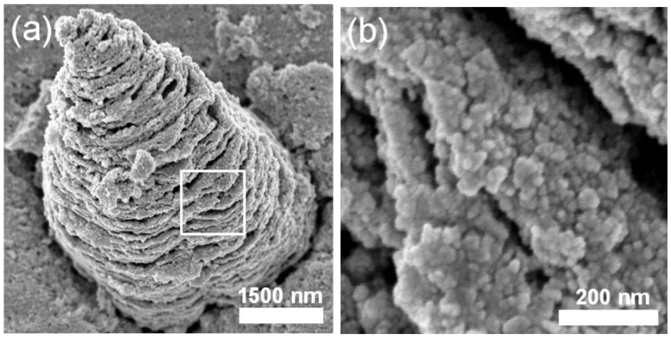

Fig. 4-12 FE-SEM images of titania nano cone (TNC) anodized at 40 V in 1.0 M H_3PO_4 with 0.5 wt % NH_4F: a Tilted view of TNC and b higher magnification of TNC ruffles (represented in square in Figure 11a decorated with titania nano sphere (TNS)

Task 4.2 Surface Characterization

Firstly, surface morphologies were examined using a Field-Emission Scanning Electron Microscope (FE-SEM, Hitachi). For PPS/CNT, there is no specific structure observed in Figure 4-13(a). On the contrary, PTFE surface shows numerous tiny holes, of which size ranges are ~ 100-500 nm in Figure 4-13(b). It is assumed that when PTFE cures at high temperature, evaporating solvents and gas from curing agent create cavities on the surface. The COSA prepared in this study shows numerous cavities, which are created by hybridized substructures.

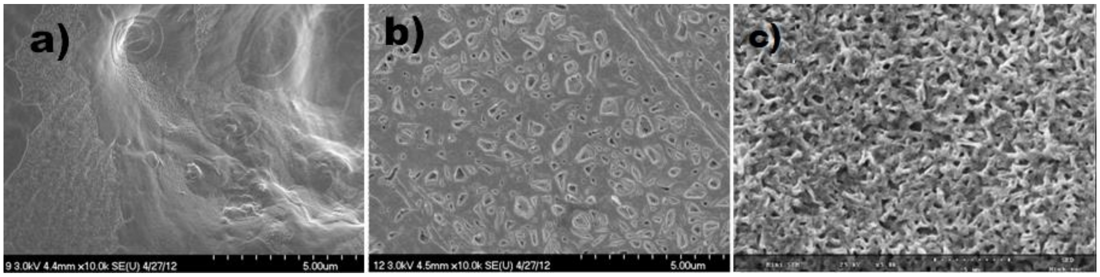

Fig. 4-13 FE-SEM images of various surfaces: (a)PPS/CNT (10k ×), (b)PTFE (10k ×), (c)COSA (5k ×)

Water Contact Angles (WCA) were measured using a goniometer (KSV CAM100) to perform surface characterization. The images of WCAs on the surfaces are shown in Figure 4-14. For PPS/CNT surface, WCA is measured ~143º in Figure 4-14(a). In general, without addition of CNT, PPS-coated surface shows little bit lower WCA ~120º. Since CNT alone shows superhydrophobicity (> 150º), the amount of added CNT determines WCA of a composite surface of PPS and CNT. In this study, the amount of CNT is limited to less than 10 wt% and it leads to approximately 20% improvement in WCA. For PTFE, WCA is measured ~120º in Figure 4-14(b). In spite of low surface energy of PTFE coating alone, WCA is not dramatically improved without substructure formation. It implies that tiny holes on the PTFE surface do not contribute to WCA improvement. The COSA shows a superhydrophobic surface (> 150º) in Figure 4-14(c). The enhanced WCA is ascribed to a combination of a self-assembly monolayer (SAM) hydrophobic coating (dodecanethiol) and a hybridized substructure. Copper surface shows WCA ~77º, which is hydrophilic (< 90º) in Figure 4-14(d). Individual WCA of various surfaces are summarized in Table 4-2.

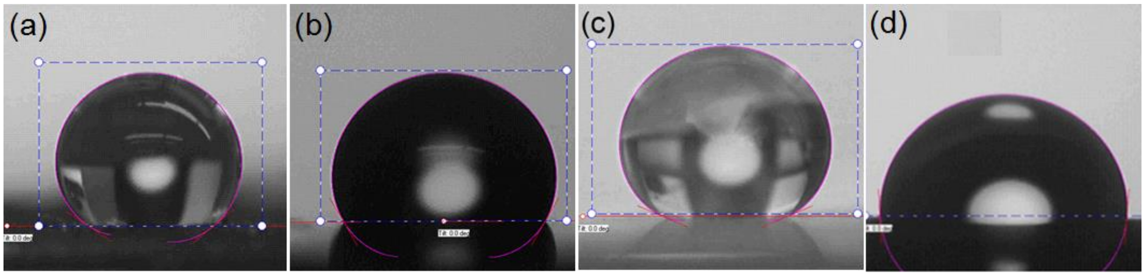

Fig. 4-14 Images of water contact angles on surface-treated substrates
(a) PPS/CNT based coating, (b) PTFE based coating, (c) COSA and (d) copper surface

Surface energy is one of the important parameters to induce DWC mechanism. Baojin et al. [41] suggested a method to estimate surface energy using following formulation:

$$\gamma = \gamma^h + \gamma^d \tag{4-37}$$

where γ is the total surface energy. γ^h is the surface energy component due to a hydrogen bonding and dipole-dipole interaction and γ^d is a dispersion component of surface energy. In order to obtain experimentally determined surface energy, Baojin et al. [41] proposed the following formulations:

$$\gamma^h = \left(\frac{137.5 + 256.1\cos\theta_{H_2O} - 118.6\cos\theta_{CH_2I_2}}{44.92} \right)^2 \tag{4-38}$$

$$\gamma^d = \left(\frac{139.9 + 181.4 \cos\theta_{CH_2I_2} - 41.5 \cos\theta_{H_2O}}{44.92} \right)^2 \tag{4-39}$$

In addition to WCA test, contact angle test using methylene iodide (CH_2I_2) was conducted as shown in Figure 4-15. The contact angle on the PPS/CNT composite shows 98° in Figure 4-15(a). Although the PTFE coating shows somewhat lower WCA ~89° compared to the PTFE case in Figure 4-15(b), contact angles for polymer-based coatings are close to 90°. It implies that liquid spreading is limited by polymer coatings with low surface energy. For the COSA, contact angle is ~75° in Figure 4-15(c). Copper surface shows much smaller number in contact angle compared to other surfaces (~33°) in Figure 4-15(d).

Based on the contact angle results, surface energies of different surfaces are estimated using Equations (4-37)-(4-39) and listed in Table 4-2. Polymer-based coatings have lower surface energies, while the COSA and copper surface have higher surface energies. The total surface energy (γ) depends mostly on the dispersion surface energy (γ^d).

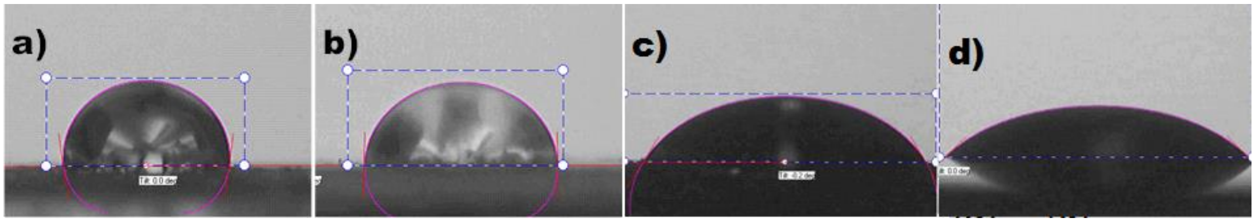

Fig. 4-15 Images of methylene iodide (CH_2I_2) contact angles on surfaces (a) PPS/CNT based coating, (b) PTFE based coating, (c) COSA and (d) copper surface

Table 4-2 Contact angles on the surfaces

Surfaces	Water (°)	CH_2I_2 (°)	γ^h (mJ/m^2)	γ^d (mJ/m^2)	γ (mJ/m^2)
PPS/CNT based coating	144	98	1.35	10.9	12.2
PTFE based coating	120	89	0.02	13.3	13.3
COSA	157	75	8.12	25.0	33.1
copper	77	33	2.51	10.8	44

For titania nano cone, series of time-elapsed morphology evolution micrographs using FE-SEM were taken. As shown in Figure 4-16, initially, numerous nanoparticles, which are nucleated from a titanium substrate during the anodic oxidation process, are observed. The diameter of each particle is approximately 20 nm. The nanoparticles begin to form aggregates as the anodizing process continues.

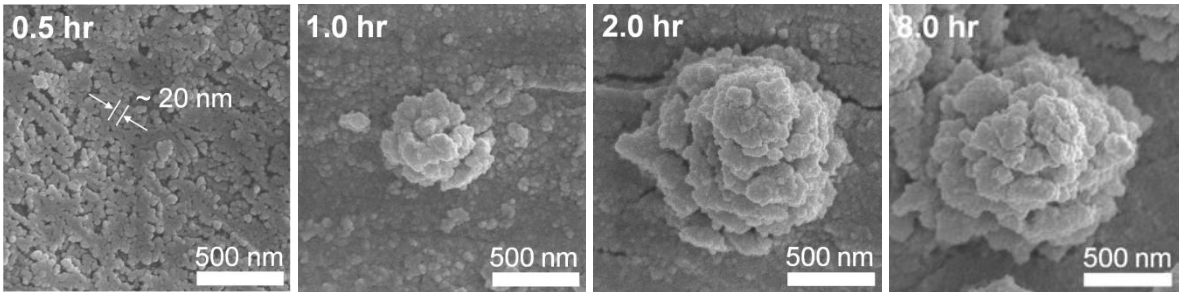

Fig. 4-16 FE-SEM images and schematic illustration of the time-lapsed TNC evolutions from TNS

One challenging issue regarding TNC and TNS is to find an effective way to create them on the surface of copper tubing where condensation occurs. Therefore, despite their interesting nano- and micro structures, the steam condensation testing for TNC and TNS was not conducted in this study.

Task 4.3 Steam Condensation Testing

The condensation heat transfer tests were conducted by using condensation experimental setup as shown in Figure 4-17. The test apparatus consists of a test section, a cooling loop, and a boiler. The test section consists of condensing chamber which can support to test thee condensing tubes, view ports, valves with plumbing, and measuring instruments. The cooling loop is operated by a chiller/circulator (Affinity, model RWE-012K) with a controlled temperature. The coolant from the chiller flows inside the test tubes. The boiler generates steam by a submerged heating coil. A hot compressed water controlled by the heater (Advantage Engineering, model Sentra SK-1035 HE) flows inside of the heating coil to generate steam. The steam line is connected to the upper parts of boiler and the test section to provide water vapor during the tests, while the condensate from test tubes falls on the bottom of the condensing chamber and flows back to the boiler through the condensate line connected at the bottom of the condensing chamber and boiler.

The inlet and outlet of the coolant temperatures were measured by RTDs (OMEGA, class A, ±0.35˚C), and the chamber and steam temperature were measured by T-type thermocouples (±0.5˚C). The pressure of the chamber and boiler were measured by pressure transducers (AST, AST4300, 0 - 345 kPa, ±0.5%). The coolant flow rate was measured by a rotameter (Blue & White, F-440, 0- 5 GPM, ±4% of full scale).

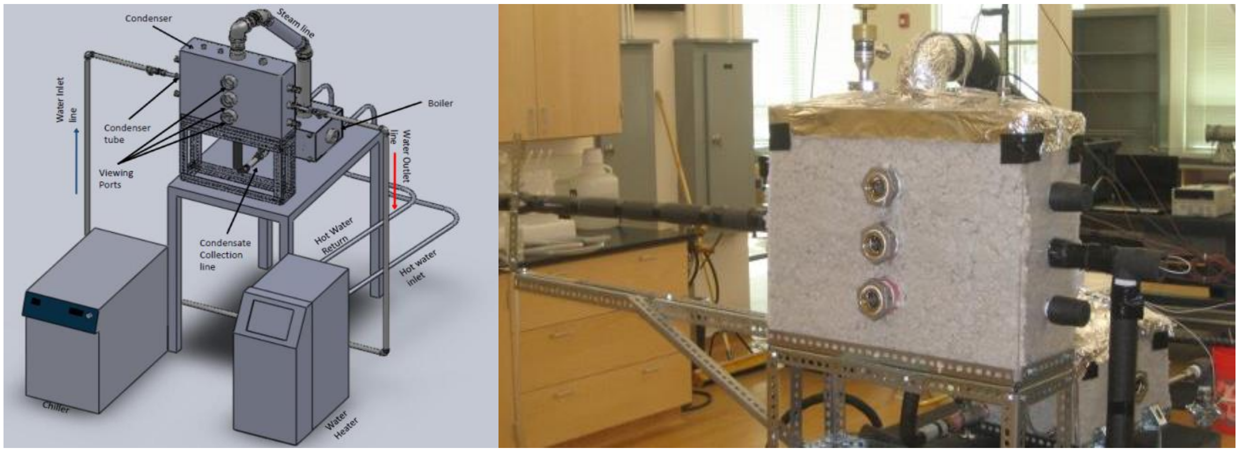

Fig. 4-17 Schematic diagrams of condensation experimental apparatus

Before experiments, the condensing chamber was vacuumed by a vacuum pump connected at the top of the condensing chamber so that non-condensable gases in the condensing chamber are expelled to the atmosphere. The camber was vacuumed until water could boil at the vacuum pressure and the pressure of the condensing chamber was monitored for any leakage. A check valve was installed in the vacuum line to prevent any back flow of air even when the vacuum pump is stopped. Once the leakage of the test setup was verified, the boiler was used to generate steam, so that the water vapor could enter the condensing chamber. During this procedure, the chiller was turned on and coolant inlet temperature was controlled to provide an appropriate temperature of subcooling. Once the system reached steady state with steady temperatures and pressures of the test section continuously for 5 minutes, data was recorded for the heat transfer performance analysis.

Steam condensation tests were conducted with water saturation pressure ranging between 95–45 kPa and the coolant inlet temperature ranging between 90-40˚C, which makes the subcooling range between 0.5–30K. Different types of surface-treated tubes were tested for external condensation performance: A plain copper, a COSA with a SAM hydrophobic coating, a PPT/CNT-coated tube, and a PTFE-coated tube. For the test, a concentric tube-and-tube heat exchanger was used to increase coolant velocity, so that effect of the coolant side thermal resistances could be minimized.

Visual inspection was conducted during the condensation experiments, which are shown in Figure 4-18. Condensates are nucleated on the tube surfaces. They grow and coalesce with adjacent condensates and form larger drops. Once the condensates reach critical size, the large condensates roll from the surfaces and sweep other immature condensates along the tube periphery, which refresh condensing surfaces. During sweep over, condensate heat transfer coefficient (CHTC) is significantly improved. At the bottom of the tubes, condensates detach from the surface. Depending on the detachment frequency, CHTC of the bottom part is determined. Figure 4-18(a) shows the steam condensation on the PPS/CNT composite surface with subcooling temperature. Once condensates nucleate on the surface, they agglomerate and transform into filmwise condensates. Overall surface is easily covered with condensate films, which flow along the periphery. At the bottom of the tube, a larger condensate lingers. Mean diameter and height of condensates are 7.8 mm and 3.3 mm, respectively. Wide base diameter prohibits detachment of condensate out of the surface. Also, enhanced condensate height plays a role of thermal resistance, which deteriorates CHTC.

For the PTFE coated surfaces, a visualized snapshot at 6.7K is shown in Figure 4-18(b). Overall, the surface is covered with numerous tiny condensates where diameter is less than 1 mm. In spite of droplet-shaped condensates, individual condensates rarely roll down due to hysteresis. Although condensate size is small enough not to prohibit heat transfer, lingering condensates retard nucleation cycle. At the bottom of the tubes, the size of condensation agglomerates is 3.1mm in width and 2.5 mm in height.

For COSA surfaces, there is a combination of different condensation modes (DWC+FWC) in Figure 4-18(c). Except the bottom section, drop-shaped condensates are usually seen on the surface. Individual condensates have high detachment frequency (>1 Hz) compared to other surfaces. Therefore, enhanced nucleation cycles increase CHTC. On the bottom, aggregated condensates are close to FWC pattern. Presumably, compared to the number of condensates, which are rolling down to the bottom, surface area is limited and several spots begin to show flooding phenomena. In spite of FWC pattern, detachment frequency is relatively high. Mean diameter and height of condensates are 8.0 mm and 1.2 mm, respectively.

Similar condensation pattern is observed for copper surface in Figure 4-18(d). However, condensate detachment frequency is relatively smaller than COSA surface. The retarded rolling motion prevents significant FWC formation at the bottom. As indicated in visualization of the COSA surface, enhanced detachment frequency can lead to over populated condensates and FWC pattern. Mean diameter and height are 6.2 mm and 1.6 mm, respectively.

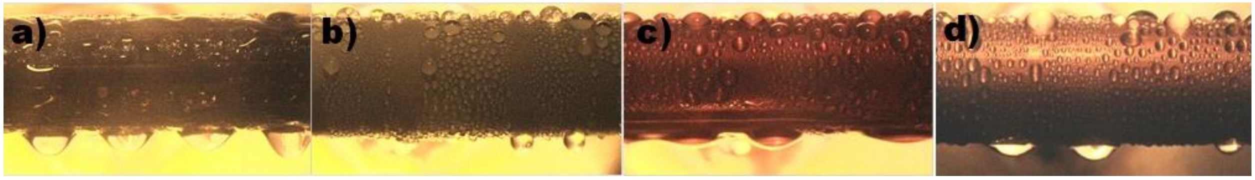

Fig. 4-18 Visualization during steam condensation
(a) PPS/CNT coating, T_{sub} = 4.7K (b) PTFE coating, T_{sub} = 6.7K (c) COSA, T_{sub} = 5.0K (d) copper, T_{sub} = 3.3K (tube diameter 15.9 mm)

After visual inspection, heat transfer data was obtained and thermal resistance analysis was conducted to evaluate the condensation performance of each specimen.

The coolant side heat duty during the condensation was obtained by

$$Q_c = \dot{m}_c \cdot cp_c \cdot \left(T_{c,o} - T_{c,i}\right) \tag{4-40}$$

The overall heat transfer coefficient is calculated by

$$Q_c = UA_{t,o} \cdot (T_{sat} - T_{c,ave}) \tag{4.41}$$

where U and $A_{t,o}$ are overall heat transfer coefficient and outer surface area of plain brass tube, respectively. T_{sat} is saturation temperature of water at the pressure of the chamber.

The total thermal resistance is obtained by,

$$R_{tot} = 1/UA_{t,o} \tag{4.42}$$

The total thermal resistance consists of thermal resistances of coolant side (R_c), tube wall (R_w) and condensations (R_{cond}), which is given by

$$R_{tot} = R_c + R_w + R_{cond} \tag{4.43}$$

The thermal resistance of coolant side is as follows,

$$R_c = 1/(h_c A_{t,i}) \tag{4.44}$$

where h_c and $A_{t,i}$ are a heat transfer coefficient of coolant and an inner surface area of plain brass tube, respectively. The heat transfer coefficient of coolant side (h_c) is obtained by,

$$\mathrm{Nu}_c = \frac{h_c D_d}{k_c} = \frac{\frac{f}{8}(\mathrm{Re}_c - 1000)\,\mathrm{Pr}_c}{1 + 12.7(f/8)^{0.5}\left(\mathrm{Pr}_c^{2/3} - 1\right)}, \quad \begin{array}{c} 3\times10^3 \le \mathrm{Re}_c \le 5\times10^6 \\ 0.5 \le \mathrm{Pr}_c \le 2000 \end{array} \tag{4.45}$$

where D_d is a hydraulic diameter of concentric tube and f is a friction factor which is given by,

$$f = [0.790 \ln(\mathrm{Re}_h) - 1.64]^{-2}, \qquad 3\times10^3 \le \mathrm{Re}_h \le 5\times10^6 \tag{4.46}$$

The thermal resistance of the tube wall (R_w) is calculated by

$$R_w = \frac{\ln\left(D_{t,o} / D_{t,i}\right)}{2\pi k_t\,(L_{t,o})} \tag{4.47}$$

where $D_{t,o}$ and $D_{t,i}$ are inner and outer diameters of the brass tube, respectively and k_t is the thermal conductivity of the brass tube.

The thermal resistance of condensation (R_c) is obtained by

$$R_c = 1/(h_{cond} A_{t,o}) \tag{4.48}$$

The temperature of subcooling is defined by

$$T_{subcool} = T_{sat} - T_w \tag{4.49}$$

where the wall temperature is calculated as

$$T_w = Q_c(R_c + R_w) - T_{c,ave} \tag{4.50}$$

Note that the thermal resistance of the condensation includes any effect of surface treatment to enhance condensation performance.

Figure 4-19(a) shows the results of heat fluxes using four different types of the condenser tubes according to the temperatures of subcooling (T_{sub}). We noticed that the heat fluxes of the condensers increase with T_{sub}. The highest heat fluxes are observed for COSA surface. Then, copper surface shows enhanced heat flux at lower T_{sub}. However, as T_{sub} increases, heat flux suddenly decreases and almost overlaps with predicted Nusselt condensation heat flux values in Equation (4-51). On the contrary, polymer-based coatings such as PPS/CNT composite surface and PTFE-coated surface show much lower heat flux compared to Nusselt values.

The overall CHTC of various surfaces are plotted over T_{sub} in Figure 4-19(b). The heat transfer coefficients of a filmwise condensation obtained from Nusselt correlation are also plotted for comparison, which is given by,

$$h_{Nusselt,FWC} = 0.728\left[\frac{g\rho_l(\rho_l-\rho_v)h_{fg}{k_l}^3}{\mu_l(T_{sat}-T_w)D_{t,o}}\right]^{0.25} \tag{4.51}$$

Generally, the overall CHTC of the condensers decreases as T_{sub} increases, which is an opposite trend to that of the heat fluxes in Figure 4-19(b). The highest CHTC is observed for COSA, which shows approximately 60% and 15% CHTC improvements compared to Nusselt FWC values and copper surface, respectively. Main cause of improvement can be ascribed to DWC pattern with high detachment frequency. Although FWC-like heat removal is shown at the bottom section, enhanced detachment frequency and condensate rupture reduce influence of thermal resistance of condensate alone. Presumably, improving irrigation of condensate on the bottom and/or enhanced hydrophobicity might contribute to a significant CHTC improvement.

Plain copper surface shows relatively improved CHTC results compared to PPS/CNT composite surface and PTFE-coated surface. As indicated in the visualization of condensation test in Figure 4-18(d), CHTC augmentation is caused by DWC on the overall surface at lower T_{sub}. As T_{sub} increases, CHTC deteriorates significantly.

For polymer-based coatings such as PPS/CNT composite surface and PTFE surface, CHTC acquired from condensation test is lower than predicted Nusselt theory values. CHTC deterioration of PPS/CNT composite surface can be explained by relating visual observation. In Figure 4-18(a), PPS/CNT-coated surface shows FWC pattern, which covers overall surface and prevents heat transfer process by acting as thermal resistance. Also, one thing to note is thermal conductivity of coating materials. Thermal conductivity of PPS/CNT coating is 2–20 W/m-K, which is a few orders of magnitude smaller than copper substrate (~400 W/m-K). Considering typical PPS/CNT coating thickness is at least a few micrometers, thermal resistance of PPS/CNT might be crucial to determine the overall heat transfer rate.

PTFE-coated surface shows lowest CHTC in Figure 4-19(b). Although DWC pattern is observed in Figure 4-18(b), CHTC is worst among a comparison group. A key to achieve improved CHTC using DWC is rolling off motion, which swipes adjacent immature condensates and replenishes nucleation sites. Due to low surface energy, individual condensates show droplet shape. However, the hysteresis on the surface-condensate could prevent condensates rolling-off from the surface. Once condensates adhere on the substrate, they grow perpendicular to axial direction. It leads to increase in thermal resistance of condensates and deteriorates CHTC. Condensate height (~2.5 mm) on the PPS/CNT surface is two times larger than that of COSA and/or plain copper surface (~1.2 mm). Another cause for CHTC deterioration might be low thermal conductivity of PTFE. As indicated in the PPS/CNT case, a few orders of magnitude difference in the thermal conductivity between copper substrate and PTFE coating (~0.25 W/m-K) might directly influence heat transfer performance during condensation process. In order to reduce thermal resistance caused by low thermal conductivity of materials, the coating thickness should be limited to a molecular level.

Validation of condensation heat transfer using a recently developed model [14-15] with the drop dynamic model is shown in Figure 4-20. Modeling results agree with experimental data within ±20% margin overall.

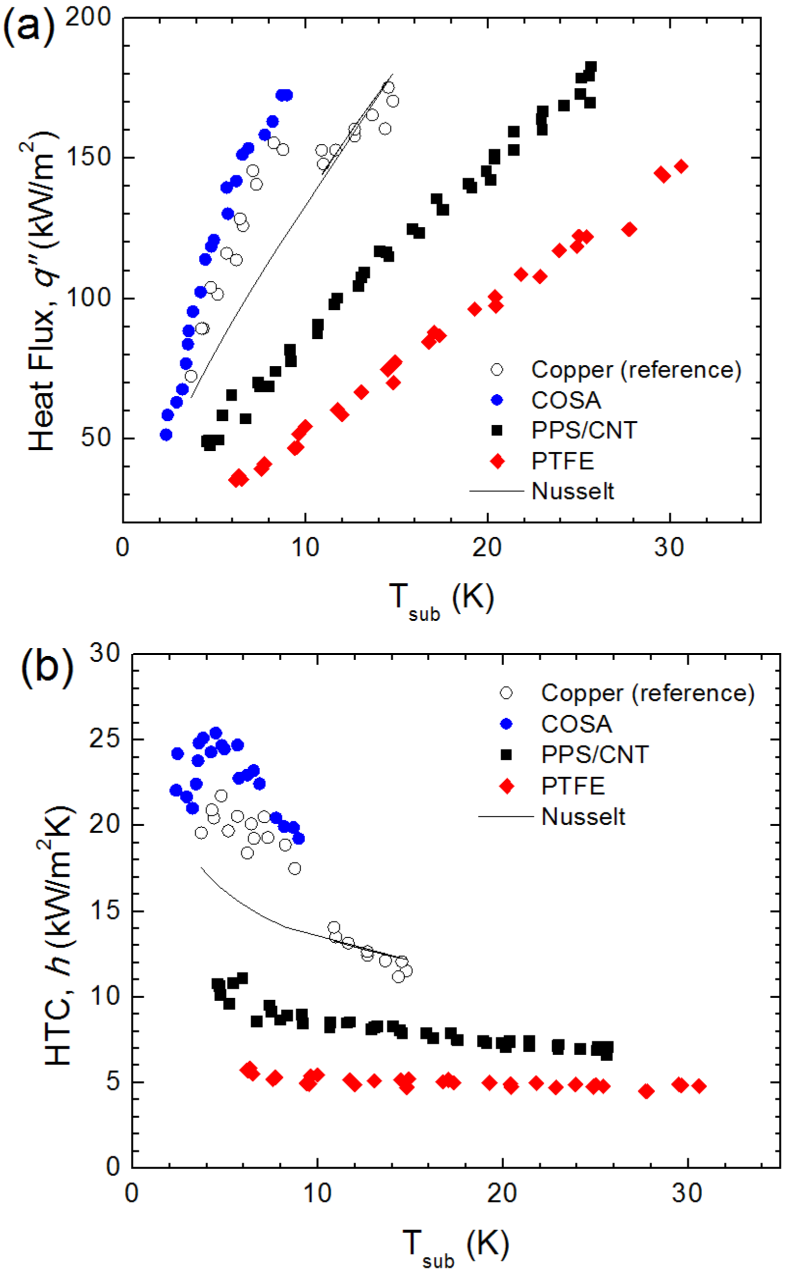

Fig. 4-19 (a) Heat flux versus subcooling temperature (b) Heat transfer coefficients versus subcooling temperature

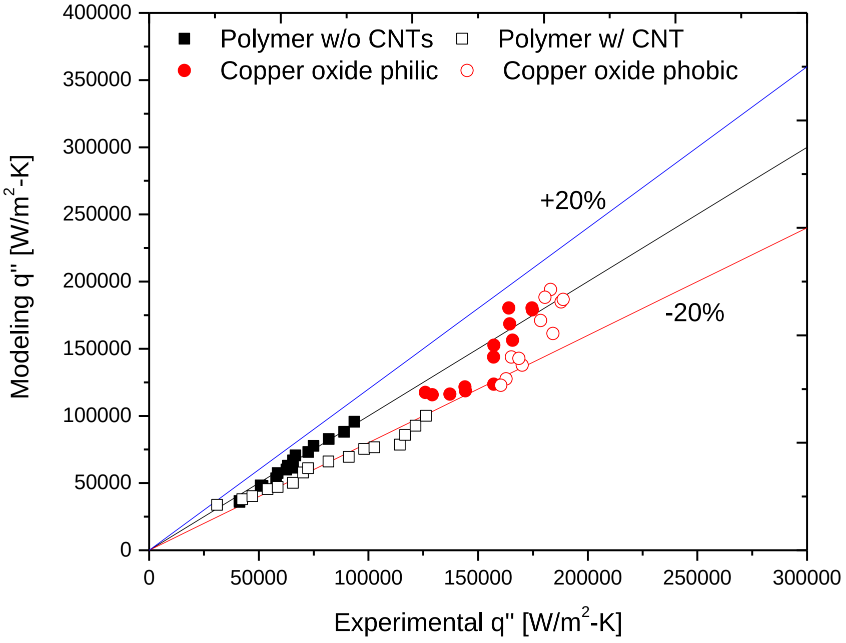

Fig. 4-20 modeling heat flux vs. experimental heat flux results comparison

Long-term condensation performance-testing of two different tubes (Copper oxide philic and Copper oxide phobic) was conducted up to 100 hours test run. It was observe that the heat flux over subcooling temperature is rarely influenced after 100 hours test run for the copper oxide philic tube. However, seemingly the copper oxide phobic tube exhibited a minor decrease (3-5%) in the heat flux. The results imply that there is no significant change of both surfaces after 100 hours of operation.

Observations and Future Study

Surface texture geometries are significant in drop size distribution and sweeping periods. Drop growth rate appears to be faster in ‘active’ dropwise condensation than ‘in-active’ condensation. Majorities of drop sizes were below 1 mm in the case of ‘active’ (Figure 4-21) dropwise-condensation while it was above 2 mm in case of ‘in-active’ (Figure 4-22) dropwise condensation. In-active drop renewal periods (~10 seconds) were also two times longer than active dropwise condensation (~5 seconds). Maximum drop radius was also shown to be two times larger in ‘in-active’ dropwise condensation compared to ‘active’ dropwise condensation (~3 mm to ~1.5 mm).

Surface textures geometries affect CAH, thus maximum drop radius. Drop sizes distribution shifted to the right as CAH increased. This means that drop radius of all drop sizes on the surface increased, thus droplets tended to stay on the surface longer. As a result, droplet thermal resistance increased and heat fluxes decreased. The study provided important insight into how surface geometries and CAH impact overall drop sizes distribution. Future works should be focused on drop population studies both experimentally and analytically in order to capture details on effect of drop dynamic on drop sizes distribution and population behaviors.

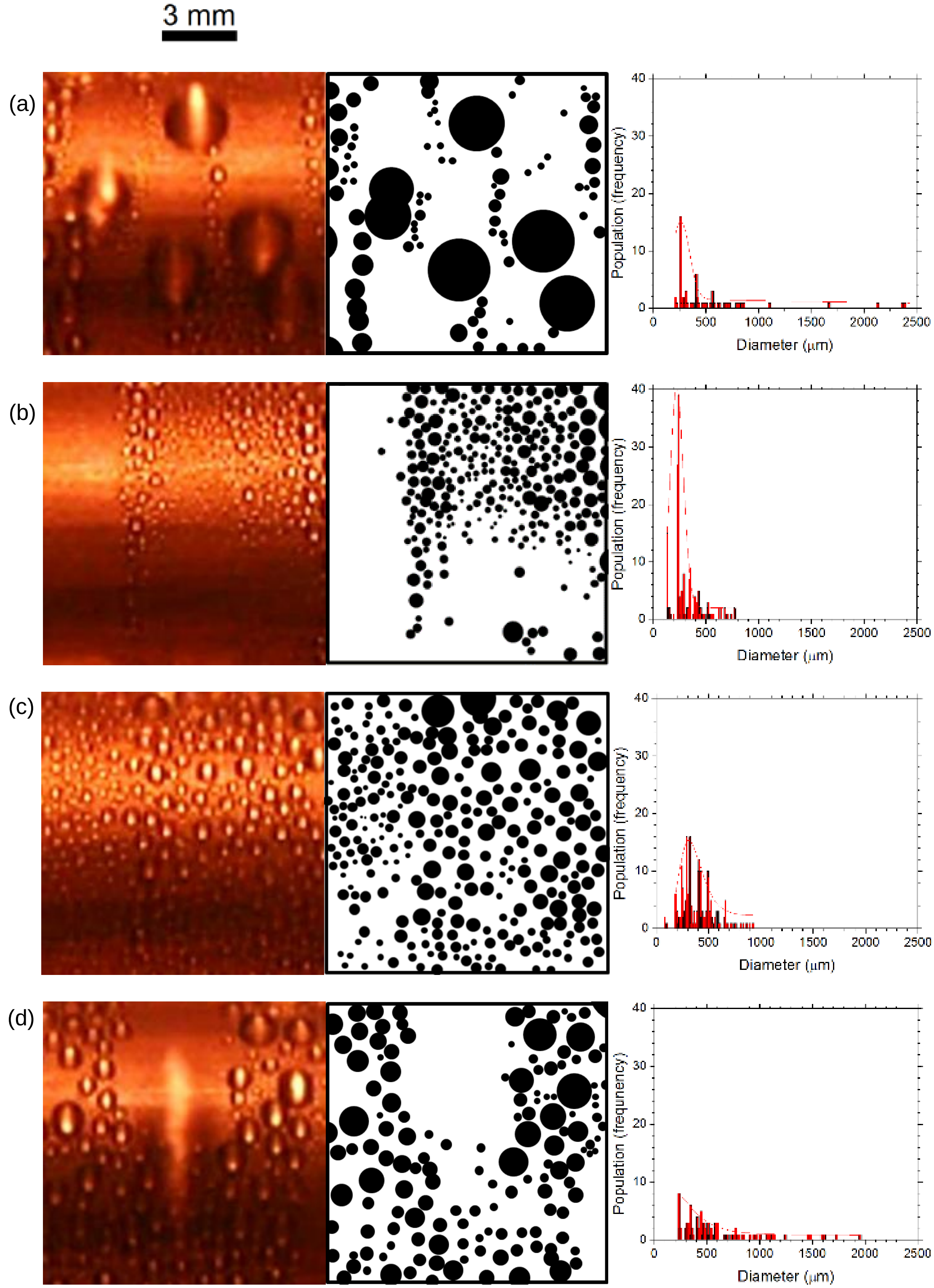

Fig. 4-21 Spatial condensate distribution and the corresponding condensate population at different time frame of ‘active” dropwise surface. Still-frame taken at (a) 4.2s, (b) 4.9s, (c) 5.3s, and (d) 5.8s

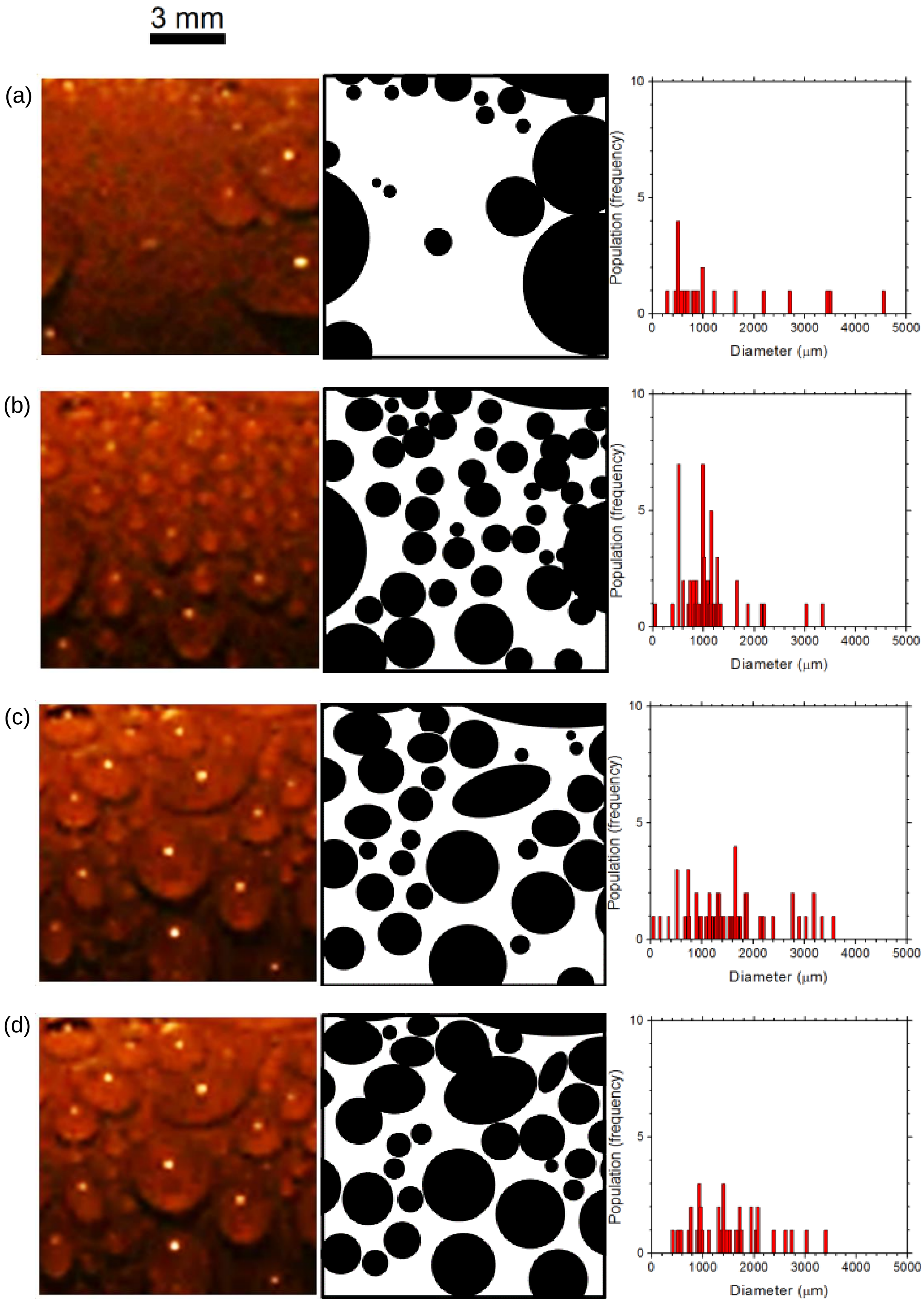

Fig. 4-22 Spatial condensate distribution and the corresponding condensate population at different time frame of 'in-active' dropwise surface. Still-frame taken at (a) 0.4s, (b) 6.2s, (c) 12.0s, and (d) 14.9s

Nomenclature

A	area [m^2]
A_C	drop cap area [m^2]
A_{LG},A_{SG},A_{SL}	liquid/gas interfacial area, solid/gas interfacial area, and solid/liquid interfacial area [m^2]
A_P	drop projection area [m^2]
c_p	thermal capacity [kJ kg^{-1} K^{-1}]
E	Surface energy [J]
E_{drop}	drop energy [J]
E_{hys}	hysteresis energy [J]
F	line force [N/m]
f	friction factor
f_w	projected area fraction for fully wetting space
g	gravitational acceleration [m s^{-2}]
h	heat transfer coefficient [W m^{-2} K^{-1}]
k	thermal conductivity [W m^{-1} K^{-1}]
m	mass flow rate [kg/s]
Nu	*Nusselt* number
Pr	*Prandtl* number
Q	heat transfer rate [kW]
q	heat flux [kW m^{-2}]
R	thermal resistance [K W^{-1}]
r	radius [m]
Re	*Reynolds* number
T	temperature [°C]
U	overall heat transfer coefficient [W m^{-2} K^{-1}]

Subscript

ave	averaged
c	coolant and/or critical
cond	condensation
d	hydraulic diameter
f	fluid
g	gas
i	in
l	liquid
Nusselt	*Nusselt* theory
o	out
sat	saturation
sub	subcool (or subcooling)
t	tube
tot	total
v	vapor
w	wall

Greeks

γ	surface energy [mJ/m^2]
μ	dynamic viscosity [kg m^{-1} s^{-1}]
ν	kinematic viscosity [m^2 s^{-1}]
θ	contact angle [degree]
θ_0	*Young*'s contact angle
θ_{adv}, θ_{rcd}	advancing contact angle, receding contact angle
θ_E	equilibrium contact angle

ϕ	ratio of the top surface area to projection area
ρ	density [kg m^{-3}]

Abbreviation

CHTC	condensation heat transfer coefficient
CNT	carbon nano tube
COSA	copper oxide self-assembly
DWC	dropwise condensation
FE-SEM	field emission scanning electron microscope
FWC	filmwise condensation
HTC	heat transfer coefficient
PPS	polyphenylene sulfide
PTFE	perfluoro ethylene
PVDF	polyvinyl difluoride
SAM	self-assembled monolayer
WCA	water contact angle

References

1. Li, W. and A. Amirfazli, *A thermodynamic approach for determining the contact angle hysteresis for superhydrophobic surfaces.* Journal of Colloid and Interface Science, 2005. **292**(1): p. 195-201.
2. Feng, L., et al., *Super-Hydrophobic Surfaces: From Natural to Artificial.* Advanced materials, 2002. **14**(24): p. 1857-1860.
3. Li, W. and A. Amirfazli, J. Colloid Interface Sci., 2005. **292**: p. 195.
4. Tongjie Yao and Chuanxi Wang and Quan Lin and Xiao Li and Xiaolu Chen and Jie Wu and Junhu Zhang and Kui Yu and Bai, Y., *Fabrication of flexible superhydrophobic films by lift-up soft-lithography and decoration with Ag nanoparticles.* Nanotechnology, 2009. **20**(6): p. 065304.
5. *Super-Hydrophobic PDMS Surface with Ultra-Low Adhesive Force.* Macromolecular Rapid Communications, 2005. **26**(22): p. 1805.
6. *Micrometrically scaled textured metallic hydrophobic interfaces validate the Cassie–Baxter wetting hypothesis.* Journal of Colloid and Interface Science, 2006. **302**(1): p. 308.
7. *Fabrication of nano-structured super-hydrophobic film on aluminum by controllable immersing method.* Applied Surface Science, 2012. **258**(16): p. 5933.
8. *Particle deposition after droplet evaporation on ultra-hydrophobic micro-textured surfaces.* Soft Matter, 2012. **8**(44): p. 11294.
9. *Plasma treatment allows water suspending of the natural hydrophobic powder (lycopodium).* Colloids and Surfaces B: Biointerfaces, 2012.
10. McHale, G., N.J. Shirtcliffe, and M.I. Newton, Langmuir, 2004. **20**: p. 10146.
11. Moradi, S., P. Englezos, and S.G. Hatzikiriakos, *Contact angle hysteresis: surface morphology effects.* Colloid and Polymer Science, 2013. **291**(2): p. 317-328.
12. Okumura, C.I.a.K., *Nucleation scenarios for wetting transition on textured surfaces: The effect of contact angle hysteresis.* EPL (Europhysics Letters), 2006. **76**(3): p. 464.
13. Zong-Han Yang and Chao-Yang Chiu and Jing-Tang Yang and, J.A.Y., *Investigation and application of an ultrahydrophobic hybrid-structured surface with anti-sticking character.* Journal of Micromechanics and Microengineering, 2009. **19**(8): p. 085022.
14. Lee, S., et al., *A dropwise condensation model using a nano-scale, pin structured surface.* International Journal of Heat and Mass Transfer, 2013. **60**(0): p. 664-671.
15. Kim, S. and K.J. Kim, *Dropwise condensation modeling suitable for superhydrophobic surfaces.* Journal of heat transfer, 2011. **133**(8).
16. Dettre, R.H. and R. Johnson, *Contact angle hysteresis II. Contact angle measurements on rough surfaces.* Adv. Chem. Ser, 1964. **43**: p. 136-144.
17. Young, T., *An Essay on the Cohesion of Fluids.* Philosophical Transactions of the Royal Society of London, 1805. **95**: p. 65-87.

18. Tadmor, R., *Line energy and the relation between advancing, receding, and young contact angles.* Langmuir : the ACS journal of surfaces and colloids, 2004. **20**(18): p. 7659-7664.
19. Swain, P.S. and R. Lipowsky, *Contact angles on heterogeneous surfaces: A new look at Cassie's and Wenzel's laws.* Langmuir, 1998. **14**(23): p. 6772-6780.
20. Cassie, A.B.D. and S. Baxter, *Wettability of porous surfaces.* Transactions of the Faraday Society, 1944. **40**(0): p. 546-551.
21. Wenzel, R.N., *Resistance of solid surfaces to wetting by water.* Industrial & Engineering Chemistry, 1936. **28**(8): p. 988-994.
22. Ishino, C. and K. Okumura, *Wetting transitions on textured hydrophilic surfaces.* The European Physical Journal E, 2008. **25**(4): p. 415-424.
23. Gao, L. and T.J. McCarthy, *Contact angle hysteresis explained.* Langmuir, 2006. **22**(14): p. 6234-6237.
24. Yuan, Y. and T.R. Lee, *Contact Angle and Wetting Properties.* 2013.
25. Forsberg, P.S.H., et al., *Contact line pinning on microstructured surfaces for liquids in the Wenzel state.* Langmuir, 2009. **26**(2): p. 860-865.
26. Barshilia, H.C., et al., *Effect of substrate roughness on the apparent surface free energy of sputter deposited superhydrophobic polytetrafluoroethylene thin films.* Applied Physics Letters, 2009. **95**(3): p. 033116-3.
27. Quéré, D., *Rough ideas on wetting.* Physica A: Statistical Mechanics and its Applications, 2002. **313**(1): p. 32-46.
28. Hejazi, V. and M. Nosonovsky, *Contact angle hysteresis in multiphase systems.* Colloid and Polymer Science, 2013. **291**(2): p. 329-338.
29. Adam, N.K. and G. Jessop, *CCL.-Angles of contact and polarity of solid surfaces.* Journal of the Chemical Society, Transactions, 1925. **127**(0): p. 1863-1868.
30. Good, R.J., *A Thermodynamic Derivation of Wenzel's Modification of Young's Equation for Contact Angles; Together with a Theory of Hysteresis1.* Journal of the American Chemical Society, 1952. **74**(20): p. 5041-5042.
31. Shepard, J.W. and F.E. Bartell, *Surface Roughness as Related to Hysteresis of Contact Angles. III. The Systems Paraffin–Ethylene Glycol–Air, Paraffin–Methyl Cellosolve–Air and Paraffin–Methanol–Air.* The Journal of Physical Chemistry, 1953. **57**(4): p. 458-463.
32. Xu, X. and X. Wang, *The modified Cassie’s equation and contact angle hysteresis.* Colloid and Polymer Science, 2013. **291**(2): p. 299-306.
33. Johnson Rulon, E. and H. Dettre Robert, *Contact Angle Hysteresis*, in *Contact Angle, Wettability, and Adhesion*. 1964, AMERICAN CHEMICAL SOCIETY. p. 112-135.
34. *Model for solid-liquid and solid-solid friction of rough surfaces with adhesion hysteresis.* The Journal of Chemical Physics, 2007. **126**(22): p. 224701.
35. *The rigorous derivation of Young, Cassie–Baxter and Wenzel equations and the analysis of the contact angle hysteresis phenomenon.* Chemical Physics Letters, 2008. **450**(4-6): p. 355.
36. Michael Nosonovsky and Bharat, B., *Roughness-induced superhydrophobicity: a way to design non-adhesive surfaces.* Journal of Physics: Condensed Matter, 2008. **20**(22): p. 225009.
37. *Preparation of a durable superhydrophobic membrane by electrospinning poly (vinylidene fluoride) (PVDF) mixed with epoxy–siloxane modified SiO2 nanoparticles: A possible route to superhydrophobic surfaces with low water sliding angle and high water contact angle.* Journal of Colloid and Interface Science, 2011.
38. Woo Kyung Cho and Sangjin Park and Sangyong Jon and Insung, S.C., *Water-repellent coating: formation of polymeric self-assembled monolayers on nanostructured surfaces.* Nanotechnology, 2007. **18**(39): p. 395602.
39. Ulrike Mock and Ralf Förster and Wolfgang Menz and Jürgen, R., *Towards ultrahydrophobic surfaces: a biomimetic approach.* Journal of Physics: Condensed Matter, 2005. **17**(9): p. S639.
40. Zhang, B. J. et al. *Biologically inspired tunable hydrophilic/hydrophobic surfaces: a copper oxide self-assembly multitier approach,* Bioinspir. Biomim., 2012. **7**: 036011.
41. Baojin, Q. et al. Exp. Therm. Fluid Sci., 2011. **35** :211-218.

Advanced Heat/Mass Exchanger Technology for Geothermal and Renewable Energy Systems

Final Report

Project 5: Nano-Coating, Structured Porous Surfaces for Evaporation/Boiling Heat Transfer Enhancement

Chanwoo Park
Mechanical Engineering Department
University of Nevada, Reno
Reno, NV 89557
chanwoo@unr.edu

December 15, 2014

Executive Summary

The objective of this project is to develop advanced nano/micro-scale, structured porous-layer surfaces for high performance two-phase heat exchangers (e.g., evaporator) which are used for air-conditioning and refrigeration systems. An experimental study was conducted to investigate the effect of the micro-scale, porous-layer coating on solution fluid wetting and heat transfer of a horizontal-tube, falling-film heat exchanger. Structured porous-layer surfaces built on the horizontal-tube, falling film evaporator was used to provide increased area and nucleation sites for the boiling/evaporation heat transfer enhancement which is assisted by capillary-driven liquid distribution. A thin uniform layer of copper particles was directly bonded onto plain copper tubes by sintering to create a micro-scale, porous mono-layer coating on the evaporator tubes. Distilled water was used as the solution and heating fluids. The visual observation performed in open ambient condition confirmed that when the solution flow was dripped onto the tubes, the plain tubes (conventional design) were partially wetted while the porous-layer coated tubes were completely wetted due to capillary action, even at low solution flow rates. The comparison of the results of evaporation heat transfer experiment using saturated conditions in a closed chamber showed that the porous-layer coated tubes exhibited a superior evaporation heat transfer rate (100% increase) to the plain tubes due to the complete solution wetting and thinned solution liquid film on the evaporator tubes. It was also observed that the heat transfer and surface wetting of the horizontal-tube, falling-film heat exchanger are significantly affected by the flow mode of the solution flow between the tubes and wall superheat of each tube. The heat transfer rate of the first row of the tube array seemed to be highly affected by the impinging solution flow from the solution dispenser. The decrease of the solution flow rate increased the external thermal resistance including surface evaporation and convection of the solution flow on the plain tubes, while the external thermal resistance for the porous-layer coated tubes remained almost constant because the surface wetting is always complete and not affected by the solution flow rates, except at very low Reynolds numbers. The nano-scale hydrophilic oxidation layer was also used in an attempt to further enhance surface wetting and the two-phase heat transfer. The visualization and heat transfer experiment results showed that the oxidized tubes had better wettability and evaporation heat transfer rate than the plain tubes. Although the oxidized tubes gave higher overall heat transfer rate than the porous-layer coated tubes at high solution flow rates, the porous-layer coated tubes outperformed the oxidized tubes at the low solution flow rates.

Introduction

Extensive studies by many researchers show that nano/micro/macro-scale surface modifications can significantly improve the surface wetting and heat transfer of evaporation and boiling. The surface modifications techniques span from mechanical to chemical methods.

Horizontal-tube falling-film evaporators have been used for various applications ranging from large refrigeration to desalination due to high heat transfer coefficients and low liquid inventory requirement. The falling-film evaporator is typically built in a horizontal tube bundle (array) where a solution fluid sprayed on the tubes drips down by gravitation while a heating fluid flows inside the evaporator tubes to heat the solution fluid. However, it is inherently unavoidable to create dry (non-heat transfer) areas on the evaporator tubes, unless the solution flow is abundant and well-distributed [1-3]. The surface wetting of the solution fluid on the evaporator tubes could be affected by many factors such as contact angle of the solution fluid, evaporator surface conditions, solution dispenser design, evaporator tube spacing, solution flow rate, temperature, and intertube flow mode [4-6].

Vasiliev et al. [7] measured boiling heat transfer coefficients of propane on horizontal, porous copper tubes using flooded and partially flooded conditions and found that the heat transfer rate using the porous tubes was almost 10 times higher than the plain tubes at low and moderate heat fluxes (less than 100 kW m^{-2}). Xia et al. [8] found that the heat transfer coefficient of a capillary-assisted evaporator with rectangular and circumferential micro-grooved tubes was increased with evaporation pressure and wall superheat. There have been studies to improve the solution-wetted area on the evaporator tubes using mechanically enhanced surfaces such as low-finned and roll-worked [9, 10]. Kuwahara et al. [11] used a machined porous structure (subsurface cavities called tunnels running along the circumference of the tube) for a horizontal-tube, falling-film evaporator and reported that the tube with the subsurface cavities could mitigate dry-outs. The solution flow mode between the vertically aligned (inline) horizontal tubes have been studied using plain tubes by Hu and Jacobi [12] and using plain and mechanically enhanced tubes by Roques et al. [13, 14]. The solution flow patterns were categorized into three main modes (droplet, column, and sheet) and two intermediate flow modes (droplet/column and column/sheet), depending on the solution flow rate.

Zhou and Bier [15] investigated the pool boiling heat transfer using the horizontal tubes coated with alumina oxide-titanium oxide ceramics. The ceramic coated tubes of 0.2 mm thickness was more effective for pool boiling than the plain copper tubes, although the thermal conductivity of the ceramic layer is much lower than copper. The authors reported that the boiling enhancement is owing to the microstructures in the ceramic coating that increases nucleation sites. Kim et. al. [16] also showed that the critical heat flux (CHF) is enhanced by the porous layer of nanoparticles of alumina, zirconia and silica ceramics resulting in improved surface wettability. Phan et. al. [17] investigated the effect of the surface wettability on nucleate boiling by nano-particle depositions of Pt, Fe_2O_3, SiO_x and TiO_2.

Copper material is preferably used for heat transfer applications because of its high thermal conductivity and reasonably good chemical compatibility with various working fluids. Over the past years, there has been studies on copper oxidation to create nano/micro-scale structures using a chemical immersion method, where alkali solutions such as NaOH, KOH, and NH_3/H_2O are used [18-21]. By controlling the process parameters of the chemical immersion, hierarchical nano/micro-scale morphology was altered to create variation in the surface wettability.

Project Objective

The objective of this project is to develop advanced nano/micro-scale, structured porous-layer surfaces for high performance two-phase heat exchangers (e.g., evaporator) which are used for air-conditioning and refrigeration and distillation applications.

Technical Approach

An experimental study using a horizontal-tube, falling-film evaporator (heat exchanger) was conducted to investigate the effect of nano/micro-scale, porous-layer coating on its surface wetting, flow modes and heat transfer performance. A thin uniform layer of copper particles was directly diffusion-bonded (sintered) to create a micro-scale, porous coating on the evaporator tubes. A chemical immersion method forming copper oxides in NaOH aqueous solutions was also used to create nano/micro-scale surface morphology on the evaporator tubes. The nano/micro-scale surface morphology of the copper oxides was characterized using Scanning Electron Microscope (SEM) images and chemical composition results from Energy Dispersive X-ray Spectroscopy (EDX). The effect of the nano/micro-scale surface morphology of the horizontal-tube, falling-film evaporator on its surface wetting, flow modes and heat transfer were experimentally investigated.

Period of Performance
September 20, 2010 – September 20, 2014 (48 months)

Personnel
Principal Investigator
Chanwoo Park,
Associate Professor
Department of Mechanical Engineering
University of Nevada, Reno
Reno, NV 89557
chanwoo@unr.edu

Researchers
Dr. Sangsoo Lee, Post-doctoral Researcher
Mr. Batikan Koroglu, MS student
Mr. Nicholas Bogan, MS student

Publications from this work

Journal Publications
[1] Nicholas Bogan, Chanwoo Park, 2013, Influences of Solution Subcooling, Wall Superheat and Porous-Layer Coating on Heat Transfer in a Horizontal-Tube, Falling-Film Heat Exchanger, International Journal of Heat and Mass Transfer, Vol. 68, pp. 141-150.
[2] Batikan Koroglu, Nicholas Bogan, Chanwoo Park, 2013, Effects of Tube Row on Heat Transfer and Surface Wetting of Microscale, Porous-Layer Coated, Horizontal-Tube, Falling-Film Heat Exchanger, ASME Journal of Heat Transfer, Vol.135, pp. 041802.
[3] Batikan Koroglu, Kee Sung Lee, Chanwoo Park, 2013, Nano/Micro-Scale Surface Modifications using Copper Oxidation for Enhancement of Surface Wetting and Falling-Film Heat Transfer, International Journal of Heat and Mass Transfer, Vol. 62, pp. 794–804.
[4] Sangsoo Lee, Batikan Koroglu, and Chanwoo Park, 2011 "Experimental Investigation of Capillary-Assisted Solution Wetting and Heat Transfer Using a Micro-Scale, Porous-Layer Coating on Horizontal-Tube, Falling-Film Heat Exchanger," International Journal of Refrigeration, Vol. 35, pp. 1176-1187.

Conference Publications
[5] Nick Bogan, Chanwoo Park, 2013, Effects of Solution Subcooling and Wall Superheat On Heat Transfer of a Horizontal-Tube, Falling-Film Heat Exchanger, 2013 ASHRAE Annual Conference, June 22-26, 2013, Denver, CO.
[6] Chanwoo Park, Nick Bogan, 2013, Effects of Solution Subcooling and Wall Superheat on Heat Transfer of a Horizontal-Tube, Falling-Film Heat Exchanger, 2013 International Conference on Multiphase Flow, May 26-31, 2013, Jeju, Korea.
[7] B. Koroglu, N. Bogan, C. Park, 2012, Experimental Study of Tube Row Effects on Evaporation Heat Transfer Using a Micro-Scale, Porous-Layer Coating on a Horizontal-Tube, Falling-Film Heat Exchanger, ASME 2012 3rd Micro/Nanoscale Heat & Mass Transfer International Conference, March 3-6, 2012, Atlanta, Georgia, MNHMT2012-75333.
[8] Sangsoo Lee, Chanwoo Park, 2010, "Enhancement of Solution Wetting and Heat Transfer on Horizontal-Tube, Falling-Film Evaporator using Porous-Layer Coating", in the proceedings of 2010 ASME International Mechanical Engineering Congress & Exposition, Vancouver, British Columbia, CANADA, November 12-18, 2010, IMECE2010-37788.

Research Results

Task 5.1 Design and Fabrication of Micro-Scale, Structured Porous Surface

In a horizontal-tube, falling-film evaporator, the surface wetting of solution fluid is very essential to enhance the heat transfer of the evaporator. As the solution fluid drips down the tubes, due to inherent misdistribution of the gravity-driven solution flow, unwetted surface (non-heat transfer) areas are usually created resulting in a dramatic decrease in the heat transfer. As the solution fluid flow rate is decreased and the surface heat transfer is increased, and the number of the tube rows is increased, the unwetted surface area is likely increased.

In an attempt to solve the dry-out problem, a capillary (passive) pumping in a porous layer was used to distribute the solution fluid evenly over entire tube surfaces and achieve a complete solution wetting even at low solution flow rates. Copper particles were diffusion-bonded (sintered) on copper tubes of the falling-film evaporators to form the porous layer.

In this task, copper tubes coated with a porous layer of Copper particles were fabricated using sintering method. First, an oxidized stainless steel tube as a mandrel of the copper particles for the sintering was prepared. The inner diameter of the stainless tube was 2 mm larger than the outer diameter of the plain tube, making a 1 mm gap (annulus shape). The copper particles having an average diameter of 75 μm was filled into the annulus. The copper particles were directly sintered to the copper tube for one hour at 800ºC in a high-temperature quartz tube under hydrogen gas environment. Fig. 5-1(a) is the photograph of the porous-layer coated tube and also shows the side view of the porous coating in Fig. 5-1(b).

Figure 5-1. (a) Photograph of the porous-layer coated tube showing (b) the porous coating (1 mm thick) of sintered copper particles (75 μm in diameter).

Task 5.2 Property Measurement of Micro-Scale, Structured Porous Surfaces

The porosity and pore diameter of the porous-layer coating on the evaporator tube was measured. The porosity can be calculated by the measured weights of a small sample of the porous-layer coating removed from the evaporator tube at dry and fully saturated conditions using water and is given by

$$porosity = \frac{\left[m_{water} / \rho_{water} \right]}{\left[m_{water} / \rho_{water} \right] + \left[m_{copper} / \rho_{copper} \right]} \tag{5.1}$$

The weight of the water absorbed in the porous sample is calculated by

$$m_{water} = m_{copper,wet} - m_{copper,dry} \tag{5.2}$$

From the weights of the copper sample at dry and wetted conditions being 3.638 g and 3.830 g, respectively, the estimated porosity of the sample ranges from 0.316 to 0.320.

Figure 5-2 shows the experimental setup to measure the pore diameter of the porous copper sample based on wicking height measurement method using ethyl alcohol as wicking fluid. The wicking height of the porous copper sample was measured after a long waiting time so that the wick liquid reached its maximum height. Once the wicking height was measured, the pore diameter r_p of the porous-layer i calculated using the Young-Laplace equation by

$$r_p = \frac{2\sigma}{g\,\rho\ H} \tag{5.1}$$

Figure 5-2. Wicking height measurement for pore diameter estimation.

where σ and ρ are the surface tension and density of ethyl alcohol, respectively. *H* is the wicking height of ethyl alcohol on the porous-layer coated tube. Using Eq. (5.3), the pore diameter ($2r_p$) of the porous-layer coating was calculated ranging from 73 to 98 µm.

The SEM (Scanning Electron Microscope) images of the porous-layer coating of the sintered copper particles shows the micro-scale surface topology in Figure 5-3 (a), (b), and (c) at various magnifications. As shown in the Figure, the diameters of the copper particles varied from 25 to 100 µm with an average diameter of about 75 µm. The necking (bonding) and pores between the particles are also shown in the figure. Note that from Eq. (5.3), the smaller pore diameter is, the larger capillary pumping head is.

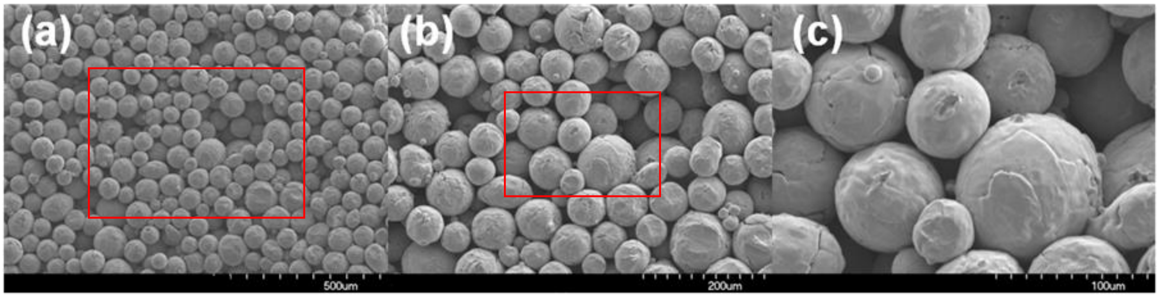

Figure 5-3. SEM images of micro-scale, porous surface of sintered copper particles: (a) magnifications of (a) 110, (b) 200 and (c) 500 times. The red boxes show the areas of the magnification.

Task 5.3 Heat Transfer Performance Characterization Experiment of Micro-Scale, Structured Porous Surface

A. Small Falling-Film Evaporator Setup

For this task, a small-scale horizontal-tube falling-film evaporator setup was designed and fabricated to perform the evaporation heat transfer experiment using a closed system under saturated conditions. Figure 5-4 shows the schematic of the experimental setup of the falling-film horizontal-tube evaporator which consists of a vacuum-tight chamber including a solution fluid dispenser and two horizontal tubes; plumbing lines for solution and heating fluids; and instrumentation. The solution dispenser and horizontal tubes were vertically aligned so that the solution fluid could drip along the tubes. The chamber was made of a transparent acrylic cylinder with an inner diameter of 108 mm and a length of 304.8 mm.

The solution fluid was pumped from the solution reservoir to the solution dispenser by a magnet-driven, variable-speed gear pump (MG 209 XPB17, Clark Solutions) controlled by a DC power supply (3006B, Proteck), and the solution fluid was distributed from the holes at the bottom of the dispenser to the top of the upper tube and then dripped to the lower tube. The excess solution fluid was collected at the bottom of the chamber and drained to the solution reservoir, which completed the cycle of solution fluid circulation. A house-made coil cooler was installed in the solution reservoir to control the solution temperature in the reservoir. The heating fluid was circulated from the lower tube to the upper tube in a cross-flow arrangement against the solution fluid. The heating fluid temperature was controlled using a thermal bath (R6L PROG 115/60, Cole Parmer). Distilled water was used as the solution and heating fluids.

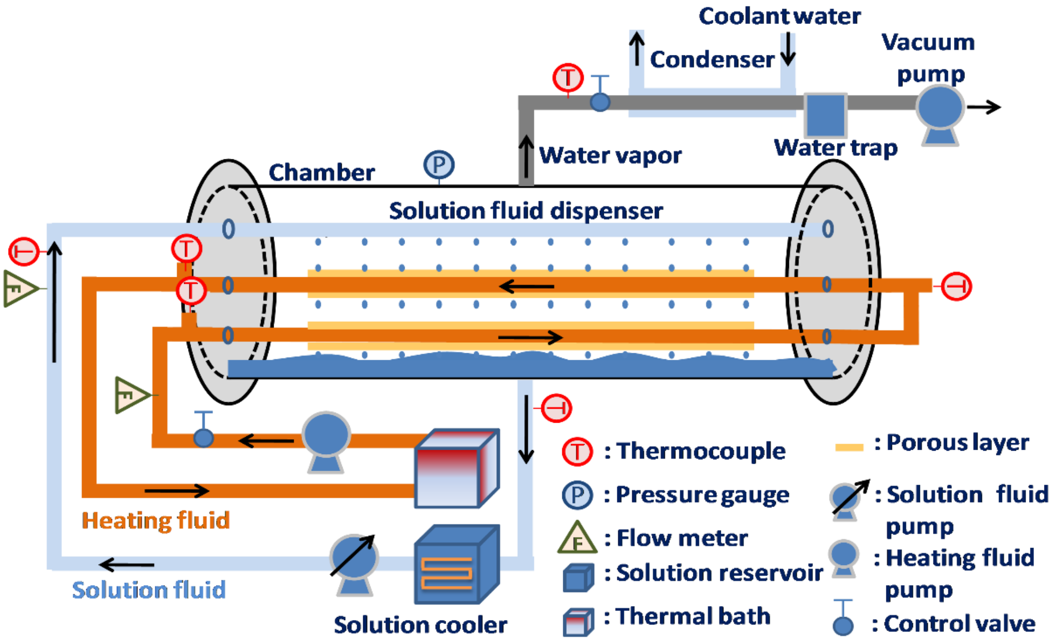

Figure 5-4. Schematic of the experimental setup for the evaporation heat transfer experiment using the falling-film horizontal-tube evaporator

The distances between the solution dispenser and the upper horizontal tube (S_{ds}) and between the test tubes (S_t) are equally distributed at 19.7 mm. The solution dispenser tube has 12 holes drilled in a row with a diameter of 1.58 mm and a spacing of 25.4 mm. The solution wetting and falling-film flow modes were visually observed using the plain and porous-layer coated tubes for solution Reynolds numbers ranging from 6 to 60 at the room temperature of 19°C and atmospheric pressure. A concentric-tube design is used for the horizontal tubes to increase the heat transfer coefficient of the heating fluid flowing in the annulus side of the tubes, between D_3 and D_2, shown in Fig. 5-5. All dimensions of the tube setup are listed in Table 5-1.

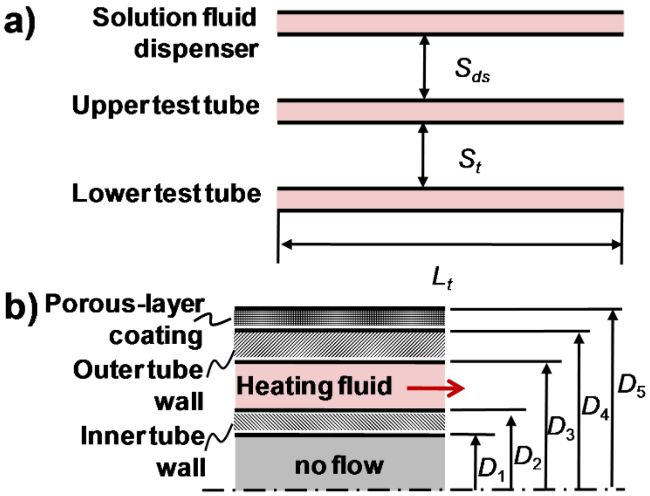

Figure 5-5. Dimensions of falling-film heat exchanger: (a) tube spacing and length and (b) cross-sectional view of tubes showing various tube diameters.

Table 5-1. Dimensions of falling-film, horizontal-tube heat exchanger.

		Unit	Dimension
Chamber	I.D.	mm	108
	O.D.	mm	127
	L	mm	304.8
	S_{ds}	mm	19.7
	S_t	mm	19.7
Inner tube	D_1	mm	6.4
	D_2	mm	9.5
	L_t	mm	304.8
Outer tube	D_3	mm	13.4
	D_4	mm	15.9
	L_t	mm	304.8
Porous-layer coating	D_5	mm	18.03
	L_{po}	mm	304.8
Solution dispenser	$d_{ds,nz}$	mm	1.58
	$S_{ds,nz}$	mm	25.4

The heat transfer rate of the heating fluid is calculated by

$$Q_h = \dot{m}_h \cdot cp_h \cdot \left(T_{h,in} - T_{h,out}\right) \tag{5.2}$$

The heat transfer rate of the heating fluid (Q_h) is balanced with the evaporation heat transfer rate, which is estimated by the overall heat transfer coefficient for the evaporation (U) and superheat (ΔT_{sh}) and is calculated by

$$Q_h = U(A_{t,o})\Delta T_{sh} \tag{5.3}$$

where U is the overall heat transfer coefficient obtained from the empirical correlation developed for the horizontal-tube, falling-film evaporator using the plain tubes including the sensible heat transfer, and is given by

$$\mathrm{Nu} = \frac{UD}{k} = \left(\mathrm{Re}^{-2/3} + 0.009\mathrm{Re}^{0.3}\mathrm{Pr}^{0.25}\right)^{0.5} \tag{5.4}$$

The superheat (ΔT_{sh}) for the evaporation heat transfer is defined by

$$\Delta T_{sh} = T_{t,o} - T_{v,sat} \tag{5.5}$$

The temperature of the outer wall is obtained by

$$T_{t,o} = T_{h,ave} - Q_h(R_h + R_t) \tag{5.6}$$

where the thermal resistances of the heating fluid and tube wall are calculated by

$$R_h = \frac{1}{h_h\left[\pi D_3 (2 L_{t,o})\right]} \tag{5.7}$$

$$R_t = \frac{\ln\left(D_4 / D_3\right)}{2\pi k_t \,(2L_{t,o})} \tag{5.8}$$

Figure 5-6 shows the solution flow modes for the test tubes [a plain tube in Fig. 5-6 (a) and a porous-layer coated tube in Fig. 5-6 (b)] for few selected solution Reynolds numbers. The solution wetting ratio for the plain tubes was determined by directly measuring the wetted area from the photos. As shown in Fig. 5-6 (a) for the plain tube, there are observed unwetted areas and the solution wetting ratio (ς) was increased from 0.35 to 0.65 as the solution Reynolds number was increased.

The solution wetting of the porous- layer coated tube was measured by directly touching the porous layer with a dry paper and confirming that the paper was wet. Using this direct contact method, it was found that complete solution wetting of the porous-layer coated tube was always achieved, even with the lowest solution Reynolds number (Re = 6.0). The complete solution wetting of the porous-layer coated tubes is the result of solution fluid distribution due to the capillary action in the porous coating. The visually wetted (thick liquid film) areas of the porous-layer coated tubes shown in Fig. 5-6 (b) are the locations where the solution fluid drips over the surface of the porous-layer coated tubes.

Two experimental conditions [single-phase (liquid) and evaporation heat transfer] were used for this study. The single-phase heat transfer experiment was performed under ambient pressure with the heating fluid temperature higher than the solution inlet temperature. The evaporation heat transfer experiment was performed under solution sub-cooled condition and the heating fluid temperature was kept higher than the saturation temperature of the solution, while also maintaining a wall superheat less than 5°C.

The vacuum pressure condition in the chamber for the evaporation heat transfer experiment was maintained by constantly evacuating water vapor generated in the chamber by a vacuum pump (Series L-BV2, Siemens). The chamber pressure was manually regulated using a control valve in the vacuum line, as shown in Fig. 5-4. To reduce the surface aging effect due to copper oxidation, the test tubes used were subject to a preliminary testing phase for many hours (~30 hours) under conditions similar to the evaporation heat transfer experiment conditions used during testing (using a heating fluid temperature up to 75°C).

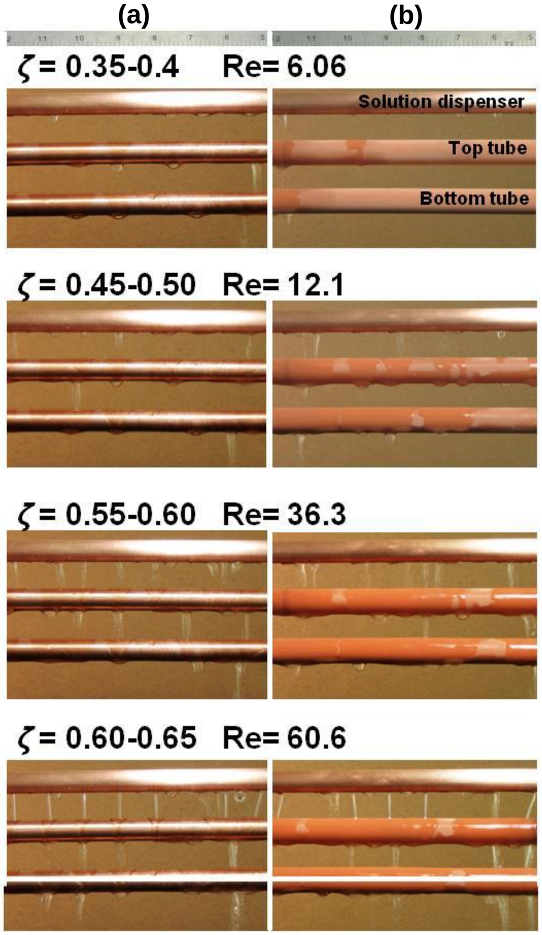

Figure 5-6. Comparison of solution wetting and falling-flow modes of (a) the plain and (b) porous-layer coated tubes.

Table 5-2. Representative test conditions used for the singe-phase heat transfer experiment.

	Variables	Unit	Plain tube	Porous-layer coated tube
Solution fluid	$\dot{V}_s$	$m^3 s^{-1}$	2.09×10^{-5}	2.09×10^{-5}
	Γ	$kg\ m^{-1} s^{-1}$	0.0341	0.0341
	$T_{s,i}$	°C	30.0	30.3
	$T_{s,o}$	°C	33.9	34.6
	Re_s		178	180
	Pr_s		5.28	5.23
	Ga_s		1.05×10^{11}	1.09×10^{11}
	U	$W\ m^{-2} K^{-1}$	3095	2130
	R_{ext}	$K\ W^{-1}$	0.0194	0.0155
	Q_s	W	340	373
Heating fluid	$\dot{V}_h$	$m^3 s^{-1}$	6.33×10^{-5}	6.33×10^{-5}
	$T_{h,i}$	°C	39.0	38.9
	$T_{h,o}$	°C	37.8	37.5
	Re_h		5348	5325
	Pr_h		4.58	4.60
	h_h	$W\ m^{-2} K^{-1}$	7198	7175
	R_h	$K\ W^{-1}$	5.72×10^{-3}	5.73×10^{-3}

Two rotameters (SMR1-010110, Omega; F-450, Blue-White), one pressure transducer (PX209-30V15G5V, Omegadyne Inc.), and seven T-type thermocouples (THS-107-160, Thermoworks) were used for the measurements. The pressure reading from the pressure transducer was used to calculate the solution saturation temperature (T_{sat}) in the chamber using the water saturation pressure-temperature curve. The chamber and the fluid lines were fully insulated during the heat transfer tests. The data were collected for 5 minutes after a steady state condition was achieved. The steady-state condition was declared when the pressure and temperatures of the system remained constant for about 10 minutes.

(i) Single-Phase Heat Transfer and Solution Wetting

The single-phase heat transfer experiment was performed to study the solution wetting and sensible heat transfer performances of the plain and porous-layer coated tubes using the experimental setup shown Fig. 5-4 under ambient pressure conditions. During the heat transfer experiment, the solution distribution and the flow mode were observed through a small window on the insulation of the chamber. The solution Reynolds number considered for the experiment was varied from 31 to 220 for a heating fluid Reynolds number of around 5400. The representative test conditions used for the single-phase heat transfer experiment are listed in Table 5-2.

Figure 5-7 shows the variation of the single phase (no evaporation) heat transfer rate of the solution fluid (Q_s) with respect to the solution Reynolds number for solution fluid inlet temperature of 30°C and a heating fluid inlet temperature of 39°C, under ambient pressure. The figure shows the heat transfer rate for the plain tube similar to that of the porous-layer coated tube. This result can be explained by the fact that, although the entire surface of the porous-layer coated tubes was fully saturated with the solution fluid, only some portion of the wetted surface is covered (flooded) by the solution fluid and therefore was directly used for the sensible heat transfer.

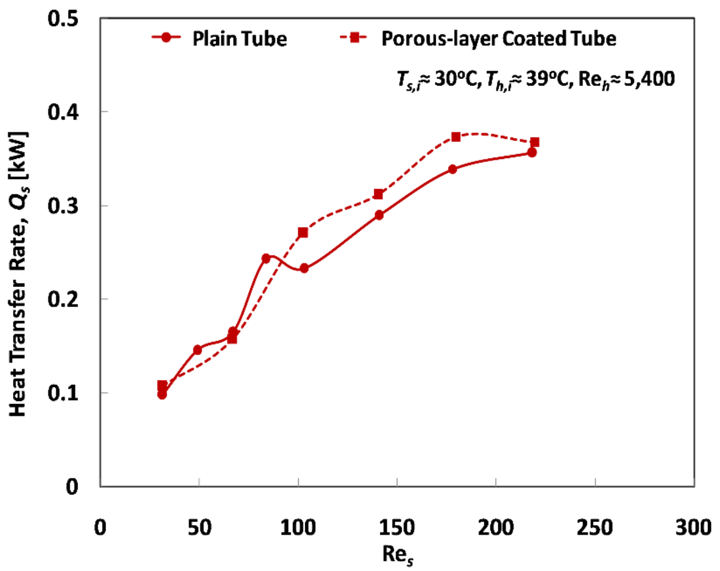

Figure 5-7. Comparison of the single-phase heat transfer rates of the plain and porous-layer coated tubes.

Considering that the heat transfer rate from the heating fluid to the solution fluid is used only to increase the solution temperature under the single-phase heat transfer condition, the solution wetting ratio ($\varsigma_{pl,sens}$) for the plain tube can be calculated by

$$\varsigma_{pl,sens} = \frac{Q_s}{U_{pl,sens} A_{t,o} \Delta T_s} \tag{5.9}$$

where the external heat transfer coefficient ($U_{pl,sens}$) for the plain tube is obtained from the empirical correlation of the falling-film, horizontal-tube heat exchanger [22], which is given by

$$\mathrm{Nu}_{pl,sens} = U_{pl,sens}\left(\nu_s^{\,2}/gk_s^{\,3}\right)^{1/3} = 0.01925\,\mathrm{Re}_s^{0.24}\,\mathrm{Pr}_s^{0.66} \tag{5.10}$$

Table 5-3. Averaged (maximum) uncertainties for the singe-phase heat transfer experiment.

		Plain tube	**Porous-layer coated tube**
Pressure	P	±0.25%	±0.25%
Temperature	T	±0.2°C	±0.2°C
Solution fluid flow rate	$\dot{V}_s$	±2.00%	±2.00%
Heating fluid flow rate	$\dot{V}_h$	±4.00%	±4.00%
Solution fluid	Q_s	±6.2% (±8.62%)	±6.3% (±8.4%)
	U	±0.5% (±0.5%)	±8.5% (±10.8%)
	R_{ext}	±8.1% (±10.2%)	±8.5% (±10.8%)
	ς	±8.0% (±10.1%)	N/A
Heating fluid	h_h	±4.1% (±4.1%)	±4.1% (±4.1%)
	R_h	±4.1% (±4.1%)	±4.1% (±4.1%)

On the other hand, the external heat transfer coefficient for the porous-layer coated tube can also be calculated using the result found from the visual observation showing the complete solution wetting ($\varsigma = 1$). Therefore, the external heat transfer coefficient for the porous-layer coated tubes is given by

$$U_{po,sens} = \frac{Q_s}{A_{t,o} \Delta T_s} \tag{5.11}$$

Figure 5-8 shows the comparisons of the external heat transfer coefficients and solution wetting ratios for the plain and porous-layer tubes. Recalling the visual inspection on the two distinctive surface wetting conditions of the porous-layer coated tube (fully saturated and flooded), it is obvious to see that the external heat transfer coefficient is underestimated, as shown in Fig. 5-8, because of the assumption of the complete (flooded) surface wetting. The external heat transfer coefficients of both the plain and porous tubes and the solution wetting ratio using the plain tube were increased as the solution flow rate was increased. The increased heat transfer coefficients are due to the steeper temperature gradient in the solution liquid film as the solution flow rate was increased. The uncertainties of the calculated values for the single-phase heat transfer are listed in Table 5-3. The external heat transfer coefficient and thermal resistance for the porous-layer coated tube showed the highest uncertainty (8.5% averaged), which was mostly related to the uncertainties of the temperature measurement.

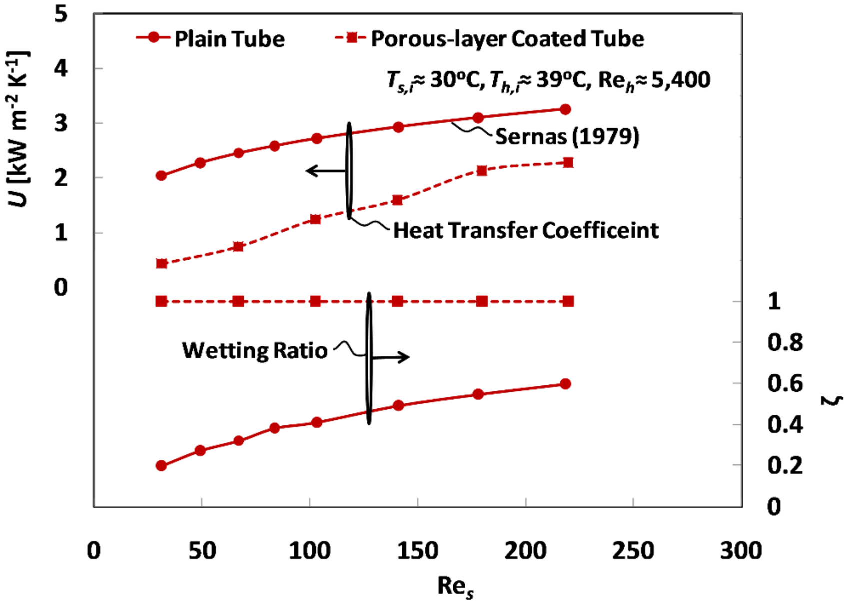

Figure 5-8. Comparison of heat transfer coefficients and solution wetting of the plain and porous-layer coated tubes using the single-phase heat transfer conditions.

(ii) Evaporation Heat Transfer and Solution Wetting

The solution wetting ratio ($\varsigma_{pl,eva}$) for the plain tubes using the evaporation heat transfer condition can be determined as below

$$\varsigma_{pl,eva} = \frac{Q_h}{U_{pl,eva} A_{t,o} \Delta T_{sh}} \tag{5.14}$$

where ΔT_{sh} is the wall superheat ($\Delta T_{sh} = T_{t,o} - T_{sat}$). The external heat transfer coefficient ($U_{pl,eva}$) for the plain tubes is obtained from the empirical correlation [1] which was [1][1][1][1][1][13]developed for the horizontal-tube, falling-film evaporator using the plain tubes including the evaporation and sensible heat transfers, and is given by

$$\mathrm{Nu}_{pl,eva} = U_{pl,eva}\left(\nu_s^{\,2} / g k_s^{\,3}\right)^{1/3} = \left(\mathrm{Re}_s^{-2/3} + 0.009\,\mathrm{Re}_s^{0.3}\mathrm{Pr}_s^{0.25}\right)^{0.5} \tag{5.15}$$

Considering the complete solution wetting ($\varsigma = 1$) for the porous-layer coated tubes, the external heat transfer coefficient can be determined by

$$U_{po,eva} = \frac{Q_h}{A_{t,o}\Delta T_{sh}} \tag{5.16}$$

The breakdown of the thermal resistances used for the design of the experimental setup using the evaporation heat transfer condition for the heating fluid Reynolds number of 9400 is shown in Fig. 5-9. It was observed that the thermal resistances of the solution fluid (R_{ext}) and the heating fluid (R_h) were the main contributors to the total thermal resistances (R_{tot}). The total thermal resistance for the porous-layer coated tubes was much lower than that for the plain tubes due to the smaller external thermal resistance of the wick tubes. It was also found from Fig. 5-9 that the differences of the thermal resistances (R_{tot} and R_{ext}) between the plain and porous-layer coated tubes were reduced as the solution flow rate was increased. This interesting result is attributed to the fact that, as the solution flow rate is increased, the solution wetting of the plain tube is increased.

The solution wetting of the porous-layer coated tube remains complete and furthermore, the external thermal resistance (R_{ext}) of the solution fluid was increased as the flow rate was increased due to the thick solution film. Therefore, it can be concluded that the best performance of the porous-layer coated tubes under the evaporation heat transfer condition is achieved with low solution flow rates when the solution fluid film is thin, yet complete solution wetting is created. In contrast, such low solution flow rates are worse for the plain tube because of poor solution wetting.

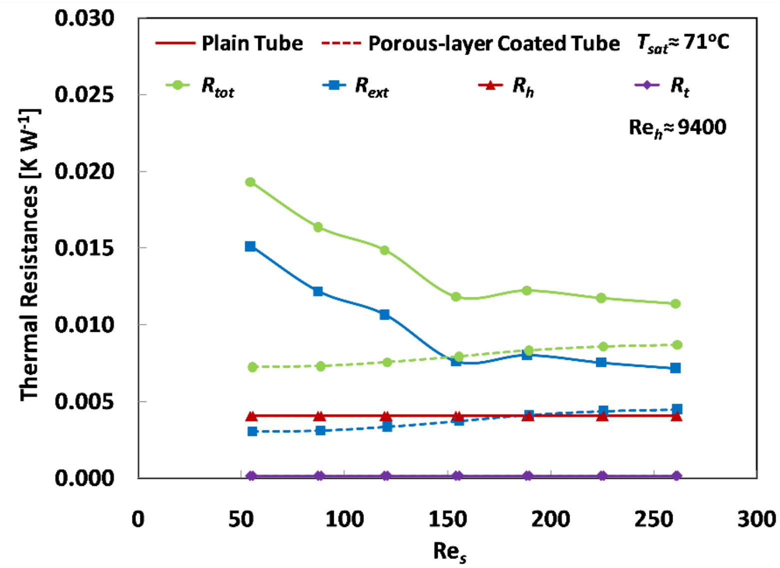

Figure 5-9. Comparison of thermal resistances of plain and porous-layer coated tubes using evaporation heat transfer conditions.

Figure 5-10 shows the comparison of the external thermal resistances of the plain and porous-layer coated tubes for various heating fluid Reynolds numbers. Again it was observed that the external thermal resistances using the porous-layer coated tubes were much lower than those using the plain tubes. In addition, as the solution Reynolds number was increased, the external thermal resistances using the plain tubes were decreased, while those for the porous-layer coated tubes were increased. These results were caused by the increased solution wetting of the plain tubes and the thickened solution fluid film on the porous-layer coated tubes. It was also shown from the Fig. 5-10 that the heating fluid Reynolds number had an insignificant influence on the external thermal resistances.

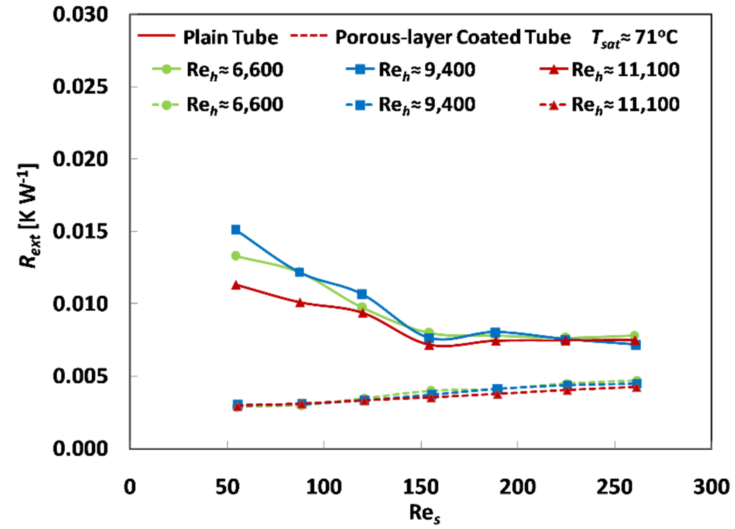

Figure 5-10. Comparison of external thermal resistances of plain and porous-layer coated tubes using evaporation heat transfer conditions.

The comparison of the external heat transfer coefficients ($U_{pl,eva}$ and $U_{po,eva}$) and solution wetting ratios for the plain and porous-layer coated tubes with respect to the solution Reynolds number is shown in Fig. 5-11. The external heat transfer coefficients were obtained from the empirical correlation for the plain tubes [1] and calculated from the heat transfer measurements for the porous-layer coated tubes. As shown in Fig. 5-11, the external heat transfer coefficients and the solution wetting ratios for the porous-layer coated tubes were higher than those using the plain tubes. The external heat transfer coefficients of both tubes were decreased as the solution flow rate was increased, which significantly differed from the results of the single-phase heat transfer experiment. This can be attributed to the fact that the surface evaporation, which induced a higher heat transfer coefficient than that of the single-phase condition, was suppressed due to the increased solution film thickness over the tubes, even though the solution turbulence was enhanced as the solution flow rate was increased.

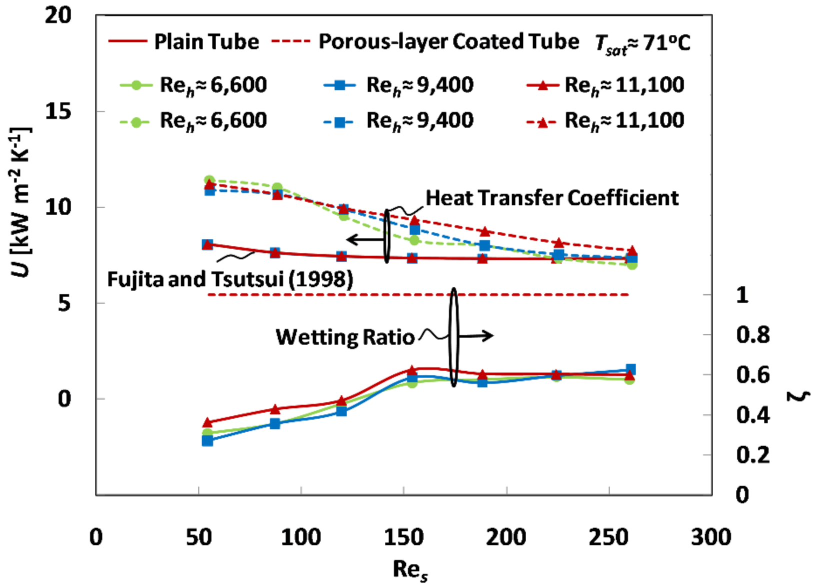

Figure 5-11. Comparisons of heat transfer coefficients and solution wettings of plain and porous-layer coated tubes using evaporation heat transfer conditions.

The solution wetting ratio using the plain tubes was increased as the solution Reynolds number was increased, which was similar to the results of the single-phase experiment. However, the heat transfer coefficient for the plain tubes remained almost constant during the evaporative condition, which were a significantly different trend as compared to the results from the single-phase heat transfer experiment. Note that two different empirical correlations [[22]) and [1]] were used for the calculation of the external heat transfer coefficients of the plain tubes for single-phase and evaporation heat transfer conditions, respectively.

Figure 5-12 shows the comparison of the solution wetting ratios of the plain tubes from the visual observation (no heat transfer), single-phase, and evaporation heat transfer experiments. It was shown from the Fig. 5-12 that the solution wetting ratios were increased as the solution Reynolds numbers (Re_s) increased, but the heating fluid Reynolds number (Re_h) had a rather weak impact on the solution wetting except at the highest heating fluid Reynolds number. It was thought that the increased solution fluid temperature due to the increased wall superheat at higher heating fluid Reynolds numbers decreased the surface tension of the solution fluid, resulting in better solution spreading on the tube.

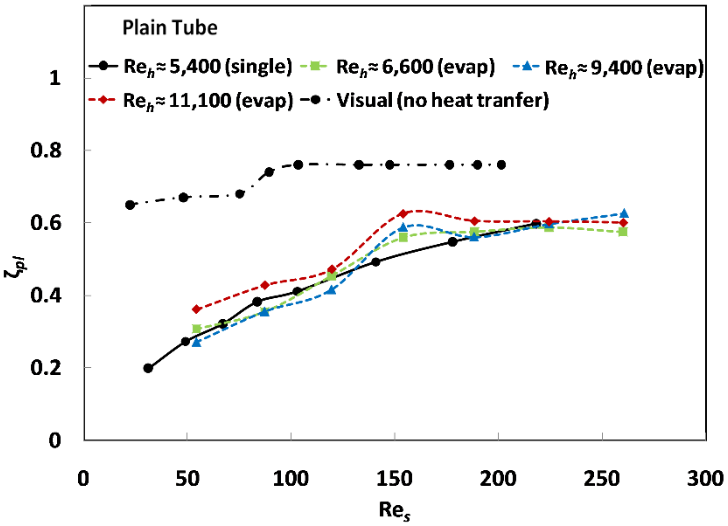

Figure 5-12. Comparison of solution wetting ratios of plain tubes.

From both the visual observation and evaporation heat transfer experiment, there were sudden shifts observed for the solution wetting ratio, which were due to the flow mode change from the droplet to droplet/column mode, while no such shift was found for the single-phase heat transfer condition. The flow mode change was visually observed using the no heat transfer condition as discussed above. Although the solution Reynolds numbers of the flow mode shifted from the visual inspection and evaporation heat transfer experiments are different, the volumetric flow rates for the shifts are similar, which was more relevant information to estimate the solution wetting. Considering the fact that the solution wetting ratios for the single-phase and evaporation heat transfer experiments were obtained using the empirical correlations developed for the plain tubes [[22]) and [1]], some discrepancies between the calculated and measured solution wetting ratios can be expected. It is interesting to see that the calculated solution wetting ratios were reasonably well matched, unlike the external heat transfer coefficients, which exhibited the opposite trend with respect to the solution flow rate. It is also shown from the Fig. 5-12 that the calculated solution wetting ratios were much lower than the measured solution wetting ratio from the visual observation.

The uncertainties of the calculated values for the evaporation heat transfer experiments are listed in Table 5-4. The external heat transfer coefficient and thermal resistance for evaporation heat transfer had the highest uncertainty (31.9% averaged), which also mostly came from the uncertainties of the temperature measurements.

Table 5-4. Averaged (maximum) uncertainties for evaporation heat transfer experiment.

		Plain tube	Porous-layer coated tube
Pressure	P	±0.25%	±0.25%
Temperature	T	±0.2°C	±0.2°C
Solution fluid flow rate	$\dot{V}_s$	±2.00%	±2.00%
Heating fluid flow rate	$\dot{V}_h$	±4.00%	±4.00%
Solution fluid	Q_s	±17.3% (±30.8%)	±26.9% (±47.4%)
	U	±0.18% (±0.34%)	±31.9% (±36.9%)
	R_{ext}	±31.9% (±38.1%)	±31.9% (±36.9%)
	ς	±31.9% (±38.1%)	N/A
Heating fluid	Q_h	±21.3% (±29.7%)	±14.2% (±15.9%)
	h_h	±3.6% (±3.8%)	±3.6% (±3.8%)
	R_h	±3.6% (±3.8%)	±3.6% (±3.8%)

Figure 5-13 shows the comparison of the heat transfer rates of the solution and heating fluids with respect to their respective flow rates for the plain and porous-layer coated tubes using the evaporation heat transfer conditions. The saturation temperature (T_{sat}) shown in Fig. 5-13 is the averaged value for all tested conditions used. As shown, the heat transfer rates of the heating fluid (Q_h) for the porous-layer coated tubes were significantly higher than those of the plain tubes, while the sensible heat transfer rates (Q_s) for the porous-layer coated tubes were slightly lower than those of the plain tubes. As a result, the evaporation heat transfer rates (Q_{eva}) for the porous-layer coated tubes were roughly twice as high as those using the plain tubes.

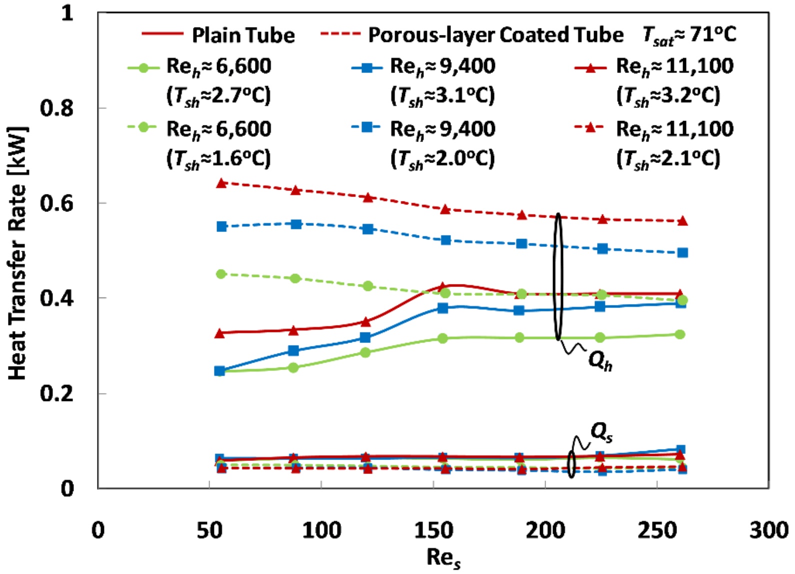

Figure 5-13. Comparison of evaporation heat transfer rates of the plain and porous-layer coated tubes.

It was also observed from Fig. 5-13 that the heat transfer rates of the heating fluid for the plain tubes were increased as the solution Reynolds number was increased, while those for the porous-layer coated tubes were decreased. Interestingly, the heat transfer rates of the heating fluid using the plain tubes were increased suddenly and then remained relatively constant once the solution flow mode was changed from droplet to droplet/column. Figure 5-13 also shows that the heat transfer rate of the heating fluid using both of the tubes was increased as the heating fluid Reynolds number (Re_h) was increased, and thus the thermal resistance (R_h) was decreased. Note that as the heating fluid flow rate was increased, the averaged temperature of the heating fluid was increased and thus the wall superheat (ΔT_{sh}) was increased.

The evaporation heat transfer experiment was conducted using the water saturation conditions at a chamber pressure much lower than ambient. The solution and heating fluid Reynolds numbers were varied from 54 to 261 and from 6600 to 11,100, respectively. Note that the maximum flow rate of the heating fluid was limited to avoid large uncertainties originated from the measurement of the small temperature difference between the inlet and outlet of the heating fluid. The representative test conditions used for the evaporation heat transfer experiment are listed in Table 5-5.

Table 5-5. Representative test conditions used for the evaporation heat transfer experiment.

		Unit	Plain tube	Porous-layer coated tube
Solution fluid	T_{sat}	°C	70.8	70.9
	$\dot{V}_s$	$m^3\ s^{-1}$	9.77×10^{-6}	9.77×10^{-6}
	Γ	$kg\ m^{-1}\ s^{-1}$	0.01567	0.01567
	$T_{s,i}$	°C	68.8	69.5
	$T_{s,o}$	°C	70.3	70.6
	Re_s		154	155
	Pr_s		2.62	2.60
	Ga_s		9.82×10^{11}	1.01×10^{12}
	U	$W\ m^{-2}\ K^{-1}$	7341	8303
	R_{ext}	$K\ W^{-1}$	8×10^{-3}	3.96×10^{-3}
Heating fluid	$\dot{V}_h$	$m^3\ s^{-1}$	4.49×10^{-5}	4.49×10^{-5}
	$T_{h,i}$	°C	76.0	76.0
	$T_{h,o}$	°C	74.3	73.8
	Re_h		6648	6627
	Pr_h		2.42	2.43
	Q_h	W	315	411
	h_h	$W\ m^{-2}\ K^{-1}$	7418	7404
	R_h	$K\ W^{-1}$	5.55×10^{-3}	5.55×10^{-3}

B. Large Falling-Film Evaporator Setup

A large horizontal-tube falling-film heat exchanger setup was built to see the effect of tube rows on the solution wetting and flow mode as well as the evaporation heat transfer. Fig. 5-14 shows the schematic of the test setup, which consisted of a vacuum-tight chamber housing two solution fluid dispensers and eight horizontal evaporator tubes in an inline arrangement of two columns and four rows; plumbing lines for solution and heating fluids; and instrumentation. The solution dispenser and horizontal tubes were vertically aligned in an inline arrangement so that the solution fluid could drip from tube to tube.

As shown in Fig. 5-14, the solution fluid was pumped from the solution reservoir to the solution dispenser by a magnetic-driven, variable-speed DC gear pump (MG 209 XPB17, Clark Solutions) controlled by a DC power supply (3006B, Proteck). The solution fluid was then sprayed from the holes at the bottom of the dispenser to the top of the first tube row and allowed to drip to the lower tube rows. The excess solution fluid was collected at the bottom of the chamber and drained to the solution reservoir, which completed the cycle of the solution fluid circulation.

The chamber was made of a transparent acrylic material to provide visibility to the interior of the chamber during the experiments as well as provide reasonably good thermal insulation because of its low thermal conductivity. The heating fluid started flowing from the bottommost tube to the topmost tube in a zigzag pattern and a cross-flow arrangement against the solution fluid. The heating fluid temperature was maintained using a thermal bath of 1 kW (HE30D, Grant Instruments) controlled by a temperature controller unit (CN7800, Omega). Two additional custom built heaters (2 kW and 1.5 kW) were also used in the heating fluid line. Distilled water was used as the solution and heating fluids.

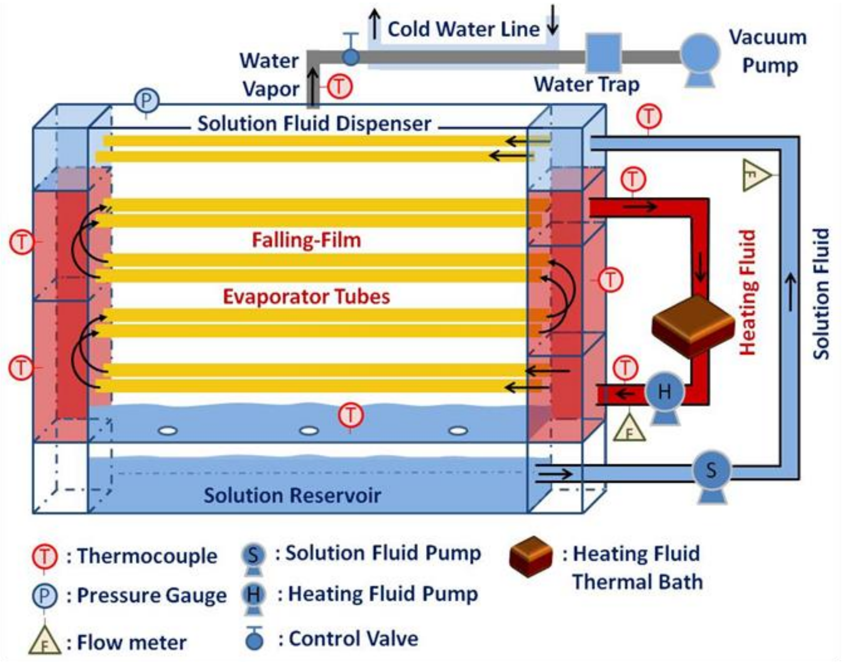

Figure 5-14. Schematic of experimental setup for horizontal-tube, falling-film heat exchanger.

The side view of the heating fluid tube array (four rows and two columns) and the two solution fluid dispensers is shown in Figure 5-15 (a). The distance between the solution dispensers and the topmost horizontal tubes (S_{ds}) and the spacing between the test tubes (S_t) and (S_c) are equal. Each solution dispenser tube has 65 holes drilled in a row each with a diameter ($d_{ds,nz}$) of 1 mm and a spacing ($s_{ds,nz}$) of 6.35 mm. A cross-sectional view of the heating fluid tube with the tube diameters is shown in Fig. 5- 15 (c). A concentric-tube design is used for the horizontal tubes to increase the heating fluid velocity and the heat transfer coefficient by flowing only in the annulus side between D_3 and D_2. All dimensions of the tube setup shown in Fig. 5-15 are listed in Table 5-6.

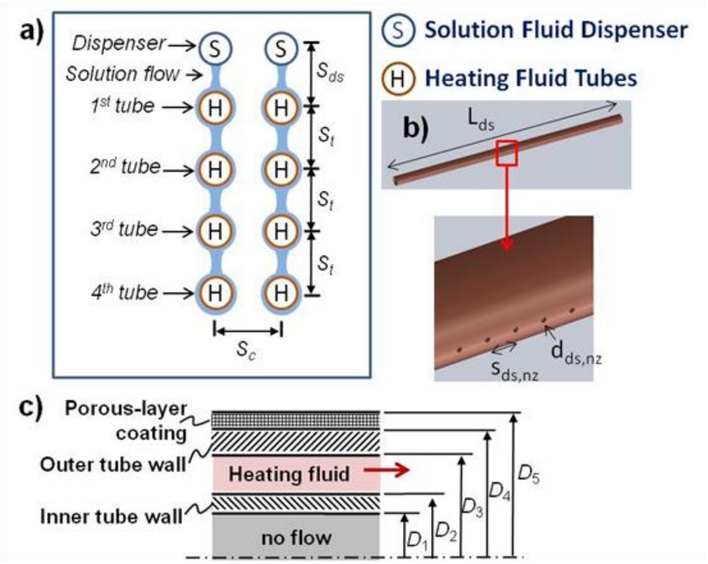

Figure 5-15. Dimensions of the horizontal-tube, falling-film heat exchanger: (a) side view of the tube array, (b) dimensions of the solution dispenser and (c) cross-sectional view of the evaporator tube.

Table 5-6. Dimensions of the experimental setup.

		Unit	Dimension
Inner tube	D_1	mm	6.4
	D_2	mm	9.5
	$L_{t,i}$	mm	457
Outer tube	D_3	mm	13.4
	D_4	mm	15.9
	L_t	mm	457
Porous-layer coating	D_5	mm	17.40
	L_{po}	mm	457
Solution dispenser	$d_{ds,nz}$	mm	1.00
	$s_{ds,nz}$	mm	6.35
	L_{ds}	mm	457
Evaporator chamber	S_{ds}	mm	50.8
	S_t	mm	50.8
	S_c	mm	50.8
	L	mm	457

Figure 5-16 shows the results of the visualization experiment using the plain and porous-layer coated tubes with varying the solution fluid flow rates. The visual observation was done under open, atmospheric pressure conditions with the solution fluid temperature of 18°C without the heat transfer from the heating fluid. The flow modes between the plain tubes were visually noted for the solution fluid Reynolds numbers ranging from 12 to 130. Fig. 5-16 (b) shows the wetting ratio of plain and porous-layer coated tubes. Fig. 5-16 (a) and (c) show the pictures taken at four different representative solution Reynolds numbers corresponding to wetting ratio values given in Fig. 5-16 (b). Fig. 5-16 (b) shows the wetting ratio for the plain and porous-layer coated tubes. Image processing toolbox of Matlab was used to obtain the wetting ratio of tubes. The pictures of 4th tube rows after image processing are shown in Fig. 5-16 (b), where the black and white colors represent the wetted and un-wetted areas, respectively.

As shown in Fig. 5-16 (b), there is a sharp increase in the wetting ratio of plain tubes (from 0.6 to 0.9) until the solution Reynolds number was increased to 49.4. This was the solution flow rate value after which the flow mode remained as droplet/column between the evaporator tubes. Similarly, it seems from Fig. 5-16 (b) that as the solution Reynolds number was increased from 49.4 to 130, the wetting ratio of plain tubes remained almost the same with only a gradual increase and a final convergence to the value of 1. In addition, the wetting ratio results for each row of plain tubes did not show a significant difference. This is an expected result since the visual observation was done under ambient conditions without heat transfer from the heating fluid. Therefore, the solution fluid loss by evaporation as the flow progresses from tube to tube was very low.

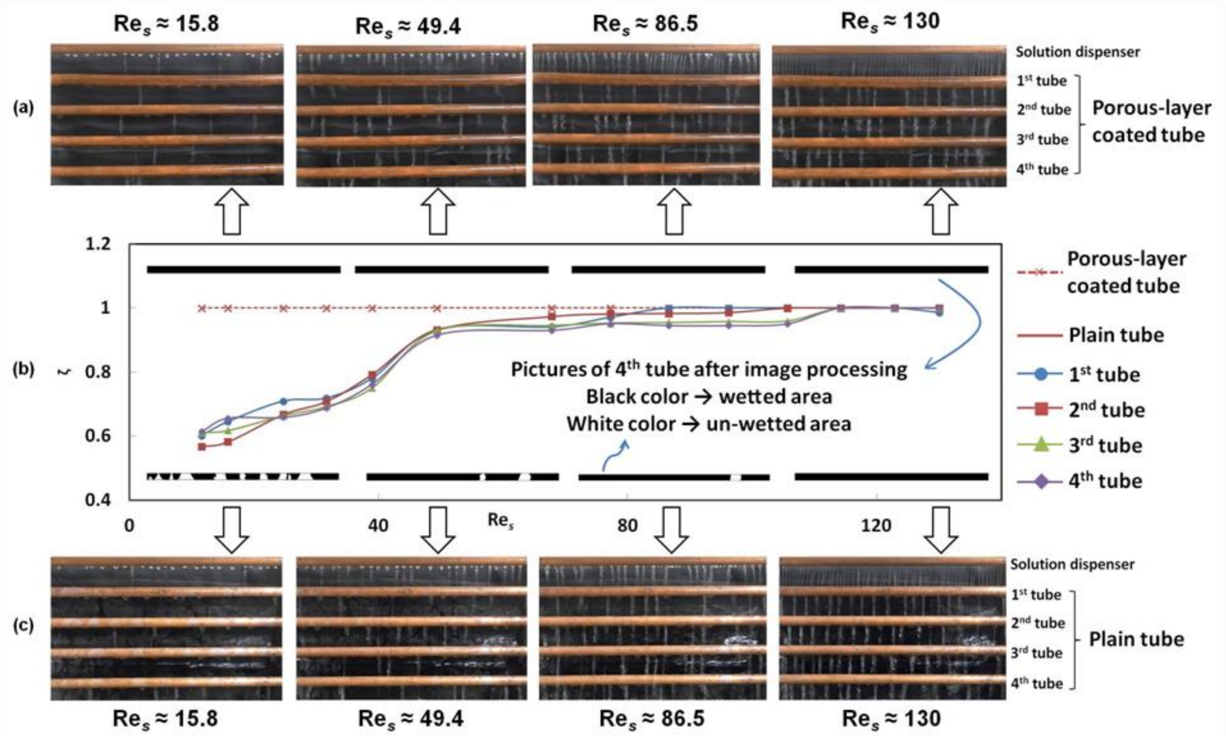

Figure 5-16. Flow mode change with the solution Reynolds number for the (a) plain and (c) porous-layer coated tubes. (b) Wetting ratio change with the solution Reynolds number.

The evaporation heat transfer experiment was conducted using the saturation condition at a chamber pressure lower than ambient pressure. The solution and heating fluid flow rates were changed to vary the Reynolds numbers from 25 to 252 and from 8770 to 13,930, respectively. The controlled parameters for the evaporation heat transfer experiment are listed in Table 5-7.

The heat transfer rate from the heating fluid to the solution fluid is calculated by

$$Q_{h,j} = \left[\dot{m} c_p \left(T_i - T_o\right)\right]_{h,j} \tag{5.17}$$

where the temperatures $T_{i,h}$ and $T_{o,h}$ are the inlet and outlet heating fluid temperatures of each evaporator tube row, and j is the tube row number in the tube array.

The total thermal resistance R_{tot} is given by

$$R_{tot,j} = R_{h,j} + R_{t,j} + R_{ext,j} \tag{5.18}$$

The convective thermal resistance (R_h) of the heating fluid flowing at the annulus side of the concentric tube is given by

$$R_{h,j} = \frac{1}{h_{h,j}\left[\pi D_3 (2L_{t,o})\right]} \tag{5.19}$$

The thermal resistance of the conduction in the outer tube wall is calculated by

Table 5-7. Controlled parameters for the evaporation heat transfer experiment.

			Unit
Solution Fluid (Distilled water)	T_{sat}	69.6 ± 0.2	°C
	Γ	0.00302 – 0.0274	kg/ms
	Re_s	23.4 – 246.4	
Heating Fluid (Distilled water)	$T_{h,in}$	75.1± 0.5	°C
	$\dot{m}_h$	0.123 – 0.185	kg/s
	Re_h	8,770 – 13,930	

$$R_{t,j} = \frac{ln\left(D_4 \big/ D_3 \right)}{2\pi k_t \, (2L_{t,o})} \tag{5.20}$$

where k_t is the thermal conductivity of the heating fluid tube and $L_{t,o}$ is the length of the heating fluid tube.

The external thermal resistance ($R_{ext,j}$) is obtained from the heat transfer rate of the heating fluid and wall superheat ($\Delta T_{sh,j}$), which is given by

$$R_{ext,j} = \frac{\Delta T_{sh,j}}{Q_{h,j}} \tag{5.21}$$

where the wall superheat ($\Delta T_{sh,j}$) is defined by

$$\Delta T_{sh,j} = T_{t,o,j} - T_{sat} \tag{5.22}$$

and the temperature of the outer wall is obtained by

$$T_{t,o,j} = T_{h,ave,j} - Q_{h,j}\,(R_{h,j} + R_{t,j}) \tag{5.23}$$

where $T_{h,ave,j}$ is the average of the inlet and outlet heating fluid temperatures for each evaporator tube row.

The total heat transfer rate from the heating fluid to the solution fluid ($Q_{h,tot}$) is calculated by summing the individual heat transfer rate terms ($Q_{h,j}$) obtained from Eq. (5.17), and is given by

$$Q_{h,tot} = \sum_{j=1}^{4} Q_{h,j} \tag{5.24}$$

The total heat transfer rate from the heating fluid to the solution fluid ($Q_{h,tot}$) is divided into sensible (Q_s) and evaporation (Q_{eva}) heat transfer rates and is given by

$$Q_{h,tot} = Q_s + Q_{eva} \tag{5.25}$$

where the evaporation heat portion (Q_{eva}) is used to evaporate the solution fluid.

The sensible heat portion of the heat transfer rate which is used to raise the solution fluid temperature is given by

$$Q_s = \left\lfloor \dot{m} c_p \left(T_o - T_i \right) \right\rfloor_s \tag{5.26}$$

where $T_{i,s}$ and $T_{o,s}$ are the inlet and outlet temperatures of the solution fluid flow, respectively.

Figure 5-17 (a) shows the comparison of the heat transfer rates ($Q_{h,j}$) of the heating fluid for each row of the tubes with varying the flow rates of the solution fluid. Note that the heating fluid flow rates were kept the same. However, the Reynolds number of the heating fluid for each row of tubes slightly varies due to the change in the fluid properties, which change with the fluid temperature. Figure 5-17(a) shows the heat transfer rates of the heating fluid for the plain tubes. The heat transfer rate of the 1st tube row, which is the topmost tube in the tube array, gave the highest value. Moving downward along the tube array, the heat transfer rates of the individual tubes decreased. The 4th tube row, which is the bottommost tube, had the lowest heat transfer rate. This result is mainly due to the decrease of wetted (heat transfer) area, although the amount of solution fluid available for the downstream tubes is slightly decreased due to evaporation loss. Since the 1st (topmost) tube had the highest wetted area compared to the other tubes, it had the highest heat transfer rate. In addition, as shown in Fig. 5-17 (a), increasing the solution flow rate increased the heat transfer rate. This is again due to the increase of wetted area as a result of higher solution flow rate. Another effect of the wetted area is seen on the wall superheat values shown in Fig. 5-17 (a). The wall superheats somewhat decreased as the solution Reynolds number was increased due to the increased evaporation heat transfer.

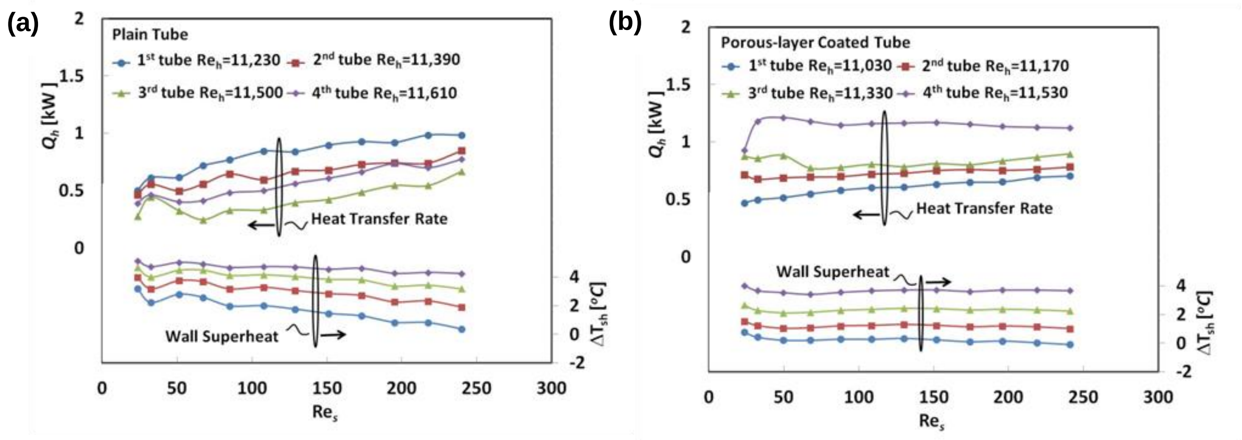

Figure 5-17. Comparisons of heat transfer rates and superheats for all (a) plain and (b) porous-layer coated test tubes.

Figure 5-17 (b) shows the heat transfer rates for the porous-layer coated tubes. The heat transfer rate of the 4th (bottommost) tube in the tube array, gave the highest value, while the heat transfer rates were decreased toward the 1st (topmost) tube, which had the lowest value. The porous-layer coated tube results shown in Fig. 5-17 (b) exhibited the opposite trend of the plain tube results shown in Fig. 5-17 (a). That is, the 4th row of the porous-layer coated tubes had the highest heat transfer rate, while 1st row of the plain tubes has the highest heat transfer rate. This result can be explained by the different superheat values shown in Fig. 5-17 (b) for each row of the setup. The 4th row of the porous-layer tubes had the highest superheat value compared to the other rows because the heating fluid started its circulation from the bottommost (4th row) tube. As the heating fluid traveled through the tubes, its temperature became lower as a result of heat transfer, reaching its lowest wall superheat value at the topmost (1st row) tube. Although the same superheat trend was seen for the plain tubes in Fig. 5-17 (a), the plain tube results differed from the porous-layer coated tube results. This is due to the lower wetting of the downstream plain tubes. As a result, even though the 4th row of plain tubes had the highest superheat in the tube array, it had the lowest heat transfer rate due to its increased un-wetted area.

Figure 5-18 shows the comparison of the heat transfer rates for each row of the porous-layer coated and plain tubes with varying flow rates of both the heating and solution fluids. Figure 5-18 (a) shows the comparison of the heat transfer rates of the 1st tube row (topmost) in the tube array. It was seen that the heat transfer rate is increased as the heating fluid Reynolds number is increased. It was also seen that increasing the solution fluid Reynolds number increased the heat transfer rate for both the plain and porous-layer coated tubes. Since the 1st tube row was the topmost tube in the tube array, it was directly affected by the solution fluid flow coming out of the dispenser. Since the velocity of the jet stream from the dispenser became higher for higher solution flow rates, the heat transfer rates further increased due to the heat transfer enhancement by jet impingement.

As shown in Fig. 5-18 (b), the 2nd row of porous-layer coated tubes gave higher heat transfer rates than those of the plain tubes, but the difference became smaller with higher solution flow rates. Although the plain tube heat transfer rate results show an increasing trend with increased solution flow rate, they seem more flat with the porous-layer coated tubes. This is attributed to the fact that the wetted area is rapidly increased for the plain tubes but remains constant for the porous-layer coated tubes as the solution flow rate is increased.

Figures 5-18 (c) and (d) show the comparison of the heat transfer rates of the 3rd and 4th tube rows, respectively. As shown in the Figures, the porous-layer coated tubes had much higher $Q_{h,j}$ values than the plain tubes whose surface wetting got worse for the downstream rows, although the wall superheats of the plain tubes were always higher than those of the porous-layer coated tubes. There is a rapid decrease in the heat transfer rate of the 4th row of porous-layer coated tubes at low solution Reynolds numbers (Re_s ~ 30). Therefore, (Re_s ~ 30) will be taken as the threshold solution flow rate value, at which a transition from partial wetting to complete wetting occurs for the 4th row of porous-layer coated tubes.

Figures 5-19 (a) and (b) show the comparison of the external heat transfer coefficients and wetting ratios of the plain and porous-layer coated tubes for the 3rd and 4th tube rows, respectively. The external heat transfer coefficients (U_{pl}) for the 3rd and 4th rows of the plain tubes were obtained from a correlation that was derived experimentally by (Fujita and Tsutsui 1998) for the 3rd and 4th row tubes in their multiple row test setup of falling-film evaporator, and is given by

$$\mathrm{Nu}_{pl} = U_{pl}\left(\nu_s^{2}/gk_s^{3}\right)^{1/3} = \left(\mathrm{Re}_s^{-2/3} + 0.010\,\mathrm{Re}_s^{0.3}\mathrm{Pr}_s^{0.25}\right)^{0.5} \qquad (5.27)$$

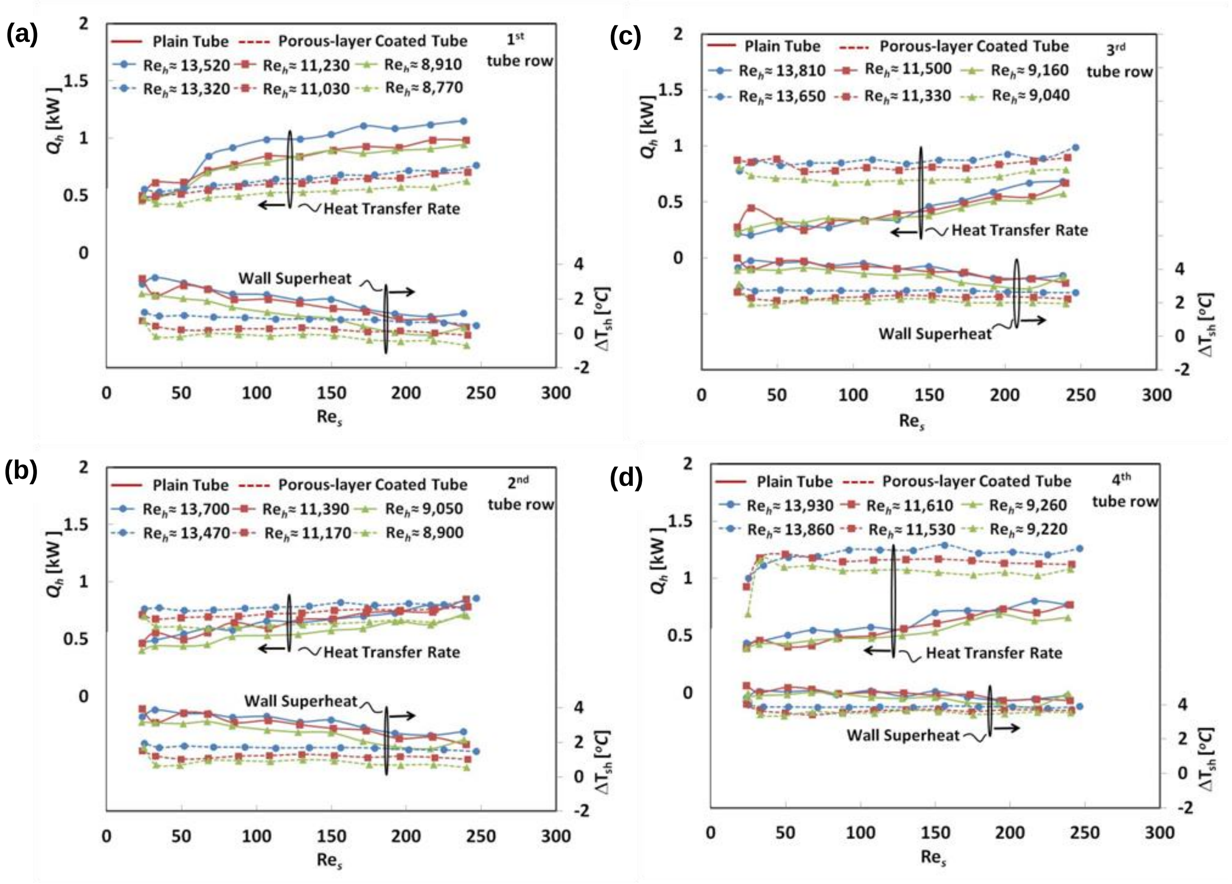

Figure 5-18. Comparison of the heat transfer rates and wall superheats of the plain and porous-layer coated tubes for (a) 1st, (b) 2nd, (c) 3rd, and (d) 4th rows in the tube array.

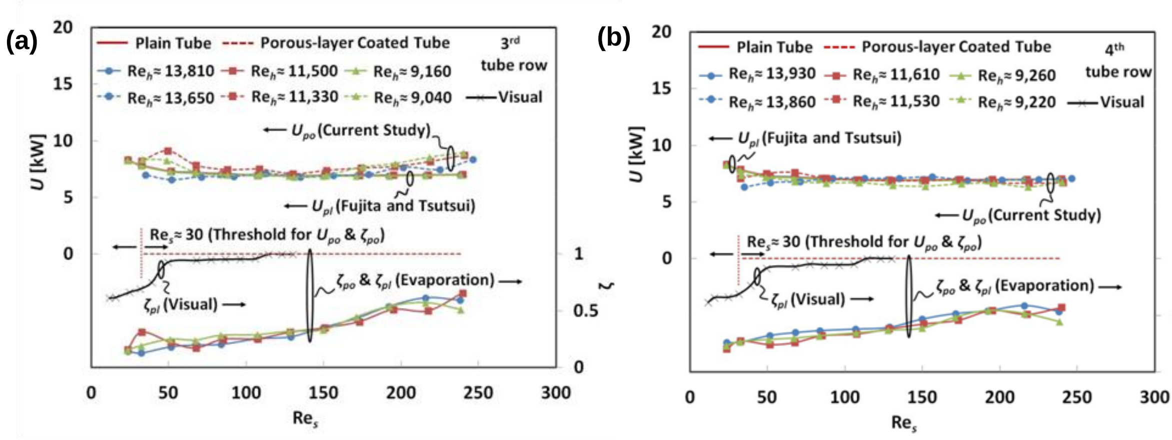

Figure 5-19. Comparison of the external heat transfer coefficients and wetting ratio of the plain and porous-layer coated tubes for the (a) 3rd and (b) 4th row in the tube array.

Since the empirical correlation above was obtained under fully wetted conditions, the solution wetting ratio ($\varsigma_{pl,j}$) for the plain tubes can be determined as below

$$\varsigma_{pl,j} = \frac{Q_{h,j}}{U_{pl,j}\ A_{t,o} \Delta T_{sh,j}} \tag{12.28}$$

In contrast, based on the results obtained from the evaporation and visualization experiments, the overall external heat transfer coefficients of the porous-layer coated tubes were obtained by assuming fully wetted condition (ζ_{po} = 1) for flow rates higher than the threshold value Re$_s$ ~ 30. The equation to obtain (U_{po}) is given by

$$U_{po,j} = \frac{Q_{h,j}}{A_{t,o} \Delta T_{sh,j}} \tag{5.29}$$

As shown in Fig. 5-19 (a), the 3rd row of the porous layer coated tubes showed a decreasing and then an increasing trend in the overall external heat transfer coefficient ($U_{po,3}$). This result may be attributed to the fact that once the solution Reynolds number is high enough to make the evaporator tubes fully wetted, further increase of the solution flow rate will decrease the heat transfer because of the increased solution flow film thickness over the evaporator tubes. This would first cause a small decrease in the heat transfer coefficient. However, further increase of the solution Reynolds number results in an increase in heat transfer due to the turbulent nature of the solution flow at such high solution Reynolds numbers.

The overall external heat transfer coefficients of the plain tubes ($U_{pl,3}$) are also shown in Fig. 5-19 (a). The $U_{po,3}$ values seem slightly higher than the $U_{pl,3}$ values at low and high solution Reynolds numbers. The wetting ratio ($\zeta_{pl,3}$) of the 3rd row of the plain tubes obtained from Eq. (5.29) is also shown in Fig. 5-15 (a). The wetting ratio of the plain tubes was increased as the solution flow rate was increased while the wetting ratio of the porous-layer coated tubes remained as one. In addition, the wetting ratio of 3rd row of plain tubes obtained from the visual observation is shown in Fig. 5-19 (a) to compare them with the results obtained from the evaporation heat transfer experiment. It was seen that there is a discrepancy in the wetting ratio results. This is due to the solution fluid loss by evaporation during the heat transfer experiments. Note that the solution Reynolds number range used for both experiments differs from each other significantly although the same solution flow rates were used for both experiments, which is due to the property variation at different temperatures.

Figure 5-19 (b) shows the comparison of the overall external heat transfer coefficients (U_4) and wetting ratios (ζ_4) of the 4th tube row in the tube array. As shown in Fig. 5-19 (b), the external heat transfer coefficient of the porous-layer coated tubes $U_{po,4}$ decrease a little as the solution Reynolds number was further increased above 50. This result is attributed to the fact that, in this solution Reynolds number range, the 4th porous-layer coated tube is still in the laminar regime, where the increase of the solution Reynolds number causes a small decrease in the heat transfer coefficient because of the increased solution flow film thickness. The U_4 values for both types of tube surfaces seem very similar. Similar to the results obtained in Fig. 5-19 (a), the wetting ratio of the plain tubes increases as a result of solution flow rate increase, whereas the wetting ratio of the porous-layer coated tubes remains as one. In addition, the wetting ratio of 4th row of plain tubes obtained from the visual observation is shown in Fig. 5-19 (b) to compare them with the results obtained from the evaporation heat transfer experiments. Similar to the results of 3rd row of plain tubes, there is a discrepancy between the two wetting ratio results.

Finally, the overall performance comparison between two types of surfaces was made. Fig. 5-20 (a) and (b) shows the overall heat transfer performance comparison of plain and porous-layer coated tubes with varying the solution flow rates while keeping the heating fluid flow rate constant. Note that Q_h values plotted in Fig. 5-20 (a) are the total heat transfer rates of the whole tube array. As shown in the Figure, the heat transfer rate of the heating fluid ($Q_{h,tot}$) for the porous-layer coated tubes is much higher than that of the plain tubes. However, the sensible heat transfer rates (Q_s) for both tubes are almost the same. As a result, the evaporation heat transfer rate (Q_{eva}) of the porous-layer coated tubes at low solution flow rates is much (~ 70%) higher than that of the plain tubes, due to the complete wetting and thin solution liquid film. The evaporation heat transfer rate was calculated by subtracting the measured solution fluid heat transfer rate, Q_s, from the measured heating fluid heat transfer rate, $Q_{h,tot}$.

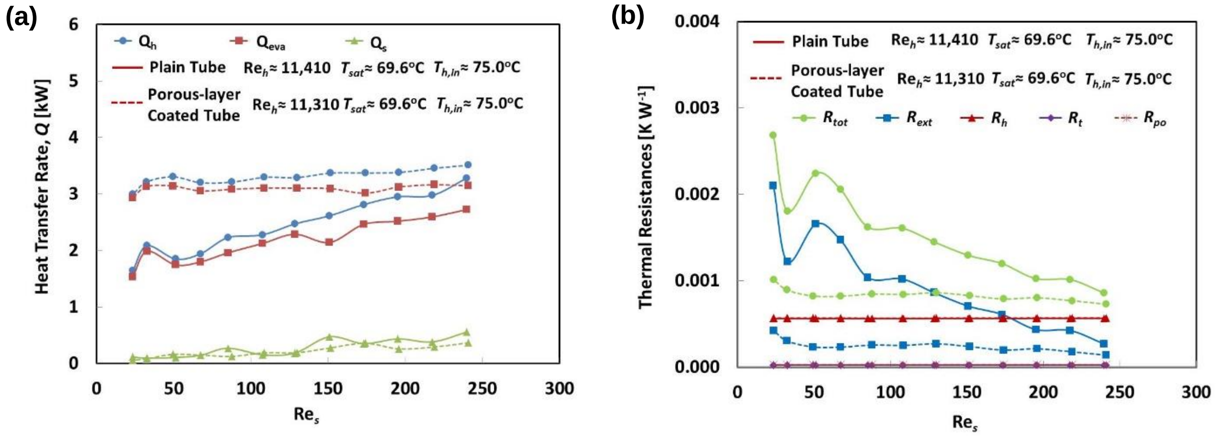

Figure 5-20. Comparison of the (a) overall heat transfer rates and (b) overall thermal resistances for the plain and porous-layer coated tubes.

Figure 5-20 (b) shows the comparison of the thermal resistances for the plain and porous layer coated tubes with varying solution flow rates while keeping the heating fluid flow rate constant. The resistances were calculated based on the total heat transfer rate of the whole tube array ($Q_{h,tot}$). It is observed from Fig. 5-20 (b) that the thermal resistances of the solution fluid (R_{ext}) and the heating fluid (R_h) are the main contributors to the total thermal resistances (R_{tot}). The total thermal resistance (R_{tot}) for the porous-layer coated tubes is always lower than that for the plain tubes due to the smaller external thermal resistance (R_{ext}) of the porous-layer coated tubes, which results from the complete wetting. Recall that the external thermal resistance (R_{ext}) for the porous-layer coated tubes includes three components due to (i) conduction resistance (R_{po}) of the water-saturated porous-layer coating, (ii) convection resistance (R_f) by the solution fluid film flow and (iii) surface evaporation resistance (R_e).

The uncertainties of the calculated values for the evaporation heat transfer experiment are listed in Table 5-8.

Table 5-8. Uncertainties of the variables used for the evaporation heat transfer experiment.

		Plain tube	Porous-layer coated tube
Pressure	P	±0.25%	±0.25%
Temperature	T	±0.2ºC	±0.2ºC
Solution Fluid Flow Rate	$\dot{V}_s$	±2.00%	±2.00%
Heating fluid flow rate	$\dot{V}_h$	±3.00%	±3.00%
Solution fluid	Q_s	±11.1% (±18.1 %)	±9.75% (±19.0%)
	R_{ext}	±16.5% (±25.3%)	±24.2% (±42.6%)
	U_3	±0.23% (±0.47%)	±29.4% (±32.9%)
	U_4	±0.23% (±0.47%)	±21.1% (±25.4%)
	ζ_3	±58.7% (±110%)	N/A
	ζ_4	±38.8% (±52.8%)	N/A
Heating fluid	Q_h	±9.01% (±13.8%)	±6.62% (±7.65%)
	R_h	±2.61% (±2.63%)	±2.61% (±2.63%)

Task 5.4 Development of Hydrophilic/Hydrophobic Coating Materials/Techniques for Surface Wetting Property Control

For this task, hydrophilic coating will be developed using ceramic materials (e.g., oxidation of metal) on metallic substrates. The ceramic coating can be created by slurry, painting, dipping or screen printing methods, followed by heat treatment and direct oxidation. The wetting and surface enhancement using the hydrophilic ceramic coating is crucial to the enhancement of two-phase heat transfer (boiling, evaporation and condensation). Table 5-9 lists the examples of performance improvements by surface coating.

Surface oxidation has been considered as an easy surface coating method to create a hydrophilic surface and to enhance the surface wetting of the solution fluid. The copper oxides (Cu_2O and CuO) have lower surface energies than fresh copper and therefore increase the surface wetting. If the porous coating made of sintered copper particles used for the evaporation experiment is oxidized, a nano-scale surface morphology can be created in addition to the micro-scale porous structure. Since copper can be easily oxidized when it is exposed to oxygen at high temperature, the oxidization could be a very cost-effective way to create a hydrophobic surface coating which can affect the solution wetting and heat transfer performance.

Table 5-9. Examples of performance improvements by surface coating.

Properties	Desirable performance improvements
Surface properties	surface damage-resistance, surface cleanness
Mechanical properties	high strength, high hardness, low friction coefficient
Electromagnetic properties	high electro-conductivity, electromagnetic radiation protection
Optical properties	high reflectivity, selective absorption
Thermal properties	high thermal resistance, high thermal barrier characteristics
Physical properties	bonding characteristics, adhesive characteristics
Chemical properties	hydrophilic/phobic characteristics, catalytic characteristics
Biochemical properties	anti-fungal characteristics
Esthetic properties	Color characteristics

Hydrophilic oxide layers were created using copper surface in order to enhance the surface wetting and evaporation heat transfer. Figure 5-21 shows the SEM images of the copper particles [Fig. 5-21 (a~c)] cleaned in a tube furnace with Hydrogen environment and *naturally* oxidized copper particles [Fig. 5-21 (d~f)] which had been in contact with water in ambient. Figure 5-22 shows the SEM images on the copper oxide (CuO) formed on the surface of copper (Cu) samples prepared from solution concentration of 0.1M NaOH aqueous solution at 60^{o}C for 72 hours. The color of Cu sample was changed into black after solution treatment. Agglomerates of nano-sized grains were observed as shown in Fig. 5-22 (c).

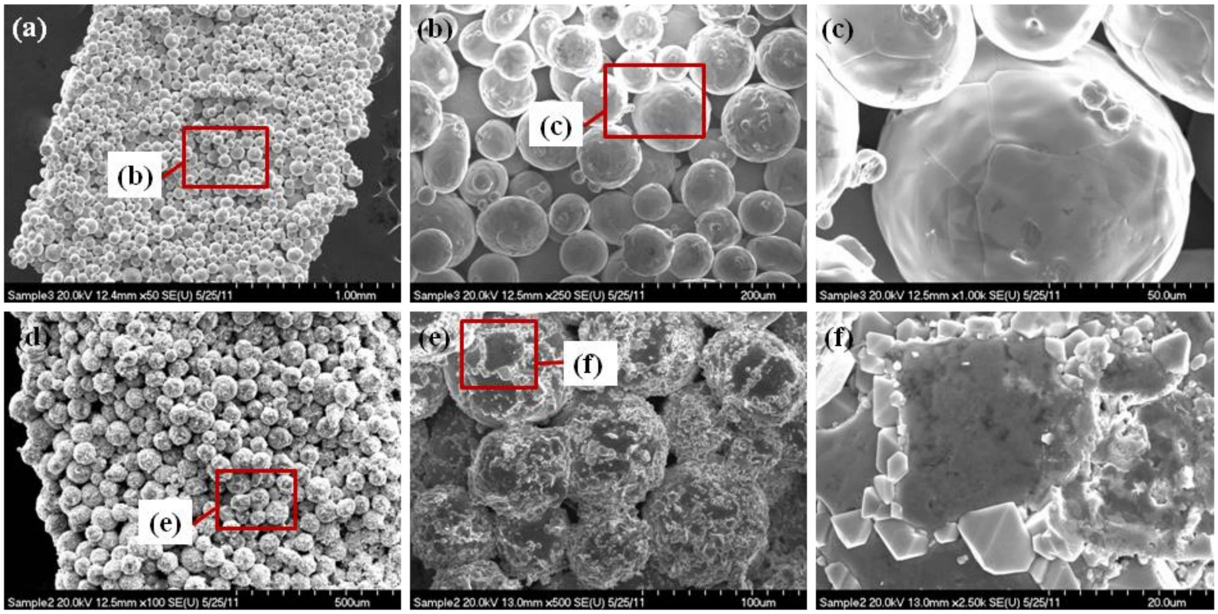

Figure 5-21. SEM images of (a-c) clean (de-oxidized in sintering furnace) and (d-f) oxidized (Cu_2O) copper particles after a long-term contact with water in ambient.

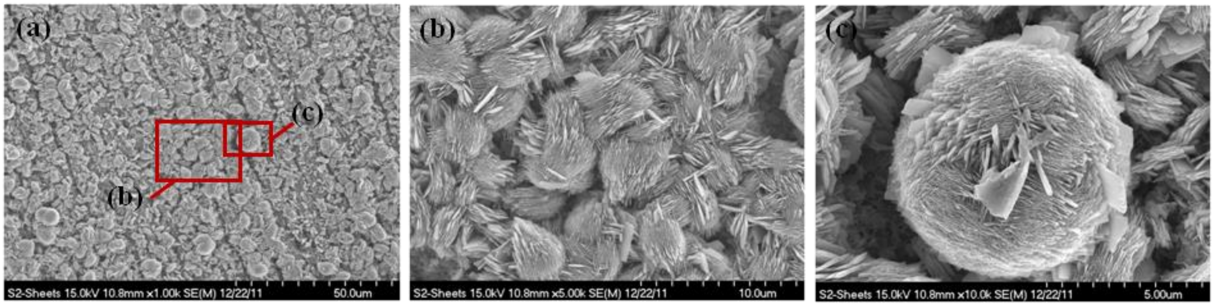

Figure5-22. (a) Chemically-oxidized (CuO) copper surface in 0.1M NaOH showing (b) hairy surface and (c) spherical ball.

Task 5.5 Fabrication of Micro-Scale, Structured Porous Surface with Hydrophilic/Hydrophobic Coating

The starting material for the copper oxidation was obtained from a copper rod. Copper samples were sandpapered prior to the chemical oxidation to improve the adhesive strength of the copper oxide layer on the copper substrate. Then, the samples were immersed in a NaOH aqueous solution.

The chemical reactions for the copper oxidation of CuO, (Cupric Oxide) are given by

$$\begin{aligned}&NaOH(s) + H_2O(l) \rightarrow Na^+(aq) + OH^-(aq) + H_2O(l)\\&2Cu + 4OH^- + 2H_2O + O_2 \rightarrow 2[Cu(OH)_4]^{2-}\\&[Cu(OH)_4]^{2-} \rightarrow CuO + H_2O + 2OH^-\end{aligned} \tag{5.30}$$

The chemical reactions for the copper oxidation of Cu_2O, (Cuprous Oxide) are given by

$$\begin{aligned}&NaOH(s) + H_2O(l) \rightarrow Na^+(aq) + OH^-(aq) + H_2O(l)\\&2Cu^+ + 2OH^-(aq) \rightarrow Cu_2O + H_2O(l)\end{aligned} \tag{5.31}$$

CuO is a black solid with an ionic structure and insoluble in water, while Cu_2O is a reddish solid and can be degraded to CuO in moist air. The nano/micro-scale surface structures of copper oxides formed on the copper samples were characterized by the images from a Scanning Electron Microscope (S4700-II, Hitachi) at various magnifications. The composition analysis of each sample was carried out using an Energy Dispersive X-ray Spectrometer, EDX [INCA Energy 200 Microanalysis system (IE200) Oxford]. The processing conditions used for the copper oxidation are summarized in Table 5-10.

Table 5-10. Treatment conditions of the chemical immersion method used for copper oxide formation.

Sample Name	Treatment Temperature [°C]	Solution Concentration [M]	Treatment Time [hr]
S0	No Treatment		
S1	60	0.03	24
S2		0.1	
S3		0.5	
S4		1	
S5		2	
S6		5	
S7		0.03	72
S8		0.1	
S9		0.5	
S10		1	
S11		2	
S12		5	

Figure 5-23 shows the SEM images at 3k magnification (insets at 30k magnification with EDX analysis results) of the copper oxide formed on the copper samples which were treated in a NaOH aqueous solution with the solution concentration of 0.03 M at 60°C for 24 hrs [S1, Fig. 5-23(a)] and (b) 72 hrs [S7, Fig. 5-23(b)], respectively. It was found from a naked eye observation that the samples were completely covered with a dark black layer after 24 hours of oxidation. Figure 5-23 shows that the nano-sized flakes were uniformly covered in a mating pattern over the entire sample. The diameters of the flakes are in the range of nanometers, while the length of the nano flakes ranges one micrometer. In Fig. 5-23(b) using a longer treatment of 72 hrs, the agglomerates like a ball shape randomly appeared. The SEM images at a higher magnification (× 30k) are shown in the insets of Figs. 5-23(a) and (b) with the chemical composition results from the EDX analysis. It can be seen from the EDX results that for both samples, the atomic ratios between Cu and O elements are close to one, which indicates that the oxides formed on the copper samples are CuO.

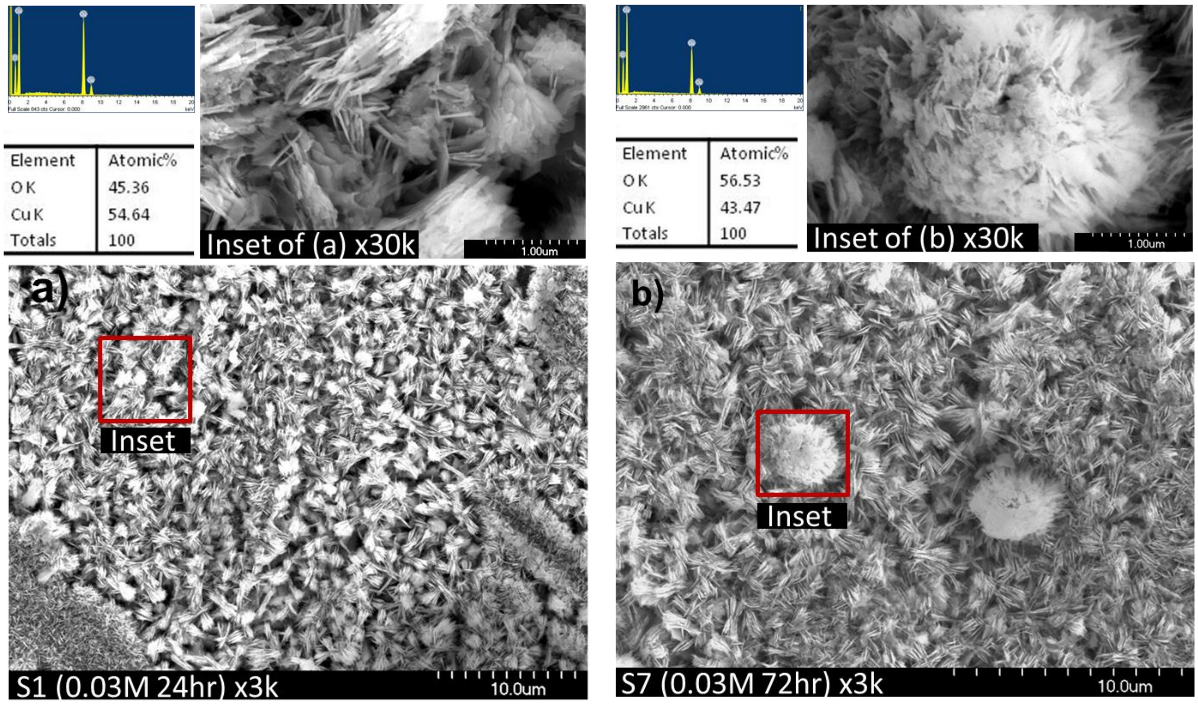

Element	Atomic%
O K	45.36
Cu K	54.64
Totals	100

Element	Atomic%
O K	56.53
Cu K	43.47
Totals	100

Figure 5-23. SEM images of the copper samples treated in 0.03 M NaOH at 60°C for (a) 24 hrs (S1) and (b) 72 hrs (S7).

Figure 5-24 shows the SEM images at 10k magnification (insets at 30k magnification) of the copper oxide formed on the surface of the copper samples which were treated in a NaOH aqueous solution with the solution concentration of 0.1 M at 60°C for 24 hrs [S2, Fig. 5-24(a)] and (b) 72 hrs [S8, Fig. 5-24(b)], respectively. Figures 5-24(a) and (b) show the similar morphology as seen in Fig. 5-23 where the surface is covered by nano-size flakes. However, as shown in Fig. 5-24(a) increasing the NaOH concentration to 0.1M resulted in the agglomerates (balls) to be seen earlier (24 hrs). The comparison of the insets shown in Figs. 5-24(a) and (b) also indicates that the size of the flower shapes is increased from 2 to 3µm when the reaction time was increased from 24 to 72 hrs. In addition, the EDX results show that the atomic ratio between Cu and O elements is close to one, which suggests that the oxides formed on the copper samples are CuO.

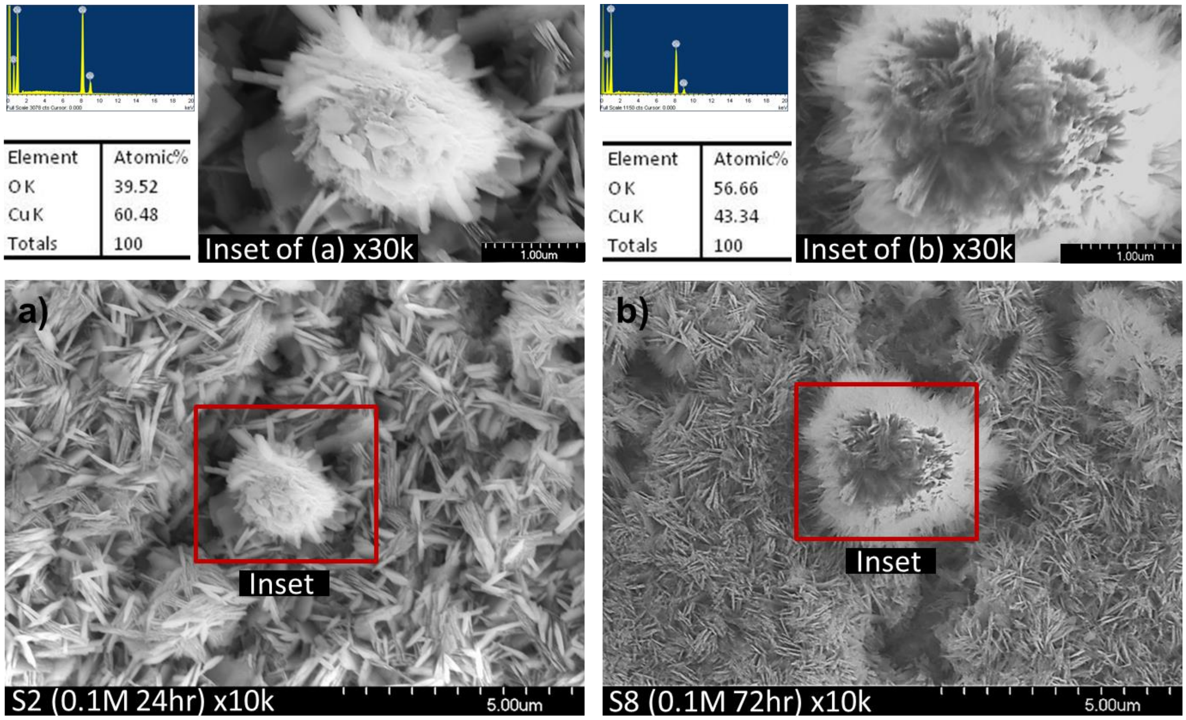

Element	Atomic%
O K	39.52
Cu K	60.48
Totals	100

Element	Atomic%
O K	56.66
Cu K	43.34
Totals	100

Figure 5-24. SEM images of the copper samples treated in 0.1 M NaOH at 60°C for (a) 24 hrs (S2) and (b) 72 hrs (S8).

Figure 5-25 shows the SEM images at 1k magnification (insets at 30k magnification) of the copper oxide formed on the surface of the copper samples which were treated in a NaOH aqueous solution with the solution concentration of 0.5 M at 60°C for 24 hrs [S3, Fig. 5-25(a)] and (b) 72 hrs [S9, Fig. 5-25(b)], respectively. Figures 5-25(a) and (b) show the similar morphology as seen in Figs. 5-1 and 5-2. The comparison of the insets shown in Figs. 5-25(a) and (b) indicates that, as the time used for the oxidation is increased, the nano-size flakes of S9 became much bigger than those of S3 in terms of width and length. In Fig. 5-25(b) it was also seen that increasing the oxidation time to 72 hr resulted in ball shapes on the surface. An enlarged view of the ball shape shown as an inset in Fig. 5-25(b) shows the ball size to be about 10 µm. This is much bigger than the size of the ball shapes seen for S2 [Fig. 5-24(a)], S7 [Fig. 5-23(b)], and S8 [Fig. 5-24(b)]. In addition, the chemical analysis of the insets also shows similar atomic ratio between Cu and O elements, which again indicates that the oxide formed over the surface is CuO.

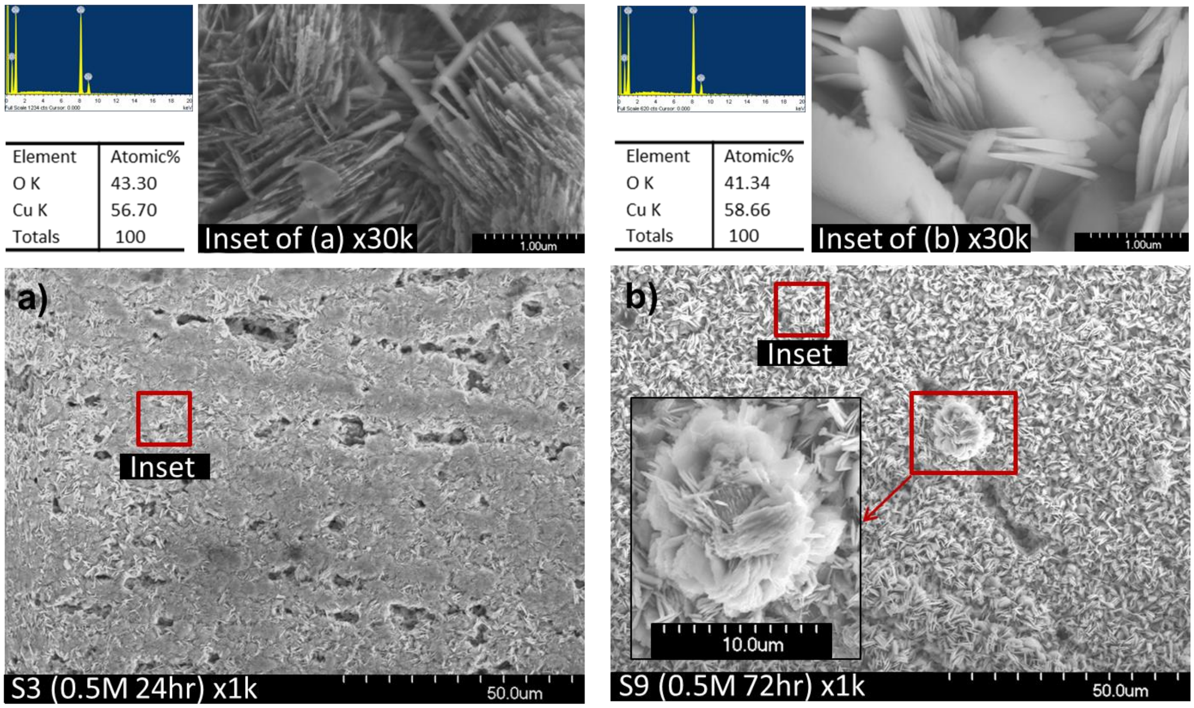

Element	Atomic%
O K	43.30
Cu K	56.70
Totals	100

Element	Atomic%
O K	41.34
Cu K	58.66
Totals	100

Figure 5-25. SEM images of the copper samples treated in 0.5 M NaOH at 60°C for (a) 24 hrs (S3) and (b) 72 hrs (S9).

Figure 5-26 shows the SEM images at 3k magnification (insets at 30k magnification) of the copper oxide formed on the surface of the copper sample which was treated in a NaOH aqueous solution with the solution concentration of 1 M at 60^{o}C for 24 hrs [S4, Fig. 5-26(a)] and (b) 72 hrs [S10, Fig. 5-26(b)], respectively. Figures 5-26(a) and (b) show a completely different surface morphology than those of the other samples treated in lower solution concentration of NaOH (0.03, 0.1, and 0.5 M). The insets of Fig. 5-26(a) and (b) show that the surfaces consist of crystal structures of round shape. It was seen from a naked eye observation that the color of S4 and S10 were reddish rather than black. The EDX results of the inset of Fig. 5-25(a) showed the compositions of Cu_2O (25.21 atomic % of O and 74.79 atomic % of Cu). The color and the EDX results of S4 indicate that the oxide formed over the surface would be Cu_2O rather than CuO. Interestingly, S10 showed a ball-like shape in addition to coarser crystal structures as shown in Fig. 5-26(b). Therefore, the EDX analysis was done for both features of the surface. The size of the flower was around 10µm, which is similar to the flower size seen for S9. It can be seen from the spectrum 1 analysis that the base surface of S10 was composed of 27.5 atomic % of O and 71.17 atomic % of Cu. This indicates that the base area of S10 would be Cu_2O. The spectrum 2 analysis shows that the flower shape consisted of 50.51 atomic % of O and 49.49 atomic % of Cu and the flower shape seen for S10 would be CuO. A very low amount of Si (1.32%) was seen in the Spectrum 1 result, which is attributed to the sand paper used during the surface preparation.

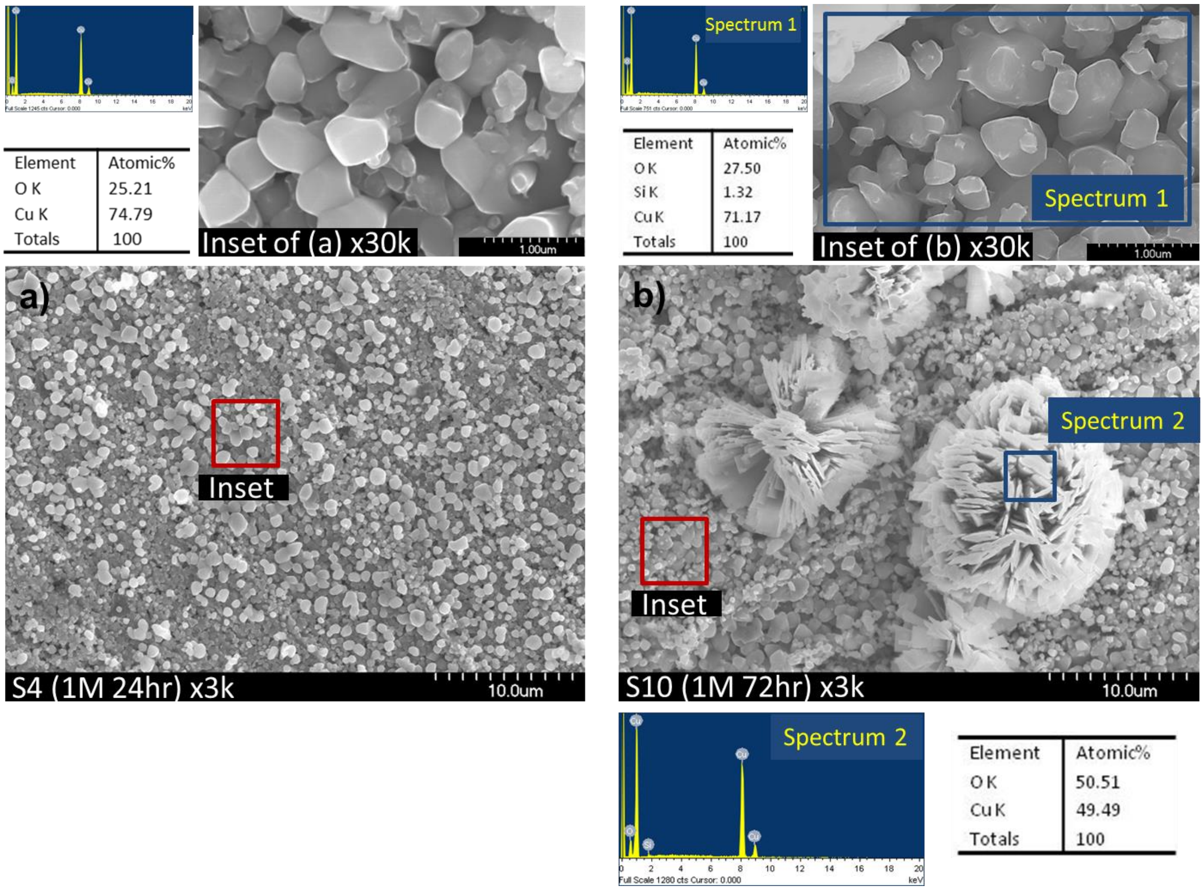

Element	Atomic%
O K	25.21
Cu K	74.79
Totals	100

Element	Atomic%
O K	27.50
Si K	1.32
Cu K	71.17
Totals	100

Element	Atomic%
O K	50.51
Cu K	49.49
Totals	100

Figure 5-26. SEM images of the copper samples treated in 1 M NaOH at 60°C for (a) 24 hrs (S4) and (b) 72 hrs (S10).

Figure 5-27 shows the SEM images at 3k magnification (insets at 10k magnification) of the copper oxide formed on the surface of the copper samples which were treated in a NaOH aqueous solution with the solution concentration of 2 M at 60^{o}C for 24 hrs [S5, Fig. 5-27(a)] and (b) 72 hrs [S11, Fig. 5-27(b)], respectively. It can be seen from the Figures that the samples have coarser crystal structures covering the entire surface. The insets of Figs. 5-27(a) and (b) show that the size and shape of the crystals are very uniform. It was found from a naked eye observation that the color of the samples S5 and S11 were rather reddish. The EDX results of the insets suggest that the oxide formed over the copper samples would be Cu_2O. In addition, the comparison of Figs. 5-26(a) and 5-27(a) of S4 and S5, respectively, shows that the surface morphologies are similar showing crystal shapes. However, it is seen that S5 has a higher number density of the crystals than S4. It is also shown that the size of the crystals of S4 is around 500 nm, whereas the size of the crystals of S5 is around 2 μm. It is concluded that increasing the NaOH solution concentration from 1 M to 2 M increased the size of the crystals as well.

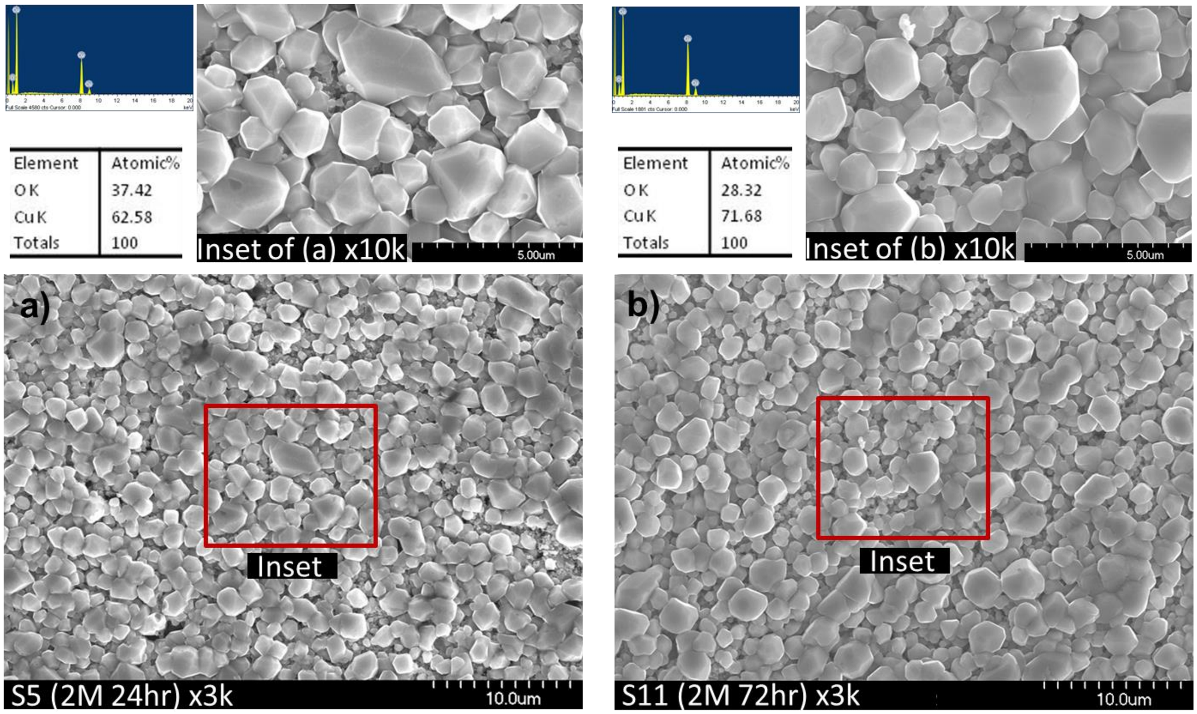

Element	Atomic%
O K	37.42
Cu K	62.58
Totals	100

Element	Atomic%
O K	28.32
Cu K	71.68
Totals	100

Figure 5-27. SEM images of the copper samples treated in 2 M NaOH at 60°C for (a) 24 hrs (S5) and (b) 72 hrs (S11).

Figure 5-28 shows the SEM images at 1k magnification (insets at 10k magnification) of the copper oxide formed on the surface of the copper sample which was treated in a NaOH aqueous solution with the solution concentration of 5 M at 60^{o}C for 24 hrs [S6, Fig. 5-28(a)] and (b) 72 hrs [S12, Fig. 5-28(b)], respectively. It can be seen from the insets of Figs. 5-28(a) and (b) that the surfaces show pyramidal crystal shapes and the number density of these structures was very low. The EDX analysis was done for two different areas of the surfaces. The EDX result for the Spectrum 1 of S6 shows that the pyramidal shapes would be Cu_2O. However, the Spectrum 2 of S6 showed no oxygen element. Similar results were obtained for the sample S12. It is concluded that increasing the NaOH solution concentration to 5M suppressed the formation of copper oxides over the substrate.

From the study of Xiao et al. [21], it was seen that flakes and agglomerates were obtained after for oxidation of copper samples using 0.2 M of NaOH solution. These structures were found by XRD to be CuO. Similarly, it was seen from the study of Oishi et al. [20] that CuO was formed when 0.1 M NaOH was used to oxidize Cu substrates. However, it was also reported in Oishi et al. that when the concentration of the solution was increased to 1 M or 10 M, Cu_2O was formed. It was mentioned that the surface morphology of Cu sample oxidized in 0.1 M of NaOH was completely different than those of the samples oxidized in 1 or 10M of NaOH. In our study, similar results were obtained in that the samples oxidized in low NaOH solution concentrations (0.03, 0.1, and 0.5 M of NaOH) showed nano/micro-scale flakes and balls, which turned out to be CuO from the EDX analysis. The samples oxidized in high NaOH solution concentrations (1, 2, and 5 M of NaOH) showed crystal structures being Cu_2O.

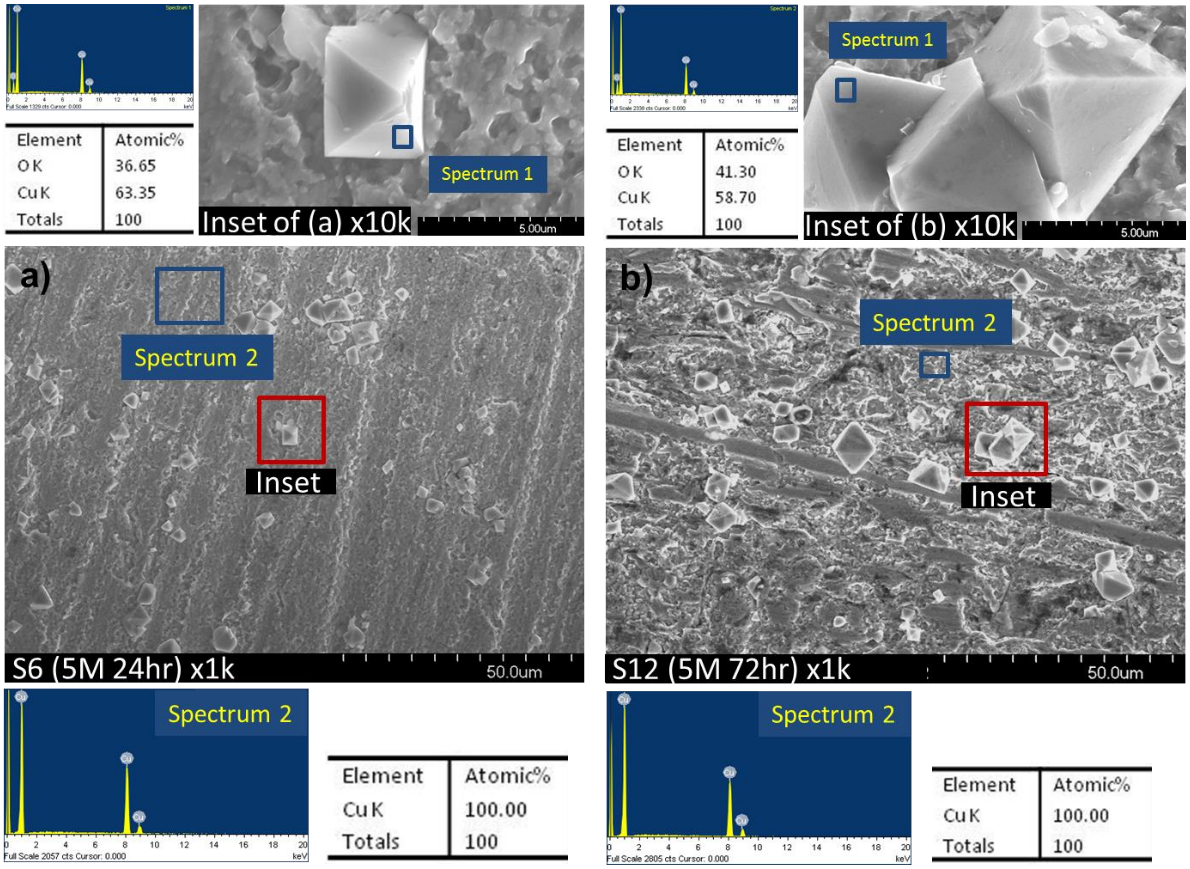

Element	Atomic%
O K	36.65
Cu K	63.35
Totals	100

Element	Atomic%
O K	41.30
Cu K	58.70
Totals	100

Element	Atomic%
Cu K	100.00
Totals	100

Element	Atomic%
Cu K	100.00
Totals	100

Figure 5-28. SEM images of the copper samples treated in 5 M NaOH at 60°C for (a) 24 hrs (S6) and (b) 72 hrs (S12).

The contact angle is used to measure the affinity of a liquid with a surface and is greatly affected by the nano/micro-scale surface morphology. In this study, using a goniometer (Theta Optical Tensiometer, Attension Biolin Scientific) based on the sessile drop method, the water droplet profile on the copper samples was taken three times and the Young-Laplace equation was fitted to the droplet profile to obtain the static contact angle. The measured contact angle was used as an indication for the surface wetting of the falling liquid flow over the evaporator tubes.

Figure 5-29 shows the variation of the measured contact angle for the copper oxide samples which were treated in the NaOH solutions of different concentrations (0.03, 0.1, 0.5, 1, 2, and 5 M) for 24 hrs and 72 hrs, respectively. The insets in Fig. 5-29 are the SEM images of the twelve samples which were discussed above. In Fig. 5-29, the dashed line represents the contact angle (59.0°) of the untreated plain copper sample (S0). It can be seen from Fig. 5-29 that the contact angle is decreased to super-hydrophilic until the solution concentration was increased to 0.5 M. Then, the contact angle started increasing until the solution concentration was increased to 2 M. As shown with the SEM images in Fig. 5-29, the samples oxidized in lower concentrations (0.03, 0.1, and 0.5M) showed the nano-sized flakes on the sample surface. When the solution concentration, however, was increased above 1 M, the surface morphology started changing to micro-scale crystal-like structures. The decreasing and then increasing contact angle with the NaOH solution concentration was attributed to the changes of nano/micro-scale surface morphology and oxide composition. Interestingly, it was also seen that increasing the treatment time from 24 to 72 hrs increased the contact angle of the samples oxidized in lower concentrations than 1 M concentration, while an opposite behavior was observed for the samples treated in 2 and 5 M concentrations. The error bars were included in the graph to show the variation in the contact angle measurements of each sample.

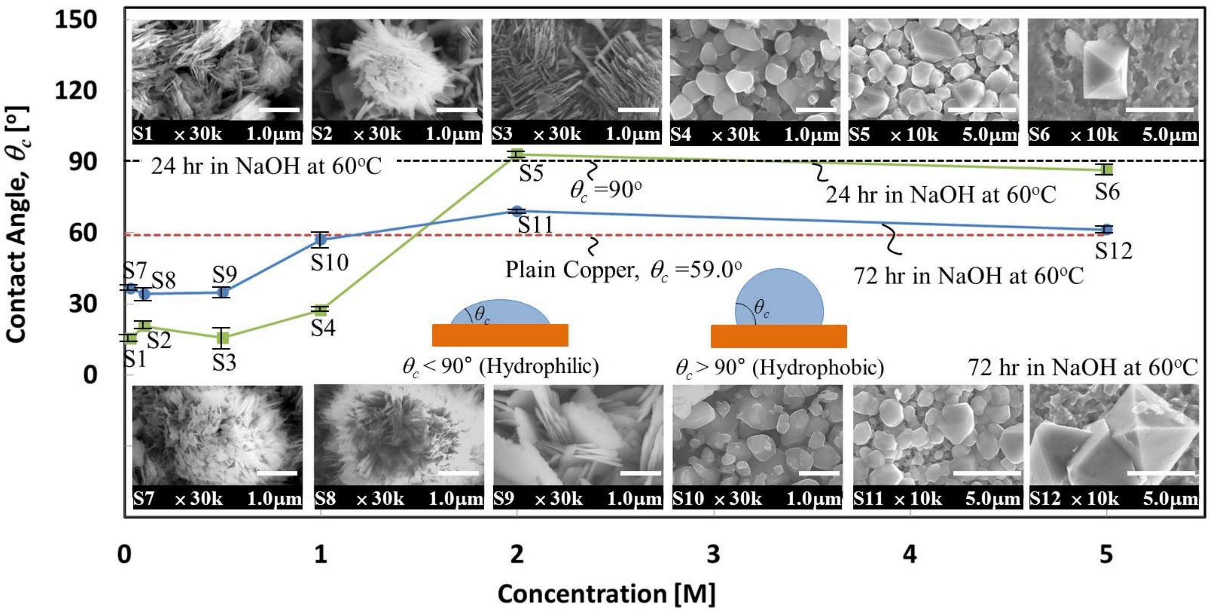

Figure 5-29. Change of the contact angle of sessile water drop with the NaOH concentration and oxidation time.

Figure 5-30 shows the photos of the (a) plain and (b) oxidized copper tubes. The plain copper tubes as shown in Fig. 5-30(a) were oxidized in 0.1M NaOH aqueous solution for 48 hours at 60°C to obtain the oxidized tubes shown in Fig. 5-30(b). This processing condition was determined based on the wettability results obtained in the previous quarterly report. It was seen in the previous report that the samples oxidized in 0.1M NaOH aqueous solution showed high wettability (low contact angle).

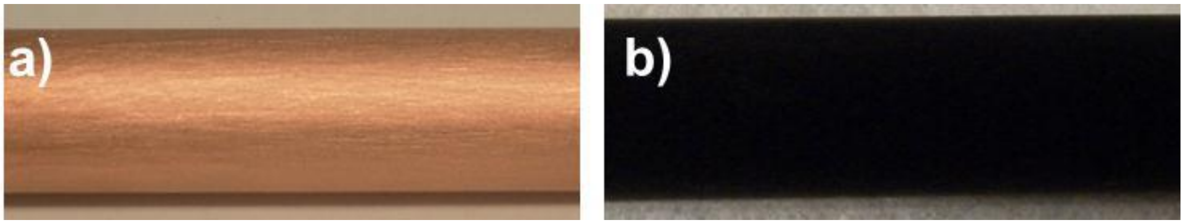

Figure 5-30. Photos of the (a) plain and (b) oxidized tubes.

Task 5.6 Heat Transfer Performance Characterization Experiment of the Micro-Scale, Structured Porous Surface with Hydrophilic/Hydrophobic Coating

Figure 5-31 shows the comparison of the heat transfer rates ($Q_{h,j}$) of the heating fluid for each row of the oxidized tubes with varying the solution fluid flow rate. Note that the heating fluid flow rates were kept the same. However, the Reynolds number of the heating fluid for each row of tubes slightly varies due to the change in the fluid properties, which change with the fluid temperature. Note that the heating fluid started its circulation from the bottommost (4th row) tube. As the heating fluid traveled through the tubes, its temperature became lower as a result of heat transfer, reaching its lowest wall superheat value at the topmost (1st row) tube.

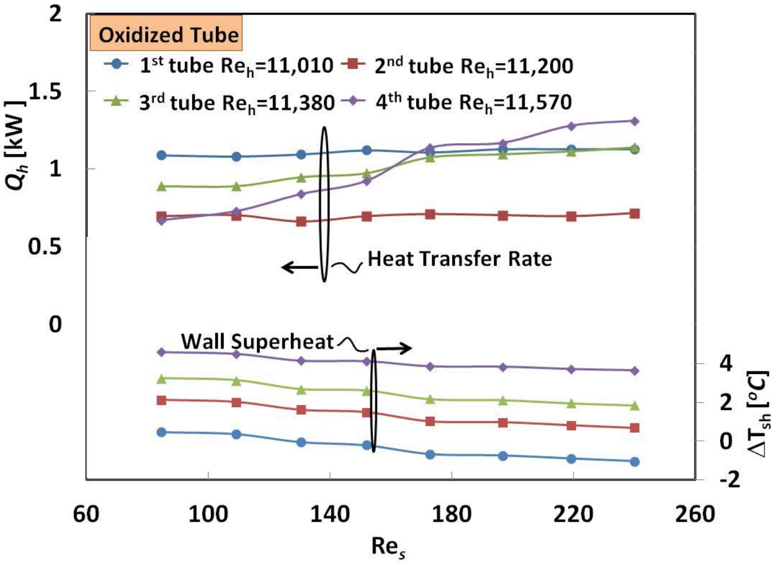

Figure 5-31. Comparisons of heat transfer rates and superheats for different rows of the oxidized tubes.

As shown in Fig. 5-31, 1st and 2nd rows of the oxidized tubes showed constant heat transfer rates with increasing solution flow rates. The visual inspection from the transparent chamber during the heat transfer experiments showed that the upstream (1st and 2nd) oxidized tubes in the setup were almost fully wetted even at the low solution flow rates. Since there was no major wetted area change with solution flow rates, the heat transfer rates remained constant as well. However, the 3rd and 4th rows of the oxidized tubes showed increasing heat transfer rates with solution flow rate. This is because the downstream (3rd and 4th) tubes suffered from dry-out patches significantly at low solution flow rates. It can also be seen from Fig. 5-31 that at high solution flow rates the 3rd and 4th rows of the oxidized tubes gave similar heat transfer rates with the 1st and 2nd tube rows. This is because the downstream tubes had higher superheat values than the upstream tubes but have similar wettability at high solution flow rates.

Figure 5-32 shows the comparison of the heat transfer rates for each row of tubes by varying flow rates of both the heating and solution fluids. The results are given for three different tube surfaces (plain, oxidized, and porous-layer coated). Figure 5-32(a) shows the comparison of the heat transfer rates for the 1st tube row (topmost) in the tube array. It was seen that the heat transfer rate is increased as the heating fluid Reynolds number is increased. It was also seen that increasing the solution fluid Reynolds number increased the heat transfer rate slightly for all three surfaces. Since the 1st tube row was the topmost tube in the tube array, it was directly affected by the solution fluid flow coming out of the dispenser. Since the velocity of the jet stream from the dispenser became higher for higher solution flow rates, the heat transfer rates further increased due to the heat transfer enhancement by jet impingement. Figure 5-32(a) also shows that the 1st row of the oxidized tubes exhibited a higher heat transfer rate ($Q_{h,j}$) than the plain and porous-layer coated tubes.

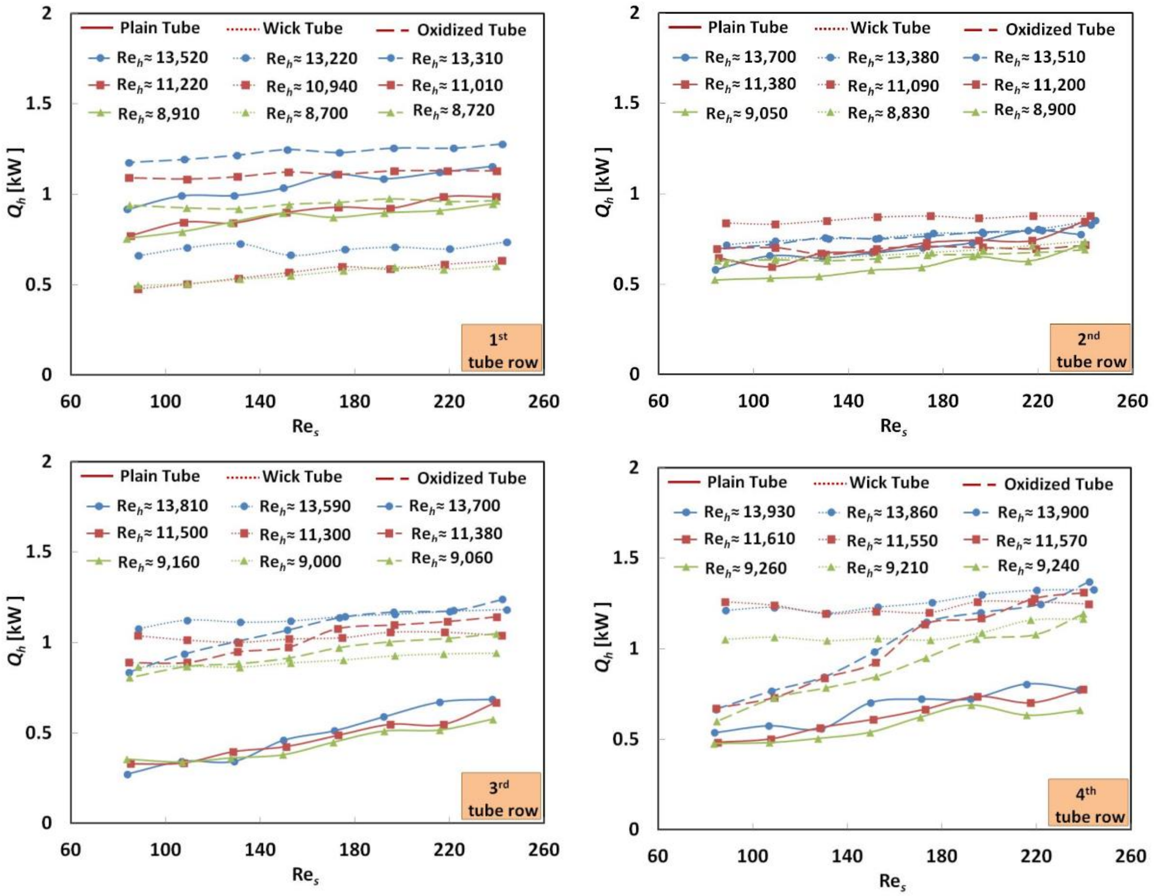

Figure 5-32. Comparison of the heat transfer rates of the plain, oxidized, and porous-layer coated tubes for (a) 1st, (b) 2nd, (c) 3rd, and (d) 4th rows in the tube array.

As shown in Fig. 5-32(b) for the 2nd tube row, all types of surfaces gave similar heat transfer rate results. Figures 5-32(c) and (d) show the comparison of the heat transfer rates for the 3rd and 4th tube rows, respectively. As shown in the figures, the porous-layer coated tubes had much higher $Q_{h,j}$ values than the plain tubes at low solution Reynolds numbers. The 3rd row of the oxidized tubes gave higher heat transfer rates than the plain tubes but gave lower heat transfer rates than the porous-layer coated tubes for low solution flow rates. Both the oxidized and the porous-layer coated tubes showed similar results at high solution flow rates. As shown in Fig. 5-32(d), the heat transfer rate difference between the plain or oxidized and porous-layer coated tubes at low solution flow rates increased for the 4th tube rows in the array. This is attributed to the fact that the wetted area is rapidly decreased as the solution flow rate is decreased for the lower rows of the plain and oxidized tubes, but remains constant for the porous-layer coated tubes for all solution flow rates.

Figure 5-32 also shows that the heat transfer rates for all rows of the plain tubes were always increased with the solution flow rate because of the increased surface wetting. In contrast, the porous-layer coated tubes showed little or no increase in the heat transfer rates with the increased solution Reynolds number indicating that the surface wetting was already complete. It was also seen that the oxidized tubes gave better results than the plain tubes due to their higher wettability; however, the 3rd and 4th rows of the oxidized tubes showed lower heat transfer rates than the porous-layer coated tubes at low solution flow rates.

Figure 5-33 shows the comparison of the heat transfer rates for the plain, oxidized, and porous-layer coated tubes with varying the solution flow rates while keeping the heating fluid flow rate constant. Note that Q_h values plotted in Fig. 5-33 are the total heat transfer rates of the whole tube array. As shown in Fig. 5-33, the heat transfer rate of the heating fluid $Q_{h,tot}$ for the oxidized tubes are lower and higher than those of the porous-layer coated tubes at low and high solution flow rates, respectively. Although there was no difference in wetted area between the oxidized and porous-layer coated tubes at high solution flow rates, the porous-layer coated tubes gave lower heat transfer rates than the oxidized tubes due their additional conduction resistance through the coating. However, the oxidized tubes suffered from un-wetted areas at low solution flow rates, which resulted in their lower heat transfer rates than the porous-layer coated tubes at low solution flow rates.

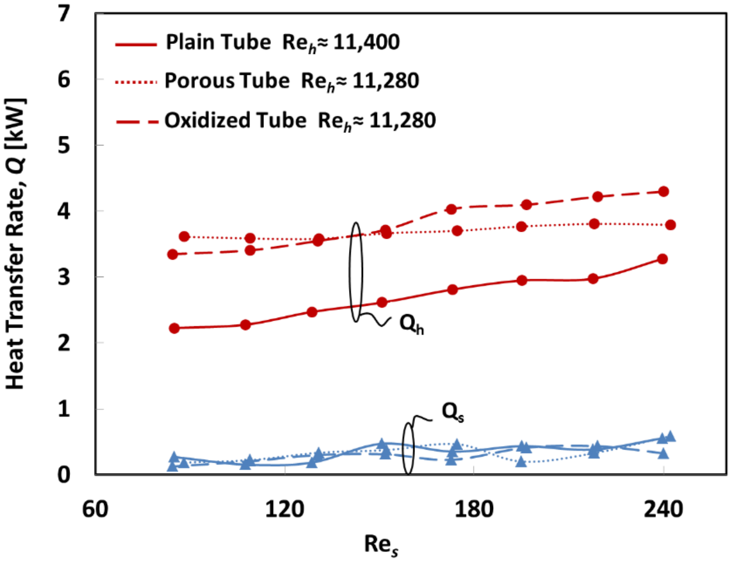

Figure 5-33. Comparison of the overall heat transfer rates for the plain, oxidized, and porous-layer coated tubes.

Figure 5-33 also shows that the plain tubes always gave lower heat transfer rates than the other two types of tubes but the difference became smaller at high solution flow rates due their higher wettability. The sensible heat transfer rates (Q_s) for all three tubes are also shown in Fig. 5-33. It was seen that the Q_s values for all three types of tubes were almost the same.

The uncertainties of the heat transfer experiment are listed in Table 5-11. It can be seen that the 3rd row of plain tubes showed the highest uncertainty in ($Q_{h,j}$). This is because of the small temperature difference across the heating side of the plain tube.

Figure 5-34 shows the photos of the surfaces of the plain, oxidized, and porous-layer coated tubes. The plain tubes were made of copper. The oxidized tubes were fabricated by chemically oxidizing the plain copper tubes in 0.1M NaOH aqueous solution for 48 hrs. The porous-layer coated tubes were obtained by directly sintering (diffusion bonding) the micro-scale copper particles (average diameter of 75μm) onto the plain copper tubes. The earlier study on the falling-film evaporation enhancement using the porous-layer coated tubes reported that a complete wetting of the evaporator tubes is achieved by the capillary action in the porous layer. A surface wetting visualization and a falling-film heat transfer experiment was carried out by using a horizontal-tube falling-film evaporator shown in Fig. 5-35. Three types (plain, oxidized, and porous-layer coated) of the evaporator tubes were tested to compare the surface wetting and heat transfer performances.

Table 5-11. Averaged (maximum) uncertainty values.

			Plain tube	Oxidized tube	Porous-layer coated tube
MEASURED VARIABLES	Pressure	P	±0.25%	±0.25%	±0.25%
	Temperature	T	±0.2^{o}C	±0.2^{o}C	±0.2^{o}C
	Solution Fluid Flow Rate	$\dot{V}_s$	±2.00%	±2.00%	±2.00%
	Heating fluid flow rate	$\dot{V}_h$	±3.00%	±3.00%	±3.00%
CALCULATED VARIABLES	Solution fluid	Q_s	±11.5% (±18.1%)	±17.5% (±42.3%)	±13.3% (±28.5%)
	Heating fluid	$Q_{h,tot}$	±7.48% (±9.94%)	±5.69% (±7.15%)	±5.89% (±6.68%)
		$Q_{h,1}$	±19.7% (±24.0%)	±16.8% (±18.9%)	±30.3% (±38.3%)
		$Q_{h,2}$	±27.6% (±37.8%)	±22.3% (±27.6%)	±23.9% (±30.6%)
		$Q_{h,3}$	±42.1% (±80.3%)	±18.4% (±26.4%)	±18.0% (±20.5%)
		$Q_{h,4}$	±29.8% (±40.9%)	±19.8% (±33.0%)	±15.5% (±18.5%)

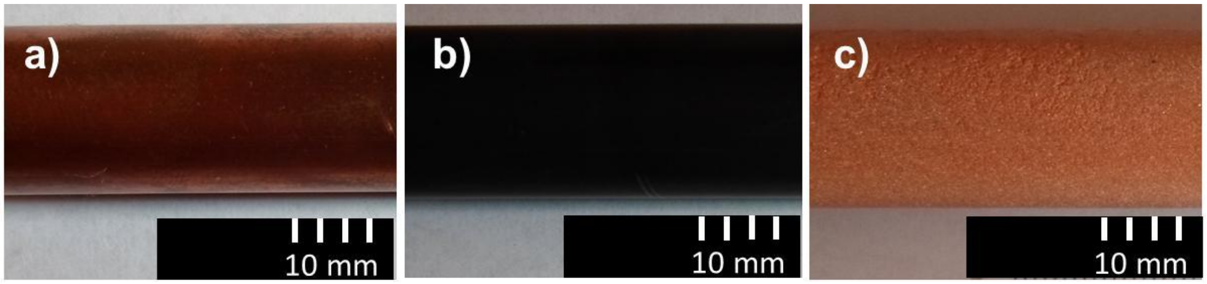

Figure 5-34. Photos of the (a) plain, (b) oxidized, and (c) porous-layer coated tubes used for the experiment.

Figure 5-35(a) shows the schematic of the setup used for the falling-film evaporation experiment, which consists of a vacuum-tight chamber housing two solution fluid dispensers and eight evaporator tubes, plumbing for solution and heating fluids, and instrumentation. The solution dispenser and evaporator tubes were vertically aligned in an inline arrangement of two columns and four rows so that the solution fluid could drip down by gravity from the upper to lower tube rows. The solution fluid was pumped from the solution reservoir to the solution dispenser by a magnetic-driven, variable-speed DC gear pump (MG 209 XPB17, Clark Solutions) controlled by a DC power supply (3006B, Proteck).

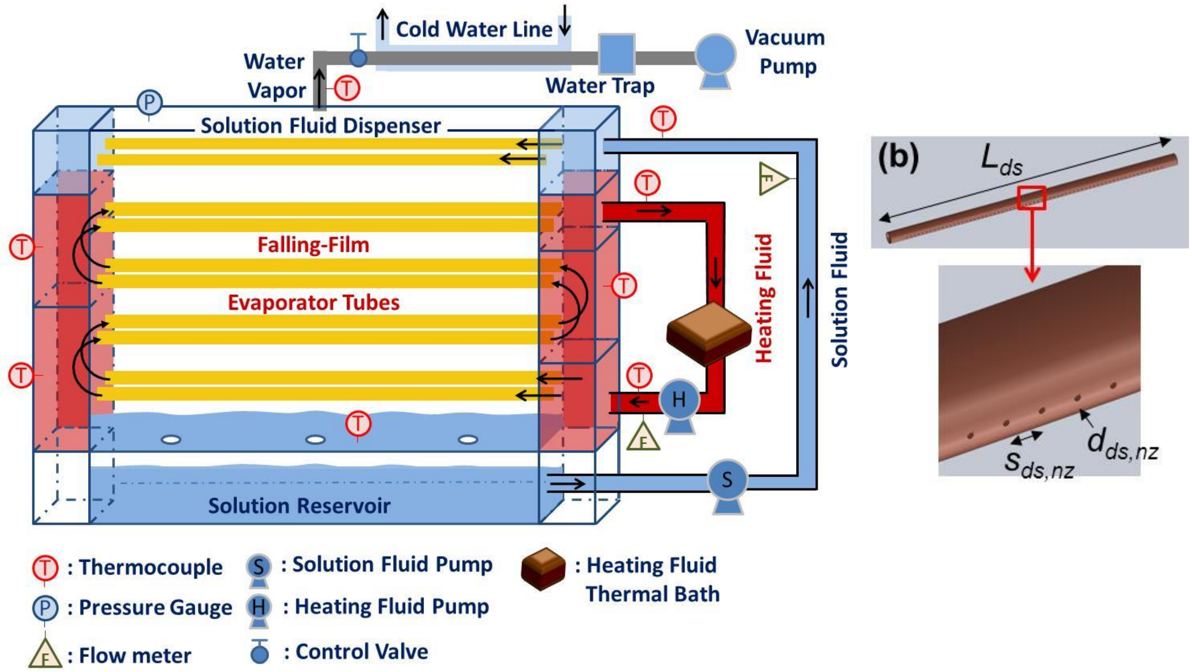

Figure 5-35. (a) Schematic of the experimental setup for a horizontal-tube, falling-film evaporator and (b) the configuration of the solution fluid dispenser.

Figure 5-35(b) shows the configuration of the solution fluid dispenser (L_{ds} = 457 mm). The solution fluid was sprayed from the circular nozzle holes ($d_{ds,nz}$ = 1 mm and $s_{ds,nz}$ = 6.35 mm) at the bottom of the dispenser toward the top of the first tube row. The excess solution fluid was collected at the bottom of the chamber and drained to the solution reservoir, which completes the cycle of the solution fluid circulation. The heating fluid started flowing through the bottommost (4th row) tube to the topmost (1st row) tube in a zigzag pattern. The heating fluid temperature was controlled using a thermal bath (HE30D, Grant Instruments) with 1 kW heating capacity and a temperature controller unit (CN7800, Omega). Additional custom-built heaters (3.5 kW) were also used in the heating fluid line. Distilled water was used for the solution and heating fluids. Note that the solution fluid used in falling-film evaporators is typically a binary fluid (e.g., ammonia solution).

In this study, the falling-film heat transfer experiment was performed using low wall superheats (ΔT_{sh}) less than about 5°C which prevents the nucleation boiling on the evaporator tubes. The sub-ambient pressure in the evaporator chamber was maintained by continually evacuating water vapor generated in the chamber by a vacuum pump (Series L-BV2, Siemens). The reduced chamber pressure was manually regulated by using a control valve in the vacuum line as shown in Fig. 5-35(a).

The visual observation experiment was performed by varying the solution flow rate without heat transfer under ambient conditions. The oxidized copper tubes were prepared by chemically oxidizing the plain copper tubes in a NaOH solution of 0.1 M at 60°C for 48 hrs. The surface wetting of the falling-film evaporator tubes was calculated using the photo images taken during the visualization observation using the plain, oxidized, and porous-layer coated tubes. The image processing toolbox in MATLAB was used to calculate the wetting ratio of plain and oxidized tubes. Each individual tube image from a camera was imported into the program. The true color images were then converted into binary images to differentiate the wetted and un-wetted areas as black (zero) and white colors (one), respectively. Finally, the wetting ratio of each tube was obtained by summing the number of black pixels and dividing it by the total number of the pixels of the tube image.

Figure 5-36 shows the variation of the surface wetting with the solution flow rate for the three different evaporator tubes. It also shows the critical solution Reynolds numbers ($\mathrm{Re}_{s,cr}$) which refer to the transition solution Reynolds numbers at which the tubes become completely wetted. It is found from the visual observation that the porous-layer coated tubes were always wetted over the entire range of the solution flow rate considered in this study. A higher surface wetting is achieved for the oxidized tubes, especially at the 1st row tubes. The critical solution Reynolds numbers for the plain and oxidized tubes were 114 and 86, respectively. The decrease in the critical solution Reynolds number for the oxidized tubes would lead to a heat transfer enhancement due to thinner liquid layer and therefore smaller thermal resistance than those of the plain tubes. The lower rows of the oxidized and plain tubes showed similar surface wetting performance which are affected by both the liquid spreading and drip locations on the tubes.

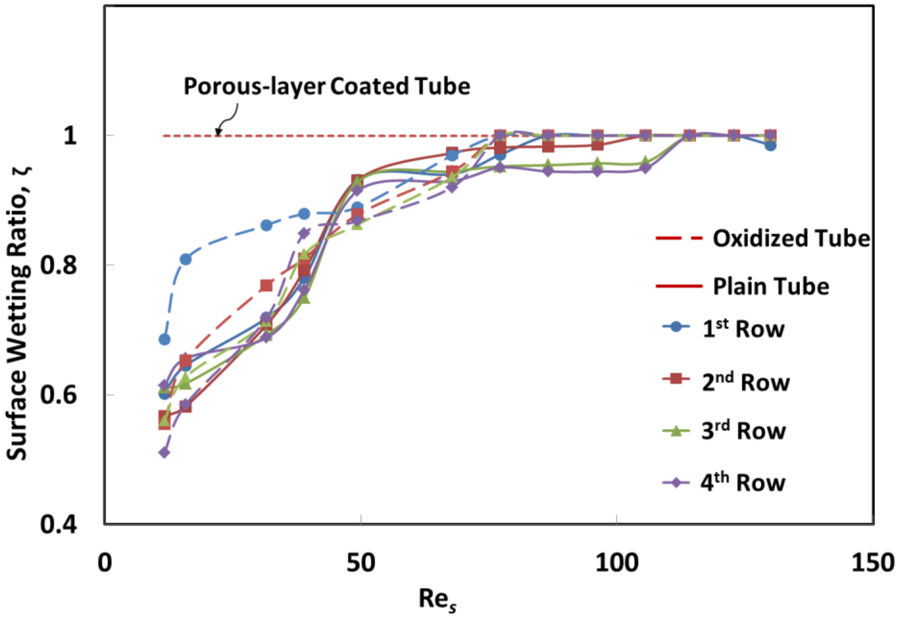

Figure 5-36. Variation of the surface wetting ratio with the solution Reynolds number for the 1st, 2nd, 3rd, and 4th rows of the plain, oxidized, and porous-layer coated tubes tested in the ambient condition.

Figure 5-37 shows the variation of the heat transfer rates ($Q_{h,j}$) of the heating fluid for each row of the oxidized tubes with the solution fluid flow rate. Note that although the heating fluid flow rate were kept constant, as the heating fluid travels through the evaporator tubes, the Reynolds number of the heating fluid for different rows slightly varies due to the change in the fluid temperature and thermo-physical properties. Since the heating fluid started its circulation from the bottommost (4th row) tube, its temperature decreased as it flows through the evaporator tubes. Eventually, the lowest wall superheat was seen for the topmost (1st row) tube. Since the measured solution fluid temperatures were always lower than the evaporator tube surface temperature, it is obvious that the 1st row (topmost) tube experienced mostly sensible heat transfer rather than evaporation heat transfer.

As shown in Fig. 5-37, the 1st and 2nd rows of the oxidized tubes showed constant heat transfer rates with the solution flow rate. Recalling that $Re_{s,cr}$ of the oxidized tubes was obtained as 86 from the visual observation and there was no major change in the wetted area of the 1st and 2nd rows of the oxidized tubes for the solution flow regime used in the heat transfer experiment, the heat transfer rates remained the same. However, the 3rd and 4th rows of the oxidized tubes showed increasing heat transfer rates with increasing solution flow rate. This is because the downstream (3rd and 4th) tubes always suffered from dry-out patches due to the loss and maldistribution of the solution fluid during the evaporation heat transfer experiment. It can also be seen from Fig. 5-32 that at high solution flow rates the 3rd and 4th rows of the oxidized tubes gave similar or exceeding heat transfer rates as compared to the 1st and 2nd tube rows. This is because the downstream tubes always had higher wall superheats than the upstream tubes and the same time, they had high surface wetting at the high solution flow rates.

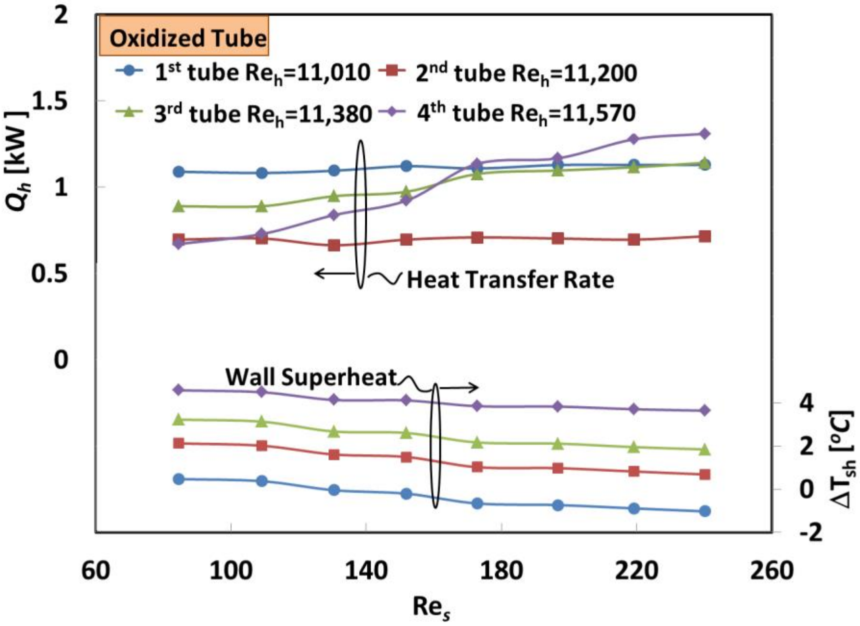

Figure 5-37. Comparisons of the heat transfer rates and wall superheats for the 1st, 2nd, 3rd, and 4th rows of the oxidized tubes tested in the evaporator.

Figure 5-38 shows the heat transfer rates ($Q_{h,j}$) of each tube row of three different evaporator tubes (plain, oxidized, and porous-layer coated) by varying flow rates of both the heating and solution fluids. Figure 5-38(a) shows the heat transfer rates for the 1st tube row (topmost) in the tube array. It was seen that the heat transfer rate was increased as the heating fluid Reynolds number was increased. It was also seen that increasing the solution fluid Reynolds number increased the heat transfer rate slightly. Since the 1st tube row in the tube array is affected by the high-velocity solution fluid flow from the dispenser holes (jet impingement), the heat transfer rate was much higher than those of the other rows. Figure 5-38(a) also shows that the 1st row of the oxidized tubes exhibited the greatest heat transfer rate than the plain and porous-layer coated tubes. In Fig. 5-38(b) for the 2nd tube row, all types of the tubes gave similar heat transfer rate results.

Figures 5-38(c) and (d) show the heat transfer rates for the 3rd and 4th tube rows, respectively. As shown in the Figures, the plain tubes gave lowest heat transfer rate as compared to the other tubes, while the porous-layer coated tubes had higher heat transfer rate than the oxidized tubes, especially at low solution flow rates. Both the oxidized and the porous-layer coated tubes showed similar results at high solution flow rates. In Fig. 5-38(d) for the 4th tube row, the heat transfer rates between the three types of the tubes are greatly different depending on the solution flow rates. The porous-layer coated tubes showed little or no increase in the heat transfer rates for all solution flow rates because of the complete surface wetting. In contrast, the heat transfer rates for the plain tubes were always increased with the solution flow rate because of the increased surface wetting. It was also seen that the oxidized tubes always outperformed the plain tubes due to better wetting.

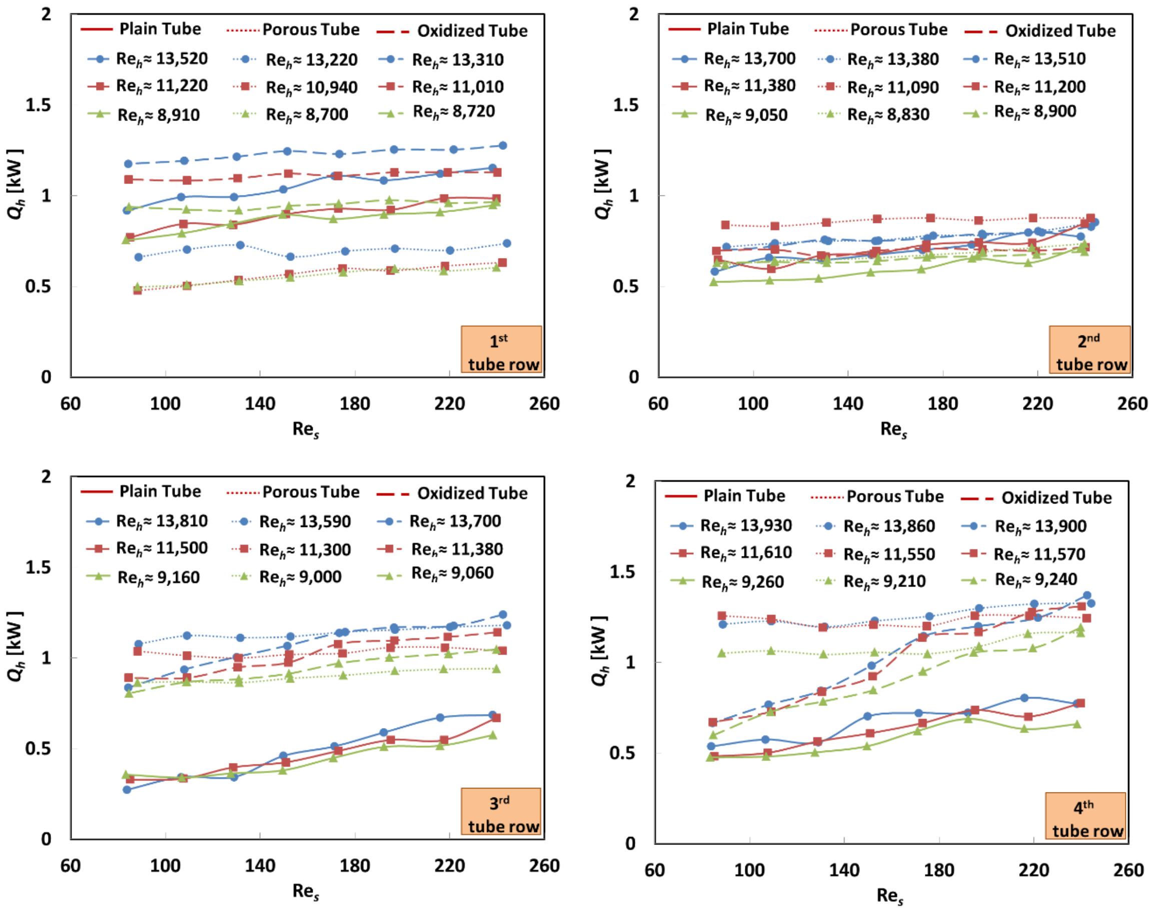

Figure 5-38. Comparison of the heat transfer rates and wall superheats of the plain, oxidized, and porous-layer coated tubes for (a) 1st, (b) 2nd, (c) 3rd, and (d) 4th rows tested in the evaporator.

Figure 5-39 shows the comparison of the total heat transfer rates ($Q_{h,tot}$) of the tube arrays for the plain, oxidized, and porous-layer coated tubes with the solution flow rates while keeping the heating fluid flow rate constant. As shown in Fig. 5-39, the heat transfer rate for the oxidized tubes was lower and then higher than the porous-layer coated tubes at low and high solution flow rates, respectively. Although there was no major difference in the wetted area between the oxidized and porous-layer coated tubes at high solution flow rates, the oxidized tubes gave higher heat transfer rates than the porous tubes. This is due to the less thermal resistance of the thin layer of liquid on the oxidized tubes as compared to the porous tubes having a porous copper coating (~0.8 mm thick) covered by a liquid layer. However, the downstream rows of the oxidized tubes suffered from un-wetted areas at low solution flow rates and thus caused lower heat transfer rates than the porous-layer coated tubes at low solution flow rates. Figure 5-39 also clearly shows that the plain tubes underperformed the other types of the tubes but the gap became smaller at high solution flow rates due improved surface wetting. The sensible heat transfer rates (Q_s) for all three tubes are also compared in Fig. 5-39. The values for all three tubes were almost the same.

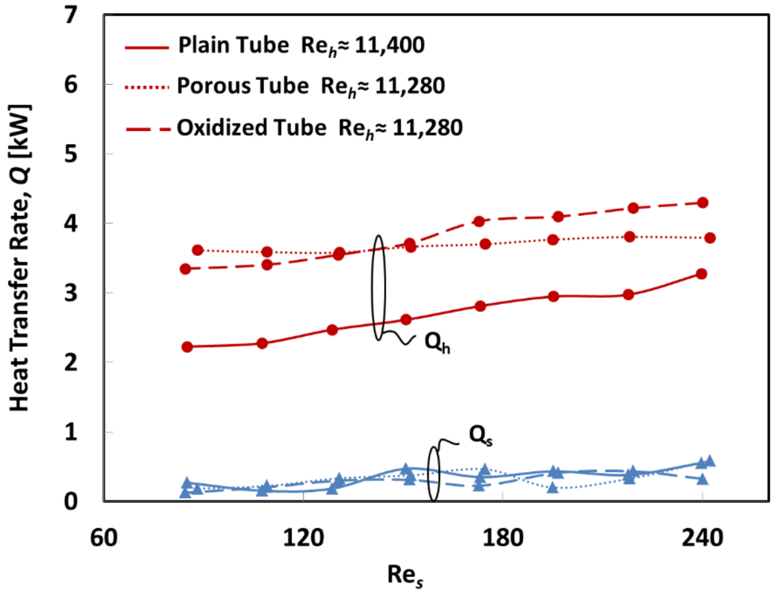

Figure 5-39. Comparison of the overall heat transfer rates for the plain, oxidized, and porous-layer coated tubes tested in the evaporator.

The first task in this project was to design a strong, reliable chamber as housing for the falling-film heat exchanger. Various improvements were made to the previous falling-film system used by this group. By changing the material of the heat exchanger body from acrylic to stainless steel, the chamber was able to withstand any vacuum pressure without fear of structural failure. The stainless steel also allows for a much longer lifetime, since it is far less likely to develop leaks over time when compared to its acrylic predecessor. The system was made to be more compact than the previous model as a means of maximizing space and minimizing cost. Although stainless steel was used for majority of the chamber, the front and chamber walls were made from 1 inch thick acrylic, such that visualization was possible. The first step in the design process was to create a model of the new falling-film heat exchanger in SolidWorks. After multiple iterations, the design was finalized for production. An exploded view of the SolidWorks model is shown in Fig. 5-40.

The body was constructed from 12 custom designed 304 SS parts. The perimeter and holes cut into the stainless steel were cut using a water jet and a CNC machine. Since water jet cutting is only suitable for through cuts, the blind cuts were made using a carbide milling tip attached to the CNC machine. The outer side plates and windows were designed to be the only removable parts on the chamber, being bolted onto the body and sealed by O-rings. This was done so that the system could be retrofitted for future changes simply by designing new side plates. Once all parts were fabricated, they were then welded together to provide maximum strength and minimal chance of leakage. A photograph taken during the welding stage of the fabrication process is given in Fig. 5-41.

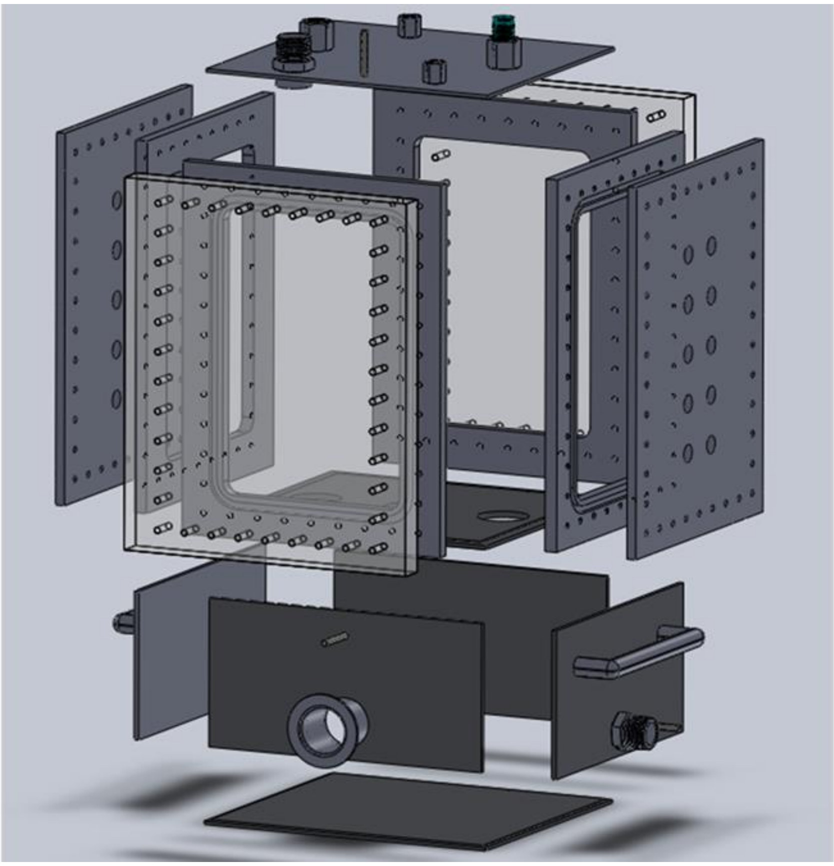

Figure 5-40. Exploded view of the falling-film heat exchanger designed in SolidWorks.

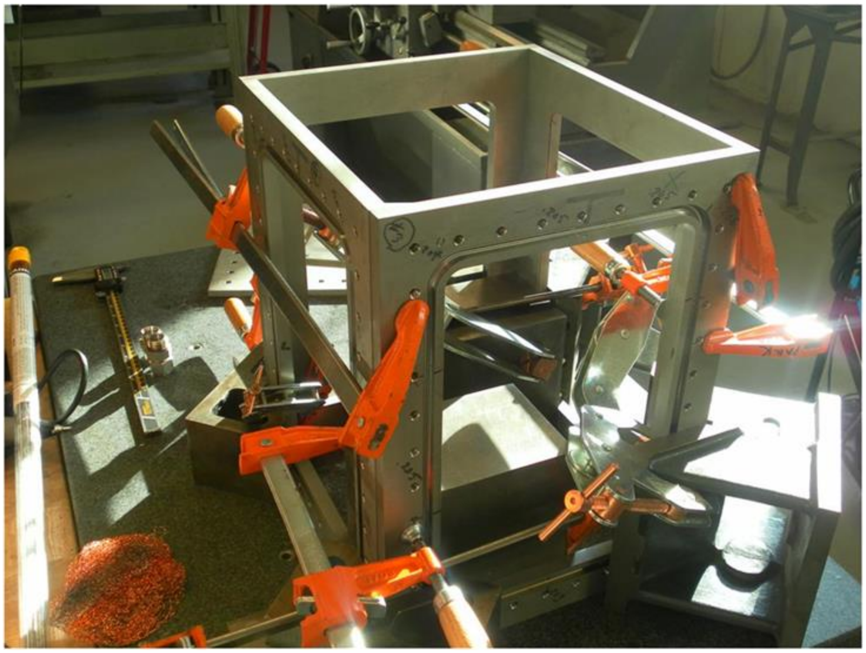

Figure 5-41. Photo of the heat exchanger body during the welding portion of the fabrication process.

Further improvement was made to the system by implementing a new manifold design. Each side consisted of multiple, separate acrylic manifolds that were connected to the evaporator tubes using Sharkbite tube fittings. This allowed for easy troubleshooting and assembly/disassembly. The manifolds also allow for easy temperature probing of tube inlet and outlets. Heat loss to the ambient from the exposed copper tubing outside of the chamber was minimized by custom fitting three inch thick cork insulation to the outer walls of the heat exchanger, as shown in Fig. 5-42(a).

The solution outlet temperature measurement method was also improved. By welding a small "slide" to the underside of the chamber floor, the fresh solution fluid was forced to run down this slide prior to reaching the lower reservoir of the system. The solution outlet temperature probe was place such that the water running down the slide always runs over the thermocouple, allowing for accurate instantaneous solution fluid temperature measurement. A schematic of this slide temperature probing method is given in Fig. 5-42(b).

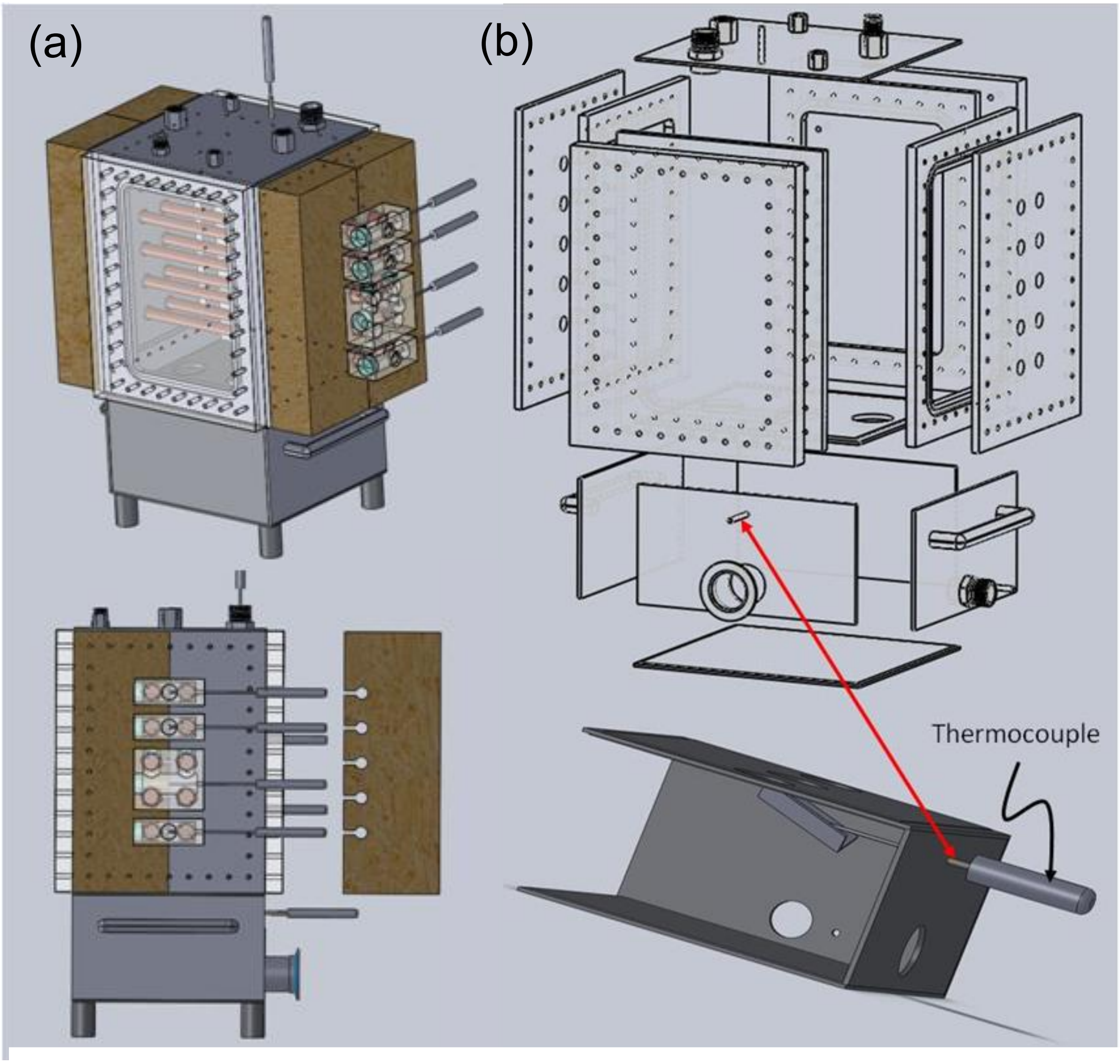

Figure 5-42. Solidworks models showing (a) insulation method and (b) solution outlet temperature probe.

The chamber was constructed in two distinct sections: the upper heat exchanger section and the lower solution reservoir section. Each section was welded and pressure tested separately with a relatively high positive pressure (>50psig) to ensure quality sealing. The bubble test method was employed as a means of finding pinhole leaks in the weld joints. Once all leaks were found and sealed, the two separate portions of the system were welded together. A final bubble test method was performed on the entire system and excellent sealing was observed. A photograph of the final evaporator system is given in Fig. 5-43.

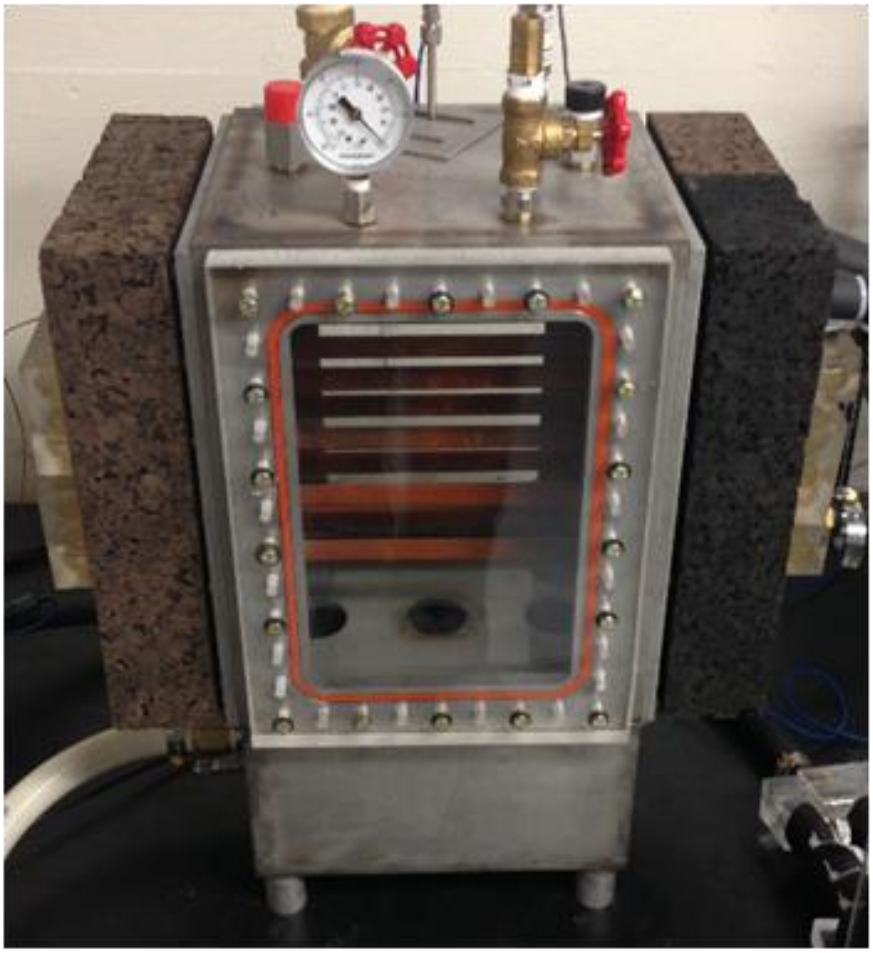

Figure 5-43. Photo of the final stainless steel, horizontal-tube, falling-film heat exchanger.

Figures 5-44(a) and (b) show the schematic of the stainless steel heat exchanger and the actual setup used for the falling-film experiment, respectively. It consists of a vacuum-tight chamber housing two solution dispensers and eight evaporator tubes, plumbing for solution and heating fluids, and all necessary instrumentation. The solution dispenser and evaporator tubes were vertically aligned in an inline arrangement of two columns and four rows such that the solution fluid could drip down from the upstream tubes to the downstream tubes via gravity. The solution fluid was pumped from the solution reservoir to the solution dispenser by a magnet-driven, variable-speed DC gear pump (MG 209 XPB17, Clark Solutions) controlled by a DC power supply (3006B, Proteck).

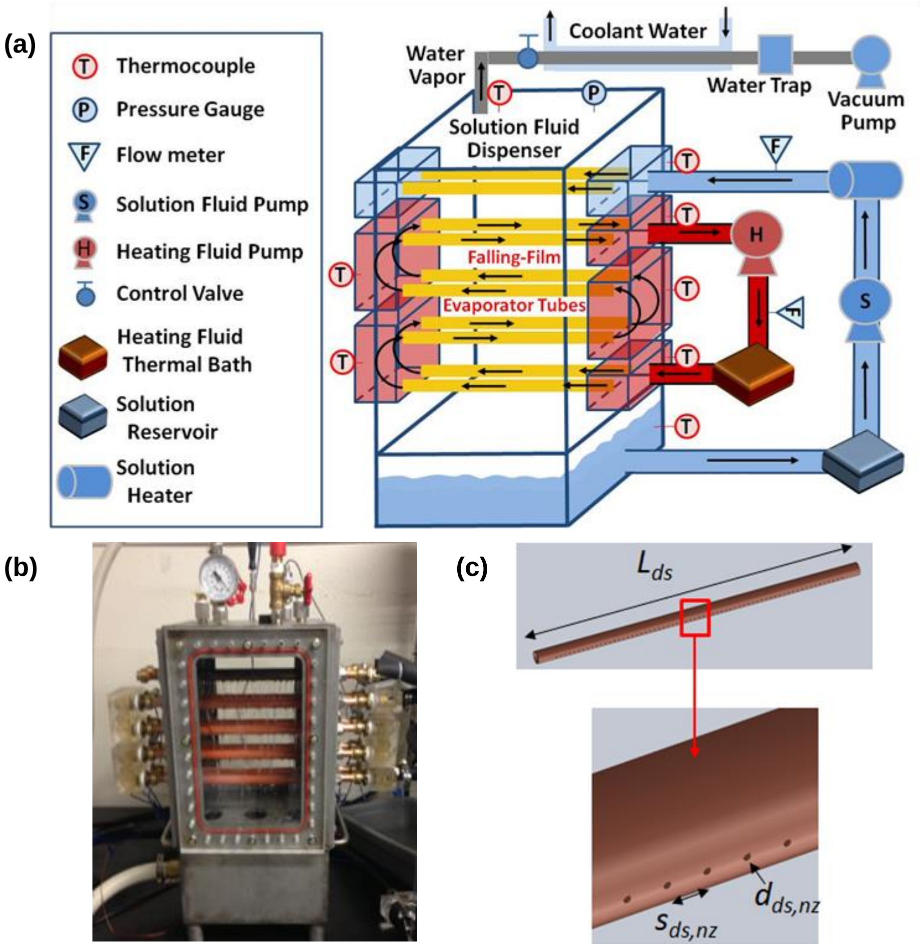

Figure 5-44. (a) Schematic and (b) actual picture of the experimental setup for a horizontal-tube, falling-film evaporator and (c) the configuration of the solution fluid dispenser.

Figure 5-44(c) shows the configuration of the solution fluid dispenser (L_{ds} = 279.4mm). The solution fluid was sprayed from the circular nozzle holes ($d_{ds,nz}$ = 1 mm and $s_{ds,nz}$ = 6.35 mm) at the bottom of the dispenser toward the top of the first tube row. The excess solution fluid was collected at the bottom of the chamber and drained to the solution reservoir, which completes the cycle of the solution fluid circulation. The heating fluid started flowing through the bottommost (4th row) tube to the topmost (1st row) tube in a zigzag pattern. The heating fluid temperature was controlled using a thermal bath (HE30D, Grant Instruments) with 1 kW heating capacity and a temperature controller unit (CN7800, Omega). Additional custom-built heaters (6.3 kW) were also used in the heating fluid line. Distilled water was used for the solution and heating fluids. Note that the solution fluid used in falling-film evaporators is typically a binary fluid (e.g., ammonia solution).

The first experiment involved comparing the heat transfer results for the plain tubes for three different subcooling conditions as well as three different wall superheat conditions. Solution subcooling is defined in this study as the temperature differential between the solution inlet and the saturation temperature of the system. With a 60°C saturation temperature, the solution inlet temperatures tested were 45, 50, and 55°C, which correspond to 15, 10, and 5°C subcooling, respectively. Each of these subcooling values was tested at three different heating fluid inlet temperatures: 55, 60, and 65°C, which correspond to a wide range of wall superheats, depending on the tube row and heating inlet temperature.

Figure 5-45 shows the comparison of heat transfer rates for these various inlet temperature conditions. The arrows stretching up from the abscissa delineate the points at which heat transfer dominance switches from evaporation dominance to sensible dominance. For the low superheat case (Fig. 5-45(a), T_{hi}=65°C), it is seen that only the lowest subcooling condition shows any substantial evaporation. This is because evaporation is governed by film thickness and wall superheat. Since the superheat is so low for the T_{hi}=65^{o}C case, the only time evaporation is substantial is at the lowest solution flow rates, where the film thickness is thinnest.

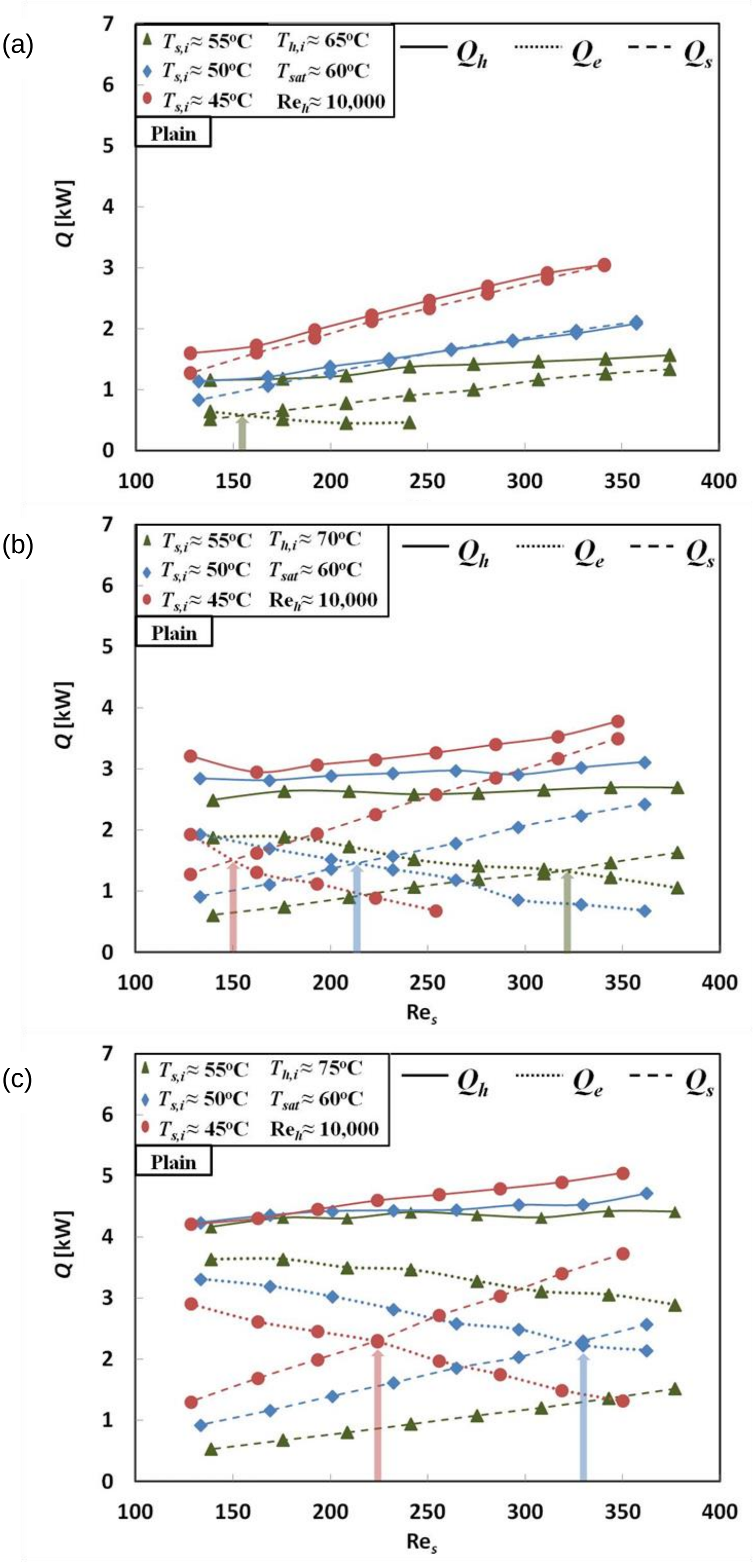

Figure 5-45. Effect of solution subcooling for heating fluid inlet temperatures of (a) 65^{o}C (b) 70^{o}C and (c) 75^{o}C.

The moderate superheat case (Fig. 5-45(b), T_{hi}=70^{o}C) shows evaporation playing a much more significant role for all of the investigated subcooling conditions, each showing a switch in dominance from two-phase to single-phase dominance. At the lowest subcooling case of 5^{o}C, the heat transfer is made up of mostly evaporation until about Re_s = 320, at which point it becomes sensibly dominant. With added subcooling, the transition Re_s decreases. This is due to the fact that more sensible energy must be added to the solution fluid before it reaches saturation temperature and is able to evaporate. It is for this reason that the high subcooling case of 15^{o}C shows a transition very early in the flow regime, at about Re_s = 150. It can also be seen from Fig. 5-45(b) that a distinct increase in the slope of the heat duty plot is seen with increasing subcooling. This is because single-phase heat transfer is a function of driving temperature differential as well as convective heat transfer coefficient. As Re_s increases, so does the convective heat transfer coefficient and therefore sensible heat transfer is enhanced.

When the superheat is raised to the highest investigated value [Fig.5-45(c), T_{hi}=75^{o}C], the transition point for each subcooling condition moves to the right, meaning that evaporation remains the dominant heat transfer method for higher solution Reynolds numbers. This is because the added superheat brings the solution to saturation temperature faster as well as promoting greater evaporation heat transfer. It can be seen from Fig. 5-45(c) that the lowest subcooling value of 5^{o}C shows no transition point, remaining evaporation dominated throughout the entire solution flow regime investigated in this study.

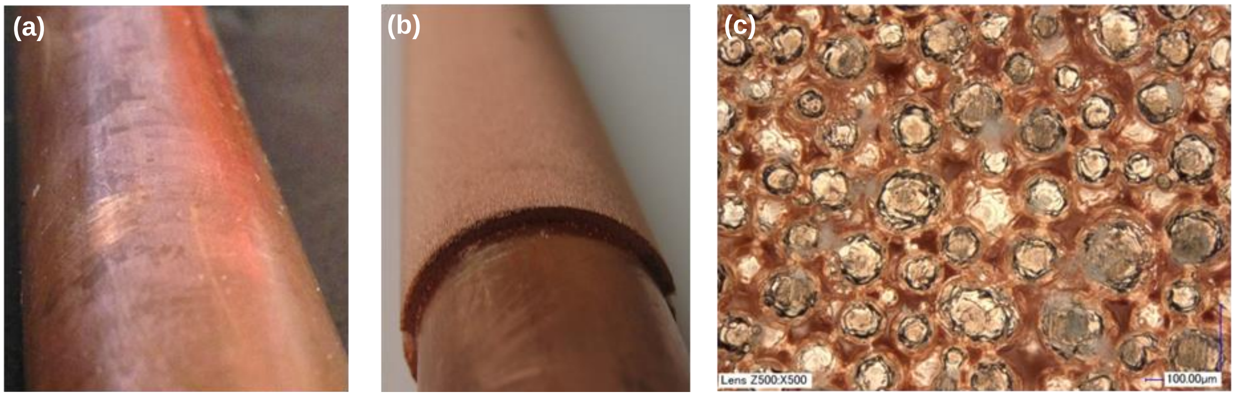

Figure 5-46. Photos of the (a) plain, (b) porous-layer coated tubes and (c) porous-layer coating at 500x magnification.

Figure 5-46 shows the photos of the surfaces of the plain and porous-layer coated tubes, along with the porous coating at 500x magnification. The plain tubes were made of copper. The porous-layer coated tubes were obtained by directly sintering (diffusion bonding) the micro-scale copper particles (average diameter of 75μm) onto the plain copper tubes. The earlier study on the falling-film evaporation enhancement using the porous-layer coated tubes reported that a complete wetting of the evaporator tubes is achieved by the capillary action in the porous layer. In this study, the two types of the evaporator tubes (plain and porous-layer coated) were to be tested to compare the heat transfer performance under various subcooling and superheat conditions.

Figure 5-47 shows the comparison of the plain and porous-layer coated tube heat transfer rates for various subcooling and wall superheat conditions. The colored arrows spanning from the abscissa designate transition from evaporation to sensible heat transfer dominance. It can be seen from Fig. 5-47 that the solution subcooling and wall superheat affect the porous-layer coated tubes in much the same way as the plain. Added superheat works to increase overall heat duty as well as promote evaporation, moving the dominance transition to a higher solution Reynolds number. Added solution subcooling works to increase sensible heat transfer by increasing the amount of energy needed to heat the solution to saturated conditions. Since sensible heat transfer is a function of driving temperature differential and convective heat transfer coefficient, an increase in solution flow rate (which in turn increases the convective heat transfer coefficient) increases sensible heat transfer. It is because of this fact that the slope of the heat duty plots with solution Reynolds number increases with added subcooling.

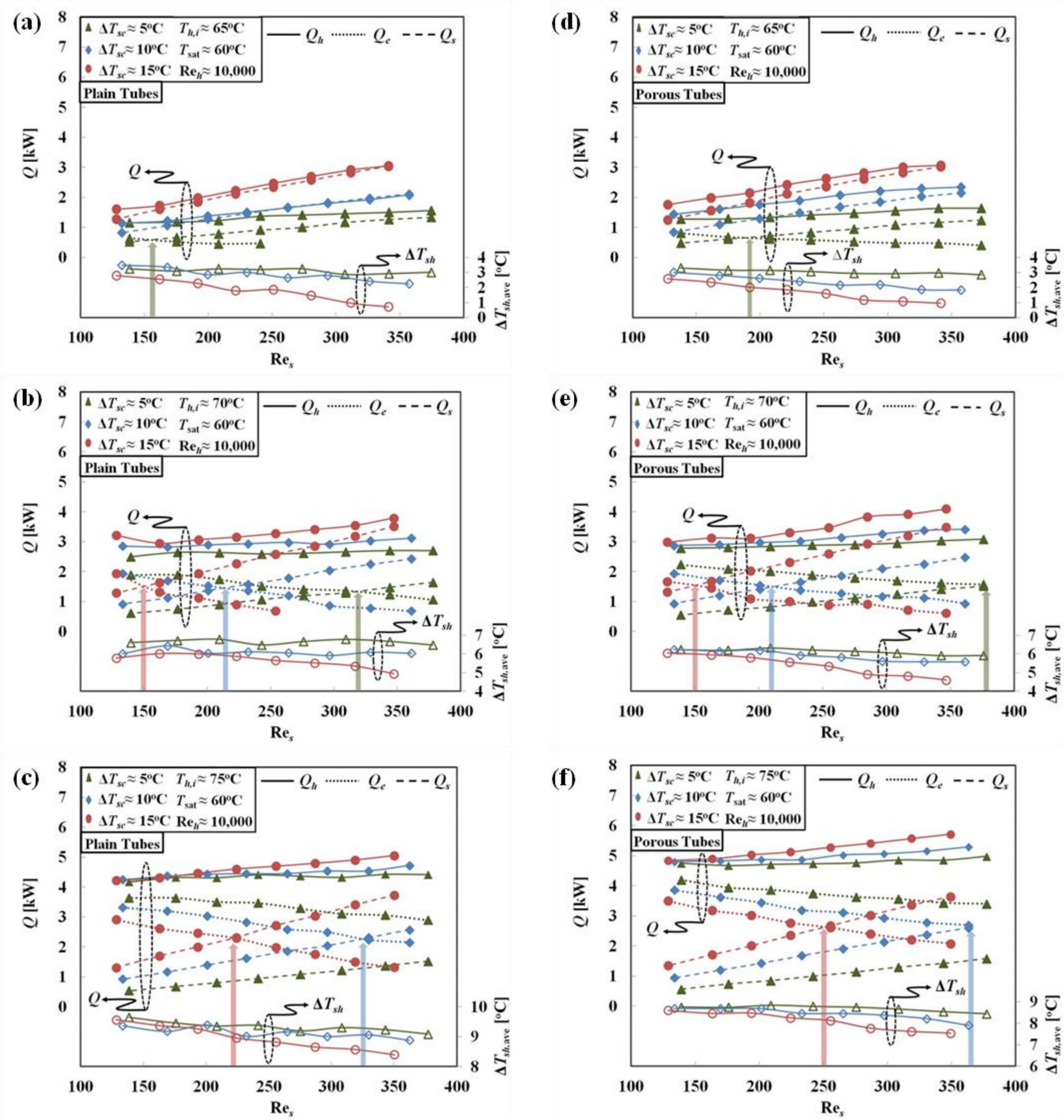

Figure 5-47. Heat transfer rates and average superheat for the plain tubes at (a) T_{hi}=65°C, (b) T_{hi}=70°C, (c) T_{hi}=75°C and for the porous-layer coated tubes at (d) T_{hi}=65°C, (d) T_{hi}=70°C, (f) T_{hi}=75°C.

Previous work has shown that the enhancement realized through use of the porous-layer coating is most significant in an evaporation dominated regime. Also, it was shown that for the plain tube surface, an evaporation dominated regime can be promoted with low solution subcooling, high wall superheat, and low solution Reynolds number. When comparing the plain and porous-layer coated tube performances, it can be seen that the dominance transition is moved to the right, meaning that evaporation dominance can be sustained at higher solution Reynolds number. For example, the high superheat case (Fig. 5-47(c) and (f) for the plain and porous-layer coated tubes, respectively) shows that the transition point has shifted right for all three subcooling conditions, although the 5°C subcooling transition point is outside of the flow regime analyzed in this study. This is due to two major effects brought about by the porous layer. First, the interconnected network of pores making up the coating works to passively pump fluid across the tube surface by capillary action, allowing for the entire tube surface to remain saturated with fluid at much lower solution flow rates when compared to the plain tube surface. Secondly, the menisci of curvature created within the coating create many triple-phase contact lines, where the liquid film is exceedingly thin and the thermal resistance to phase change is minimal. Since both of these unique features enhance evaporation heat transfer, the dominance transition shifts to a later point.

Figure 5-48 shows a direct comparison of the two tube surfaces under evaporation dominated conditions, i.e. high superheat, low solution subcooling. It can be seen from Fig. 5-48 that the porous-layer coated tubes outperform the plain tubes by as much as 20% throughout the entire flow regime investigated. It is also evident from the individual sensible and evaporative heat transfer plots that the sensible heat transfer remains almost the same while the evaporation plot is increased. This proves that once the flow rate is such that the plain tubes are fully wetted, the enhancement brought about by the porous-layer coated tubes is strictly through increased evaporation heat transfer.

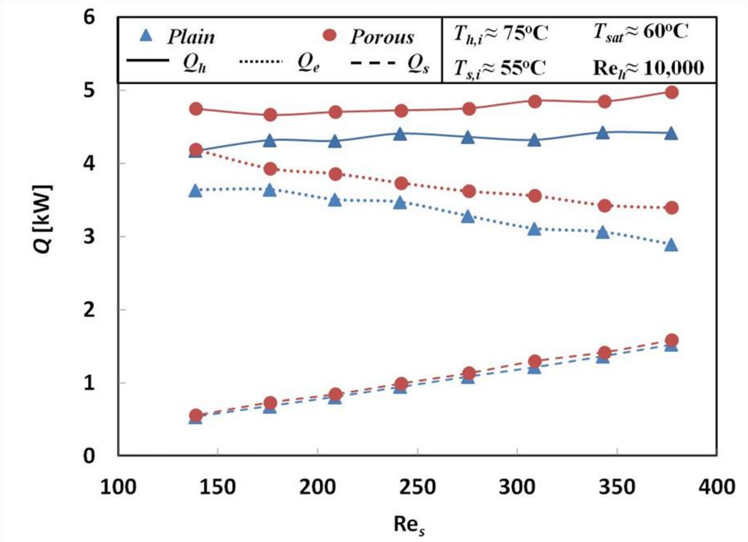

Figure 5-48. Heat transfer comparison of the plain and porous –layer coated tubes under evaporation dominant conditions i.e., low solution subcooling, high wall superheat.

Reference

[1] Y. Fujita and M. Tsutsui, "Experimental investigation of falling film evaporation on horizontal tubes," *Heat Transfer - Japanese Research,* vol. 27, pp. 609-618, 1998.

[2] G. Ribatski and A. M. Jacobi, "Falling-film evaporation on horizontal tubes - A critical review," *International Journal of Refrigeration,* vol. 28, pp. 635-653, 2005.

[3] J. R. Thome, "Falling film evaporation: State-of-the-art review of recent work," *Journal of Enhanced Heat Transfer,* vol. 6, pp. 263-277, 1999.

[4] S. Lee, B. Köroğlu, and C. Park, "Experimental investigation of capillary-assisted solution wetting and heat transfer using a micro-scale, porous-layer coating on horizontal-tube, falling-film heat exchanger," *International Journal of Refrigeration,* vol. 35, pp. 1176-1187, 2012.

[5] B. Köroğlu, N. Bogan, and C. Park, "Effect of the Tube Row on Heat Transfer and Surface Wetting of Micro Porous-Layer Coated, Horizontal-Tube, Falling-Film Evaporator," *Journal of Heat Transfer,* vol. 135, p. 041802, 2013.

[6] B. Koroglu, N. Bogan, and C. Park, "Experimental Study of Tube Row effects and Evaporation Heat Transfer Enhancement Using a Micro-Scale, Porous-Layer Coating on a Horizontal-Tube, Falling-Film Heat Exchanger," in *ASME 2012 3rd Micro/Nanoscale Heat & Mass Transfer International Conference*, Atlanta, Georgia, 2012, pp. MNHMT2012-75333.

[7] L. Vasiliev, A. Zhuravlyov, A. Shapovalov, and V. Litvinenko, "Vaporization heat transfer in porous wicks of evaporators," *Archives of Thermodynamics,* vol. 25, pp. 47-59, 2004.

[8] Z. Z. Xia, G. Z. Yang, and R. Z. Wang, "Experimental investigation of capillary-assisted evaporation on the outside surface of horizontal tubes," *International Journal of Heat and Mass Transfer,* vol. 51, pp. 4047-4054, 2008.

[9] J.-K. Kim, C. W. Park, and Y. T. Kang, "The effect of micro-scale surface treatment on heat and mass transfer performance for a falling film H2O/LiBr absorber," *International Journal of Refrigeration,* vol. 26, pp. 575-585, 2003.

[10] Z.-H. Liu and J. Yi, "Enhanced evaporation heat transfer of water and R-11 falling film with the roll-worked enhanced tube bundle," *Experimental Thermal and Fluid Science,* vol. 25, pp. 447-455, 2001.

[11] H. Kuwahara, A. Yasukawa, W. Nakayama, and T. Yanagida, "Evaporative heat transfer from horizontal enhanced tubes in thin film flow," *Heat Transfer - Japanese Research,* vol. 19, pp. 83-97, 1990.

[12] X. Hu and A. M. Jacobi, "The intertube falling film: Part 1: flow characteristics, mode transitions, and hysteresis," *Journal of Heat Transfer,* vol. 118, pp. 616-625, 1996.

[13] J. F. Roques, V. Dupont, and J. R. Thome, "Falling film transitions on plain and enhanced tubes," *Journal of Heat Transfer,* vol. 124, pp. 491-499, 2002.

[14] J.-F. Roques and J. R. Thome, "Falling film transitions between droplet, column, and sheet flow modes on a vertical array of horizontal 19 FPI and 40 FPI low-Finned tubes," *Heat Transfer Engineering,* vol. 24, pp. 40-45, 2003.

[15] X. Zhou and K. Bier, "Pool boiling heat transfer from a horizontal tube coated with oxide ceramics," *International Journal of Refrigeration,* vol. 20, pp. 552-560, 1997.

[16] S. J. Kim, I. C. Bang, J. Buongiorno, and L. W. Hu, "Surface wettability change during pool boiling of nanofluids and its effect on critical heat flux," *International Journal of Heat and Mass Transfer,* vol. 50, pp. 4105-4116, 2007.

[17] H. T. Phan, N. Caney, P. Marty, S. Colasson, and J. Gavillet, "Surface wettability control by nanocoating: The effects on pool boiling heat transfer and nucleation mechanism," *International Journal of Heat and Mass Transfer,* vol. 52, pp. 5459-5471, 2009.

[18] J. Liu, X. Huang, Y. Li, K. M. Sulieman, X. He, and F. Sun, "Hierarchical nanostructures of cupric oxide on a copper substrate: controllable morphology and wettability," *Journal of Materials Chemistry,* vol. 16, pp. 4427-4434, 2006.

[19] J. Liu, X. Huang, Y. Li, Z. Li, Q. Chi, and G. Li, "Formation of hierarchical CuO microcabbages as stable bionic superhydrophobic materials via a room-temperature solution-immersion process," *Solid State Sciences,* vol. 10, pp. 1568-1576, 2008.

[20] T. Oishi, M. Goto, A. Kasahara, and M. Tosa, "Low frictional copper oxide film prepared with sodium hydroxide solution," *Surface and Interface Analysis,* vol. 36, pp. 1259-1261, 2004.

[21] J. Xiao, Y. Chu, Y. Zhuo, and L. Dong, "Amphiphilic molecule controlled synthesis of CuO nano/micro-superstructure film with hydrophilicity and superhydrophilicity surface," *Colloids and Surfaces A: Physicochemical and Engineering Aspects,* vol. 352, pp. 18-23, 2009.

[22] V. Sernas, "Heat transfer correlation for subcooled water films on horizontal tubes," *Journal of Heat Transfer,* vol. 101, pp. 176-178, 1979.